UC Berkeley
UC Berkeley Electronic Theses and Dissertations

Title

New Frontiers in Extragalactic Stellar Metallicity Measurements with Hubble Space Telescope

Permalink

https://escholarship.org/uc/item/9372f4p6

ISBN

9798293893102

Author

Fu, Sal Wanying

Publication Date

2025-07-01

Peer reviewed|Thesis/dissertation

eScholarship.org Powered by the California Digital Library
University of California

New Frontiers in Extragalactic Stellar Metallicity Measurements with Hubble Space Telescope

By

Sal Wanying Fu

A dissertation submitted in partial satisfaction of the

requirements for the degree of

Doctor of Philosophy

in

Astronomy

in the

Graduate Division

of the

University of California, Berkeley

Committee in charge:

Associate Professor Daniel R. Weisz, Chair
Associate Professor Raffaella Margutti
Associate Professor Jessica Lu

Summer 2025

New Frontiers in Extragalactic Stellar Metallicity Measurements with Hubble Space Telescope

Copyright 2025
by
Sal Wanying Fu

Abstract

New Frontiers in Extragalactic Stellar Metallicity Measurements with Hubble Space Telescope

by

Sal Wanying Fu

Doctor of Philosophy in Astronomy

University of California, Berkeley

Associate Professor Daniel R. Weisz, Chair

Detailed studies of our Local Group benchmark our understanding of galaxy formation. Stellar metallicities are key tracers of the baryonic astrophysics shaping galactic properties, but they are challenging to measure in distant and faint galaxies. Narrow-band imaging offers a powerful way to measure stellar metallicities in systems that push our understanding of dwarf galaxy formation to new regimes in luminosity, star formation history, and environment. In this dissertation, I present hundreds of new stellar metallicities in faint, Local Group dwarf galaxies measured via a novel application of Ca H&K imaging on the Hubble Space Telescope. These metallicities measurements encompass: 1) 463 stars in 13 ultra-faint dwarf galaxies (UFDs) around the Milky Way, which effectively doubles the number of stellar metallicities in all known UFDs, b) 374 stellar metallicities in the quenched field dwarf galaxy Tucana ($M_V = -8.8$, $D \sim 1$ Mpc), a factor of ~ 7 increase over literature spectroscopy, and c) 286 stellar metallicities in two M31 dwarfs Andromeda XVI and And XXVIII where there were previously 0 and 13, respectively. These homogeneous metallicity measurements enable a wide range of science: 1) chemical evolution modeling to put novel constraints on the baryon cycle in UFDs, 2) new metallicity benchmarks for cosmological simulations of the faintest galaxies, 3) high-fidelity metallicity gradients that constrain stellar feedback and dark matter core formation models in dwarf galaxies, 4) ~ 120 Extremely Metal Poor (EMP; [Fe/H] < -3.0) star candidates that will be priority spectroscopic follow-up targets in the era of Extremely Large Telescopes (ELTs). I conclude with a discussion of interpretive and observational studies that follow from this dissertation.

奉献给姥姥、给爸爸妈妈

Contents

Contents **ii**

List of Figures **v**

List of Tables **xviii**

1 Introduction **1**
1.1 The Cosmological Context 1
1.2 Stellar Metallicity Measurements in Dwarf Galaxies 2
1.3 The Value of Photometric Metallicities 3
1.4 This Dissertation 5

2 Metallicity Distribution Function of the Eridanus II Ultra-Faint Dwarf Galaxy **6**
2.1 Overview 6
2.2 Introduction 7
2.3 Data and Observations 9
2.4 Metallicity Measurements 13
2.5 Results 16
2.6 Discussion 25
2.7 Conclusion 33
2.8 Impact of alpha element abundances on CaHK photometry 34
2.9 Select Metallicity Posterior Distributions of Eri II Stars 35
2.10 Recovery of Synthetic MDF 35
2.11 Posterior Distributions of Analytic MDF Parameters 39
2.12 Table of measurements 39

3 Metallicity Distribution Functions of 13 Ultra-Faint Dwarf Galaxy Candidates **46**

3.1 Overview . . . 46
3.2 Introduction . . . 47
3.3 Observations and Data reduction . . . 49
3.4 Determining Metallicity Distribution Functions . . . 55
3.5 Illustrative Examples of MDF Measurements . . . 59
3.6 Results . . . 68
3.7 Discussion . . . 80
3.8 Conclusion . . . 92
3.9 Foreground Contaminants . . . 94
3.10 Systematic Uncertainties in Individual Star Metallicities . . . 95
3.11 Comparisons to Literature Methods . . . 102
3.12 Metallicity Measurements as a Function of Stellar Evolutionary Phase and Brightness . . . 104
3.13 Additional MDF Summary Statistics . . . 104
3.14 Tables of Metallicity Measurements . . . 108

4 Stellar Metallicities and Gradients in the Isolated, Quenched Low-Mass Galaxy Tucana 112
4.1 Overview . . . 112
4.2 Introduction . . . 113
4.3 Observations . . . 114
4.4 MDF Measurements . . . 119
4.5 Results . . . 122
4.6 Discussion . . . 132
4.7 Conclusion . . . 143
4.8 Impact of α Assumptions on MDF Measurement . . . 145
4.9 Metallicity Gradient Measurements . . . 147
4.10 Table of Metallicity Measurements . . . 147

5 Stellar Metallicities and Gradients in the Faint M31 Satellites Andromeda XVI and Andromeda XXVIII 156
5.1 Overview . . . 156
5.2 Introduction . . . 157
5.3 Observations & Data Reduction . . . 159
5.4 Metallicity Property Determination . . . 161
5.5 Results . . . 164
5.6 Discussion . . . 167
5.7 Summary . . . 176
5.8 Table of Metallicity Measurements . . . 177

6 Conclusion **180**

Bibliography **182**

List of Figures

1.1 Figure adapted from Starkenburg et al. 2017 [291], showing the near-ultraviolet portion of the stellar spectrum where the Ca H&K lines are located. The gray line shows the Skymapper v filter, which has been used for photometric metallicity studies in the MW, but which struggle to effectively identify low-metallicity [Fe/H] < -3.0 stars due to potential contaminating absorption from C and N enhancements. In contrast, a narrow-band filter (red) specifically targeting the Ca II H&K lines enables effectively recovery of stellar metallicity. 4

2.1 On-sky rendering of Eri II and our HST frames. 10

2.2 **Left:** The broadband CMD of the Eri II field population for stars that pass the quality cuts. We color-code points with their corresponding S/N in F395N for S/N > 3. In this panel and the next, the photometry plotted excludes stars within two half-light radii of the galaxy's cluster. **Right:** CMD of the Eri II field population with F395N. The blue error bars show the typical uncertainty as a function of F395N. Uncertainties on $F395N - F475W$ color are dominated by F395N. 12

2.3 **Left:** Broadband CMD of Eri II. Black points are photometry with $F395N$ S/N > 10. The orange outline is the box that we used to select RGB stars in Eri II for our MDF analysis, and the color-coded points are the 60 selected stars. Our final sample reaches past the horizontal branch of Eri II. **Center:** The sample of Eri II stars that we use for our MDF analysis, plotted in the CaHK photometry color space defined by [291]. We also apply extinction in the line-of-sight of Eri II to the MIST mono-metallic isochrone tracks for 13 Gyr stellar populations with $[\alpha/\mathrm{Fe}] = +0.4$. We plot these tracks here to demonstrate how they separate in this particular color space. **Right:** MDF of Eri II, constructed from point estimates. Binsizes are the median uncertainty of Eri II metallicity measurements (0.35 dex). The outlined histogram includes point metallicity estimates of stars whose posterior distributions describe an upper limit on metallicity due either to model limitations or S/N, which we elaborate on in Section 2.5. 13

2.4 Example of a star (Star 9) with a well-constrained metallicity posterior distribution. **(left)** The location of Star 9 in CaHK color space, plotted with the MIST isochrone models corresponding to the median, 16th, and 84th percentiles of its metallicity posterior distribution. **(right)** The metallicity posterior distribution for Star 9. 16

2.5 Results of fitting the metallicities of individual stars to CaHK photometry. **Left:** Histogram of point measurements from this work, compared against those from L17, Z20, and MV21. Binsizes are the median uncertainty of Eri II metallicity measurements (0.35 dex). **Right:** 1-1 comparison of our measurements against those from L17 for the 10 stars common to both of our samples. 17

2.6 Comparing histogram of Eri II measurements to best-fit one zone chemical evolution models. Binsizes are the median uncertainty of Eri II metallicity measurements (0.35 dex), and the one zone models have also been convolved with a Gaussian of the same width. 24

2.7 **Left:** CMD of Eri II RGB stars, highlighting the metal-poor star candidates (blue) that we discuss in Section 2.5 as being potential candidates for spectroscopic follow-up. **Center:** Location of these stars in CaHK color space. **Right:** Histogram demonstrating the contribution that these stars make to the MDF of Eri II. Binsizes are the median uncertainty of Eri II metallicity measurements (0.35 dex). 25

2.8 Subset of mean metallicity (top) and mean metallicity dispersions (bottom) for known Milky Way satellites, color coded by number of stars used to make the measurement (compiled partly from [277], with updated measurements for Boo I from [142] and including our Eri II measurement). The dash-dotted line separates the ultra-faint dwarfs from the classical dwarfs. We indicate Eri II with the purple circle. 27
2.9 Orbital history of of Eri II in two different MW mass potentials using Gaia eDR3 proper motions [210]. MW1 has a virial mass of $10^{12}\,M_{\odot}$ while MW2 is more massive with a virial mass of $1.5 \times 10^{12}\,M_{\odot}$. Dashed lines represent orbits computed in a MW-only potential, solid lines indicate a MW+LMC potential with an LMC mass of $1.8{\times}10^{11}\,M_{\odot}$, and dotted lines represent a MW+LMC+SMC potential with an SMC mass of $5{\times}10^{9}\,M_{\odot}$. All of the above scenarios illustrate that Eri II is on first infall into the Milky Way's halo. 28
2.10 Comparison of the MDF that we derive for Eri II (gray shaded histogram; $M_{star} \sim 1 \times 10^{5} M_{\odot}$, [Fe/H] $=-2.50$, $\sigma = 0.42$, skew $= -0.21$) with the 6 UFD MDFs simulated from [143]. Following convention in previous histogram plots, binsizes are 0.35 dex wide. The stellar mass of the corresponding halo at $z = 0$ are in the title of each panel. We also compute the mean metallicity, metallicity dispersion, and skew of the simulated MDFs. All of the simulated MDFs are skewed relative to Eri II, with long metal-poor tails. 33
2.11 Comparing MIST isochrones in CaHK color space for isochrone models with [α/Fe]= 0.0 (left panel) vs [α/Fe]= +0.40 (right panel). For an isochrone of a given metallicity, the α-enhanced model reaches redder extents in $F475W - F814W$, and is also redder in CaHK color index. . . 35
2.12 Well-constrained posterior distributions. 36
2.13 Posterior distributions of stars that we flag as spectroscopically accessible EMP candidates for follow-up studies, and which we discuss in Section 2.5. 37
2.14 Posterior distributions of stars that are truncated at the 2σ level on the metal-poor end. The thin dotted red line is the most metal-poor ([Fe/H] $= -4.0$ model in our grid. 38

2.15 **(top left)** The 60 model photometry points that we draw from isochrone models, with metallicity counts set by a Gaussian MDF with a mean and spread consistent with what we measure for Eri II. Points are color-coded by their known metallicities. We also apply extinction to the tracks and the photometry in this plot, but it is negligible (on order of ∼0.01 mag). **(top right)** Synthetic photometry after appying bias and uncertainty from the ASTs (described in Section 2.3 to the model photometry. As in the previous panel, points are color-coded by their known metallicities. **(bottom left)** Comparing the input MDF to the MDF recovered after measuring individual stellar metallicities of the synthetic photometry, following the procedures in Section 2.4. **(bottom right)** Comparing the input metallicity to the recovered metallicity measurements for individual stars. Points are color-coded by their synthetic F395N S/N, as determined from the ASTs. The dash-dotted line is a 1-1 relation. 40
2.16 Joint distribution of the mean metallicity ([Fe/H]) and metallicity dispersion ($\sigma_{\rm [Fe/H]}$) of Eri II. The dashed lines mark the 16th, 50th, and 84th percentile of the 1D posterior distributions. 41
2.17 Posterior distribution of $p_{\rm eff}$ for the Leaky Box model. 41
2.18 Posterior distribution corner plots of $p_{\rm eff}$ and $\rm [Fe/H]_0$ for the Pre-Enriched gas model. 42
2.19 Posterior distribution corner plots of $p_{\rm eff}$ and M for the Accretion model. 43

3.1 A gallery of $F606W - F814W$ CMDs for our galaxies in order of decreasing luminosity from the top left to the bottom right. We color-code stars by their $F395N$ S/N for $F395N$ S/N > 5 and have not yet applied any membership selection or removed spurious detections. 52
3.2 The same as Figure 3.1 only for $F475W - F814W$ CMDs. The broader CMD features are partially driven by the lower S/N of the $F475W$ data and the increased metallicity sensitivity of $F475W - F814W$ vs. $F606W - F814W$. 53

3.3 An illustrative example of our process for measuring a galaxy's MDF from HST imaging using CVn II. The upper left panels show the CMDs of CVn II, with members shown in red and stars in common with other studies highlighted in blue. The upper right panels show the scatter and bias in the artificial star tests (ASTs) for each filter. The bottom left panel shows the CaHK diagram with member stars plotted in red and select metallicity tracks as lines. The high-opacity lines are the convolution of the intrinsic models low-opacity with the ASTs. The lower right panel shows the MDF of CVn II. The shaded red regions are well-constrained metallicity fits for individual stars, while the unshaded regions reflect stars with poorly constrained fits (e.g., off the metallicity grid, truncated PDFs). The blue line shows a Gaussian fit to all stars on the histogram. 60
3.4 Example posterior distribution functions of stars in CVn II. (upper left) Position of example stars in CaHK space, plotted against the MIST monometallic tracks used to infer metallicities in this work. (upper right) Example of a star with a well-constrained PDF. (lower left) Example of a star with a well-constrained PDF peak that is truncated at the metal-poor end; we also designate this star as an EMP candidate. (lower right) Example of a star for which we only constrain an upper limit, also an EMP candidate. 62
3.5 Same as Figure 3.3 only for the fainter, less populated system, Grus I. . 63
3.6 Same as Figure 3.3 only for Dra II, which has no RGB stars. The monometallic tracks shown in the bottom left panel are for MSTO and MS stars. Accordingly, the MDF is entirely based on stars from these evolutionary phases. 65
3.7 A comparison of metallicities for stars in common for our example galaxies CVn II, Grus I, and Dra II. The top row shows a one-to-one comparison for stars common to both studies. Our metallicities and those in the literature generally agree to $\sim 1.5\sigma$. The lower panels show a comparison between our MDFs (grey) and all MDFs in the literature for each galaxy. The histogram bins are 0.4 dex wide. 66
3.8 A gallery of $F606W - F814W$ CMDs with membership selection indicated by the orange boxes drawn around the RGB. After making this initial selection, we crossmatch against literature radial velocity data where available to remove foreground interlopers. Stars used to infer MDFs are color-coded with $F395N$ S/N > 10. 79

3.9 A gallery of CaHK diagrams for each UFD, ordered by decreasing luminosity. We have overplotted the MIST alpha-enhanced ($[\alpha/\mathrm{Fe}] = +0.40$) CaHK tracks for RGB stars in most cases and MS tracks for Ret II, Wil 1, Seg 1, and Dra II, which are dominated by MS and MSTO stars. The tracks have been convolved with ASTs run for each galaxy. These tracks are solely for illustrative purposes to demonstrate the impact of ASTs, and actual tracks used for fitting individual stars may look different due to the process described in §3.4. It is clear from the distribution of stars that each galaxy hosts stars over a wide range of metallicities. 81

3.10 A gallery of MDFs for each galaxy based on our CaHK fitting. Metallicity bin sizes are 0.4 dex wide, which is comparable to typical stellar metallicity uncertainties. Well-constrained fits are indicated by shaded grey regions, whereas poorly constrained fits- largely upper limits- are shown as open histograms. We overplot the MDFs with the best-fit Gaussian (red). With the exception of Ret III, we resolve $\sigma_{[\mathrm{Fe/H}]}$ above at least the 2σ level for our UFD sample. 82

3.11 The composite MDF for all UFDs in our sample, shown against select UDF MDFs from the literature. **Left:** The breakdown of the composite MDF by contribution from each UFD in our sample. **Right:** Our MDF (red) compared to the literature. The maroon line is the composite MDF made from all literature measurements available for the same galaxies in our sample, including stars not observed by our program. Our program increases the number of stellar metallicities in these galaxies by nearly a factor of 5. The gray line is the composite UFD MDF made from all available UFD stellar metallicity measurements, compiled by [277]. Our work more than doubles the number of metallicities in all UFDs. There is a significant increase in the number of EMP star candidates in these systems compared with previous studies. In all cases, our work demonstrates the excellent ability for space-based CaHK narrow-band imaging to significantly expand the number of UFD stars with metallicity measurements. 84

3.12 The mass-metallicity relation for dwarf galaxies, updated with results from this work. **Left:** We add our $\langle$[Fe/H]$\rangle$ measurements to the $\langle$[Fe/H]$\rangle$ measurements of other Milky Way dwarf galaxies, using the table compiled by [277]. Our results show a clear floor in the mass-metallicity relation in the UFD regime. We characterize this putative floor using only our measurements, assuming that the floor can be described by a Gaussian mean and scatter, placing the mean of the floor at [Fe/H]$= -2.61 \pm 0.08$ dex. **Right:** Our $\langle$[Fe/H]$\rangle$ measurements compared to those from select cosmological simulations. While simulations can broadly reproduce the mass-metallicity relation for the more luminous dwarf galaxies, they currently struggle to enrich less-luminous dwarf galaxies to the same level as we observe. 86
3.13 We compare our $\sigma_{\rm [Fe/H]}$ measurements, made assuming a Gaussian characterization of the MDF, to the $\sigma_{\rm [Fe/H]}$ measurements of other Milky Way dwarf galaxies (compiled by [277]). Our results confirm the large internal metallicity variations in these systems. 87
3.14 The mean metallicities of our UFDs compared to those of recent streams characterized by S5 [183] and Pristine [199]. The distributions are noticeably different, suggesting UFDs are not the main progenitors of the currently known MW stream population. 91
3.15 The potential impact of foreground contamination on our results illustrated using Reticulum II. **Left:** CMD of the TRILEGAL foreground model [304] by querying 0.5 deg^2 centered around Ret II, color-coded by metallicity. **Middle:** Remaining MW foreground stars (colored) from applying the same isochrone cut used to select Ret II members. **Right:** Impact of foreground contamination when scaling down number of expected interlopers by the WFC3 FoV. We typically expect $\sim$ 1 MW interloper in our final stellar sample. The nature of our observations and selection criteria combine to make foreground contamination minimal. . . 95
3.16 The effect of unresolved binaries on the CaHK color. The y-axis shows the difference in CaHK color between a single MS star at 0.7 $M_\odot$ and a binary system composed of a 0.7 $M_\odot$ MS star with companions from 0.1 $M_\odot$ to 0.7 $M_\odot$, for different metallicities spanned by our CaHK color grid. The impact of binary stars on our metallicities is small-to-modest compared to other sources of uncertainty. 97
3.17 Comparing MIST and BaSTI stellar evolution models in CaHK space for α-enhanced, 13 Gyr RGB (left) and MS (right) stars. 98

3.18 HST data of the M92 GC, a mono-metallic population, that we use to determine systematic uncertainties for our metallicity measurements. (left) CMD of M92 in $F475W - F814W$. (right) The position of M92 members on CaHK diagram. The majority of these stars lie between the [Fe/H] $= -3$ and [Fe/H] $= -2$ tracks. 100
3.19 Comparisons between our measurements and those from the literature, between different measurement methods. The vast majority of literature metallicity measurements come from medium-resolution studies, particularly those leveraging the calcium triplet metallicity calibration. The ground-based CaHK narrow-band measurements are from the Pristine study of Dra II [184]. 102
3.20 Stellar metallicities used for fitting the mean and dispersion (§3.4) of our MDFs as a function of brightness across our entire sample of galaxies. The measurements shown here are specifically for the process of fitting the MDFs, and may not fully reflect the final reported measurements (e.g., asymmetric uncertainties, upper limit constraints). The uncertainties shown here also take into account the systematic uncertainties we adopt as discussed in §3.10, and statistical uncertainties for our brighter stars are often smaller. **Top:** Metallicity measurements as a function of absolute magnitude, where absolute magnitude is a stand-in for stellar evolutionary phase. **Bottom:** Metallicity measurements as a function of apparent magnitude. 105

4.1 FoV of our HST WFC3 $F395N$ imaging compared to the center (blue star) and the 1, 2, and 3 half-light radii contours of Tucana (red ellipses). Small black points are stars which pass our S/N selection criteria. Our data enable stellar metallicity measurements within ~ 2.5 R_e of the galaxy, allowing us to measure a global MDF as well as characterize spatial metallicity trends. 116

4.2 **Left:** The broadband CMD of Tucana. To demonstrate the depth of the narrow-band data, we color code stars with $F395NS/N > 3$ by their narrow-band S/N value. Our data reach $F395NS/N \sim 10$ at about $F475W$ 24.5 mag, enabling stellar metallicity measurements for stars at least 1 mag fainter than the brightness limit of studies from current ground-based instruments. **Right:** Narrow-band $F395N$ CMD of Tucana. The blue error bars show the typical uncertainty as a function of $F395N$. Uncertainties in $F395N - F475W$ color are driven by uncertainties in $F395N$. The high concentration of stars running along the diagonal line faintward of $F395N \sim 25.75$ mag are HB stars. Stars above the diagonal line are the bright RGB stars that ultimately comprise our analysis sample. 117

4.3 **Left:** Selection of Tucana stars along RGB and their $F395N$ S/N. **Center:** Location of member stars on *Pristine*-like CaHK space. Overplotted are mono-metallic CaHK tracks convolved using the AST error profile of a star at $F475W = 24.14$, the median brightness of stars in our sample. The stars are color-coded by their inferred metallicity, which can also be upper limits on the metal-poor (MP) end and lower limits on the metal-rich (MR) end. Reasons why the color-coding of the stars does not perfectly follow the trend implied by the mono-metallic tracks can be attributed to the reporting of measurement limits for $\sim 50\%$ of stars more MR than [Fe/H] $= -1.0$ (e.g. §4.5), as well as the varied S/N of stars blueward of $F475W - F814W = 2.0$, which span about 2 magnitudes in brightness. **Right:** Resulting MDF of Tucana. Empty histograms represent stars for which we were only able to constrain either an upper limit (on the MP end) or a lower limit (on the MR end). Our data has enabled metallicity measurements for 374 stars down to $F475W \sim 25$ mag. . . . 119

4.4 Example posterior distributions for examples of stars with a well-constrained measurement (90% of our sample), an upper limit constraint (1% of our sample), and a lower limit constraint (9% of our sample), and their corresponding positions in CaHK color-color space, as well as their corresponding summary statistic. The AST-convolved tracks plotted here are the same as the ones in Figure 4.3. 126

4.5 Comparing our metallicity measurements to the most comprehensive ground-based CaT EW spectroscopic study of Tucana to-date [296, VLT/FORS2]. **Left:** HST broadband CMD that shows our stars (red), the stars we have in common with [296] (blue). **Center:** One to one comparison of our metallicity measurements with the measurements that we have in common with [296]. **Right:** Overall MDF comparisons between our metallicity measurements with the MDF from [296]. Our imaging technique permits recovery of metallicities at a similar level of fidelity to state-of-the-art ground-based spectroscopic calibrations, with vastly better sampling along the LF of Tucana to fill out the tails of the MDF. . . 127
4.6 Comparing metallicity measurements made using *HST* CaHK narrow-band photometry (UFDs Eri II, Grus I, [96], [97]; Tucana, this work) against those made using ground-based spectroscopy relying on the CaT EW calibration ([180], [296], [55]). We include a one-to-one line for visual reference. The measurements show remarkable agreement, and demonstrate that CaHK narrow-band imaging is a competitive method for measuring stellar metallicities compared with the most commonly-used method for Local Group dwarf galaxies. 128
4.7 The spatial distribution of our CaHK-based stellar metallicities for Tucana. Overplotted are the elliptical half-light radii at 1 R_e, 2 R_e and 3 R_e. Visually, it's clear that the central region of Tucana has more MR stars and the outer regions have more MP stars. 130
4.8 Result of fitting a linear model to our Tucana data as a function of elliptical R_e from its center. From our well-sampled MDF, which gives clear shape to the MP and MR tails, we are able to robustly recover a metallicity gradient. 131
4.9 MDFs of stars along the respective bifurcations of Tucana's RGB. **Left:** Hess diagram of Tucana stars analyzed in this work, color-coded by the boxes used to select stars on the blue and red bifurcations of the RGB. We select stars above a certain magnitude range to ensure better completeness for our comparison. **Right:** Comparing the MDFs of stars that fall on the blue and red branches of the bifurcation respectively. Empty histograms on the metal-poor and metal-rich ends of the MDF respectively denote upper and lower limits. The metallicity difference between stars on the two branches is apparent even by eye, and the corresponding summary statistics in the legend quantify these differences: the MDF of the blue RGB is more MP than the MDF of the red RGB by ~ 0.7 dex. 133

4.10 Spatial properties of stars along the respective bifurcations of Tucana's RGB. The left panels of each row present the spatial distribution of stars in each bifurcation, color-coded by their metallicity. The right panels of each row present stellar metallicities as a function of elliptical half-light radii, and the corresponding metallicity gradient fit. Stars in the more metal-rich red RGB are more centrally concentrated than stars in the blue RGB. We recover a steeper metallicity gradient for stars along the blue RGB than for stars along the red RGB. 134
4.11 Comparing the metallicity gradient in Tucana from our work with gradients of LG dwarf galaxies across a range of morphological type measured with spectroscopy [295]. The gradient of Tucana is one of the significant ones known among LG dwarfs. Additionally, while the spectroscopic gradients do not show a clear relation with t_{50} (median stellar age), we demonstrate in Figure 4.12 that our gradient measurement for Tucana is consistent with predictions from cosmological simulations that posit feedback as the primary mechanism for gradient formation in isolated dwarf galaxies [214]. 135
4.12 Comparing our metallicity gradient measurement for Tucana with those from the FIRE-2 simulations (e.g., [214]), which posit that metallicity gradients in isolated dwarf galaxies are driven by feedback-induced breathing modes [16]. **Left:** Comparing our gradient measurement and gradients from simulations as a function of stellar mass. The weak correlation between stellar mass and gradient strength is an emerging consensus among simulations, and we present this panel largely for completeness reasons. **Center:** Comparing our gradient measurement and gradients from simulations as a function of t_{50} (Gyr). The orange dotted line is the relation between t_{50} and gradient strength as found by [214]. Our gradient measurement for Tucana is consistent with this theoretical relation. **Right:** Examining trends in metallicity dispersion as a function of R_e. The radial dispersion trend in Tucana is consistent with those from simulations. . . 137
4.13 Impact of varying the [α/Fe] assumption on the recovered MDF of Tucana. The top row presents our fiducial assumption, while the middle and bottom rows present the recovered mean metallicity and dispersion by assuming a relation that shifts the ankle and knee by 0.5 dex backwards and forwards respectively. Additional summary statistics are presented in Table 4.3. The different α do not change the major conclusions of this work. 146
4.14 Corner plot of metallicity gradient fit using elliptical R_e. 148

4.15 Result of fitting line to our Tucana data as a function of circular arcmin from the center. The gradient from this method is comparable to the gradient from fitting as a function of elliptical half-light radius. 149
4.16 Corner plot of metallicity gradient fit using distance from the center of Tucana in circular arcmin. 150
4.17 Corner plot of metallicity gradient fit to Tucana's blue RGB, using elliptical R_e distance from the center of Tucana. 151
4.18 Corner plot of metallicity gradient fit to Tucana's red RGB, using elliptical R_e distance from the center of Tucana. 152

5.1 Illustrating the coverage of our HST imaging. The black dots are detected sources from the archival ACS archival image for each galaxy from which we measure broadband $F475W$ and $F814W$ photometry. The blue squares are the WFC3/$F395N$ FoV. Each galaxy's elliptical half-light contours are plotted in red, corresponding to 1, 2, and 3 half-light elliptical radii. 159
5.2 Presenting the CMD, CaHK color data, and resulting MDF for And XVI **(top row)** and And XXVIII **(bottom row)**. **Left column:** Broadband CMD of each galaxy, centered on its RGB, with stars analyzed color-coded by their $F935N$ S/N. Stars in cyan circles are velocity interlopers determined using the datasets of [62, 64, 63]. **Center column:** The position of analyzed stars in the *Pristine*-like color-color space, color-coded by their inferred metallicities. Mono-metallic CaHK tracks, convolved by the AST error profile of a star of median luminosity in each galaxy's sample, are overplotted to guide the eye. Since stars of different luminosity have different AST error profiles, the CaHK model tracks used to infer the metallicity of each star may be different from the ones presented here. Some of these metallicities are inferred upper limits due to either falling at the edge of the model grid for bright stars, or being low S/N for fainter stars. **Right column:** The resulting MDF for each galaxy. Solid histograms are well-constrained measurements, and empty histograms are stars for which we can only derive an upper limit. 162

5.3 **(Left)** Spatial distribution of stars in And XVI **(top)** and And XXVIII **(bottom)**, color-coded by their inferred metallicities. Also presented are each galaxy's half-light contours at 1, 2, and 3 R_e, and a scale bar indicating physical distance. **(Right)** Result of fitting a linear model to our data as a function of elliptical half-light radius. Gray dots are individual data points in each galaxy, while red dots are the mean metallicity in spatial bins of 0.5 R_e for And XVI and 0.25 R_e for And XXVIII. We are able to robustly recover a metallicity gradient for And XXVIII. We also tentatively detect a gradient in And XVI. These are among the few metallicity gradients of M31 satellites more generally, and for And XVI, one of few gradients detected in UFDs to-date. 165

5.4 Contextualizing our gradient measurements for And XVI and And XXVIII in the current landscape of gradients in M31 dwarfs. Literature gradients for M31 satellites are from the re-analysis of the [131] dataset in [295, NGC205, NGC185, NGC 147, And VII], and [169, And XVIII]. The galaxies are color-coded by the number of stars used to make the gradients measurement. We have measured gradients in these faint galaxies using a comparable number of stars that Keck/DEIMOS spectroscopy was able to reach in dwarf galaxies several orders of magnitude more luminous. 172

5.5 Comparing M31 and MW satellite metallicity gradients to predictions from the FIRE-2 simulations. **(Left)** Presenting gradients of M31 satellites relative to the age-metallicity gradient strength relation from FIRE-2 simulations [214]. All galaxies, simulated and observed, are color-coded by their stellar masses. The linear form of the relation is orange, and light circles denote the publicly-available FIRE-2 simulated galaxies. Diamonds are M31 satellites from the literature, and the 'X' and star points are respectively And XVI and And XXVIII. Our dwarf galaxy gradient measurements trace out the age-gradient relation. **(Right)** Presenting gradients of MW satellites as compared to the FIRE-2 simulations. The simulated relations are presented in the same fashion as the previous panel. Gradient measurements are sourced from [295]. The MW satellites show large scatter about the age-gradient relation. 174

List of Tables

2.1 Properties of Eri II. Note: Structural parameters of Eri II, derived from [68]. . . . 14
2.2 Parameters of Analytic MDF Fits to Eri II for the Gaussian, Leaky Box, Pre-enriched Gas, and Accretion Models . . . 23

3.1 Observational Properties of UFDs . . . 50
3.2 Summary of MDF Measurements . . . 83
3.3 Additional MDF Summary Statistics . . . 107
3.4 Metallicity Measurements of All Stars . . . 109
3.5 Extremely Metal-poor Star Candidates . . . 110
3.6 Metal-rich ([Fe/H] > -2.0) Stars . . . 111

4.1 Tucana Characteristics . . . 118
4.2 Tucana MDF Characteristics . . . 124
4.3 Tucana MDF Assuming Different [α/Fe] vs. [Fe/H] Relationships . . . 145
4.4 Metallicity Measurements for All Stars . . . 153
4.5 EMP Star ([Fe/H] < -3.0) Candidates . . . 154
4.6 MR Stars ([Fe/H] > -1.0) . . . 155

5.1 Dwarf Galaxy Characteristics . . . 160
5.2 Metallicity Properties of And XVI and And XXVIII . . . 168
5.3 **Note.** Summarizing metallicity properties of And XVI and And XXVIII derived from this work, along with the number of stars used to infer each property. . . . 168
5.4 Individual Stellar Metallicities . . . 178
5.5 **Note.** Measurements for all of the stars analyzed in this work. (This table is available in its entirety in machine-readable form in the online article.) . . . 178
5.6 Candidate EMP Stars . . . 179

5.7 **Note.** All of our identified EMP candidates in And XVI and And XXVIII.
(This table is available in machine-readable form in the online article.) . 179

Acknowledgments

This work has been financially supported by a Paul & Daisy Soros Fellowship, the NSFGRFP under grants DGE 1752814 and DGE 2146752, and the Space Telescope Science Institute via HST grants HST-GO-15901, HST-GO-15902, HST-AR-16159, HST-GO-16226, and HST-GO-16686. Significant portions of the analysis herein used the Savio computational cluster resource provided by the Berkeley Research Computing program at the University of California, Berkeley (supported by the Berkeley Chancellor, Vice Chancellor for Research, and Chief Information Officer). This dissertation would also not have been possible without the work of essential workers at Berkeley and all the other facilities where academic work is hosted, particularly during the years of the COVID-19 pandemic.

I have been incredibly fortunate to work with my PhD advisor, Dan Weisz, whose compassionate mentorship through all of these years provided important space for me to grow as a scientist amidst all the circumstances of graduate school. I am also grateful for the support of the many astronomy colleagues and friends with whom I've crossed paths throughout my career: Fatima Abdurrahman, Ellie Abrahams, Yumi Choi, Mia de los Reyes, Dillon Dong, Raja Guhathakurta, Myoungwon Jeon, Alex Ji, Erin Kado-Fong, Nicolas Martin, Rohan Naidu, Ekta Patel, Gwen Rudie, Nathan Sandford, Alessandro Savino, Josh Simon, Yong Zheng, Jingyao Zhu. I remain grateful to Phil Choi for his mentorship, since the earliest years of my astronomy career, about the discipline and about ways of seeing the world. My particular thanks to David Khatami, whose friendship has been formative for my career, and whose encouragement was particularly crucial for seeing this work across the finish line.

Beyond the world have astronomy, I have been blessed with the companionship of these friends: Scar Guo, Yu Xuan Hong, James Li, Victoria Lu, Yajushi Mattegunta, Shao Yie Soh, Danielle Wharton, Anthony Zhang. I am grateful to the PD Soros Fellowship community for its wisdom and inspiration, and to Ariel Chu in particular for her friendship. I am also lucky to have had neighbors as community-minded as Pete Goldstein, Dana DeKalb, and Nooshi Boorhan. Art has also been an important part of my graduate school experience, and I am grateful to the artists 安溥, James Baldwin, 福禄寿, Yiyun Li, Ryuichi Sakamoto, and 宋冬野 for the worlds that their work have opened up.

To my particular corner of the Chinese diaspora community, in the Shengmeng Education circle at Tri-Valley and beyond: you have been such generous friends to my family these last two decades, and are remarkable role models for resilience and integrity. My particular thanks goes to 小武阿姨, Rachel 阿姨, 赵兴叔叔, 刘牙医, Angela 阿姨, and 傅红阿姨 for their loving support throughout graduate school; to those in my generation, too, family friends who have grown up alongside me, 我亲

爱的发小: Connie 姐姐，小宝 Tercel，小墨 Mo. I am also grateful to the staff at 上海胸科医院, particularly 叶波主任 and 冯护工阿姨, for taking such good care of my family in the final months of my degree.

My final words of gratitude I reserve my family: my grandmother 姥姥, who taught me to love learning and gave me the gift of Chinese language. 舅舅, 舅妈, for your warm reception whenever I am in New Jersey; 小姨, for whenever I am in Beijing. 贝贝, for your company and humor, and especially during the pandemic. 丫丫, for coming home to us as I was choosing graduate schools, and the warmth you continue to bring us. My father, for inspiring me to be curious and to see the world from many perspectives. My brother, for his unabashed and unconditional faith in me.

And finally, my mother, for standing alongside me throughout all of my dreaming and aspiring and becoming; for everything that I am today.

Chapter 1

Introduction

This dissertation has been chiefly adapted and compiled from four first-author journal articles published throughout the course of my degree [96, 97, 99, 98]. These articles pertain to the novel application of photometric metallicity imaging techniques to deliver stellar chemistry measurements in Local Group (LG) dwarf galaxy systems that cannot be recovered using other, contemporary techniques.

In this chapter, I provide the big-picture motivation for work presented in this dissertation. Section 1.1 establishes the broader astrophysical and cosmological context for detailed chemistry studies within the LG. Section 1.2 presents the landscape of landscape of stellar chemistry measurements in dwarf galaxies prior to this work. Section 1.3 introduces the technique of photometric metallicities. Section 1.4 provides an overview of the remaining dissertation chapters.

1.1 The Cosmological Context

Dwarf galaxies ($M_\star < 10^9\ M_\odot$) are the smallest and the most numerous types of galaxies in the universe at all redshifts. They occupy the lowest-mass dark matter halos capable of forming galaxies, and are therefore important for probing small-scale predictions of dark matter particle models [43]. Under the hierarchical structure formation theory of galaxy evolution, posited by the standard Λ Cold Dark Matter (CDM) cosmology, dwarf galaxies are also the building blocks of larger galaxies in the universe [44, 127, 229]. Finally, owing to their low mass, they are particularly sensitive to the impact of baryonic processes, and offer opportunities to study individual chemical enrichment events that have outsized effects on their chemical properties [152].

The LG is our cosmic neighborhood, anchored by the Milky Way (MW) and

Andromeda (M31) spiral galaxies. In the last two decades, our census of dwarf galaxies within the LG has grown exponentially, owing to advances in extensive imaging surveys (SDSS, PAndAS, Pan-STARRS, DES, UNIONS, HSC-SSP) and increasingly sophisticated dwarf galaxy search algorithms [26, 197, 170, 23, 82, 134, 53]. These advances have established the LG as home to a diverse cast of dwarf galaxies along axes of luminosity ($L \sim 10$ to 10^9 $L_\odot$), environment (satellites of either the MW or M31, or in the field), and star formation history (SFH; ending 12 Gyr ago, persisting until 5 Gyr ago, and forming stars at the present day [319]). In composite, these galaxies provide important windows into the interplay of galaxy formation processes: the small-scale behavior of dark matter, and its interaction with baryonic physics.

Owing to their relative proximity, we are able to resolve LG galaxies down to the level of individual stars. This is a level of observational detail that is prohibitive for the vast majority of galaxies in the cosmos. Thus, studies of the LG – i.e., the discipline of near-field cosmology – anchor our understanding of galaxy formation, structure formation, and the origin of life, across cosmic time.

1.2 Stellar Metallicity Measurements in Dwarf Galaxies

The chemical composition of individual stars in a galaxy encodes the archaeological fingerprints of baryonic processes that contribute to small-scale and global galaxy formation processes. Detailed chemical abundances are used to trace evidence of individual chemical enrichment events– Type II and Type Ia SNe, *s*- and *r*-process nucleosynthetic channels– and their composite impacts on a galaxy's evolutionary history [300, 93, 152, 147], while the global metallicity distribution (MDF) of stellar metallicities– [Fe/H][1] – encodes the aggregated consequence of gas inflow and outflow throughout a galaxy's star-forming lifetime [299, 237, 165, 315].

Stellar chemistry is measured from absorption lines in stellar spectra. Historically, equivalent width analysis of high-resolution ($R > 10000$), high signal-to-noise ($S/N > 30$) stellar spectra had been the gold standard technique for chemistry measurements [213, 60, 301]. However, these techniques are limited to stars brighter than $g < 20$, and thus can only probe the brightest stars in bright galaxies within ~ 120 kpc [231].

The use of spectral indices and full-spectrum synthesis fitting techniques applied to medium resolution spectra ($R \sim 5000$) has enabled chemistry (Fe, bulk α element)

[1]Defined further as $[\mathrm{Fe/H}]_\star = \log_{10}(N_{\mathrm{Fe}}/N_{\mathrm{H}})_\star - \log_{10}(N_{\mathrm{Fe}}/N_{\mathrm{H}})_\odot$.

inferences in fainter, more distant targets, with contemporary studies using multi-object spectrograph (MOS) 10-meter class telescopes recovering measurements for stars brighter than $g \sim 22.5$ [277]. This technique has been the state-of-the-art for following up dwarf galaxy discoveries enabled by the expansion of imaging survey science at the turn of the 21st century. However, owing to the small field-of-view (FoV) of MOSs, complex selection effects in multiplexing, and number of bright stars spectroscopically accessible, spectroscopic techniques have still struggled to recover well-sampled stellar MDFs for dwarf galaxies beyond the Milky Way virial radius ($>$ 300 kpc), and for many faint galaxies within. Thus, spectroscopic techniques alone will likely be challenging for following up on dwarf galaxy discoveries anticipated by next-generation photometric surveys, most notably the Legacy of Survey of Space and Time on the Vera C. Rubin Observatory.

1.3 The Value of Photometric Metallicities

Photometric techniques offer an expansive avenue for inferring stellar metallicities. The Ca H&K absorption lines at 3933.7 and 3968.5 Angstroms (Fig. 1.1) have long known to be sensitive to stellar metallicity [293]. Narrow-band photometric filters specifically aimed at measuring flux around these features while avoiding contaminating absorption introduced by any potential enhancements in C and N, can therefore provide effectively a very low resolution technique for measuring stellar iron abundance. By trading in detail in spectral features, photometric metallicity imaging enables recovery of all stars within a field-of-view (FoV) at fainter limiting brightnesses than achievable through spectroscopy, and results in orders of magnitudes gains in sample size.

This technique was proposed as early as 1966 by Strömgren [293], and has been used to map the metallicity populations of the MW through the 1990s [e.g., 331, 24, 9]. Since 2010, this technique has seen a resurgence in utility, and has been used by many teams, notably *Pristine* and MAGIC, in the last decade to measure stellar metallicities in the MW halo and to search for metal-poor stars [**barbosa2025magicsculptor** , e.g., 291, 2, 308, 184, 119, 56, 188]. However, owing to small telescope apertures (4m) and low blue-sensitivity, ground-based studies have largely been confined to the Milky Way ecosystem.

As part of a 2009 WFC3 servicing mission, the $F395N$ narrow-band filter, targeting the Ca H&K absorption features in an analogous way to that of *Pristine* and MAGIC, was added to the *Hubble Space Telescope's* (*HST*) observational repertoire. *HST* has long been at the forefront of resolved stellar populations and star formation history studies of the Local Group [e.g., 61, 318, 102, 281], but prior to work

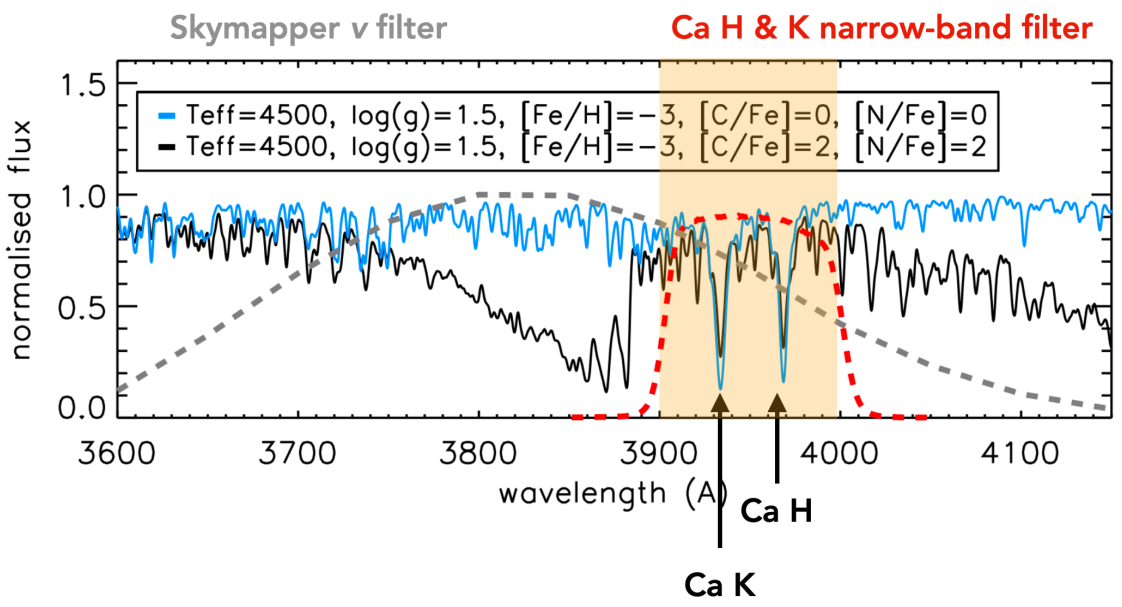


Figure 1.1: Figure adapted from Starkenburg et al. 2017 [291], showing the near-ultraviolet portion of the stellar spectrum where the Ca H&K lines are located. The gray line shows the Skymapper v filter, which has been used for photometric metallicity studies in the MW, but which struggle to effectively identify low-metallicity [Fe/H] < -3.0 stars due to potential contaminating absorption from C and N enhancements. In contrast, a narrow-band filter (red) specifically targeting the Ca II H&K lines enables effectively recovery of stellar metallicity.

in this dissertation, its capability for transforming extragalactic stellar metallicity measurements have decidedly been under-utilized. Prior to this work, the only other studies on photometric metallicity measurements with *HST* have been those of Ross et al. 2013 and 2015 [247, 248] targeting some of the more LG dwarfs. These studies were conducted with the $F390M$ filter, which, while encompassing the Ca H&K feature, also is vulnerable to C and N contamination (Fig. 1.1), and thus renders the characterization of the metal-poor MDF challenging.

1.4 This Dissertation

In this dissertation, I demonstrate that photometric metallicity imaging techniques targeting the Ca H&K spectral feature using *HST* is a powerful and complimentary way to measure stellar metallicities in dwarf galaxies that are otherwise not possible to reach from ground-based spectroscopy. In Chapter 2, I begin with a proof-of-concept by applying this technique to the Eridanus II ultra-faint dwarf galaxy (UFD; $M_\star < 10^5\ M_\odot$), and demonstrate its comparability with state-of-the-art medium resolution spectroscopy. In Chapter 3, I apply this technique to an additional 12 MW UFDs observed by HST in this filter, demonstrating a doubling of stellar metallicities across all known MW UFDs at the time ($N \sim 60$). In Chapter 4, I present 463 stellar metallicities in the distant ($\sim$1 Mpc), isolated dwarf galaxy, Tucana, whose properties render it an important site for studying secular quenching mechanisms in dwarf galaxies. In Chapter 5, I present ~ 300 new stellar metallicities in two faint ($M_\star < 10^6\ M_\odot$) satellites around M31, which is a population that is important to characterize as a foil to the well-studied MW satellite dwarf galaxy population. In composite, these studies represent orders-of-magnitude increases in MDF sampling in these systems. In Chapter 6, I summarize my results and offer forward-looking remarks on future work.

Chapter 2

Metallicity Distribution Function of the Eridanus II Ultra-Faint Dwarf Galaxy

2.1 Overview

We use deep narrowband Ca H&K ($F395N$) imaging taken with the Hubble Space Telescope (HST) to construct the metallicity distribution function (MDF) of Local Group (LG) ultra-faint dwarf (UFD) galaxy Eridanus II (Eri II). When combined with archival $F475W$ and $F814W$ data, we measure metallicities for 60 resolved red giant branch stars as faint as $m_{F475W} \sim 24$ mag, a factor of $\sim 4\times$ more stars than current spectroscopic MDF determinations. We find that Eri II has a mean metallicity of [Fe/H]$=-2.50^{+0.07}_{-0.07}$ and a dispersion of $\sigma_{\rm [Fe/H]} = 0.42^{+0.06}_{-0.06}$, which are consistent with spectroscopic MDFs, though more precisely constrained owing to a larger sample. We identify a handful of extremely metal-poor star candidates (EMP; [Fe/H] < -3) that are marginally bright enough for spectroscopic follow up. Eri II's MDF appears well-described by a leaky box chemical evolution model. We also compute an updated orbital history for Eri II using Gaia eDR3 proper motions, and find that it is likely on first infall into the Milky Way. Our findings suggest that Eri II underwent an evolutionary history similar to that of an isolated galaxy. Compared to MDFs for select cosmological simulations of similar mass galaxies, we find that Eri II has a lower fraction of stars with [Fe/H] < -3, though such comparisons should currently be treated with caution due to a paucity of simulations, selection effects, and known limitations of Ca H&K for EMPs. This study demonstrates the power of deep HST CaHK imaging for measuring the MDFs of UFDs.

This chapter has been adapted from Fu, Weisz et al. (2022), which was published in the Astrophysical Journal. This chapter was coauthored by the following individuals, and is included in this dissertation with their permission: Daniel R. Weisz, Else Starkenburg, Nicolas Martin, Alexander P. Ji, Ekta Patel, Michael Boylan-Kolchin, Patrick Côté, Andrew E. Dolphin, Nicolas Longeard, Marion L. Mateo, Nathan R. Sandford.

2.2 Introduction

The advent of wide-field photometric surveys at the turn of the 21st century has accelerated the discovery of ultra-faint dwarf galaxies (UFD; e.g., [326], [26], [23], [167], [170]) around the Milky Way (MW). These galaxies currently make up the faintest end of the galaxy luminosity function, defined tentatively by [277] as being fainter than $10^5\ L_\odot$. There are strong cosmological motivations to study UFDs: their presence constrains the small-scale behavior of dark matter models (e.g., [43], [226], [160]), and their ages ($\sim$ 13 Gyr, e.g., [41], [319]) make them ideal candidates for being pristine relics from the era of reionization (e.g., [35], [33], [316]).

Additionally, despite having short periods of star formation (SFHs), UFDs with resolved metallicity dispersions display significant internal spreads in stellar metallicity (e.g., [328], [93]). These observations suggest that they experienced complex chemical enrichment histories that distinguish them from star clusters [e.g., 325]. Any complete theory of galaxy formation must be able to reproduce the properties of this population, and the small sizes of UFDs make them particularly sensitive to the specific implementation of physics in cosmological simulations (e.g., [221], [1]).

Previous studies of the more luminous Local Group (LG) dwarf galaxies have demonstrated that well-populated metallicity distribution functions (MDFs) can be used to trace gas dynamics throughout their star formation histories (e.g., [300], [165], [166], [248], [162], [142]). To learn about the physics of galaxy formation at the lowest-known masses to-date, it is of great scientific interest to extend the availability of well-populated MDFs to the lower-luminosity UFDs. However, current spectroscopic studies have struggled to resolve metallicity dispersions in UFD candidates due to very few stars that are bright enough to be efficiently targeted, or observed at all, by current spectrographs (e.g., [313], [201], [181], [274]). Although next-generation photometric surveys such as those from the Rubin Observatory are predicted to find many more UFDs at farther distances (e.g., [322], [11], [225]), spectroscopic facilities on future ELT-class telescopes may at best reach down to the sub-giant branch for Segue 1-luminosity UFD galaxies beyond 100 kpc (e.g., Figure

9 from [277]).

One well-established alternative approach to measuring stellar metallicities is using medium or narrowband photometry (e.g., [293], [205], [49], [108], [178], [155], [247]). Photometric filters are designed to target specific features in a star's spectrum that are sensitive to intrinsic properties such as temperature or metallicity. Thanks to extensive calibration efforts, photometric metallicities are now used expansively to study the Milky Way (e.g., [126], [141], [7], [136], [330], [12], [51], [57], [324]), and can provide accurate metallicities for fainter stars than are accessible through spectroscopy.

One particularly useful photometric band for stellar metallicity is the Calcium H&K (CaHK) doublet in the blue optical at 3968.5 and 3933.7 Å (e.g., [331], [24], [9]). More recently, the Pristine survey verified the promise for Ca H&K imaging around the CaHK feature to trace stellar metallicity for FGK stars [e.g. 291] and search the Milky Way for metal-poor stars (e.g., [329], [2], [308]). Subsequent ground-based imaging studies that leverage similar filters targeting CaHK features in Milky Way satellites (e.g., [184], [119], [56], [187]) have demonstrated that this technique can substantially expand the sample of stars with metallicity measurements in these systems.

We extend this existing narrowband work in UFDs to even fainter stars and more distant galaxies using the *Hubble Space Telescope* (HST). Specifically, HST-GO-15901 (PI D. Weisz) observed 18 UFD candidates in the F395N filter, which is analogous to the narrow-band CaHK filter used by the Pristine survey. This paper is the first in a series based on these observations. Here, we demonstrate the power of HST Ca H&K imaging for uncovering the MDFs of UFDs using new and archival HST imaging of the MW satellite, Eridanus II (Eri II).

Eri II was initially discovered in Dark Energy Survey data by [23] and [167]. Subsequent deeper imaging by [68] and [220] confirm that at $M_V = -7.1$[1], Eri II is the faintest known galaxy to host a star cluster. Spectroscopic studies of Eri II by [180, 16 stars on Magellan/IMACS] and [332, 26 stars on VLT/MUSE] confirm that Eri II is a dark matter-dominated dwarf galaxy ($\sigma_{vel} = 6.9^{+1.2}_{-0.9}$ km s^{-1}) with a substantial internal spread in metallicity ($\langle$[Fe/H]$\rangle = -2.38\pm0.13$ and $\sigma_{\rm [Fe/H} = 0.47^{+0.12}_{-0.09}$; [180]). Star formation history (SFH) studies of Eri II, measured from HST broad-band imaging ([280], [101], and [5]), show that its color-magnitude diagram is consistent with having formed stars in a short burst ($\sim$100 Myr) that ended $\sim$13 Gyr ago.

Eri II is ideal for demonstrating the efficacy of MDF inference from narrow-band photometry. As the most luminous galaxy in our program, it not only provides a large sample of stars from which to measure a secure MDF, it also has a modest

[1]We note that the exact luminosity depends on the adopted distance of Eri II.

sample of spectroscopic metallcities, which is unusual for most UFDs, allowing us to cross-check our findings.

In this paper, we combine HST WFC3/UVIS imaging of Eri II in the narrow-band $F395N$ filter with broadband archival HST photometry to measure metallicities for 60 stars in Eri II. In Section 2.3, we describe our observations and data reduction process. In Section 2.4, we describe our process for translating our data into metallicity measurements. In Section 2.5, we present the resulting MDF of Eri II, as well as analytic fits. In Section 2.6, we discuss the our results in the broader context of galaxy formation and cosmology. We conclude with forward-looking remarks in Section 2.7.

2.3 Data and Observations

Photometry

We observed Eri II using HST on February 19, 2020 as part of HST-GO-15901 (PI D. Weisz) using the WFC3/UVIS camera and in the $F395N$ narrow-band filter for two orbits. We performed small dithers to remove hot pixels and reject cosmic rays, choosing patterns that were used to measure proper motions of nearby galaxies from previous Treasury program HST-GO-14734 (PI N. Kallivayalil). In this study, we also used spatially overlapping archival ACS/WFC $F475W$ and $F814W$ broadband imaging of Eri II, taken as part of HST-GO-14224 (6 orbits; PI C. Gallart, [101]).

Figure 2.1 shows the placement of our WFC3/UVIS imaging relative to Eri II and to the footprint of the archival ACS observations. At the distance of Eri II, the WFC3/UVIS and ACS/WFC imaging subtends $\sim$290 and $\sim$360 pc, respectively, across one side of the image. We also note that both frames capture Eri II's star cluster, which will analyze the cluster in a future paper.

We use `DOLPHOT` ([76], [77]) to perform point-spread function (PSF) photometry simultaneously on the $F395N$, $F475W$, and $F814W$ `flc` images of Eri II. From the resulting catalog of objects recovered by `DOLPHOT`, we select stars by applying a quality cut to the deep broadband imaging. Specifically, we only include stars with S/N > 5, $|\mathrm{sharp}|^2 < 0.3$ and crowd < 1 in each band.

Figure 2.2 shows the broadband color-magnitude diagram (CMD) of stars that pass the quality cuts in each filter. Color-coded stars in the left panel are those with $F395N$ S/N > 3. The right panel shows the $F395N$ narrow-band CMD. The blue error bars show the typical uncertainty in color as a function of $F395N$.

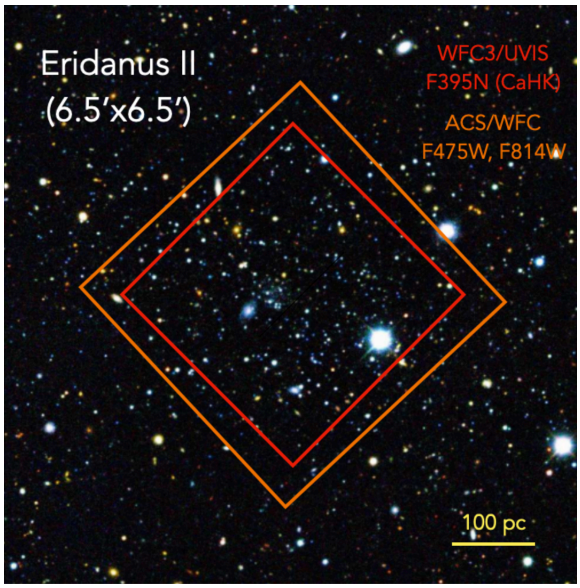


Figure 2.1: On-sky rendering of Eri II and our HST frames.

Selection of Stars for Photometric Metallicity Determination

We apply further cuts to select stars for our metallicity inference in Section 2.4, following the convention of past studies that use narrow-band photometry of the Ca H&K lines to study the MDF of Milky Way satellites. To begin, we select stars with $F395N$ S/N > 10: this is the S/N threshold above which the photometric measurements can provide reliable metallicities (e.g., [184]). We also remove any stars that fall within two half-light radii of the galaxy's star cluster using the structural parameters provided by [280] ($r_h \sim 0.16'$), as the focus of this paper is on the field population. From the resulting sample, we limit our analysis to only stars that fall along the red giant branch (RGB) of Eri II. We exclude horizontal branch stars in the galaxy that also have sufficient S/N in $F395N$ because the wavelength region of the narrow-band filter is dominated by the Balmer lines in these hot stars, rather than the metallicity sensitive H&K lines [e.g., 291].

The left panel of Figure 2.3 presents the final sample of stars that we use for our analysis. The orange box on the broadband CMD indicates the box used to select the final sample of stars. These 60 stars have $F395N$ S/N ranging from ~ 10 to 36. We verify that the star at $F475W \sim 20.8$ and $F475W - F814W \sim 2.0$, which falls right above the selection box, is brighter than the TRGB of a metal-poor isochrone

shifted to the distance modulus of Eri II from [68] and reported in Table 2.1, and therefore exclude it from our analysis.

The center panel of Figure 2.3 shows where our sample falls on the SDSS-Pristine color space defined by the Pristine survey, and which was derived from a similar color space defined by [157] for the Skymapper survey. [291] demonstrated that the color space $(g_{SDSS} - i_{SDSS})^2$ vs. $(CaHK - g_{SDSS}) - 1.5\,(g_{SDSS} - i_{SDSS})$ was effective for separating stars of different metallicities. For our study, we use the equivalent HST filters $F395N$, $F475W$, $F814W$ to construct an analogous color space where the x axis is defined as $F395N - F475W$, and the y axis of this space is defined as $(F395N - F475W) - 1.5(F475W - F814W)$. We henceforth refer to the y axis color as the CaHK color index, and to the entire color space as the CaHK color space. As shown in the center panel of Figure 2.3, the synthetic HST photometry from MIST isochrones ([58], [79]) also separate in this space according to metallicity. We discuss the data, relative to these models, in Section 2.4.

Artificial Star Tests

We use artificial star tests (ASTs) to compute the uncertainties on our photometry. The procedure for an AST is as follows: we insert an artificial star with input magnitudes in $F395N$, $F475W$, and $F814W$ onto a random position in the corresponding HST `flc` image. We only input stars whose broadband photometry fall within the isochrone selection box in the left panel of Figure 2.3, and with $F395N$ photometry that fall within the CaHK color space in the middle panel of Figure 2.3.

We then attempt to recover the star in all of these photometric bands using the same PSF-fitting procedure and the same culling properties for our photometric measurements. Additionally, we require that ASTs are within 0.75 mag of their input magnitudes, which helps mitigate spurious blends. The output of an AST is the difference between the measured magnitude and the input magnitude (out-in). We perform 85,580 ASTs. This large sample allows us to quantify (i) average offsets in measured photometry (bias) and (ii) the variance of out-in (error) at all locations in CaHK space. In Section 2.4, we describe how we apply the resulting error profile from ASTs to our metallicity inference.

[2]Technically, [291] apply the extinction correction to their data, whereas we apply extinction to the model as described in Section 2.4.

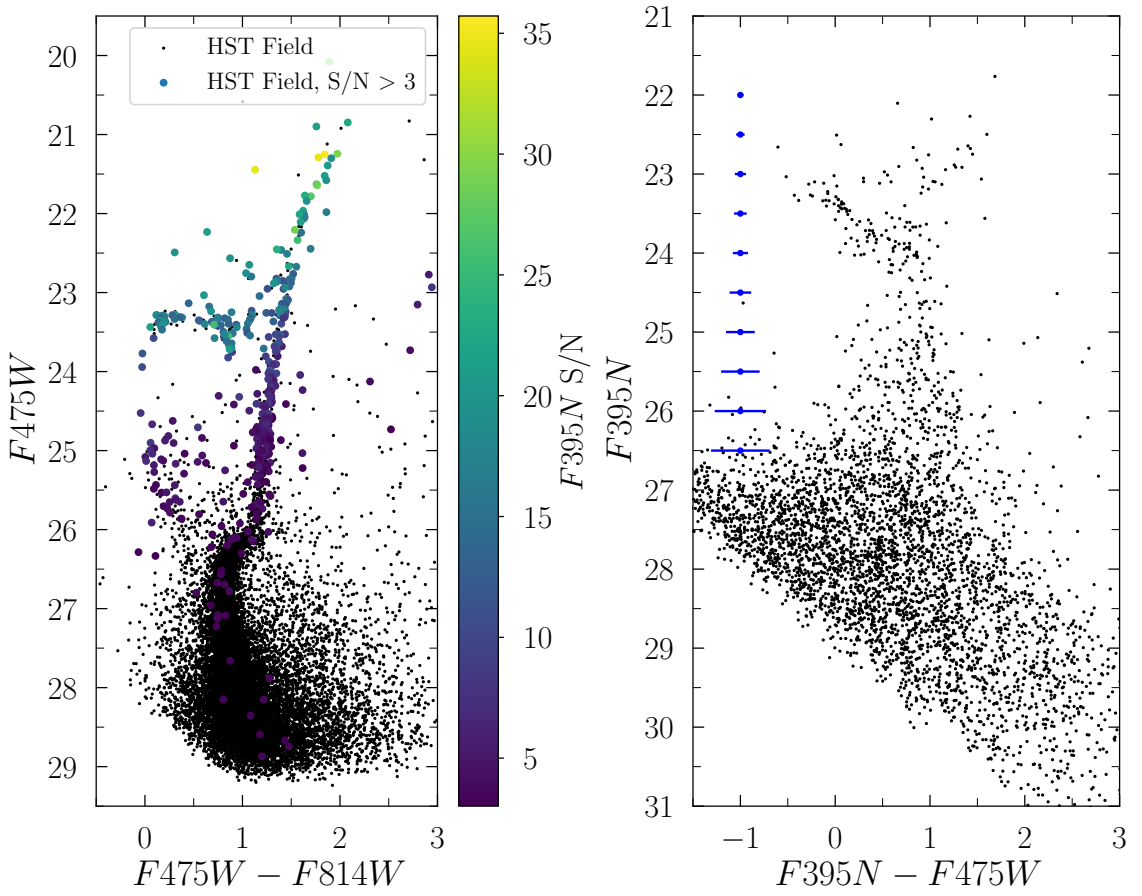


Figure 2.2: **Left:** The broadband CMD of the Eri II field population for stars that pass the quality cuts. We color-code points with their corresponding S/N in F395N for S/N > 3. In this panel and the next, the photometry plotted excludes stars within two half-light radii of the galaxy's cluster. **Right:** CMD of the Eri II field population with F395N. The blue error bars show the typical uncertainty as a function of F395N. Uncertainties on $F395N - F475W$ color are dominated by F395N.

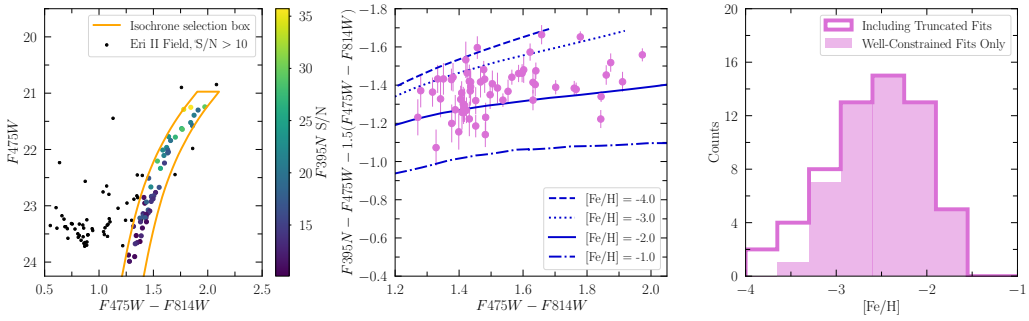


Figure 2.3: **Left:** Broadband CMD of Eri II. Black points are photometry with $F395N$ S/N > 10. The orange outline is the box that we used to select RGB stars in Eri II for our MDF analysis, and the color-coded points are the 60 selected stars. Our final sample reaches past the horizontal branch of Eri II. **Center:** The sample of Eri II stars that we use for our MDF analysis, plotted in the CaHK photometry color space defined by [291]. We also apply extinction in the line-of-sight of Eri II to the MIST mono-metallic isochrone tracks for 13 Gyr stellar populations with $[\alpha/\mathrm{Fe}] = +0.4$. We plot these tracks here to demonstrate how they separate in this particular color space. **Right:** MDF of Eri II, constructed from point estimates. Binsizes are the median uncertainty of Eri II metallicity measurements (0.35 dex). The outlined histogram includes point metallicity estimates of stars whose posterior distributions describe an upper limit on metallicity due either to model limitations or S/N, which we elaborate on in Section 2.5.

2.4 Metallicity Measurements

The middle panel of Figure 2.3 shows the location of our 60 Eri II field RGB stars on the CaHK color-color plot. We overplot the alpha-enhanced ($[\alpha/\mathrm{Fe}] = +0.40$), 13 Gyr MIST isochrones for giant stars. The models have been extinction corrected using the dust maps of [268] and bolometric extinction corrections provided with the MIST models [58] which enable us to calculate the extinction for the $F395N$ filter. We also consult the TRILEGAL Milky Way model [304] to determine the extent to which contaminants would affect our sample: due to the small field of view and our particular CMD cuts, the chance that our sample contains contaminants are low. Moreover, the CaHK photometry of potential contaminants imply that they would likely be more metal-rich than $[\mathrm{Fe/H}] > -1.0$, which we do not observe in our data. Finally, we also verify that none of the stars in our sample have been deemed Eri II non-members through spectroscopy ([180], [332]).

Parameter	**Eri II**
R.A. (h:m:s)	03:44:20.1 ± 10".5
Decl. (d:m:s)	−43:32:0.1 ± 5".3
Distance modulus (mag)	22.8 ± 0.1
Distance (kpc)	366 ± 17
Absolute magnitude (M_V)	−7.1
Luminosity ($L_\odot$)	6×10^4
Eccentricity (e)	0.48 ± 0.04
Half-light radius (')	2.3 ± 0.12
Half-light radius (pc)	277 ± 14

Table 2.1: Properties of Eri II. Note: Structural parameters of Eri II, derived from [68].

The majority of our sample lie between the [Fe/H] = −3 and [Fe/H] = −1 tracks, with a mean value somewhere between [Fe/H] = −3 and [Fe/H] = −2. Even by eye, it is apparent that the stars in Eri II span a range of ∼ 2 dex in metallicity. This observation is robust for both the bright stars and the faint stars in our sample.

We derive metallicities for each star by first retrieving synthetic HST photometry for mono-metallic MIST isochrones; we use the MIST models for our analysis because it is the only currently-available set of evolutionary models that include stellar populations as metal-poor as [Fe/H] = −4.0[3]. We limit our analysis to using tracks only for a 13 Gyr stellar population, in accordance with star formation histories (SFH) of Eri II from broadband HST data (i.e., [280], [101], and [5]). We obtained advance access to the MIST v2 models, which are the alpha-enhanced version of the MIST v1 models. We use these models, instead of Solar-scale alpha models, to fit Eri II, because UFDs with short bursts of star formation are generally expected to have enhanced alpha element abundances over a large range of their stellar metallicities (e.g., [307], [93]). We refer readers to the Appendix for additional discussion on the impact of alpha enhancements.

Next, we apply the results of the ASTs to each mono-metallic model. For each mono-metallic isochrone, we match each model isochrone point to its closest set of

[3]We recognize that there are known issues with the performance of MIST/MESA isochrones for metal-poor stars (see, e.g., [159], and references therein), and that refining the models of metal-poor stars remains an active area of research [e.g., 156]. However, as we show in Section 2.5, the metallicities we derive using MIST are consistent with other Eri II metallicity measurements in the literature. We deem this result sufficient for this paper in demonstrating the power of CaHK photometry to recover broad features of Eri II's MDF.

AST input magnitudes. From those ASTs, we calculate the bias and apply it to each isochrone point as offsets. We find for the ASTs that the CaHK color index has a positive color bias that increases for lower S/N points. A star with $F475W - F814W = 1.4$ and a CaHK color index of -1.0, corresponding to a point on the lower RGB of Eri II, would have a color bias of $+0.1$ in CaHK. In contrast, a star with $F475W - F814W = 1.8$ and a CaHK color index of -1.3, corresponding to the upper RGB of Eri II, would have a color bias of $+0.025$ in CaHK. As a result, all of the isochrone tracks are shifted redward in CaHK space, though based on the spacing between the tracks and the S/N of our data, they do not result in drastically different metallicities. This bias effect is driven by the shallower $F395N$ observations, and may arise from charge transfer efficiency corrections and/or post-flash effects on the photometry that cause us to lose signal for fainter stars. We intend to investigate this issue in greater detail in future work.

After applying the bias from the ASTs, we apply extinction using the dustmaps of [268] and bolometric corrections from the MIST models [58]. Once we apply the instrumental error profile and extinction models to the synthetic photometry, we linearly interpolate the CaHK color index as a function of $F475W - F814W$ to allow for the evaluation of the model at any color value.

As the middle panel of Figure 2.3 shows, the uncertainty in $F475W - F814W$ color of each star is small compared to the uncertainty in the CaHK color index. While the largest uncertainty in $F475W - F814W$ is ~ 0.01 mag, the uncertainty in the CaHK color index is at least 0.03 mag for the highest S/N points, and 0.1 mag for the lowest S/N. For simplicity in our fitting, we assume that the error in the $F475W - F814W$ color is negligibly small. We verify that scatter from the ASTs at a given CaHK location are statistically identical to the photometric errors reported by `DOLPHOT`. For simplicity, we adopt the photometric errors reported by `DOLPHOT` for our analysis.

For each star, we hold its $F475W - F814W$ color as constant and compute the corresponding model CaHK photometry at every metallicity using the tracks interpolated from MIST. To measure the metallicity of an individual star, we adopt a Gaussian likelihood function of the form:

$$\log L = -\frac{1}{2}\frac{(CaHK - CaHK_m([\mathrm{Fe/H}]))^2}{(\sigma^2_{CaHK})} \tag{2.1}$$

where $CaHK$ and σ_{CaHK} are the corresponding CaHK color index measurement and measurement uncertainty, and $CaHK_m([\mathrm{Fe/H}])$ is the model CaHK color index corresponding to a particular metallicity at a fixed $F475W - F814W$ color. We adopt uniform priors on metallicity over the range of the grid that includes the star's $F475W - F814W$ color. We sample the resulting posterior distribution using `emcee`

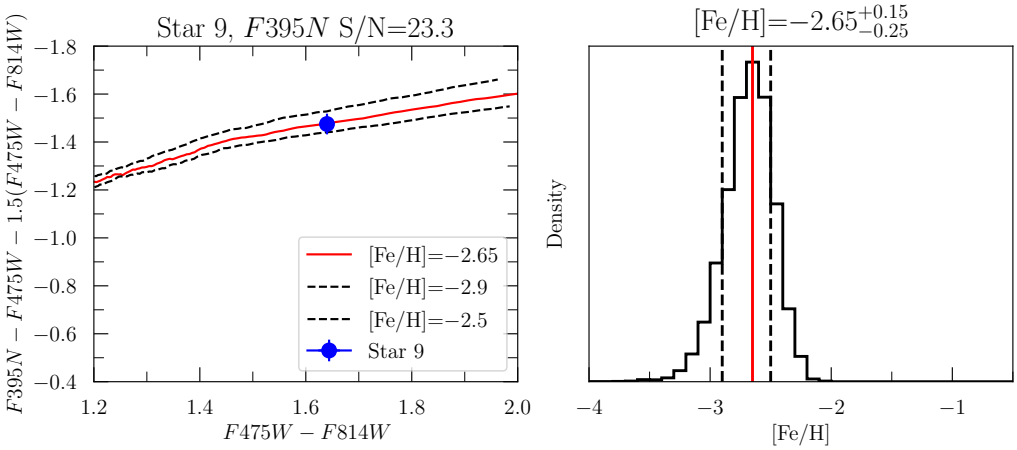


Figure 2.4: Example of a star (Star 9) with a well-constrained metallicity posterior distribution. **(left)** The location of Star 9 in CaHK color space, plotted with the MIST isochrone models corresponding to the median, 16th, and 84th percentiles of its metallicity posterior distribution. **(right)** The metallicity posterior distribution for Star 9.

[90] by initializing 50 walkers and running the MCMC chain for 10000 steps, with a burn-in time of on average 50 steps per star. We monitor for convergence using the Gelman-Rubin statistic [109].

We present sample metallicity fits for individual stars in the Appendix and the table of metallicity measurements in Table 2.12.

2.5 Results

Individual Measurements

In the right panel of Figure 2.3, we present the MDF of Eri II. The reported metallicities are the median of the marginalized posterior distribution for each star. Table 2.12 lists the median and 68% confidence interval for each star. Metallicity uncertainties are typically on the order of 0.1 dex, though they vary depending on the SNR, metallicity of the star, and location on the RGB, as we discuss below.

Our MDF of Eri II has a peak between −2.5 and −2.0. It spans a range of at least 2.0 dex: as we discuss below, some of the most metal-poor stars are consistent with metallicities lower than what our model grid allows. We also present our mea-

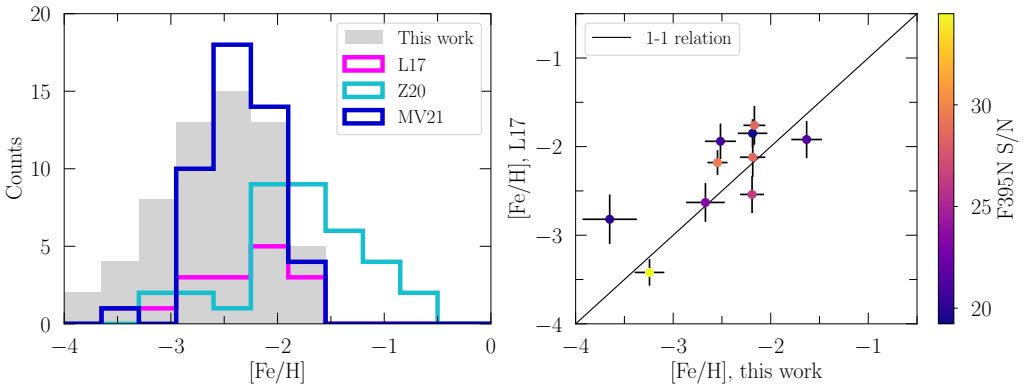


Figure 2.5: Results of fitting the metallicities of individual stars to CaHK photometry. **Left:** Histogram of point measurements from this work, compared against those from L17, Z20, and MV21. Binsizes are the median uncertainty of Eri II metallicity measurements (0.35 dex). **Right:** 1-1 comparison of our measurements against those from L17 for the 10 stars common to both of our samples.

surements in Table 2.12, and now discuss features in the posterior distributions of our metallicity measurements.

Figure 2.4 presents an example of a star with a well-constrained metallicity posterior distribution. A well-defined metallicity posterior distribution has a clear peak and clear tails, and are narrower for higher S/N stars. Metallicity posterior distributions also tend to have longer metal-poor tails because the CaHK models are less distinguishable at the metal-poor end (e.g., middle panel of Figure 2.3). We present additional examples in Figure 2.12 in the Appendix.

There are 3 stars for which we derive only upper limits on the metallicity. These are stars with high S/N in $F395N$ (S/N>15) and whose photometry places them at the edge or beyond the grid of models that we use to make our metallicity inference. We flag these stars as candidate extremely metal-poor stars (EMP; [Fe/H] < -3.0) that may be of interest for future spectroscopic studies, and discuss them in more detail in Section 2.5. We also present the posterior distributions of these stars in Figure 2.13.

There are 10 stars in our sample whose photometric error bars fall within 1 sigma of the metal-poor grid edge, but whose metal-poor posterior distribution truncates within 2 sigma; we also note these stars in Table 2.12. It is possible that at least some of these stars are more metal-poor than the value that we report, and that the measurements we derive here are limited by the models that we use. We provide

posterior distributions of these stars in Figure 2.14. In the same vein, there are 4 stars whose 1 sigma error bars are at the edge of our grid, meaning that their posterior distributions show a clear peak, but the metal-poor tail is even more truncated.

Finally, there are 4 stars for which we report only an upper limit because of their low S/N photometry (S/N$\sim$10). These are stars whose posterior distributions show no clear peak.

Comparison to Literature

In this section, we compare our MDF of Eri II to those currently in the literature: [180], [332], [101], and [202], henceforth L17, Z20, G21, and MV21, respectively. LZ17 and Z20 target RGB members of Eri II using spectroscopy and obtain metallicity measurements for some of the same stars in our sample. From these studies, we can directly compare individual measurements using different methods to evaluate the efficacy of CaHK metallicities. In contrast, for G21 and MV21, we cannot do star-by-star comparisons, but we can compare the overall MDF derived from the various methods. G21 uses deep HST photometry to measure the SFH of Eri II, inferring an MDF in the process. MV21 studies variable stars in Eri II, and measures the galaxy's MDF from its RR Lyrae stars.

We first discuss how our metallicity measurements compare against the spectroscopic studies. For context, L17 targeted candidate Eri II members within 8 arcmin of the galaxy using Magellan/IMACS spectroscopy. They report metallicities derived using the calcium triplet (CaT) equivalent width calibration [50] for 16 RGB members of Eri II, down to a magnitude of $g_{DES} \sim 21.7$ mag. Z20 targeted candidate Eri II members within 1 arcmin centered on Eri II using VLT/MUSE spectroscopy. They report metallicities derived using full-spectrum fitting with the PHOENIX model spectra [137] for 26 Eri II member stars, down to a magnitude of $F606W \sim 23.8$ mag.

In Figure 2.5, we compare our measurements against those of L17 and Z20. The histogram in the left panel compares our MDF with those from L17 and Z20. The right panel compares our metallicity measurements with the 10 common stars we have with the L17 sample.

We find good agreement between our metallicites and those in L17: while the scatter is a little larger than expected from the reported uncertainties, there is no evidence of a systematic offset between the two studies. In contrast, we find disagreement with the results of Z20. Z20 find systematically more metal-rich stars and report systematically smaller uncertainties. The MDF of Z20 implies that Eri II would be a more metal-rich system than implied by the dwarf galaxy luminosity-metallicity relationship (LZ; see Section 2.6). Z20 noted a similar disagreement with

L17, but did not explore the origin of this tension. Resolving this issue is beyond the scope of this paper.

Next, we compare our results against those from the photometric studies. G21 studied the SFH of Eri II from deep HST broadband data and inferred an MDF for the galaxy as part of their work. While their MDF spans the same metallicity range as ours, the shape is qualitatively different from the one that both we and MV21 (below) derive. Given the differences in the technique and the part of the CMD used to infer the metallicities, it is challenging to discern the source of discrepancy.

MV21 studied RR Lyrae (RRL) stars in Eri II using multi-epoch g, r, and i imaging on the Goodman and Dark Energy Cameras, as well as $F475W$, $F606W$, $F814W$ from HST/ACS. They derive metallicities from 46 RRL stars using the period-luminosity relations from [45] and [194].

The left panel of Figure 2.5 compares our MDF against those derived from the RRL sample in MV21. The peak of our MDF is consistent with that of MV21, though we are able to recover more metal-poor stars. This discrepancy may be expected from using different populations of stars to trace the MDF: MV21 point out that stars in the metal-poor tail of the MDF may not fall into the instability strip as RR Lyrae stars. As a result, MV21 also recover a smaller metallicity dispersion ($\sigma_{\rm [Fe/H]} = 0.3$ dex) compared to what we derive in Section 2.5 ($\sigma_{\rm [Fe/H]} = 0.42$ dex).

Overall, these comparisons suggest that our metallicity measurements can recover results that are consistent with those from the literature.

Gaussian MDF Fit

Following long-standing practice in spectroscopic studies of UFDs (e.g., [274], [181], [161], [325]), we fit a Gaussian to Eri II's MDF[4]. In particular, we use the two-parameter Gaussian likelihood function used by L17, and which was adapted from [311]:

$$\begin{aligned} \log L = &-\frac{1}{2}\sum_{i=1}^{N}\log(\sigma^2_{\rm [Fe/H]} + \sigma^2_{\rm [Fe/H],i}) \\ &-\frac{1}{2}\sum_{i=1}^{N}\frac{({\rm [Fe/H]}_i - \langle {\rm [Fe/H]} \rangle)^2}{\sigma^2_{\rm [Fe/H]} + \sigma^2_{\rm [Fe/H],i}} \end{aligned} \tag{2.2}$$

[4]Although, we note that studies such as [174] suggest that the MDFs of dwarf galaxies are not well-represented by a Gaussian form. We will explore this further in a study of the full galaxy sample.

where $\langle$[Fe/H]$\rangle$ and $\sigma_{\rm [Fe/H]}$ are the mean metallicity and metallicity dispersion of Eri II, and $\rm [Fe/H]_{\it i}$ and $\sigma_{\rm [Fe/H],\it i}$ are the metallicity and metallicity uncertainties for each star. We assume uniform priors on the mean, with the maximum and minimum set by the range of the point metallicity measurements, and require that the metallicity dispersion be greater than zero ($\sigma_{\rm [Fe/H]} > 0$). We use `emcee` to sample the posterior distribution, initializing 50 walkers for 10000 steps. The autocorrelation time for this run is 30 steps. The GR statistic indicates that the chains are converged.

For stars with different lower and upper uncertainties measured from the 16th and 84th percentiles of their PDFs, we adopt the average of the error bars to use in our fit. For stars that have only upper limit constraints, we include them in our fit using the medians of their PDFs as the point estimate and 16th/84th percentile values to compute uncertainties. All of these are approximations, and in principle, a more rigorous approach would be to use individual PDFs in our MDF inference. We will consider such an approach in subsequent papers in this series.

From 60 stars, we measure a mean metallicity of $-2.50^{+0.07}_{-0.07}$ dex and metallicity dispersion of $0.42^{+0.06}_{-0.06}$ dex. We present the resulting joint distribution in the Appendix as Figure 2.16, and tabulate these values in Table 2.2.

In comparison, L17 measure a mean metallicity of -2.38 ± 0.13 dex and a metallicity dispersion of $0.43^{+0.12}_{-0.09}$. Thus, using a completely independent approach to measuring the MDF, we find consistency with and improved precision over the CaT MDF. Beyond enabling a precise measurement of Eri II's MDF, this finding also demonstrates the power of CaHK imaging in practice.

Analytic Chemical Evolution Models

The MDF of a galaxy is shaped by the gas dynamics throughout the course of its star formation history. One zone chemical evolution models are simple analytic MDFs that have long been used for interpreting the formation process of various Milky Way components (e.g., [269], [189], [236], [122], [299]), as well as those of its nearby dwarf galaxies (e.g., [125], [166], [248]).

Prior to this work, the only UFD whose MDF was sufficiently populated enough to fit one-zone chemical evolution models is Bootes I, which has been analyzed by [142], [246] and [171]. In this section, we follow precedent set by the aforementioned studies by fitting the Leaky Box, Pre-Enriched, and Accretion/Extra Gas chemical evolution models to the MDF of Eri II.

The Leaky Box model defined by [237] describes the scenario where a galaxy forms stars from gas that is initially devoid of metals, and loses gas in the process of successive star formation and enrichment. Its single parameter is $p_{\rm eff}$, the effective

yield, which encapsulates contributions from both supernova enrichment and gas outflow to the stellar MDF.

The Pre-Enriched model and the Accretion/Extra Gas models are more complex versions of the Leaky Box. The Pre-Enriched model assumes that star formation starts from pre-enriched gas of metallicity $[\mathrm{Fe/H}]_0$. As a result, it imposes a floor on the lowest metallicity stars in the galaxy, and simplifies to the Leaky Box in the limit of $[\mathrm{Fe/H}]_0 \to -\infty$. The Accretion/Extra Gas model of [189] describes a system that is allowed to accrete pristine gas during the process of star formation. This model adds an extra parameter, M, which is the final stellar mass in terms of the initial gas mass at the onset of star formation. An Accretion model with $M > 1$ implies that the galaxy experienced accretion during its star formation history, resulting in an MDF with a larger peak and a smaller metal-poor tail. When $M = 1$, the Accretion model reduces to the Leaky Box.

We find the best-fit parameters for these analytic MDFs following [142, 150][5]. Briefly, we adopt the Gaussian likelihood from [165] and [166]: i.e., the likelihood for each star i is the convolution between the MDF and a Gaussian with standard deviation corresponding to that star's metallicity uncertainty $\sigma_{[\mathrm{Fe/H}],i}$ evaluated at the observed metallicity $[\mathrm{Fe/H}]_i$. We treat error bars in our sample the same way as for the Gaussian MDF fit described in the previous section.

We use dynamic nested sampling with `dynesty` [287] to sample the parameters' posterior distribution. We use fairly wide priors: log-uniform for p_{eff} from 10^{-3} to $10^{-1.1}$; uniform in $[\mathrm{Fe/H}]_0$ from -4 to -2 for the Pre-Enriched model; and uniform in M from 1 to 30 for the Accretion model.

We present the posterior distributions in the Appendix as Figures 2.17 (Leaky Box), 2.18 (Pre-Enriched), and 2.19 (Accretion), and tabulate fit parameters in Table 2.2. We report the median of the posterior distributions for each parameter, and compute error bars using the 16th and 84th percentiles. For the pre-enriched model, the posterior distribution of $[\mathrm{Fe/H}]_0$ is truncated at the metal-poor end. For the accretion model, the posterior distribution of M shows that our data can constrain an upper limit on M, but cannot rule out $M = 1$ with high confidence.

We present the best-fit MDFs in Figure 2.6. By eye, it looks that all models fit the MDF of Eri II reasonably well, and so we investigate whether the Eri II data prefer an MDF more complex than a Leaky Box. One way to quantify the model comparison is by using the corrected Akaike Information Criterion [AICc 165], which is a penalized likelihood ratio test. We compute this statistic for the Leaky Box, Pre-Enriched, and Accretion models. We tabulate the AICc for the Leaky Box in Table 2.2, and for the other two models, their difference in AICc ΔAICc from that of the

[5]Code available at `https://github.com/alexji/mdfmodels`

Leaky Box. A positive value for ΔAICc would suggest that the model is preferred over the Leaky Box, but we find that there is no strong preference between the three models that we fit since the ΔAICc is small. `dynesty` also computes the Bayesian evidence, which we choose not use here as it is sensitive to the exact prior volume choice, but it provides similar conclusions as the AICc.

We now discuss limitations in our methodology that could change the analytic chemical evolution model interpretation. As we lay out in the previous subsection, we approximate the posterior distribution of measurements for individual stellar metallicities as Gaussian, despite posterior distributions having longer metal-poor tails due to the indistinguishability of CaHK metallicities in metal-poor regimes. As a result, our current methodology downweighs the metal-poor tail of Eri II's MDF. Fitting analytic models using the full PDFs of individual stellar metallicities would remedy this issue, and could bring the MDF of Eri II closer to the Leaky Box model.

Additionally, we caution that the one-zone models used in this work oversimplify the problem by assuming that galaxies quench via turning the last of its available gas into stars. This assumption is likely incorrect because star formation is rarely that efficient, and low-mass galaxies can be quenched via reionization, ram pressure stripping, and/or SNe feedback (see [84] for example of a 10^5 $L_\odot$ galaxy in the field at $z = 0$ that has been observed to experience SNe feedback, and also the discussion in Section 2.6). While one way to remedy this issue in future work would be to fit models that truncate star formation at a particular metallicity (see, e.g., the ram pressure stripping model from [166]), additional detailed modeling would be fruitful for developing intuition around interpreting various components of a UFD's MDF.

With the above caveats and the minimal differences in AICc between the three models in mind, we also note that the results of our Pre-Enriched and Accretion fits suggest that they are also consistent with the Leaky Box limit. We therefore suggest that within the scope of our analysis in this work, the MDF of Eri II is best represented by the Leaky Box model, and discuss the implications in Section 2.6.

Noteworthy Individual Stars

Direct descendants of the first stars (Pop III) are hypothesized to be more easily identifiable in UFDs, owing to these systems' comparatively simpler enrichment histories in contrast to those of their more luminous counterparts (e.g., [148]). The chemical abundances of EMPs in UFDs are of great scientific interest because they are thought to trace directly back to past rare chemical enrichment events (e.g. [152]) or to supernovae (SNe) ejecta from Pop III stars (e.g., [92], [143]). In this section, we discuss the pathfinding potential for CaHK photometry to contribute to the search for these stars.

Model	Parameters	Values
Gaussian	[Fe/H]	$-2.50^{+0.07}_{-0.07}$
	$\sigma_{\rm [Fe/H]}$	$0.42^{+0.06}_{-0.06}$
Leaky box	$p_{\rm eff}$	$0.005^{+0.001}_{-0.001}$
	AICc	96.04
Pre-enriched	$p_{\rm eff}$	$0.004^{+0.001}_{-0.001}$
	$\rm [Fe/H]_0$	$-3.73^{+0.21}_{-0.17}$
	ΔAICc	-1.06
Accretion	$p_{\rm eff}$	$0.005^{+0.001}_{-0.001}$
	M	$2.77^{+2.59}_{-1.14}$
	ΔAICc	-0.04

Table 2.2: Parameters of Analytic MDF Fits to Eri II for the Gaussian, Leaky Box, Pre-enriched Gas, and Accretion Models

In Figure 2.7, we highlight spectroscopically accessible stars that are at the metal-poor edge of our fitting grid, that may be particularly enlightening for spectroscopic follow-up observations. In particular, we identify 3 stars that are candidate EMPs. As shown in Figure 2.13, these stars have truncated metal-poor posteriors distributions, so they may be more metal-poor than our grids allow. They are also located on the upper RGB of Eri II, with the faintest star being $m_{F475W} \sim 22.5$ mag. Although their CMD position on the blue edge of the RGB raises the possibility that they are asymptotic red giant branch (AGB) stars, the purely ancient stellar population of Eri II (~ 13 Gyr) suggests that it is unlikely to have many, or any, AGB stars.

Of these 3 stars, two of them have CaT metallicities measured by L17. For star 2 ($m_{F475W} = 21.3$, $F395N$ S/N = 34.5), we find that it has [Fe/H] $= -3.50 \pm 0.15$, compared to the L17 measurement of [Fe/H] $= -3.42 \pm 0.15$: these measurements are in good agreement with each other. For star 11, we obtain a 95% upper limit of [Fe/H] $= -3.15$, compared to the L17 metallicity of [Fe/H] $= -2.82 \pm 0.28$. For these two stars, both our measurements and measurements from the literature affirm that they are consistent with having [Fe/H] < -3.0, demonstrating the potential for CaHK to identify EMP candidates. Additional spectroscopic observations could aim to ascertain the behavior of α element and C abundances in Eri II at low metallicities, which in turn can be used to infer the properties of the SNe whose yields contributed to these patterns (α, [228], [147]; C, [145]).

Unlike the other two EMP stars that we identify, Star 21 ($m_{F475W} = 22.5$, $F395N$ S/N = 17) does not have spectroscopic data. We estimate the upper limit of

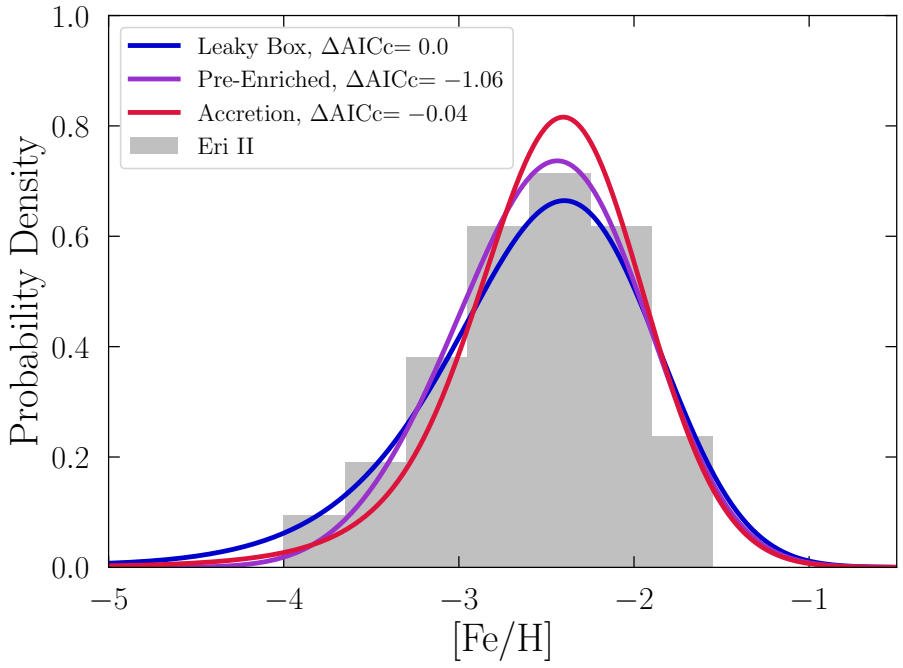


Figure 2.6: Comparing histogram of Eri II measurements to best-fit one zone chemical evolution models. Binsizes are the median uncertainty of Eri II metallicity measurements (0.35 dex), and the one zone models have also been convolved with a Gaussian of the same width.

its metallicity to be [Fe/H] = −3.05. Additional observations to measure metallicities from CaT spectroscopy or full spectral fitting would be fruitful both for verifying that it is an EMP, as well as measuring its other chemical abundances.

Searching for a Metallicity Gradient in Eri II

Radial metallicity gradients have long been observed in Local Group dSph galaxies (e.g., [124], [260], [262], [120], [303], [71], [154]). The physics responsible for the origin and steepness of these gradients remain an active area of research, with proposed mechanisms such as natal angular momentum [e.g., 270], stellar feedback [e.g., 15], and star formation histories [e.g., 214]. To-date, however, studies of metallicity gradients in dwarf galaxies have mostly been limited to those more luminous than 10^5 $L_\odot$ (e.g., [305], [131]).

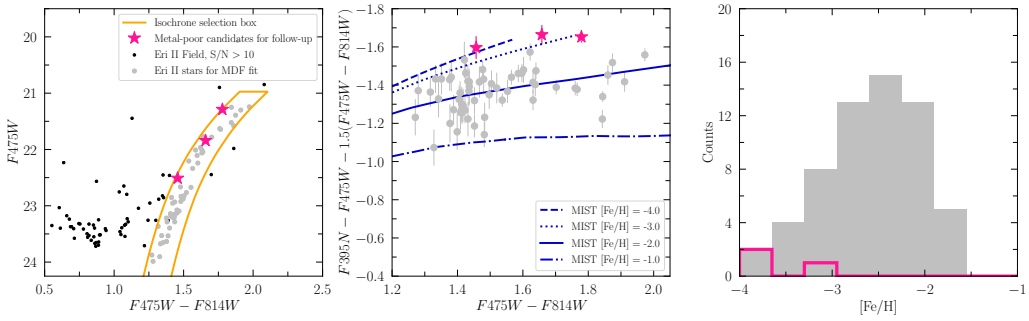


Figure 2.7: **Left:** CMD of Eri II RGB stars, highlighting the metal-poor star candidates (blue) that we discuss in Section 2.5 as being potential candidates for spectroscopic follow-up. **Center:** Location of these stars in CaHK color space. **Right:** Histogram demonstrating the contribution that these stars make to the MDF of Eri II. Binsizes are the median uncertainty of Eri II metallicity measurements (0.35 dex).

Motivated by recent searches for metallicity gradients in UFDs ([54], [188]), we search for a spatial trend in our data. We find none. This could be because: (1) There is none, (2) Our imaging, which covers $< 1\ r_h$ of Eri II, is too limited in spatial extent to find one; and/or (3) the uncertainties on the metallicity measurements need to be smaller, if the gradient is weak but non-zero.

2.6 Discussion

Improved MDF Statistics for Eri II

Figure 2.8 compares the mean and sigma from fitting a Gaussian to our MDF of Eri II with those derived for other LG dwarf galaxies (data compiled by [277], with updated measurements for Boo I from [142]), where the data points are color-coded by the number of stars used to measure the MDF in each system. The vertical line in both panels delineates the separation between UFDs and the classical dwarf galaxies as defined by [277]. The top panel shows that the mean metallicity we derive for Eri II is fully consistent with its expected location along the mass-metallicity relationship for dwarf galaxies [166]. The bottom panel shows that the metallicity dispersion we derive is on par with that of more luminous dwarf spheroidal galaxies, and within the range of dispersions observed so far in LG satellites. The agreement between our

Eri II results and the broader dwarf galaxy MDF provides further support for the power of Ca HK-based metallicities.

As discussed in Section 2.5, our MDF fit of Eri II provides a twofold increase in precision in metallicity dispersion over those of the measurements from L17 due to the expanded sample of stars with metallicity measurements. Out of all the UFDs with measured MDFs so far, Eri II is also now better-characterized for the same reason: MDF measurements for other UFDs have been limited due to few stars that have been accessible through spectroscopic studies. These results affirm the potential for CaHK imaging to deliver improved UFD MDF statistics.

Quenching Mechanisms for Eri II

In this section, we address the questions around quenching mechanisms for Eri II. As part of this process, we derive the direct orbital history of Eri II following the methodology outlined in [238], using updated Gaia eDR3 proper motions from [210], the radial velocity from [180], and a distance consistent with that reported in Table 2.1.

Figure 2.9 summarizes the orbital history of Eri II in a low (MW1; $1 \times 10^{12}\,M_{\odot}$) and high mass (MW2; $1.5 \times 10^{12}\,M_{\odot}$) MW model. Orbits are computed in a MW-only (dashed lines), MW+LMC (solid lines), and a MW+LMC+SMC (dotted lines) potential. We only integrate our orbits as far back as 6 Gyr because attempts to ascertain the orbital history of Eri II earlier than that will also need to account for the growth of the Milky Way potential, and because orbital uncertainties become significantly larger beyond 6 Gyr ago.

In all scenarios, we find that Eri II is on first infall into the halo of the MW. Following [238], we also account for the measurement uncertainties in proper motion, line-of-sight velocity [180], and distance by computing one thousand orbits using Monte Carlo drawings of the joint uncertainties as initial conditions. Regardless of assumed MW mass, our models suggest that Eri II is statistically most likely to be on first infall as well (e.g., $\sim 98\%$ of all orbits result in the same orbital history). Moreover, we also verify that Eri II does not pass within 800 kpc of M31 at any point in its trajectory.

In summary, our updated orbit for Eri II suggests that it was isolated throughout most of its evolutionary history, though we caution that this orbital history is still informed by large uncertainties on the proper motion of Eri II. However, this result is also consistent with the results from [19], who also derive an orbital history for Eri II using Gaia eDR3 proper motions and find that it is on first infall into the MW. The revised orbital history of Eri II from Gaia eDR3 proper motions is a departure from results of previous studies of Eri II, which suggested that Eri II has either completed

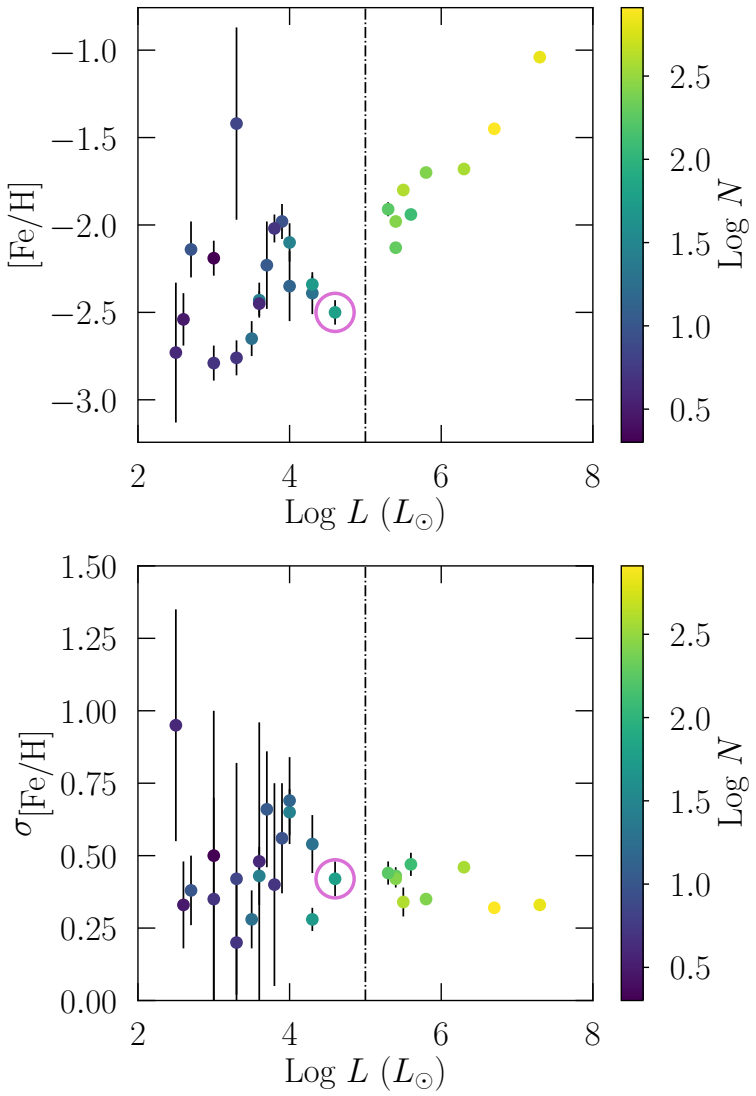


Figure 2.8: Subset of mean metallicity (top) and mean metallicity dispersions (bottom) for known Milky Way satellites, color coded by number of stars used to make the measurement (compiled partly from [277], with updated measurements for Boo I from [142] and including our Eri II measurement). The dash-dotted line separates the ultra-faint dwarfs from the classical dwarfs. We indicate Eri II with the purple circle.

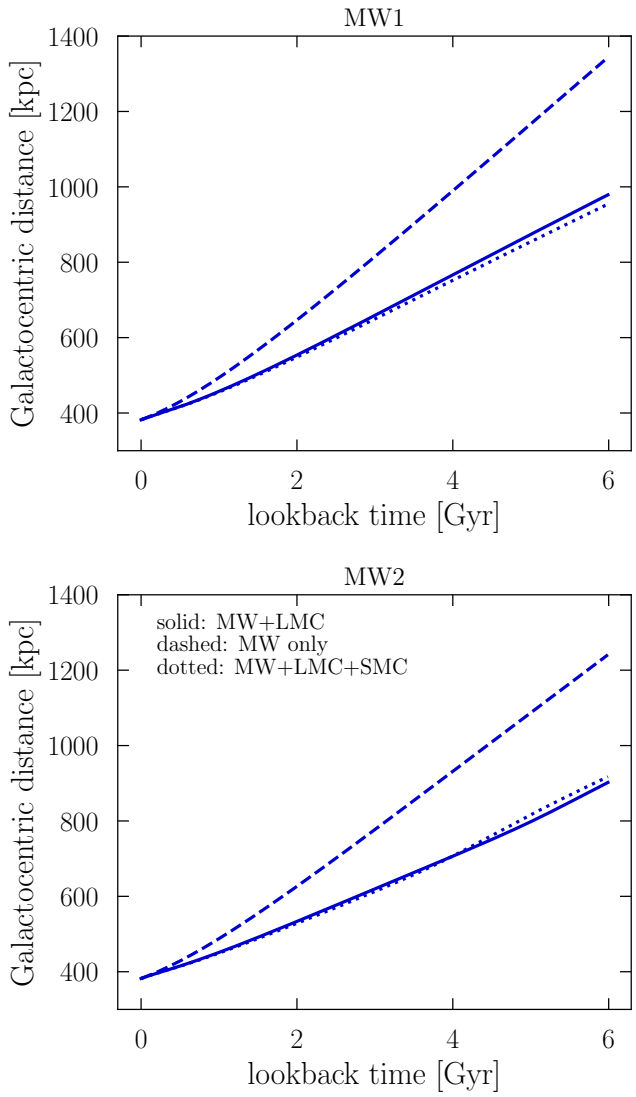


Figure 2.9: Orbital history of of Eri II in two different MW mass potentials using Gaia eDR3 proper motions [210]. MW1 has a virial mass of $10^{12}\,M_{\odot}$ while MW2 is more massive with a virial mass of $1.5 \times 10^{12}\,M_{\odot}$. Dashed lines represent orbits computed in a MW-only potential, solid lines indicate a MW+LMC potential with an LMC mass of $1.8 \times 10^{11}\,M_{\odot}$, and dotted lines represent a MW+LMC+SMC potential with an SMC mass of $5 \times 10^{9}\,M_{\odot}$. All of the above scenarios illustrate that Eri II is on first infall into the Milky Way's halo.

multiple orbits around the MW (e.g., [180], [95]) or is a backsplash galaxy [42]. The discrepancies in these results are likely due to a combination of: 1. Different proper motion measurements between Gaia eDR3 and DR2 for Eri II[6], 2. Orbit model-specific considerations (MW-only vs. including the Large Magellanic Cloud), and 3. Calculating the past orbit of Eri II vs. orbital history inference by following Eri II analogs in cosmological simulations.

We now turn to the question of how Eri II quenched. At the time of its discovery, [167] noted the presence of blue stars in the CMD of Eri II that suggest Eri II may have stopped forming stars only recently ($\sim$ 250 Myr ago). This scenario had also seemed viable because Eri II is $\sim$ 380 kpc from the Milky Way, and thus less likely to have experienced ram pressure stripping that could have removed gas before the suspected burst of recent star formation.

Subsequent studies, however, increasingly point away from this recent quenching scenario. [244] study Eri II analogs in the Fat ELVIS simulations and find that it is unlikely for them to have quenched through infall into the Milky Way halo. The orbital history of Eri II that we derive suggests that it fell into the Milky Way only recently, which does not correlate with deep HST studies of Eri II suggesting that it formed the majority, if not all, of its stars before $z \sim 6$.

Finally, if Eri II was quenched through ram pressure stripping, we should expect to observe a sharp truncation in its MDF at the metal-rich end (e.g., the one-zone model of ram pressure stripping fit by [166]), although accretion models with large M could also produce a similar feature. While our MDF does not uniquely rule out ram pressure stripping, it adds to the growing body of evidence in the literature pointing away from ram pressure stripping as a possible source of quenching for Eri II.

Beyond that, the interpretation of Eri II's old SFH is still up for debate. While [280] interprets Eri II's SFH as evidence of quenching by reionization, [101] suggests that SNe alone would be sufficient to quench Eri II. The MDF of Eri II that we derive does not provide definitive power to distinguish between these two mechanisms, as the one-zone models we fit do not distinguish between the details of how star-forming gas is depleted. However, any proper account of the physics driving star formation and quenching in Eri II should also be able to reproduce its large internal metallicity spread. Similar theoretical benchmarks are also set by observations of the Segue 1 UFD, a much fainter UFD ($M_V = -1.3$) that appears to have experienced a short burst of star formation, but whose stars span almost 2 dex in metallicity [93].

[6] As an example to illustrate this, the east component of Eri II's proper motion changes between DR2 [209] and DR3 [210] from $\mu_\alpha \cos\delta = 0.35^{+0.21}_{-0.20}$ mas yr^{-1} to $\mu_\alpha \cos\delta = 0.21 \pm 0.09$ mas yr^{-1} using the inference method that does not place prior expectations on the tangential velocity dispersion of the MW halo.

Environmental Impacts on Dwarf Galaxy Evolution

In this section, we discuss the role of environment on dwarf galaxy evolution by comparing our results for Eri II to two other galaxies that are close to Eri II in luminosity, and which have published MDFs and one-zone chemical evolution model fits: Leo T, and Boo I.

Leo T is similar to Eri II in luminosity ($L \sim \ 4 \times 10^4\ L_\odot$; [140]) and distance ($d_{MW} \sim 410$ kpc; [59]) from a more massive host. The key distinction between these two galaxies is that Leo T displays an extended SFH that continues past reionization ([59], [320]), with a substantial reservoir of H I gas ($M \sim 2.8 \times 10^5\ M_\odot$; [249]), while Eri II stopped forming stars 13 Gyr ago. The orbital history of Leo T suggests that like Eri II, it also seemed to have evolved in isolation [19]. Finally, similar to Eri II, the MDF of Leo T is best described by a Leaky Box [166].

On the other hand, Boo I has a CMD which suggests that it underwent a similar SFH to Eri II: a short starburst that ended also around 13 Gyr ago [41]. Unlike Eri II, the orbital history of Boo I suggests that it is bound to the Milky Way ([276], [95]) and, as a result, possibly formed in a denser environment relative to that of Eri II.[7] Finally, the MDF of Boo I is best represented by an Accretion model [142], suggesting that the dense environment it was born in could have allowed it access to extra gas.

As a point of reference, [166] fit one-zone models to the MDFs of the more massive Local Group dwarf galaxies, and found that while the MDFs of dwarf spheroidal galaxies, which are bound to the Milky Way, are better described by Accretion models, the MDFs of isolated dIrrs are better described by Leaky Box or Pre-Enriched models. To the best of the data that we currently have for galaxies of lower luminosities, these distinctions between MDFs seems to also hold for UFDs that have long been bound to a more massive host versus UFDs that likely evolved in more isolated environments.

Instead of present-day morphology, [102] offer a framework for interpreting the role of environment in dwarf galaxy formation by classifying dwarf galaxies into *fast dwarfs* and *slow dwarfs* based on their SFH. *Fast dwarfs* are those with SFHs consisting of a single short, but dominant, event. *Slow dwarfs* show current or recent SFH, with continuous activity starting from the oldest epochs. Under this framework, distinctions in SFH arise from the environments in which the galaxies were forming stars: *fast dwarfs* formed in dense environments where they frequently experienced interactions that would result in rapid star formation (e.g., gas accretion, mergers) and its rapid truncation (e.g. feedback from SNe and reionization from within and

[7] Although, [87] show that it is also possible for the star formation epoch of Boo I to have ended prior to infall into the Milky Way.

from adjacent galaxies), while *slow dwarfs* formed throughout cosmic time in a lower-density environment far from the influence of massive hosts.

While the characteristics of Boo I and Leo T respectively fit into the *fast dwarfs* and *slow dwarfs* categories, Eri II complicates this picture: it resembles a *fast dwarf* on the basis of its short and early burst of SFH, but the updated orbit that we derive for Eri II and the similarity of its MDF to those of several other isolated dIrrs suggests that Eri II has largely evolved in isolated like *slow dwarfs*.

Using the SFH of Eri II, [101] argue that it is possible for Eri II to self-quench entirely through SNe feedback rather than reionizing radiation, e.g. from adjacent massive hosts. If this is the case, then UFDs with SFHs that would render them as *fast dwarfs* can also quench early, independent of environment. On the other hand, the similarity between the MDFs of Eri II and Leo T, and of some other isolated dIrrs, despite their different SFHs, raises the possibility of common formation pathways for *fast* and *slow* dwarfs that evolve in isolation.

We of course offer the above discussions with the caveat that they consider limited numbers of UFDs, and with results that would benefit from further refinement; e.g. the Leaky Box fit for Leo T was made using only 16 stars. In any case, this line of investigation could be furthered with studies of more UFDs. Here, the CaHK imaging technique will also be useful, as it will allow us access to stellar metallicities of the less luminous and more distant galaxies currently known (e.g. Andromeda XVI, as part of HST-GO-16686; PI D. Weisz), and that are expected to be discovered in upcoming surveys.

Interpretation of UFD MDFs in Cosmological Simulations

While one-zone chemical evolution models have been pivotal in building intuition around the relationship between galaxy MDFs and the physics driving their evolution, detailed simulations show that a subset of dwarf galaxies are affected by a combination of reionization (e.g., [69], [113]), local environment (e.g., [11]), and internal stellar feedback ([294], [285]). While some studies have produced certain observed features, such as the SFH of isolated dwarf galaxies (e.g., [88], [243]), and have begun to resolve bulk properties such as mean metallicity in UFDs [e.g., 322], the lack of robust MDF observations of UFDs have motivated few studies to extensively simulate UFD MDFs as tracers of their formation processes. [143] is one of the few studies so far that predict MDFs of UFDs by following the evolution of 6 halos with present-day stellar masses from 10^4 $M_\odot$ to almost 10^6 $M_\odot$. We use their MDFs as a point of comparison.

Figure 2.10 presents the MDF of Eri II, compared to the MDFs of the 6 simulated UFDs from [143]. Halos labeled Halo1, Halo2, and Halo3 are UFD analogs whose

star formation was ultimately shut off after reionization, though the study finds that both SNe and reionization are necessary to quench these galaxies. We consider these halos to have a SFH that is most analogous to that of Eri II. The remaining massive halos simulated were able to form stars after reionization through gas accretion and mergers. Comparing the MDF of the first 3 halos to Eri II, Halo2 has the MDF that is most similar to that of Eri II, although within the simulation there is still variation in MDFs between halos that experienced similar SFHs and quenching mechanisms.

Regardless of mass, all of the simulated MDFs display long, metal-poor ([Fe/H] < -4.0) tails. In the simulation, these stars represent Pop II stars that were directly enriched by the death of Pop III stars at $z > 11$ in mini halos that later merged to form the final UFD analogs. This interpretation of the origin of the metal-poor tail is in contrast with the results of our one-zone fit to Eri II's MDF, which also predicts a long, metal-poor tail, but which attributes it through chemical enrichment taking place in a single system rather than in the aggregate of many. Additional theoretical work to refine the interpretation of various components of MDFs would be of great interest in understanding small-scale galaxy formation. In any case, both comparison to one-zone models and cosmological simulations point to additional theoretical basis for expecting to find EMP stars in Eri II, and possibly in other UFDs as well. CaHK imaging studies with larger FoVs and increasing depths could uncover additional EMP candidates, but since these stars would have metallicities at the limit of discernment via CaHK, future discoveries would need to confirmed via low-resolution spectroscopic studies on current facilities or observations on the next generation of ELTs [see, e.g., 255].

Finally, for each of the simulated MDFs, we also compute their mean metallicity, metallicity dispersion, and skew. The skew metrics confirm what we also verify visually: that all of the simulated MDFs from [143] are left-skewed compared to that of Eri II, in part because our models do not reach below [Fe/H] $= -4.0$. As a result, the simulated MDFs tend to have a lower average metallicity than Eri II, and also larger metallicity dispersions.

Since there are stars in our sample that may be more metal-poor than [Fe/H] $= -4.0$ to within 2 sigma, improved metallicity measurements may populate the metal-poor tail of Eri II's MDF. If Eri II also has a radial metallicity gradient decreasing outwards, then measuring the metallicity of Eri II members out to larger radii may also bring the MDF of Eri II closer to predictions from this study.

More generally, since a viable theory of galaxy formation should be able to produce features of the UFD population, we suggest that future population-level comparisons between simulated and observed UFD MDFs could also account for MDF statistics. While the population of mean metallicity and metallicity dispersions would be useful baseline statistics to compare, we also suggest that higher-order moments

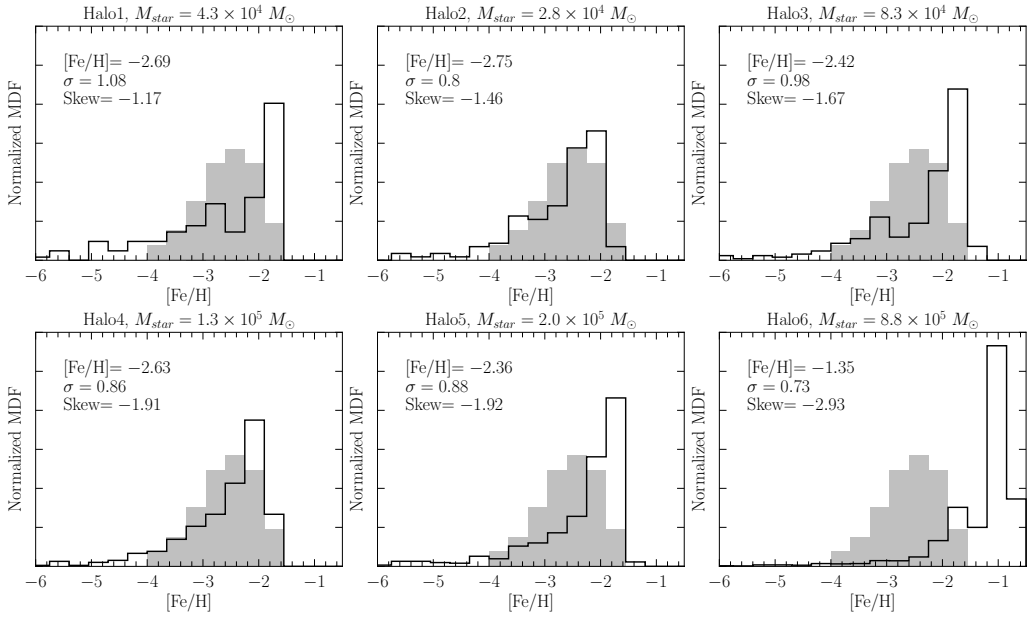


Figure 2.10: Comparison of the MDF that we derive for Eri II (gray shaded histogram; $M_{star} \sim 1 \times 10^5 M_\odot$, [Fe/H] $=-2.50$, $\sigma = 0.42$, skew $= -0.21$) with the 6 UFD MDFs simulated from [143]. Following convention in previous histogram plots, binsizes are 0.35 dex wide. The stellar mass of the corresponding halo at $z = 0$ are in the title of each panel. We also compute the mean metallicity, metallicity dispersion, and skew of the simulated MDFs. All of the simulated MDFs are skewed relative to Eri II, with long metal-poor tails.

such as skew and kurtosis would be important for capturing asymmetries in the shape of UFD MDFs, which are currently also represented in the one-zone models.

2.7 Conclusion

In this work, we combined HST WFC3/UVIS imaging in the narrow-band $F395N$ filter with broadband archival photometry to measure metallicities for 60 stars in Eri II, increasing the sample of member stars with known metallicities by a factor of nearly 4. We derive a mean metallicity of [Fe/H] $=-2.50^{+0.07}_{-0.07}$ and metallicity dispersion $\sigma_{\rm [Fe/H]} = 0.42^{+0.06}_{-0.06}$, which is consistent with results from spectroscopic studies and with known trends about UFDs. We are able to independently confirm

that Eri II is a UFD whose mean metallicity is consistent with properties of the general UFD population, and that it has a large internal metallicity dispersion. These results affirm the promise for HST Ca H&K narrow-band photometry to faithfully recover the MDF properties of Eri II's fainter UFD counterparts.

From an expanded sample of stellar metallicities, we fit one-zone chemical evolution models to the MDF of Eri II and find that it is best-represented by a Leaky Box, similar to results from studies of LG isolated dwarf galaxies. We also present an updated orbit for Eri II, which suggests that it only recently fell into the Milky Way. The composite of these results suggest that Eri II likely formed in an underdense region of the universe at high redshifts.

We also use our photometry to identify outliers in our derived MDF that may be promising targets for follow-up spectroscopy to 1) verify kinematic membership with Eri II, 2) refine the shape of the Eri II MDF at the most metal-poor end, and 3) conduct detailed chemical abundance analysis to infer sources of past enrichment events. Since the field of our narrow-band imaging also includes the central cluster of Eri II, future work will also involve measuring the metallicity of the cluster as well.

Finally, having verified the efficacy of Ca H&K narrow-band imaging for inferring the MDF of UFDs, our forthcoming publications will characterize the MDFs of the rest of the 18 UFD candidates observed by HST-GO-15901.

2.8 Impact of alpha element abundances on CaHK photometry

Figure 2.11 compares the MIST models in CaHK color space for Solar-scaled alpha abundances (left) to those for $[\alpha/\mathrm{Fe}] = +0.4$ (right). At a given metallicity, the alpha-enhanced tracks are shifted down (redward) in CaHK space relative to the Solar-scaled alpha tracks. For the more metal-poor models, the alpha-enhanced models also extend redder in $F475W - F814W$. Stars which fall outside the Solar-scaled alpha grid are within the alpha-enhanced models.

If we re-compute our MDF using the Solar-scaled alpha models, we derive a mean metallicity of $[\mathrm{Fe/H}] = -2.26 \pm 0.07$, and a metallicity dispersion of $\sigma_{[\mathrm{Fe/H}]} = 0.44 \pm 0.06$. Thus, the MDF we derive would be more metal-rich, but the metallicity dispersion would remain unchanged. While alpha abundances changes our inferred stellar metallicities, these differences are not enough to account for the discrepancies between our measurements and those of Z20, since as Figure 2.5 shows, the discrepancies in measurements are at least 1 dex or more.

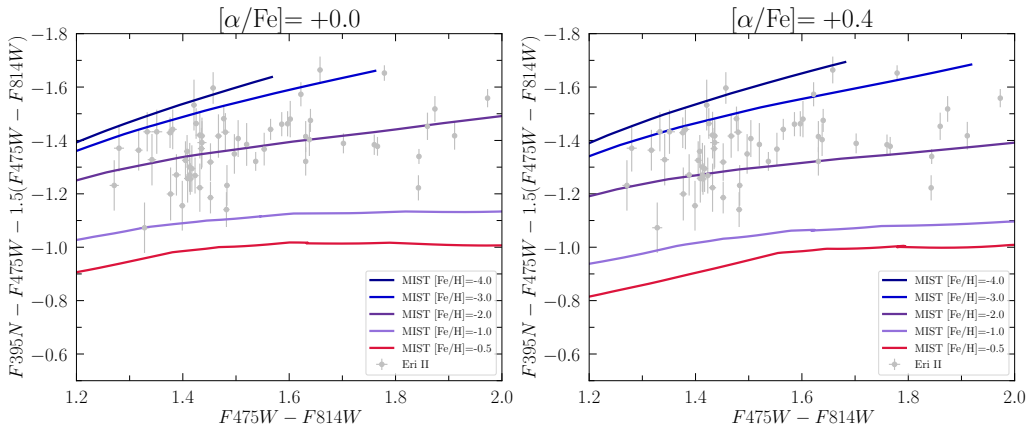


Figure 2.11: Comparing MIST isochrones in CaHK color space for isochrone models with [α/Fe]= 0.0 (left panel) vs [α/Fe]= +0.40 (right panel). For an isochrone of a given metallicity, the α-enhanced model reaches redder extents in $F475W - F814W$, and is also redder in CaHK color index.

2.9 Select Metallicity Posterior Distributions of Eri II Stars

In this section, we present select marginalized posterior distributions that result from our measurements of individual stellar metallicities.

Figure 2.12 presents well-constrained marginalized posterior distributions. These distributions have a clear peak with clear tails. Because CaHK is less effective at distinguishing between lower metallicities (e.g., Figure 2.11), the tails of these posterior distributions are often longer at the metal-poor end.

Figure 2.13 shows the posterior distributions of stars that we identify as promising candidates for spectroscopic follow-up in Section 2.5 and Table 2.12.

Figure 2.14 shows the posterior distributions of stars whose 2 sigma metal-poor tail extends beyond the lowest metallicity of our grid.

2.10 Recovery of Synthetic MDF

In this section, we demonstrate the efficacy of the CaHK stellar metallicity inference methods applied in Section 2.4 by recovering a theoretical MDF from synthetic photometry. Figure 2.15 summarizes the results of this exercise.

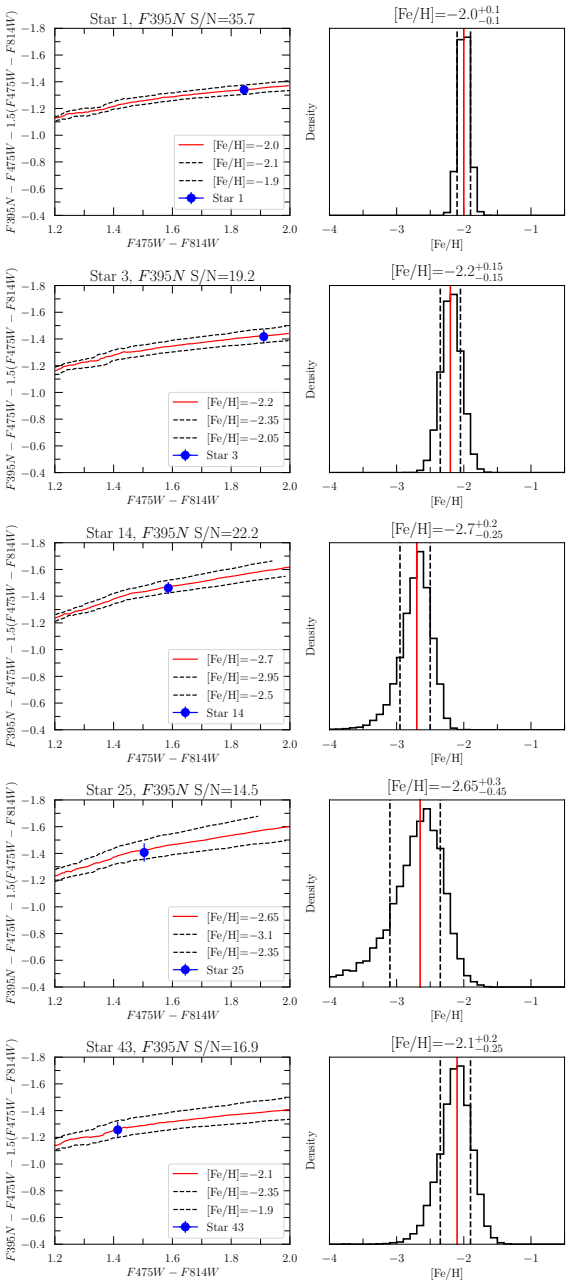


Figure 2.12: Well-constrained posterior distributions.

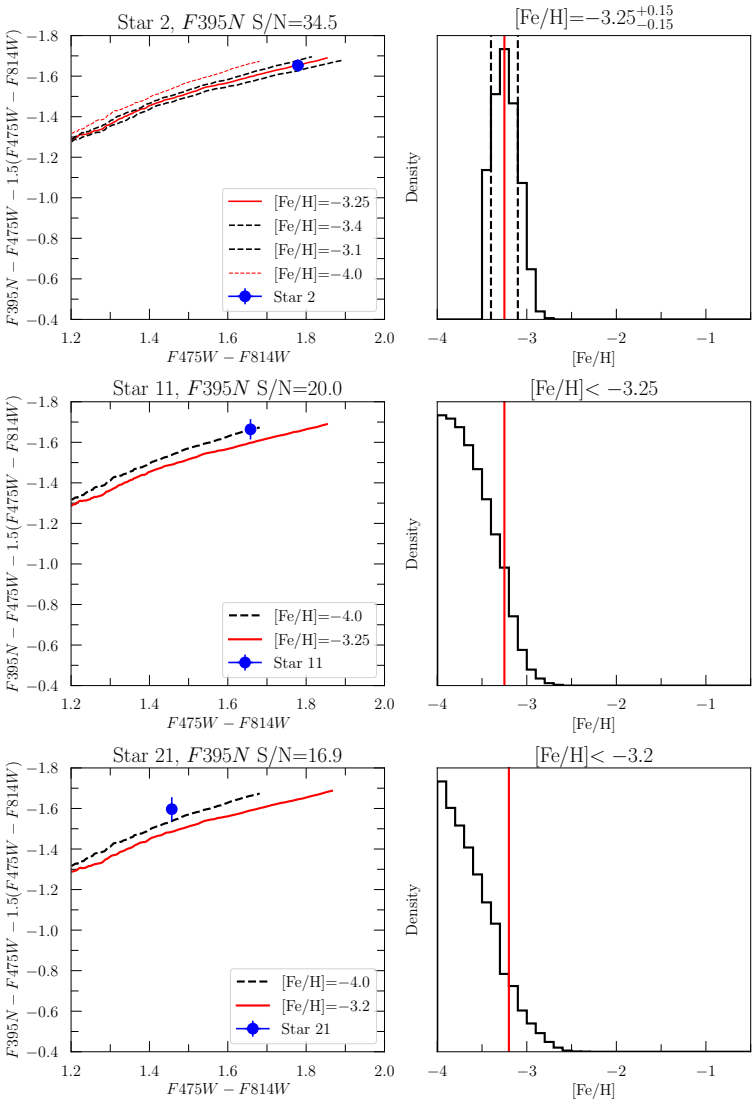


Figure 2.13: Posterior distributions of stars that we flag as spectroscopically accessible EMP candidates for follow-up studies, and which we discuss in Section 2.5.

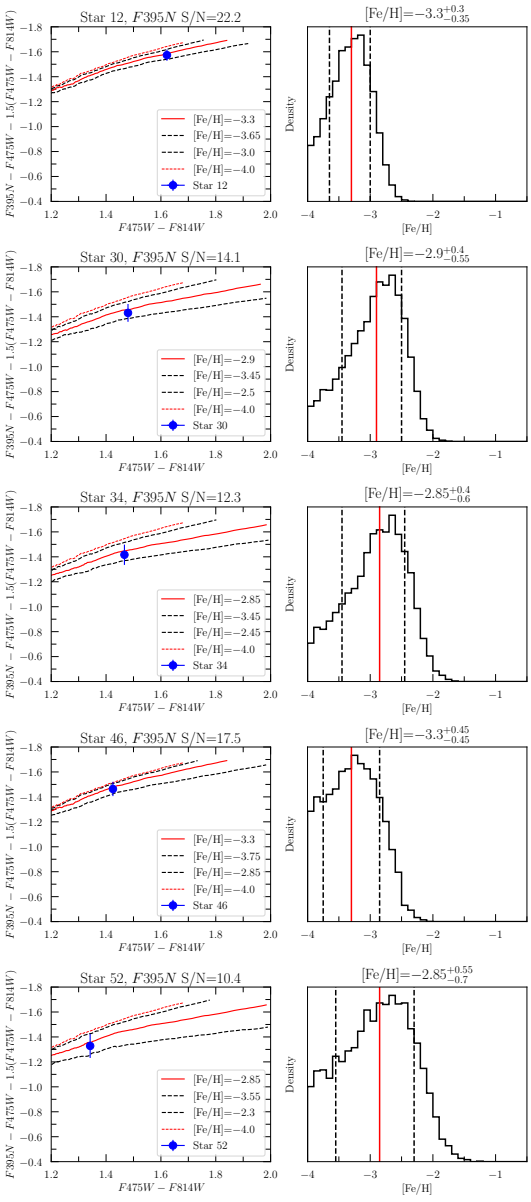


Figure 2.14: Posterior distributions of stars that are truncated at the 2σ level on the metal-poor end. The thin dotted red line is the most metal-poor ([Fe/H] = −4.0 model in our grid.

First, we draw 60 stars from a Gaussian MDF with a mean and spread set by the values that we infer for Eri II in Section 2.5. We use the metallicities of those stars to draw model photometry from isochrones of corresponding metallicity, and ensure that the synthetic colors fall within the CaHK color space range set by our Eri II data. The top left panel of Figure 2.15 shows the location of the resulting model photometry in CaHK color space.

To arrive at the final catalog of synthetic photometries, we apply a bias and error to each model photometry point following its corresponding error profile as determined by the ASTs from Section 2.3. We apply bias as an offset, and apply error as a random draw from a Gaussian corresponding to its AST uncertainty. We also adopt the error bar from our ASTs as the corresponding uncertainties for each synthetic photometric point. The top right panel of Figure 2.15 shows the final synthetic photometry in CaHK color space, with their corresponding uncertainties.

We then measure metallicites from the synthetic photometry following the procedures of Section 2.4. The bottom left panel of Figure 2.15 compares the input MDF to the recovered MDF, and the bottom right panel of Figure 2.15 compares the input metallicities to the recovered metallicities for individual stars. We verify that we can recover the input MDF and individual stellar metallicities following our method for inferring the MDF of Eri II.

2.11 Posterior Distributions of Analytic MDF Parameters

2.12 Table of measurements

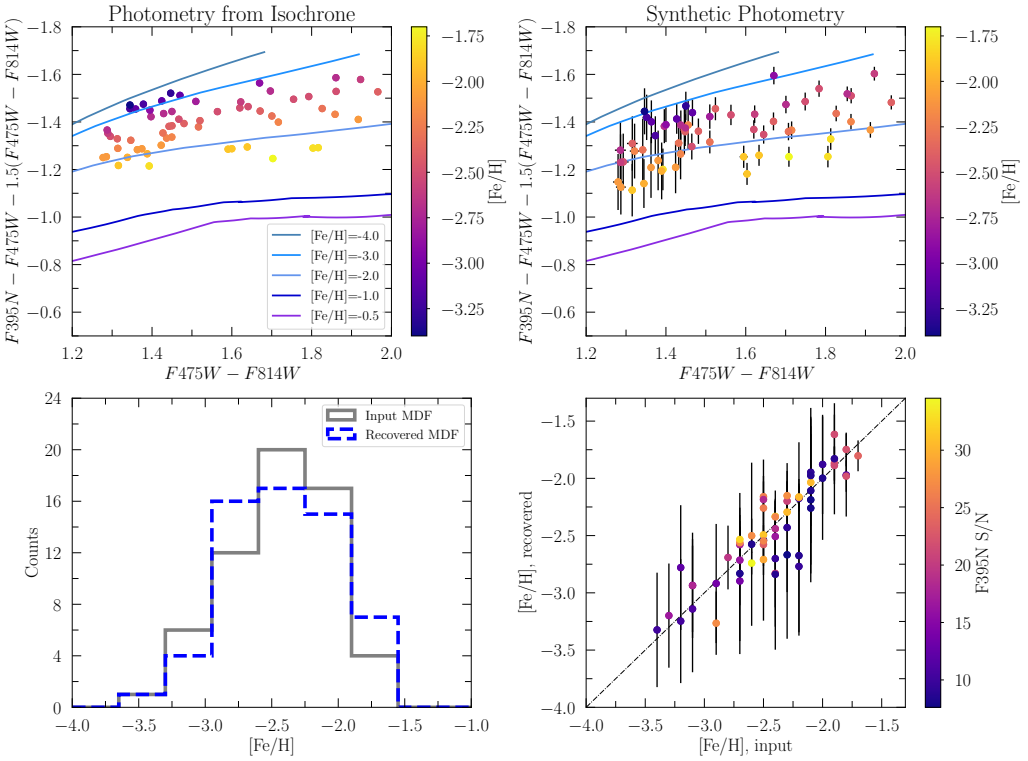


Figure 2.15: **(top left)** The 60 model photometry points that we draw from isochrone models, with metallicity counts set by a Gaussian MDF with a mean and spread consistent with what we measure for Eri II. Points are color-coded by their known metallicities. We also apply extinction to the tracks and the photometry in this plot, but it is negligible (on order of ∼0.01 mag). **(top right)** Synthetic photometry after appying bias and uncertainty from the ASTs (described in Section 2.3 to the model photometry. As in the previous panel, points are color-coded by their known metallicities. **(bottom left)** Comparing the input MDF to the MDF recovered after measuring individual stellar metallicities of the synthetic photometry, following the procedures in Section 2.4. **(bottom right)** Comparing the input metallicity to the recovered metallicity measurements for individual stars. Points are color-coded by their synthetic F395N S/N, as determined from the ASTs. The dash-dotted line is a 1-1 relation.

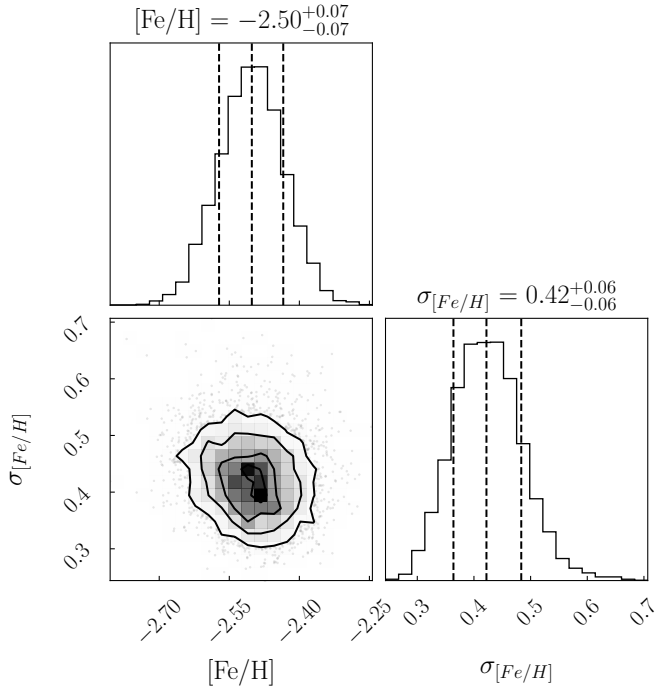


Figure 2.16: Joint distribution of the mean metallicity ([Fe/H]) and metallicity dispersion ($\sigma_{\rm [Fe/H]}$) of Eri II. The dashed lines mark the 16th, 50th, and 84th percentile of the 1D posterior distributions.

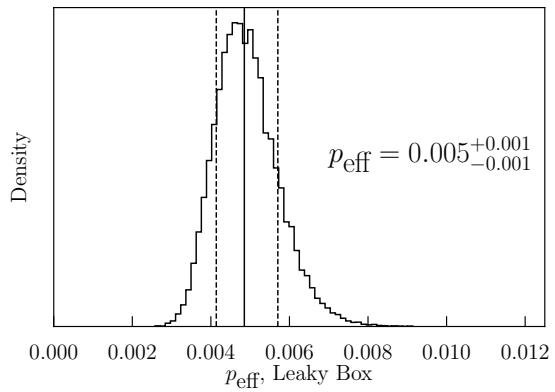


Figure 2.17: Posterior distribution of $p_{\rm eff}$ for the Leaky Box model.

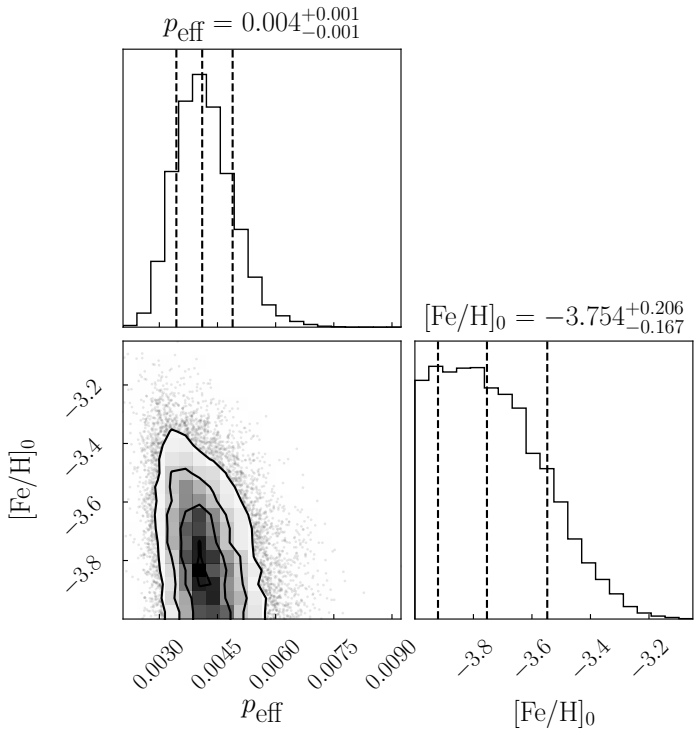


Figure 2.18: Posterior distribution corner plots of $p_{\rm eff}$ and $[{\rm Fe/H}]_0$ for the Pre-Enriched gas model.

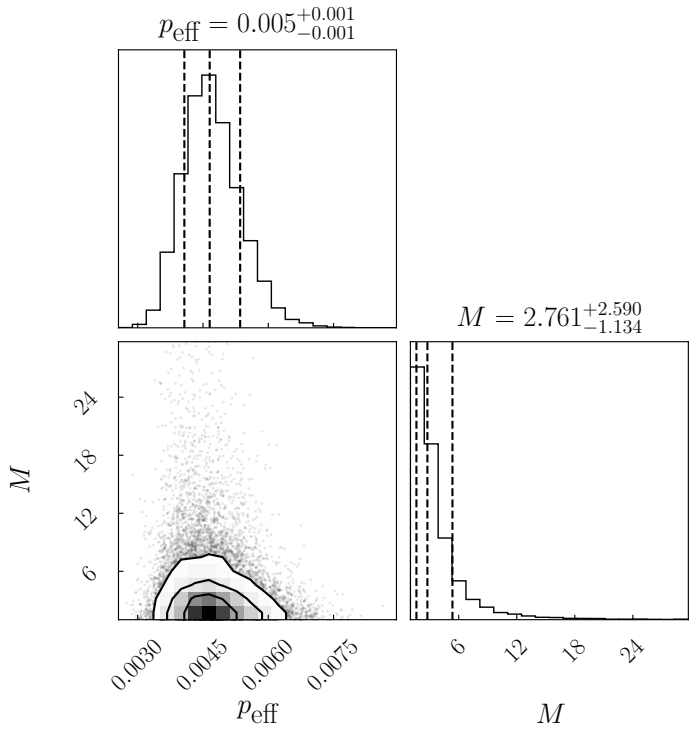


Figure 2.19: Posterior distribution corner plots of $p_{\rm eff}$ and M for the Accretion model.

Table 3
Metallicity Measurements for Eri II Stars

Star ID	R.A. (J2000) (deg)	Decl. (J2000) (deg)	F475W (mag)	F475W−F814W (mag)	CaHK (mag)	[Fe/H]$_{perc}$ (dex)	[Fe/H]$_{ulim}$ (dex)	[Fe/H], L17 (dex)	[Fe/H], Z20 (dex)
0	56.09955	−43.54543	21.243	1.973 ± 0.003	-1.558 ± 0.034	$-2.55^{+0.18}_{-0.16}$	···	-2.18 ± 0.14	···
1	56.11482	−43.52865	21.251	1.844 ± 0.002	-1.340 ± 0.028	$-2.28^{+0.15}_{-0.15}$	···	···	···
2[a]	56.12385	−43.52998	21.288	1.779 ± 0.002	-1.653 ± 0.029	-3.42 ± 0.15	···	···	···
3	56.11106	−43.52301	21.300	1.911 ± 0.003	-1.418 ± 0.036	$-1.85^{+0.16}_{-0.15}$	···	···	···
4	56.08681	−43.52011	21.392	1.874 ± 0.003	-1.518 ± 0.038	$-2.09^{+0.18}_{-0.17}$	···	···	···
5	56.09896	−43.51122	21.392	1.843 ± 0.003	-1.508 ± 0.034	$-2.01^{+0.17}_{-0.16}$	···	···	···
6	56.08422	−43.53636	21.578	1.860 ± 0.004	-1.453 ± 0.031	$-2.18^{+0.15}_{-0.14}$	···	···	-1.00 ± 0.10
7	56.09088	−43.52634	21.629	1.784 ± 0.003	-1.481 ± 0.035	$-2.30^{+0.15}_{-0.14}$	···	···	···
8	56.11060	−43.54553	21.642	1.766 ± 0.003	-1.378 ± 0.033	$-2.17^{+0.12}_{-0.12}$	···	-2.54 ± 0.21	···
9	56.07579	−43.51972	21.700	1.806 ± 0.004	-1.475 ± 0.038	$-2.49^{+0.15}_{-0.14}$	···	···	···
10	56.12467	−43.54148	21.781	1.707 ± 0.004	-1.389 ± 0.037	$-2.03^{+0.17}_{-0.17}$	···	···	···
11[a]	56.09614	−43.52345	21.841	1.664 ± 0.005	-1.664 ± 0.055	$-3.31^{+0.43}_{-0.40}$	< -3.15	-2.82 ± 0.28	-2.14 ± 0.17
12[b]	56.08598	−43.55225	21.961	1.622 ± 0.004	-1.573 ± 0.045	$-3.31^{+0.34}_{-0.35}$	···	···	···
13	56.07777	−43.53295	21.993	1.631 ± 0.004	-1.322 ± 0.055	$-2.00^{+0.27}_{-0.24}$	···	···	···
14	56.07042	−43.54281	22.007	1.586 ± 0.004	-1.461 ± 0.045	$-2.43^{+0.26}_{-0.25}$	···	···	···
15	56.07485	−43.53030	22.030	1.638 ± 0.004	-1.404 ± 0.058	$-2.17^{+0.26}_{-0.26}$	···	···	···
16	56.08938	−43.54092	22.045	1.615 ± 0.004	-1.452 ± 0.047	$-2.29^{+0.26}_{-0.25}$	···	···	···
17	56.07336	−43.54081	22.059	1.604 ± 0.004	-1.462 ± 0.037	$-2.40^{+0.21}_{-0.20}$	···	···	···
18	56.08373	−43.50977	22.064	1.537 ± 0.004	-1.367 ± 0.080	$-2.20^{+0.36}_{-0.35}$	···	···	···
19	56.07061	−43.54157	22.146	1.602 ± 0.004	-1.480 ± 0.068	$-2.38^{+0.25}_{-0.24}$	···	···	···
20	56.11415	−43.54755	22.336	1.565 ± 0.005	-1.441 ± 0.039	$-2.63^{+0.17}_{-0.17}$	···	···	···
21[a]	56.10017	−43.53988	22.622	1.457 ± 0.005	-1.597 ± 0.045	$-3.18^{+0.44}_{-0.47}$	< -3.05	···	···
22[b]	56.10017	−43.53988	22.666	1.477 ± 0.005	-1.482 ± 0.045	$-3.06^{+0.33}_{-0.34}$	···	···	···
23	56.10017	−43.53988	22.717	1.450 ± 0.004	-1.367 ± 0.084	$-2.19^{+0.38}_{-0.37}$	···	···	···
24	56.08373	−43.54495	22.741	1.520 ± 0.004	-1.385 ± 0.068	$-2.54^{+0.33}_{-0.32}$	···	···	···
25	56.11438	−43.55020	22.773	1.482 ± 0.006	-1.410 ± 0.065	$-2.96^{+0.34}_{-0.33}$	···	···	···
26	56.07288	−43.52963	22.805	1.413 ± 0.006	-1.232 ± 0.076	$-2.10^{+0.35}_{-0.34}$	···	···	···
27	56.11173	−43.52711	22.831	1.413 ± 0.006	-1.301 ± 0.090	$-2.49^{+0.43}_{-0.42}$	···	···	···
28	56.11173	−43.52711	22.885	1.349 ± 0.004	-1.349 ± 0.074	$-2.03^{+0.35}_{-0.34}$	···	···	···
29	56.09227	−43.52357	22.923	1.480 ± 0.008	-1.431 ± 0.071	$-2.89^{+0.38}_{-0.35}$	···	···	-1.77 ± 0.16
30[b]	56.12728	−43.53167	22.928	1.436 ± 0.006	-1.417 ± 0.055	$-3.11^{+0.27}_{-0.26}$	···	···	···
31	56.08301	−43.52886	22.954	1.421 ± 0.006	-1.532 ± 0.095	$-3.41^{+0.48}_{-0.45}$	< -2.60	-2.08 ± 0.21	···
32	56.09623	−43.50661	23.007	1.466 ± 0.006	-1.186 ± 0.095	$-2.23^{+0.49}_{-0.46}$	···	···	···
33	56.10423	−43.55268	23.093	1.467 ± 0.007	-1.416 ± 0.081	$-2.87^{+0.39}_{-0.37}$	···	-1.88 ± 0.25	···
34[b]	56.06574	−43.54151	23.094	1.402 ± 0.007	-1.319 ± 0.078	$-2.90^{+0.38}_{-0.36}$	···	···	···
35	56.08264	−43.51725	23.140	1.405 ± 0.007	-1.326 ± 0.071	$-2.91^{+0.33}_{-0.31}$	···	···	···
36	56.09634	−43.51185	23.149	1.432 ± 0.008	-1.420 ± 0.087	$-3.15^{+0.40}_{-0.37}$	···	···	···
37	56.04644	−43.53675	23.161	1.409 ± 0.007	-1.258 ± 0.099	$-2.19^{+0.48}_{-0.45}$	···	···	···
38[b]	56.09625	−43.50623	23.162	1.405 ± 0.007	-1.259 ± 0.095	$-2.18^{+0.47}_{-0.44}$	···	···	···

(continued on next page)

(continued from previous page)

Star ID	R.A. (J2000) (deg)	Decl. (J2000) (deg)	F475W (mag)	F475W−F814W (mag)	CaHK (mag)	[Fe/H]$_{perc}$ (dex)	[Fe/H]$_{ulim}$ (dex)	[Fe/H], L17 (dex)	[Fe/H], Z20 (dex)
39	56.07188	−43.53692	23.175	1.423 ± 0.007	-1.269 ± 0.067	$-2.16^{+0.36}_{-0.34}$	···	···	···
40	56.07565	−43.52075	23.178	1.413 ± 0.008	-1.271 ± 0.067	$-2.21^{+0.36}_{-0.34}$	···	···	···
41	56.07524	−43.52644	23.178	1.408 ± 0.006	-1.359 ± 0.061	$-2.65^{+0.36}_{-0.35}$	···	···	···
42	56.10678	−43.53106	23.179	1.414 ± 0.007	-1.256 ± 0.065	$-2.13^{+0.36}_{-0.34}$	···	···	···
43	56.10915	−43.53941	23.197	1.417 ± 0.007	-1.294 ± 0.087	$-2.33^{+0.42}_{-0.40}$	···	···	···
44	56.10678	−43.53106	23.201	1.429 ± 0.009	-1.231 ± 0.090	$-2.11^{+0.47}_{-0.44}$	···	···	···
45	56.07194	−43.51962	23.055	1.373 ± 0.006	-1.460 ± 0.082	$-2.45^{+0.36}_{-0.35}$	···	···	···
46	56.06780	−43.52577	23.070	1.369 ± 0.006	-1.470 ± 0.080	$-2.47^{+0.35}_{-0.34}$	···	···	···
47	56.09853	−43.54670	23.100	1.365 ± 0.006	-1.480 ± 0.079	$-2.49^{+0.34}_{-0.33}$	···	···	···
48	56.07988	−43.51930	23.150	1.355 ± 0.006	-1.490 ± 0.078	$-2.51^{+0.33}_{-0.32}$	···	···	···
49	56.09217	−43.53084	23.180	1.345 ± 0.006	-1.500 ± 0.077	$-2.53^{+0.32}_{-0.31}$	···	···	···
50	56.08666	−43.52544	23.251	1.336 ± 0.009	-1.181 ± 0.079	$-2.07^{+0.45}_{-0.42}$	···	···	···
51	56.09814	−43.54478	23.395	1.399 ± 0.006	-1.155 ± 0.093	$-1.76^{+0.36}_{-0.35}$	···	···	···
52[b]	56.12947	−43.53420	23.529	1.342 ± 0.008	-1.328 ± 0.096	$-2.86^{+0.54}_{-0.68}$	···	···	···
53	56.12470	−43.53207	23.534	1.388 ± 0.008	-1.271 ± 0.077	$-2.30^{+0.33}_{-0.42}$	···	···	···
54	56.06552	−43.53220	23.635	1.377 ± 0.007	-1.200 ± 0.099	$-2.03^{+0.39}_{-0.50}$	···	···	···
55	56.10222	−43.51683	23.655	1.351 ± 0.010	-1.433 ± 0.083	$-3.32^{+0.52}_{-0.46}$	< -2.49	···	···
56	56.07829	−43.51428	23.675	1.333 ± 0.007	-1.433 ± 0.073	$-3.41^{+0.50}_{-0.40}$	< -2.64	···	···
57[b]	56.11031	−43.54366	23.875	1.271 ± 0.009	-1.232 ± 0.094	$-2.59^{+0.55}_{-0.74}$	···	···	···
58	56.11346	−43.54091	23.903	1.328 ± 0.009	-1.073 ± 0.094	$-1.62^{+0.36}_{-0.37}$	···	···	···
59	56.11659	−43.54202	23.987	1.280 ± 0.009	-1.371 ± 0.088	$-3.28^{+0.60}_{-0.49}$	< -2.34	···	···

Notes. The columns are as follows: (1) Internal Star ID; (2) and (3) R.A. and decl.; (4) F475W mag; (5) F475W−F814W color; (6) CaHK index defined in Section 2; (7) [Fe/H] measurement based off the 16th, 50th, and 84th percentiles of each star' s PDF; (8) upper limit on [Fe/H] where relevant; (9) metallicity measurement from L17 where available; (10) metallicity measurement from Z20 where available.

[a] Stars that we identify in Section 2.5 as being spectroscopically accessible for chemical abundance studies and/or to verify their EMP nature. We discuss them in Section 2.5.

[b] Stars whose posterior distributions display clear peaks, but which are truncated at the metal-poor end, as discussed in Section 2.5.

Chapter 3

Metallicity Distribution Functions of 13 Ultra-Faint Dwarf Galaxy Candidates

3.1 Overview

We present uniformly measured stellar metallicities for 463 stars in 13 Milky Way (MW) ultra-faint dwarf galaxies (UFDs; $M_V = -7.1$ to -0.8) using narrowband CaHK ($F395N$) imaging taken with the Hubble Space Telescope (HST). This represents the largest homogeneous set of stellar metallicities in UFDs, increasing the number of metallicities in these 13 galaxies by a factor of 5 and doubling the number of metallicities in all known MW UFDs. We provide the first well-populated MDFs for all galaxies in this sample, with $\langle$[Fe/H]$\rangle$ ranging from -3.0 dex to -2.0 dex, and $\sigma_{\rm [Fe/H]}$ ranging from 0.3 dex to 0.7 dex. We find a nearly constant [Fe/H] ~ -2.6 over 3 decades in luminosity ($\sim 10^2 - 10^5$ $L_\odot$), suggesting that the mass-metallicity relationship does not hold for such faint systems. We find a larger fraction (24%) of EMP ([Fe/H] < -3) stars across our sample compared to the literature (14%), but note that uncertainties in our most metal-poor measurements make this an upper limit. We find 19% of stars in our UFD sample to be metal-rich ([Fe/H]> -2), consistent with the sum of literature spectroscopic studies. MW UFDs are known to be predominantly > 13 Gyr old, meaning that all stars in our sample are truly ancient, unlike metal-poor stars in the MW, which have a range of possible ages. Our UFD metallicities are not well-matched to known streams in the MW, providing further evidence that known MW substructures are not related to UFDs. We include a catalog of our stars to encourage community follow-up studies, including priority targets

for ELT-era observations.

This chapter has been adapted from Fu, Weisz et al. (2023), which was published in the Astrophysical Journal. This chapter was coauthored by the following individuals, and is included in this dissertation with their permission: Daniel R. Weisz, Else Starkenburg, Nicolas Martin, Alessandro Savino, Michael Boylan-Kolchin, Patrick Côté, Andrew E. Dolphin, Alexander P. Ji, Nicolas Longeard, Mario L. Mateo, Ekta Patel, Nathan R. Sandford.

3.2 Introduction

The development of wide-field photometric surveys and deep imaging capacities has revolutionized the discovery of ultra-faint dwarf galaxies (UFDs) around the Milky Way and within the Local Group (LG; e.g., [26], [170], [23], [82], [135], [53]). With luminosities fainter than 10^5 $L_\odot$, these galaxies occupy the faintest-known end of the galaxy luminosity function [277]. Hubble Space Telescope (*HST*) star formation history (SFH) studies of these galaxies reveal stellar populations that appear uniformly old, suggesting that they may be some of the faintest and earliest galaxies to have formed in the universe ([41], [319], [101], [280], [250]). As high-redshift UFDs are expected to be beyond the observational reach of even the recently-launched *JWST* due to their intrinsic faintness (e.g., [38], [316], [144]), resolved stellar population studies of UFDs in our local neighborhood remain our only window into understanding galaxy formation at the faintest-known scales and the earliest epochs of the universe.

Paramount to these efforts is the characterization of stellar chemical abundances in these systems. At the broadest level, the presence of internal [Fe/H] dispersion is understood to be the distinguishing characteristic between a galaxy and a star cluster, as it has become difficult to categorize many of the newly-discovered satellites on the basis of size and luminosity alone (e.g., [161], [170], [274]).[1] On a more detailed level, the stellar chemistry in a galaxy encodes the astrophysical circumstances of their formation, providing constraints on parameters such as supernovae (SNe) yields, gas inflow/outflow, star formation efficiency, timescales, and burstiness (e.g., [8], [315]). Additionally, the low masses of UFDs make them particularly sensitive to the baryonic physics implemented in cosmological simulations, and reproducing their

[1]Historically, the defining difference between a galaxy and a star cluster is that the former is embedded in a dark matter halo. An internal metallicity dispersion has been understood as observational evidence for multiple epochs of star formation, which is only possible with a gravitational potential well deep enough to retain supernovae ejecta for successive star formation episodes [325].

internal chemistry remains a key theoretical challenge for the community ([143], [243], [322], [1], [242]).

For the classical LG dwarf galaxies, the astrophysical circumstances of their star formation have been inferred using well-sampled stellar metallicity distribution functions (MDFs; e.g., [48], [172], [300], [165]). However, similar observations have historically been challenging to make in the UFD regime. [277] highlights the paucity of metallicity information in UFDs. Nearly half of known MW UFDs lack any metallicity information, while the remainder only have a handful of stars bright enough to observe with current ground-based facilities. Next-generation photometric surveys are already delivering on their promise to discover more faint satellites and out to larger distances (e.g., [134], [225], [52], [286]), and even observations with next-generation spectrographs on extremely large telescopes (ELTs) will not be able to observe adequate numbers of stars in these galaxies to sufficiently populate the galaxy's MDF. For example, Fig. 9 from [277] projects that medium-resolution spectroscopy on forthcoming ELTs may only be able to reach $\lesssim 10$ stars at best in a Ret II equivalent UFD at 250 kpc.

An alternative solution is through photometric metallicities. Though optical broadband photometry is largely insensitive to metallicity[2], medium and narrow bands that target specific absorption features in cool stars, e.g., red giant branch stars (RGB), have a long history of metallicity measurements in the Milky Way. Building on a long legacy of Ca H&K imaging surveys of stars in the MW, the CFHT/Pristine survey [291] has shown that the combination of Ca H & K, *g*-, and *i*-band imaging can be used to measure metallicities of individual stars to a precision of 0.2-0.3 dex for stars as metal-poor as [Fe/H]$= -3.0$ enabling the detection of extremely metal-poor stars ([Fe/H]< -3.0) candidates in the MW (e.g., [329], [308]).

Motivated by the success of the PRISTINE survey, we designed an *HST* program (GO-15901; PI: Weisz) that leverages its excellent blue-optical sensitivity and its underused Ca H&K filter (UVIS/F395N) to measure metallicities of faint stars in a sizable sample of UFD satellites of the MW. The first published results from this program analyzed Eridanus II (Eri II), the brightest galaxy observed by this program. Specifically, [96] demonstrated that the *HST* Ca H&K photometric metallicities are in good agreement with the Calcium Triplet (CaT) calibration [180] that is the current community standard for ground-based spectroscopic studies characterizing UFDs ([161], [182], [184], [94], [274], [55]), as well as its agreement with less-often used photometric metallicity calibrations such as those from RR Lyrae stars [202]. The well-populated *HST*-based MDF served as a basis for demonstrating that the star formation of Eri II was characterized by strong outflows and low star-formation

[2]An exception is the metallicity-sensitive SDSS *u* band, e.g. [141], [7].

efficiency [257], which are in good agreement with theoretical expectations [223]. These results demonstrate *HST*'s unique ability to provide insight into the baryon cycle of the faintest galaxies in the Universe.

In this paper, we present MDF measurements for the 13 UFDs observed by our program. This work represents the largest homogeneous set of stellar metallicity measurements in UFDs to date and will enable a wide range of science in future papers from this program. The goals of this paper are to detail the metallicity determinations and provide qualitatively new insight into our knowledge of the MDFs of UFDs.

This paper is organized as follows. We describe our observations and photometry in §3.3 and detail our methodology for measuring metallicities in §3.4. We apply our method to a few detailed examples in §3.5 and discuss caveats and systematics. We discuss the MDFs for each galaxy in the sample individually in §3.6 and place our results into a broader context in §3.7. We summarize our work in §3.8.

3.3 Observations and Data reduction

In this section, we detail the target sample selection process, summarize the observations, and describe the photometric reduction process. The design of this program sought to balance observational efficiency with the need to obsereve enough UFDs to broadly characterize MDFs across a population of faint galaxies using the *HST*-equivalent of the Ca H&K color-color space used by the Pristine survey. This typically required acquiring new $F395N$ and $F475W$ (SDSS g-band) imaging with *HST*/UVIS and pairing it with archival ACS/$F814W$ and ACS/$F606W$ data. All of the *HST* data analyzed in this program can be found in MAST at this link: http://dx.doi.org/10.17909/cfn9-gt96.

Target Selection

To select our sample, we started from all known UFDs within $\sim$ 300 kpc of the MW as listed in [277]. We first eliminated galaxies with existing well-populated MDFs and removed galaxies that are angularly too large on the sky for *HST* to efficiently observe them in a single pointing (i.e., HST must cover $\gtrsim 70\%$ r_h). For observational efficiency, we removed a small number of galaxies that did not have archival $F814W$ imaging. We also eliminated galaxies that would have required large numbers of orbits due to a paucity of sufficiently bright stars, i.e., the galaxy is distant and/or didn't have more than $\sim$ 20 stars that could be observed in 4 orbits of *HST* time.

This process resulted in 18 systems that range in distance from $20 \lesssim D \lesssim 300$ kpc and spans a factor of ~ 1000 in luminosity.

Following the execution of our program (see §3.3), some of the systems in the original sample changed status. At the time of proposal, Sgr II was a UFD candidate [186], but there is now strong evidence it is a globular cluster (GC; [187], [22]). Additionally, our analysis of the Sgr II data is also consistent with its GC status. Thus, we omit this system from our study. Dra II is also a UFD candidate whose status is still under debate (e.g., [184], [22]); we chose to include it due to this ambiguity. Finally, Indus II was originally classified as an extremely faint UFD, but subsequent studies revealed that it was a spurious detection of noise [47]; our reduction of this data also confirms that there is no stellar system at this location. As discussed in [96], we used existing deep $F475W$ and $F814W$ imaging for Eri II and only added new $F395N$ imaging. Owing to unresolvable alignment issues (i.e., lack of bright stars in the field) in the photometry process for the remaining 3 UFDs observed by our program (Pisces II, Pictor I, and Segue II), we exclude them from our analysis for this work.

Thus for this work, we focus on only 13 systems. Table 3.1 lists the observational characteristics of our UFD sample.

Table 3.1: Observational Properties of UFDs

Galaxy	M_V (mag)	r_h (arcmin)	$(m-M)$ (mag)	r_h, WFC3 FoV	Exp. Time F395N (s)	Exp. Time F475W (s)	Exp. Time F606W (s)	Exp. Time F814W (s)	S/N$_{F395N}$ = 5 F395N (mag)	S/N$_{F395N}$ = 5 F475W (mag)
Eridanus II	-7.1	2.3 ± 0.12^{a}	22.8 ± 0.3^{a}	1.13	5517	7644	28,580	7900	26	26
Canes Venatici II	-5.2	1.83 ± 0.2^{b}	21.02 ± 0.3^{c}	1.26	6584	1014	20,860	20,860	26	26
Hydra II	-4.9	1.7 ± 0.3^{d}	20.89 ± 0.11^{e}	1.53	6584	1014	4746	4746	26	26
Reticulum II	-4.0	6.3 ± 0.4^{f}	17.5 ± 0.1^{f}	0.41	4534	780	4627	4627	25.5	25
Horologium I	-3.8	1.1 ± 0.15^{g}	19.18 ± 0.09^{g}	2.36	4526	780	4627	4627	26	26
Grus I	-3.5	1.77 ± 0.4^{h}	20.4 ± 0.2^{h}	1.47	9481	1314	4766	4766	26	26
Reticulum III	-3.3	2.4 ± 0.9^{i}	19.81 ± 0.31^{i}	0.92	8040	919	4662	4662	26	26
Willman 1	-2.9	2.52 ± 0.21^{j}	17.9 ± 0.4^{k}	0.97	4534	780	4627	4627	26	25
Phoenix II	-2.7	1.5 ± 0.3^{l}	19.6 ± 0.2^{l}	1.73	4534	780	4627	4627	26	25.5
Eridanus III	-2.1	0.315 ± 0.03^{l}	19.8 ± 0.04^{l}	8.25	4534	780	4627	4627	25.5	25.5
Tucana V	-1.6	1.0 ± 0.3^{l}	18.71 ± 0.34^{l}	2.6	3120	730	4661	4661	25	25
Segue 1	-1.3	4.5^{m}	16.8 ± 0.2^{m}	0.58	8776	1314	4605	4605	26	25
Draco II	-0.8	2.7 ± 1.0^{n}	16.9 ± 0.3^{n}	0.96	8040	919	4662	4662	26	25

Notes. Observational characteristics of the UFDs analyzed by this program are presented in order of descending luminosity. We provide information on their on-sky size in relation to the HST FoV, their distance modulus, and exposure times of the images used in this study. As a summary of data depth, for each UFD, we report the F475W and F395N magnitudes where F395N S/N = 5. In all cases except Eri II and CVn II, the archival F606W and F814W imaging are from GO-14734 (PI: Kallivayalil). For CVn II, the F606W and F814W imaging are from GO-12549 (PI: Brown). For Eri II, all of the broadband imaging is from programs GO-14224 (PI:

Gallart) and GO-14234 (PI: Simon). All of the data can be found in MAST at the following doi:10.17909/cfn9-gt96.

References. a. [68], b. [253], c. [114], d. [195], e. [309], f. [224], g. [146], h. [167], i. [82], j. [220], k. [327], l. [65], m. [26], n. [170].

Observations and Data Reduction

We acquired new $F395N$ and $F475W$ observations for our 18 systems between Jan and Oct 2020. The $F395N$ and $F475W$ filters are equivalent to the *Pristine* Ca H&K narrow-band and g band filters used for measuring stellar metallicities, and as shown in [96], are also able to recover MDFs. We required that the UVIS fields spatially overlapped archival ACS imaging, but did not place any roll angle constraints in order to maximize scheduleability. Visits were 1-2 orbits in duration.

We use DOLPHOT to perform point-spread function (PSF) photometry simultaneously on $F395N$, $F475W$, $F606W$, and $F814W$ `flc` images for each of our galaxies. We then perform a quality cut on the resulting catalog by requiring that every star has $S/N > 5$, $|\mathrm{sharp}|^2 < 0.3$, and crowd < 1 in $F606W$ and $F814W$, which are the highest S/N data.

Color-Magnitude Diagrams

Figure 3.1 shows the gallery of CMDs for our sample in $F606W - F814W$, and Figure 3.2 shows the corresponding $F475W - F814W$ CMDs. The stellar population sequence for all of our galaxies is narrower in $F606W - F814W$ than in $F475W - F814W$ because (i) the former color combination is less sensitive to temperature, metallicity, and age and (ii) the $F606W$ photometry has much higher S/N owing to longer integration. We therefore use $F606W - F814W$ CMD for UFD candidate member selection, as described in several sections in the paper.

Member selection

As most of our stars are too faint for radial velocities or proper motions, we primarily determine the membership of each star by selecting stars that fall on/near the RGB and/or MSTO on the $F606W - F814W$ CMDs. For each UFD, we then cross-match each star to catalogs of radial velocities to remove MW foreground stars. We provide detailed discussions on membership vetting for each UFD in §3.6.

We note a few difficulties of relying on spectroscopic velocities for cleaning our entire sample: (i) The on-sky footprint of spectroscopic studies extends beyond our

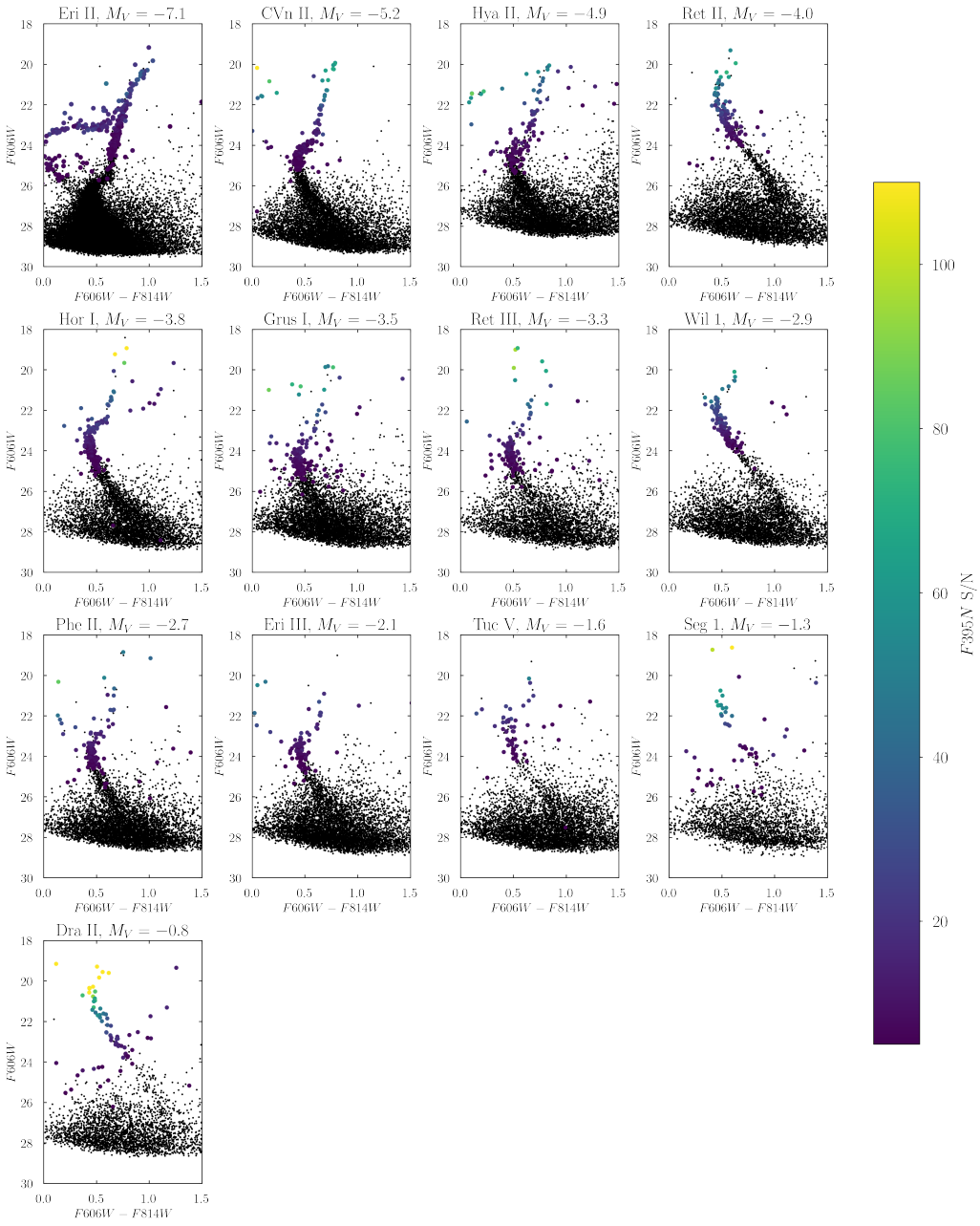


Figure 3.1: A gallery of $F606W - F814W$ CMDs for our galaxies in order of decreasing luminosity from the top left to the bottom right. We color-code stars by their $F395N$ S/N for $F395N$ S/N > 5 and have not yet applied any membership selection or removed spurious detections.

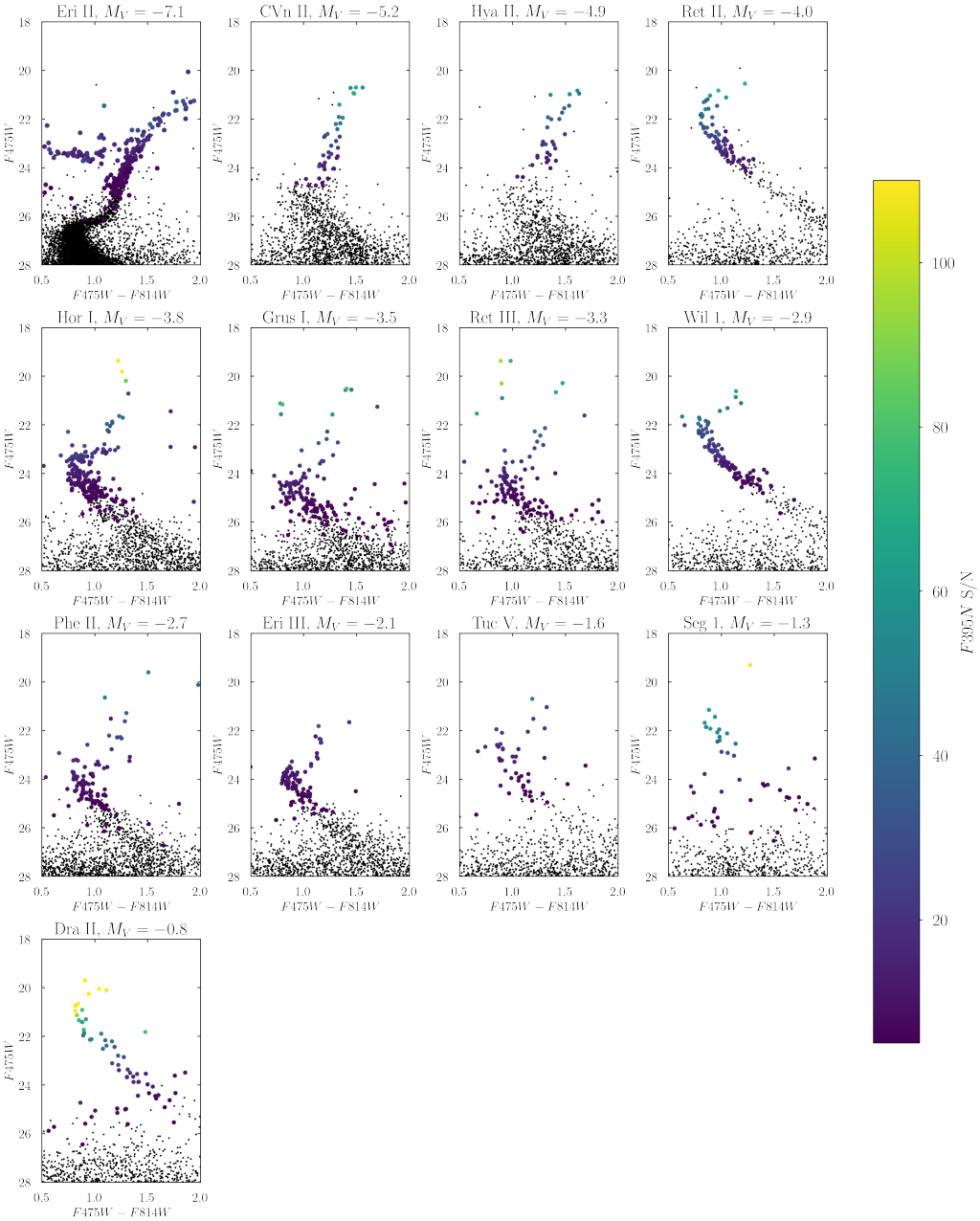


Figure 3.2: The same as Figure 3.1 only for $F475W - F814W$ CMDs. The broader CMD features are partially driven by the lower S/N of the $F475W$ data and the increased metallicity sensitivity of $F475W - F814W$ vs. $F606W - F814W$.

HST field of view and the target density for spectroscopy is smaller due to limitations in slit and fiber placement; (ii) The stars observed spectroscopically are often much brighter than the stars in our sample; (iii) The brightest stars observed by spectroscopy are often missing from our data due to saturation effects in the archival broadband *HST* data. Using kinematic information, we were able to remove a total of 8 contaminants: 6 contaminants in Seg 1 [279][3], 1 contaminant in Ret II [275], and 1 contaminant in Grus I [55]. Some stars in the thirteen UFDs we present in this work have been studied via spectroscopy, and 10 of our UFDs have at least some stars in common with spectroscopic studies. For these stars, we compare our metallicities to those in the literature in §3.6 and §3.11.

Additionally, we manually remove stars which pass the CMD selection criteria, but which, upon closer inspection, have colors that are inconsistent with their presumed astrophysical properties. We perform the following checks: 1) That member stars fall within the [Fe/H] $= -4$ and [Fe/H] $= -1$ isochrones of the [α/Fe] $= +0.4$ MESA Stellar Isochrones and Tracks (MIST) models ([58], [79]) on both the $F606W - F814W$ and $F475W - F814W$ and CMDs, and 2) that the metallicity of stars inferred from the $F395N$ photometry in subsequent sections are consistent with their positions on the broadband CMD: that metal-poor stars should be on the bluer side of the stellar population sequence, and the inverse for metal-rich stars. The stars removed from this process tend to have low S/N in $F395N$, around the cutoff threshold of 10. This manual vetting criteria is still quite broad, and in the absence of kinematic and astrometric data for membership studies, we choose to err on the side of inclusivity in determining our sample of members. We provide a table of observed stars in this paper and invite the community to follow up with complementary observations.

Finally, we expect MW foreground to be a minimal source of contamination for our member samples due to the small HST FoV. We provide an illustration of this expectation in the Appendix: §3.9. Where applicable we also discuss the concern of potential foreground impact for individual galaxies in §3.6. We do not expect the foreground to significantly affect our MDFs or the general results of our paper.

Artificial Star Tests

We use artificial star tests (ASTs) to compute uncertainties on photometry and construct an error profile (bias and scatter) for individual star metallicity fitting as described in §3.4. ASTs involve inserting a star of a known magnitude, in our

[3]Of the contaminants removed using this method, 4 were MW foreground and 2 were stars from the 300S stellar stream in the same field.

case $F395N$, $F475W$, $F606W$, and $F814W$, into each image, and attempting to recover its magnitudes using the same DOLPHOT procedure that we use for the original photometric reduction. By running many ASTs, we build up the statistics to construct well-sampled error profiles for each of our UFDs.

In advance of the metallicity fitting procedure, we generate ASTs around each member star that we identify in each UFD, with about 10^4 ASTs run per star. The general idea is to distribute the ASTs such that they (a) cover all model tracks in Ca H&K space and (b) sample the relevant regions of the CMD. To do this, we center the ASTs for each star within 0.2 mag of its $F475W$ magnitude. We then require the input AST list to satisfy the criteria $0.7 < F475W - F814W < 2.0$ and $-2.0 < CaHK < -0.4$. This is a departure from the procedure for generating ASTs for the Eri II sample in [96], as it provides more efficient coverage of the 4 dimensional AST space. We apply this procedure to each galaxy, including Eri II.

We discuss and illustrate the ASTs in greater detail for select galaxies in our sample in §3.5 and only provide a general summary here. Our error profile is based on difference between the recovered magnitude and its known input magnitude in each filter, (Out - in). At a given magnitude, we use the (Out - in) quantity at that magnitude to define the scatter. We use the mean of the (Out - in) quantity to compute the bias.

In all of our galaxies, the error and bias introduced by $F606W$ and $F814W$ is minimal ($\lesssim 0.01$ mag) because the imaging is much deeper. The scatter in $F475W$ is larger (>0.05 mag) at fainter magnitudes, and there is a modest bias (~ 0.02 mag at $F475W = 24.5$ mag) in recovered magnitudes vs. input magnitudes for fainter ASTs. However, the error and bias in the $F395N$ filter are the chief sources of photometric uncertainty for the metallicity measurements as it has the shallowest imaging of all the data sets (uncertainty ~ 0.1 mag, bias~ 0.1 mag for $F475W \sim 23.5$ mag). We provide concrete examples in §3.5.

3.4 Determining Metallicity Distribution Functions

Individual Metallicity Measurements

To build MDFs, we first infer metallicities for individual stars by adapting the technique used for CMD-based SFH fitting as described in [75]. We first construct the equivalent of a Hess diagram with the x-axis as $F475W-F814W$ and on the y-axis as $CaHK = F395N-F475W-1.5*(F475W-F814W)$, which is motivated by the *Pristine* survey. The resulting Hess-like diagram runs from $0.7 < F475W-F814W < 2.0$

and $-2.0 < CaHK < -0.4$, and bins are 0.025 mag by 0.025 mag. Individual stars are then modeled in this pixelated space. Stellar metallicities are inferred by comparing the overlap of an individual star's Hess-like diagram with that of model CaHK tracks of various metallicities that have been corrected for observational effects. We now describe the process of constructing the metallicity models for fitting each individual star.

We begin with α-enhanced ([α/Fe] = +0.40), 13 Gyr MIST CaHK color-color tracks. We use the MIST suite because they have the most metal-poor limit ([Fe/H] = -4.0) out of all isochrones currently available.[4] Additionally, we choose to use [α/Fe] = +0.40 models because observations thus far have demonstrated that stars at the typical UFD metallicity of [Fe/H] ~ -2.5 tend to be α-enhanced [307] and that UFD stars are uniformly old [41].[5] The impact of our choice in α enhancement is within the uncertainties as verified in §3.10. The mono-metallic tracks we use are 0.05 dex apart. We apply dust corrections to the MIST CaHK tracks using the filter appropriate extinction values from [268]; for most of our galaxies, the extinction is minimal ($A_V \lesssim 0.05$). We use the extinction coefficient for $F395N$ provided by the MIST models for our corrections.

For every point in the model CaHK tracks, we select ASTs that match its color in CaHK color space, and the magnitude of the star in $F475W$. We use the results of those ASTs to calculate the expected bias to apply to that point. As a result of the bias effects discussed in §3.3, the model tracks become redder in CaHK color index and $F475W - F814W$ color. The overall impact of accounting for bias effects is lowering the inferred metallicity. We illustrate these effects in the CaHK color panels in Figures 3.3, 3.5, 3.6.

Next, we pixelate the bias-applied model CaHK tracks into Hess-like diagrams. We use the ASTs to calculate the standard deviation for the ASTs in each pixel, and to convolve it with the number of expected stars from the model tracks. The result at the end of this process are a series of hess diagrams for mono-metallic populations that have been applied with the specific observational characteristics of each UFD. We refer to the hess diagram corresponding to individual metallicities is as a basis function. We normalize the counts in each basis function so that it is equal to 1, and infer a star's metallicity measurement by comparing the overlap of its Hess-like diagram with that of basis functions of various metallicities. Because the number counts can be low in many cases, we adopt a Poisson likelihood function:

[4] As an example, the Dartmouth Stellar Evolution Database [80] Bag of Stellar Tracks and Isochrones (BaSTI; [129]) models only extend down to [Fe/H] = -2.5 and [Fe/H] = -3.2 respectively.

[5] We also note that for these models, the mapping of CaHK color to metallicity in CaHK space is largely invariant with age for old stars.

$$\log L = \sum_{m_i \neq 0} d \ln m_i - m_i - \ln(d_i!), \tag{3.1}$$

where m_i are the number of counts in the model bin, and d_i is the data in each bin.

We adopt uniform priors on the metallicity, ranging between the limits of our metallicity grid: -4.0 and $+0.0$ and then sample the posterior distribution using `emcee` [90] by initializing 50 walkers and running the Markov chain Monte Carlo sampler for 10,000 steps, with a burn-in time of about 50 steps per star. We assess convergence using the Gelman-Rubin (GR) statistic [109]. Compared to [96], this approach allows us to account for uncertainties in both $CaHK$ and $F475W-F814W$. The result of this process is a posterior distribution for the metallicity of each star. We determine metallicity measurements and statistical and systematic uncertainties in the following ways:

For stars with well-constrained posterior distributions, we report the median measurement and their uncertainties corresponding to the 68% confidence interval. Following the investigation into systematics in §3.10, we assign a systematic uncertainty of either 0.2 dex or 0.3 dex depending on if the star is on the RGB or MSTO/MS, respectively.

For stars with posterior distributions that have a well-defined peak but truncation at the MP end, we also report the median measurement and their uncertainties corresponding to the 68% confidence interval. We assign a systematic error of 0.5 dex if their median measurement is below -3.0; if their median measurement is above that, then we follow the schema based on the star's evolutionary phase.

For stars with posterior distributions that only show an upper limit (i.e., no clear peak), we report that upper limit. For stars that fall outside the metal-poor end of the grid, with undefined posterior distributions, we assign them an upper limit of -4. For stars that are unconstrained altogether, we remove them from the sample; since they are low S/N to begin with, their measurements should not significantly change the nature of our inferred MDFs.

We discuss our measurement reporting procedure in greater detail by using the example of CVn II in §3.5 and present example fits to CVn II stars in Figure 3.4. We present the table of measurements in Table 3.4, reporting both the random uncertainties from photometry, and from systematic uncertainties that we determined following our procedure in §3.10.

Fitting the MDF

Following standard practices in the field, we model the MDF of each UFD assuming a Gaussian distribution, for which the parameters of interest are the mean and dispersion of the MDF. For the MDF of each galaxy, we adopt the two-parameter Gaussian likelihood function from [311]:

$$\begin{aligned} \log L = &-\frac{1}{2}\sum_{i=1}^{N}\log(\sigma^2_{\mathrm{[Fe/H]}} + \sigma^2_{\mathrm{[Fe/H]},i}) \\ &-\frac{1}{2}\sum_{i=1}^{N}\frac{(\mathrm{[Fe/H]}_i - \langle\mathrm{[Fe/H]}\rangle)^2}{\sigma^2_{\mathrm{[Fe/H]}} + \sigma^2_{\mathrm{[Fe/H]},i}}, \end{aligned} \tag{3.2}$$

where $\langle\mathrm{[Fe/H]}\rangle$ and $\sigma_{\mathrm{[Fe/H]}}$ are the mean metallicity and metallicity dispersion of the galaxy, and $\mathrm{[Fe/H]}_i$ and $\sigma_{\mathrm{[Fe/H]},i}$ are the metallicity and metallicity uncertainties for each star. In this procedure, we assume Gaussian uncertainties on the individual metallicity measurements, and discuss their derivation later in this section. We adopt a uniform prior on the mean and require that it remain within the range set by the most metal-poor and metal-rich stars for a galaxy. We also require that $\sigma_{\mathrm{[Fe/H]}} \geq 0$. We use `emcee` to sample the posterior distribution, initializing 50 walkers for 10,000 steps. The autocorrelation time for each galaxy is about 50 steps, and the corresponding GR statistic indicates the chains have likely converged.

The above likelihood function assumes symmetric uncertainties on the individual star metallicity measurements. Due to the uneven spacing between mono-metallic CaHK tracks, that is not the case for the vast majority of stars. We thus make the following adjustments:

For stars with posterior distributions that are well-constrained enough where we can report a median and 68% confidence interval uncertainties, we average the asymmetric uncertainties and then add them in quadrature with their corresponding systematic uncertainty (see §3.10 for more detail) order to arrive at the final uncertainty used for the MDF measurement.

For stars whose posterior distributions allow us to constrain an upper limit, we adopt a point measurement that is the median of the posterior distribution. We adopt a Gaussian uncertainty by averaging the uncertainties from the 68% confidence interval. If the upper limit of the star is below -3 (i.e., an EMP candidate), then we add the uncertainties in quadrature with a systematic error of 0.5 dex. If the upper limit of the star is above -3, then we add the uncertainties in quadrature with their corresponding systematic uncertainty.

The above schematic accounts for the vast majority of stars analyzed in our study. Finally, there are a few stars whose CaHK color places them beyond the metal-poor end of the grid. These stars are particularly low S/N ($\lesssim$ 15). We adopt a point measurement of -4.0 with an uncertainty floor of 1.0 dex, which reflects our low confidence in our estimate.

3.5 Illustrative Examples of MDF Measurements

To illustrate the process of measuring MDFs, we provide detailed examples for three systems that represent the range of data quality and galaxy type across our sample. The systems are CVn II (§3.5), Grus I (§3.5), and Dra II (§3.5). CVn II is a bright UFD with a fairly well-populated RGB. Grus I is an intermediate-luminosity UFD with an RGB present. Dra II is a faint UFD with no RGB at all.

CVn II

Figure 3.3 illustrates the MDF derivation process for CVn II. Using the $F606W$ broadband CMD, we select 34 candidate member stars (red points) along the RGB that have $F395N$ S/N$>$ 10. We highlight stars in common with [166] (circled in light blue) and [307] (circled in dark blue), two other spectroscopic studies of CVn II. We compare our metallicities to these literature values in §3.5.

The four panels in the top-right corner of Figure 3.3 show the ASTs (i.e., the difference in input and recovered magnitude vs. input magnitude). The uncertainties in photometry are dominated by $F395N$ and $F475W$. The typical scatter in $F395N$ and $F475W$ towards the faint magnitude limit of $F475W \sim 24$ mag are 0.15 and 0.02 mag respectively. Toward fainter magnitudes, there is also a bias in (Out - in) in both filters. Characteristic to all the UFDs that we analyze, the bias effect is largest in $F395N$ (~ 0.1 mag).

The bottom left panel of Figure 3.3 shows the CVn II RGB stars in CaHK color space, with mono-metallic MIST isochrone tracks for [α/Fe]$= +0.4$ overplotted. The low-opacity lines are the mono-metallic models without ASTs applied, and the high-opacity are the same models with the AST noise model applied. While the bias effect is less prominent for brighter and redder stars, it does become significant for stars bluer than $F475W - F814W = 1.4$. Without accounting for this bias effect, a star's inferred metallicity would be larger than it actually is. For example, a star at $F475W = 23.5$ and with $F475W - F814W = 1.20$, $CaHK = -1.1$ would have an inferred metallicity of -2.0 and -2.3 before and after applying the bias effect, respectively.

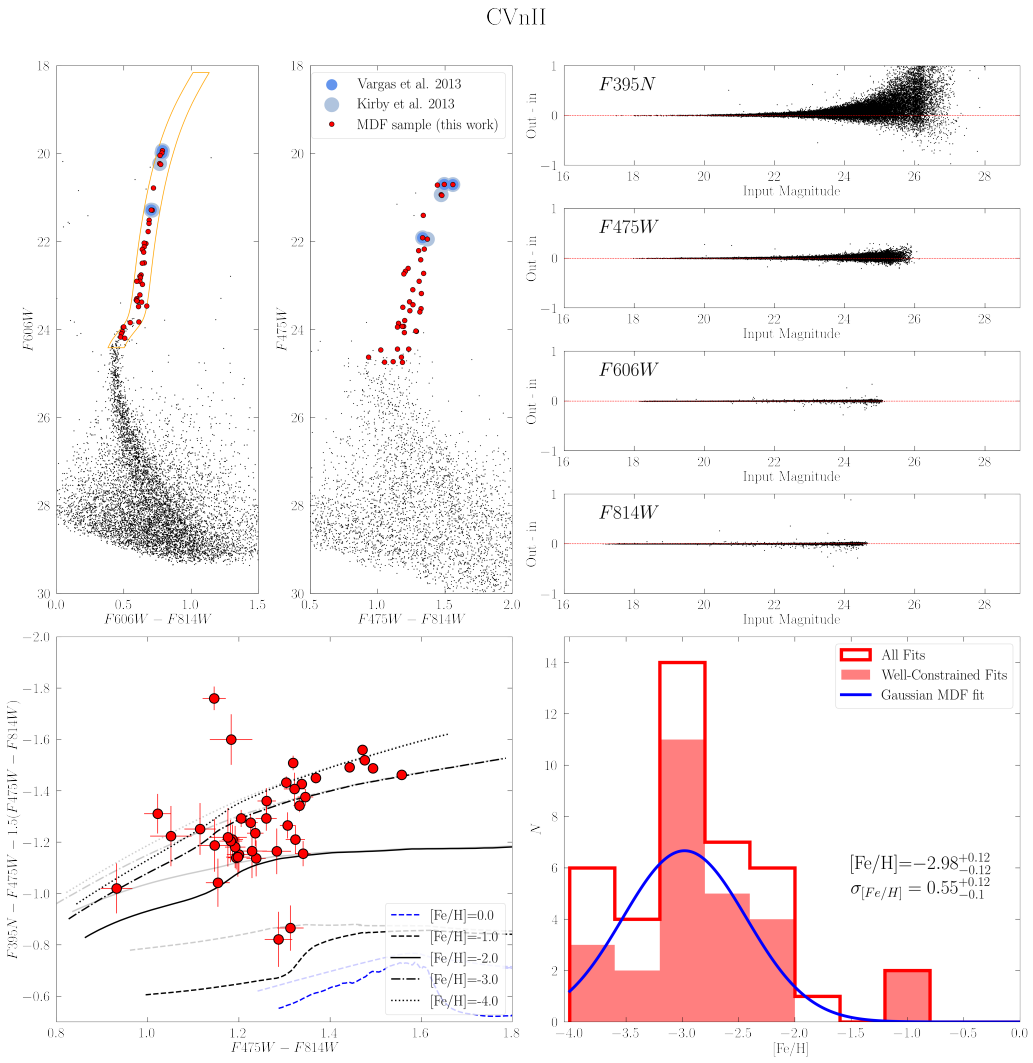


Figure 3.3: An illustrative example of our process for measuring a galaxy's MDF from HST imaging using CVn II. The upper left panels show the CMDs of CVn II, with members shown in red and stars in common with other studies highlighted in blue. The upper right panels show the scatter and bias in the artificial star tests (ASTs) for each filter. The bottom left panel shows the CaHK diagram with member stars plotted in red and select metallicity tracks as lines. The high-opacity lines are the convolution of the intrinsic models low-opacity with the ASTs. The lower right panel shows the MDF of CVn II. The shaded red regions are well-constrained metallicity fits for individual stars, while the unshaded regions reflect stars with poorly constrained fits (e.g., off the metallicity grid, truncated PDFs). The blue line shows a Gaussian fit to all stars on the histogram.

Plotted in CaHK space, it is apparent by eye that the stars in CVn II span a range of metallicities because they do not fall along a single mono-metallic track. The placement of stars in CVn II suggests that there are stars as metal-rich as [Fe/H] $= -1.2$ and at least as metal-poor as [Fe/H] $= -4$, with the bulk of them centered at [Fe/H] $= -3.0$.

We now discuss the nature of our individual metallicity measurements by describing the broad categories of individual posterior distributions and presenting examples in Fig 3.4. Some posterior distributions are well within the metallicity grid and have well-defined peaks; this is usually the case for stars at intermediate metallicities ($\gtrsim -3.0$) and intermediate-to-high S/N in $F395N$ (Fig 3.4, top right). Others are truncated at the metal-poor end, corresponding to the metal-poor limit of the metallicity grid, but with well-defined peaks; these are often stars with [Fe/H]< -3 of intermediate or high S/N (Fig 3.4, bottom left) There are also stars that fall outside of the metallicity grid, so their metallicities are not constrained by the fitting process, and we can only obtain an upper limit (Fig 3.4, bottom right). This includes stars across a range of S/N.

The bottom-right panel of 3.3 shows the MDF of CVn II (red) and our Gaussian fit to the MDF (blue line). We infer $\langle$[Fe/H]$\rangle = -2.98^{+0.12}_{-0.12}$ dex and $\sigma_{\rm [Fe/H]} = 0.55^{+0.12}_{-0.10}$ dex. We identify 15 stars as EMP candidates for spectroscopic follow-up. We also find two stars with metallicity [Fe/H] ~ -1.2, albeit with uncertainties of about 0.5 dex. As we discuss in §3.5, spectroscopic studies of CVn II find similarly metal-rich member stars at larger radii, supporting the notion that our metal-rich stars may be *bona fide* members of CVn II. In §3.5, we compare our metallicities to literature values.

Grus I

Figure 3.5 illustrates the MDF process for Grus I. Grus I has a sparsely populated RGB and the S/N of our F395N data is sufficiently high that we are able to include MSTO stars in our analysis (i.e., the $F395N$ S/N is > 10 down to the MSTO). The layout of Figure 3.5 is identical to the CVn II example (Figure 3.3).Stars in common with the literature study of [55] are indicated in light blue. One of the stars that passed our isochrone selection was ruled by [55] to be a kinematic non-member, so it is represented in the CMD panel plots as a purple point. The ASTs for Grus I also reveal a systematic bias for $F395N$ and $F475W$ for fainter stars that results in the reddening of the mono-metallic tracks in CaHK space (e.g., at $F475W = 24$, a bias of 0.17 mag in $F395N$ and 0.02 mag in $F475W$).

In CaHK color space (bottom left), the highest S/N stars show a clear scatter,

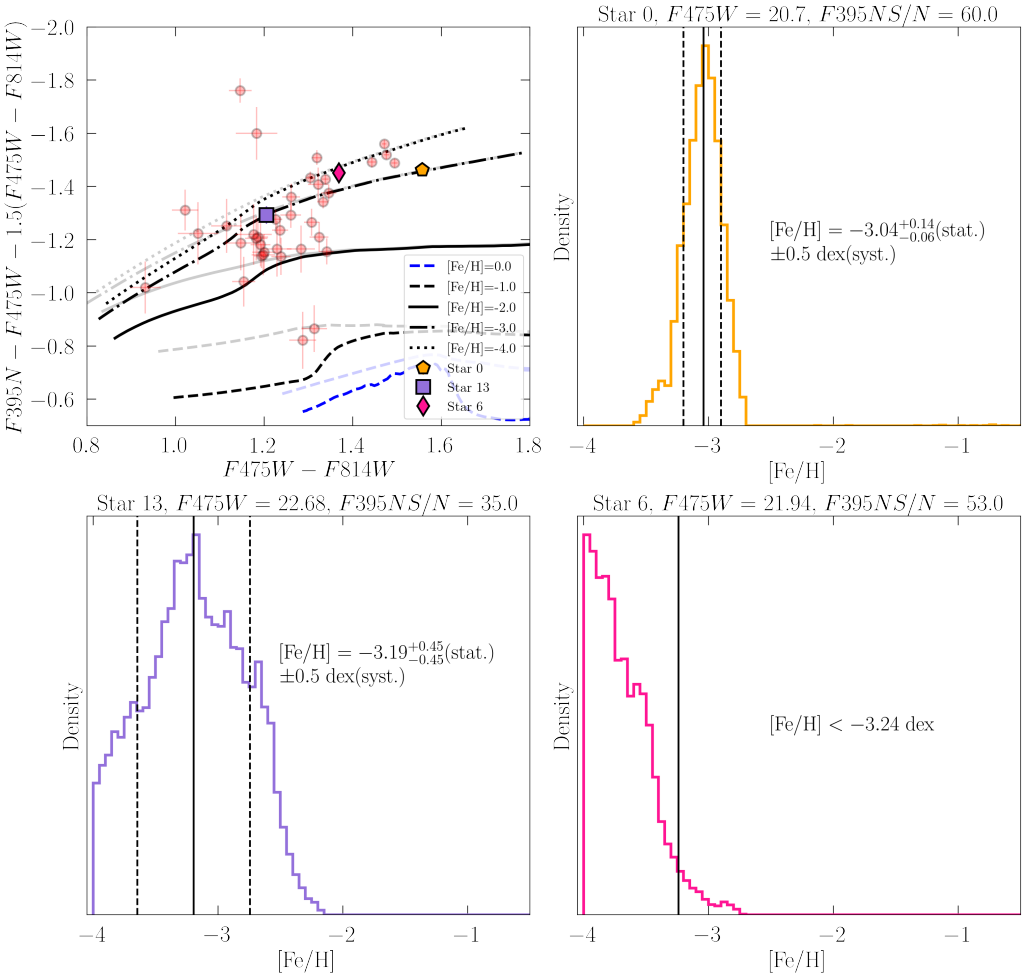


Figure 3.4: Example posterior distribution functions of stars in CVn II. (upper left) Position of example stars in CaHK space, plotted against the MIST mono-metallic tracks used to infer metallicities in this work. (upper right) Example of a star with a well-constrained PDF. (lower left) Example of a star with a well-constrained PDF peak that is truncated at the metal-poor end; we also designate this star as an EMP candidate. (lower right) Example of a star for which we only constrain an upper limit, also an EMP candidate.

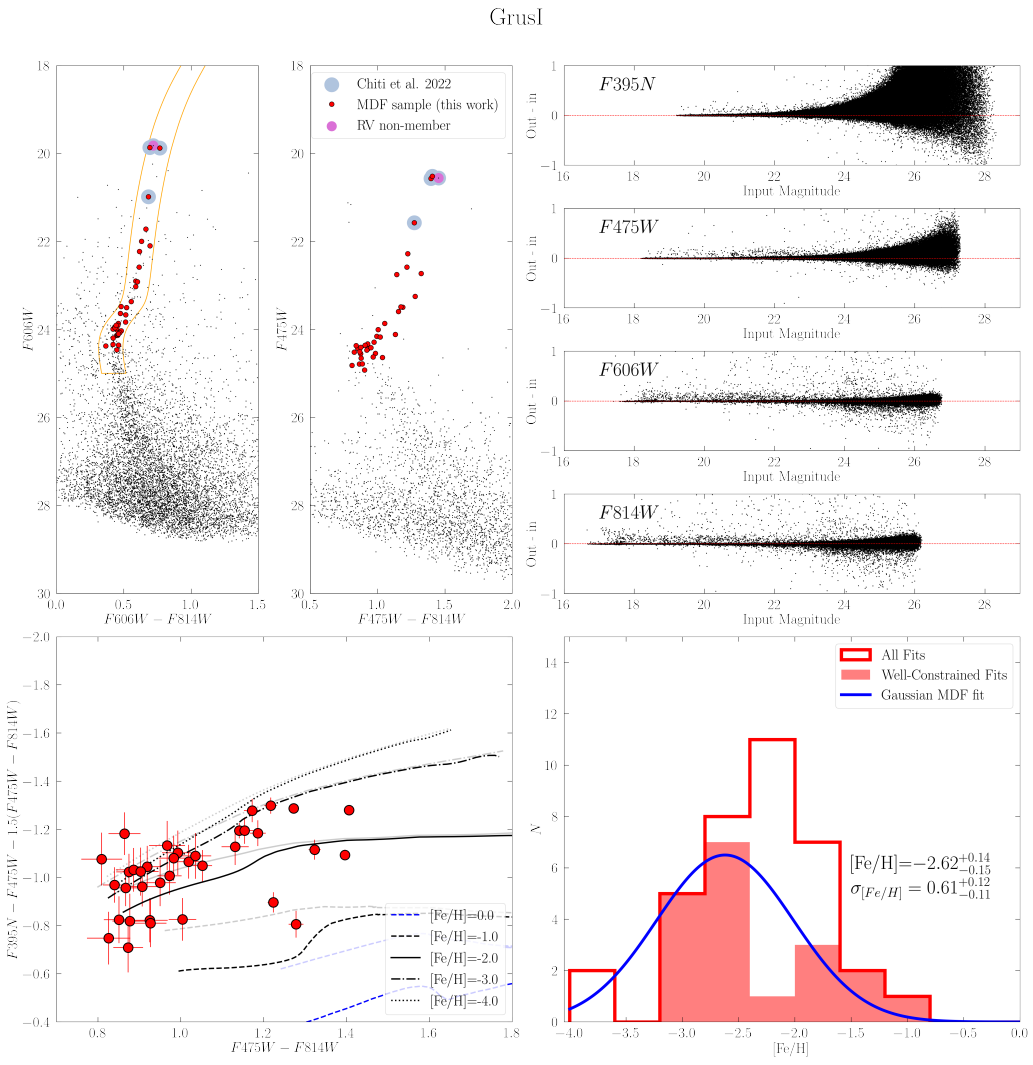


Figure 3.5: Same as Figure 3.3 only for the fainter, less populated system, Grus I.

indicative of a metallicity spread. This is also present for the lower S/N stars, though it is more difficult to visually discern. We identify 5 EMP candidates that would be compelling for spectroscopic follow-up studies. On the metal-rich end, we also find stars with [Fe/H] up to −1.0. From this sample, we infer $\langle$[Fe/H]$\rangle = -2.62^{+0.14}_{-0.15}$ dex and $\sigma_{\rm [Fe/H]} = 0.61^{+0.12}_{-0.11}$ dex.

Dra II

Figure 3.6 shows our detailed MDF derivation for Draco II. Dra II has no RGB at all and thus the metallicities all come from lower MS stars. Our narrow-band data for Dra II reaches $S/N = 10$ at $F475W \sim 24$. The layout of Figure 3.6 is the same as the previous two examples. We highlight stars in common with the ground-based CaHK study of Dra II by [184] in light blue.

The bottom left panel of Figure 3.6, shows the Dra II stars on the CaHK color space. Overplotted are two versions of the mono-metallic MIST isochrone tracks for [α/Fe]-enhanced lower main sequence star models, which illustrate the bias profile computed from the ASTs. The effect of the AST bias is to lower the inferred metallicity of the star, similar to the case of RGB stars. For the case of Dra II, the highest S/N stars are also the stars that are bluest in $F475W - F814W$.

The MDF of of Dra II (bottom right panel) spans a metallicity range of −4.0 to −1.5. From our Gaussian MDF fitting, we infer $\langle$[Fe/H]$\rangle = -2.72^{+0.10}_{-0.11}$ dex and $\sigma_{\rm [Fe/H]} = 0.40^{+0.12}_{-0.12}$ dex.

Comparison to the Literature

Figure 3.7 compares the metallicities and MDFs derived from our data to what is available in the literature for each galaxy. For CVn II, our sample includes 5 stars that were spectroscopically studied by [166], and of those 5 stars, 3 were also analyzed by [307]. We color code stars with [α/Fe] measurements by the value of their alpha. For this limited sample, we generally find that point estimate metallicities from [166] are systematically 0.6 dex more metal-rich than our findings. Including uncertainites, this level of disagreement is $\sim 1.5\sigma$. Given the use of different models, spectral features, and broad approaches, we are encouraged by the similarity of our findings. The stars which have alpha measurements from [307] are also color-coded by the literature point estimates, and typical [α/Fe] uncertainties from that study are 0.2 dex. Their point estimates are indicated in the color-coding. As discussed in [96], increasing α-enhancements in our modeling leads to lower inferred metallicities. For the single star that has a slightly lower value of α from [307] than we assume, re-inferring the metallicity with our α value would bring the measurements into

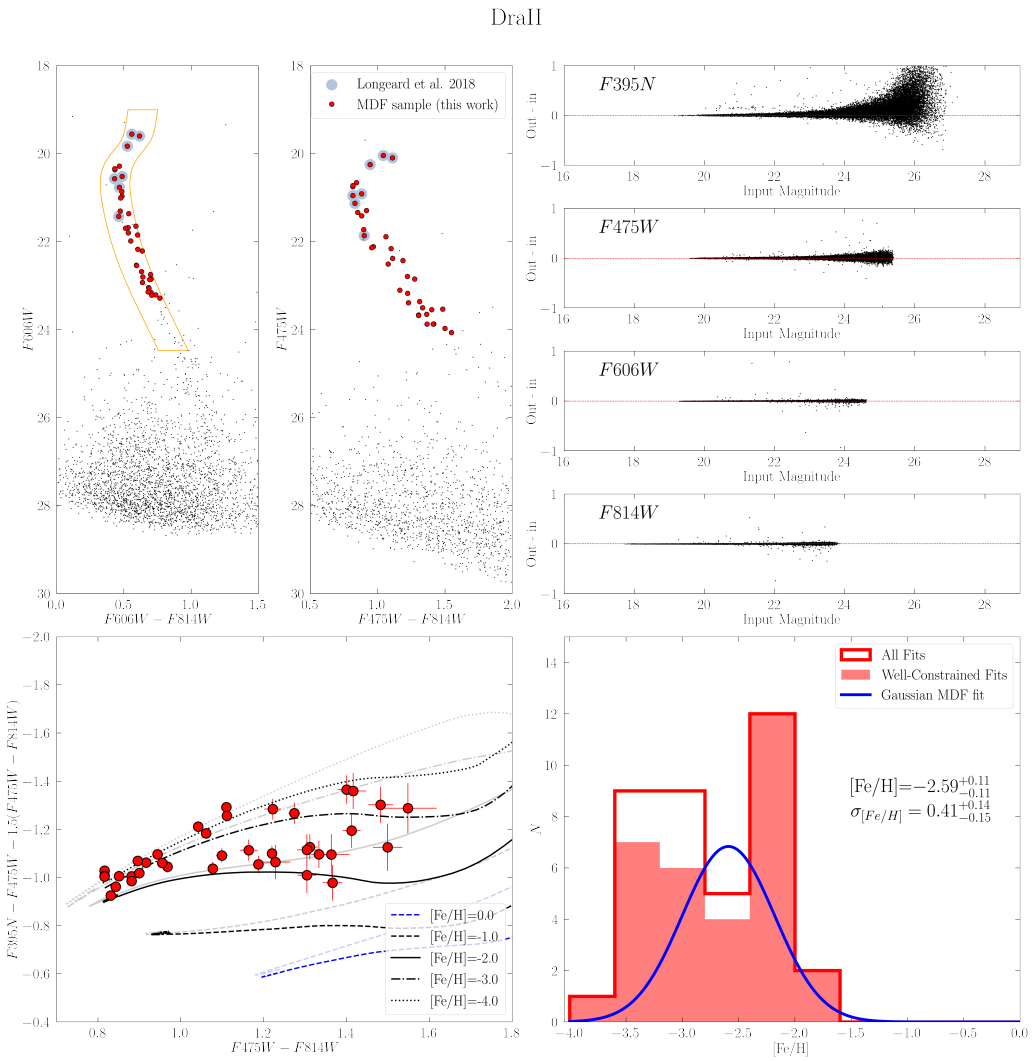


Figure 3.6: Same as Figure 3.3 only for Dra II, which has no RGB stars. The mono-metallic tracks shown in the bottom left panel are for MSTO and MS stars. Accordingly, the MDF is entirely based on stars from these evolutionary phases.

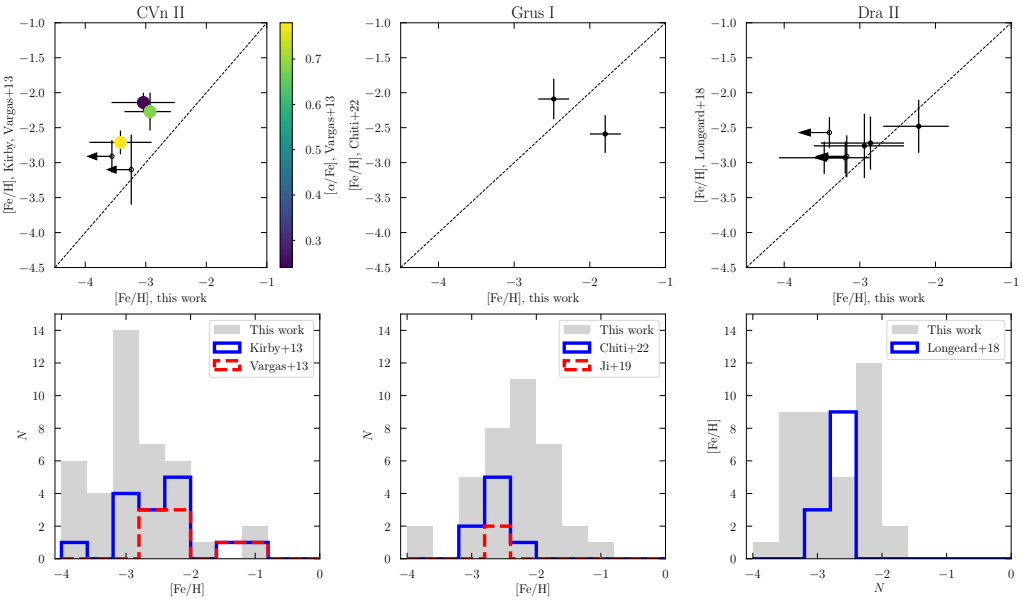


Figure 3.7: A comparison of metallicities for stars in common for our example galaxies CVn II, Grus I, and Dra II. The top row shows a one-to-one comparison for stars common to both studies. Our metallicities and those in the literature generally agree to $\sim 1.5\sigma$. The lower panels show a comparison between our MDFs (grey) and all MDFs in the literature for each galaxy. The histogram bins are 0.4 dex wide.

closer agreement. For the other two stars which are α enhanced, differences in α enhancements alone cannot reconcile the differences.

We also compare our MDF against those from [166] and [305]. [166] infer $\langle$[Fe/H]$\rangle = -2.12 \pm 0.05$ dex and $\sigma_{\rm [Fe/H]} = 0.59$ dex from 14 stars in CVn II. While our $\sigma_{\rm [Fe/H]}$ measurement is in agreement with [166], they infer a mean that is higher than ours by ~ 0.8 dex. This is because our MDF includes more stars that are below [Fe/H] $= -3.0$. Given the agreement shown in the 1-1 comparisons, it is unlikely that all of our EMP stars are systematically too metal-poor. Additionally, it is likely that we are finding more EMP stars in CVn II simply by virtue of an expanded sample size of 40. On the metal-rich end, the stars that we detect between -1.5 and -1.0 are not the same as from [166], but that there are spectroscopically confirmed metal-rich stars affirms our confidence that the ones in our sample are also *bona fide* members of CVn II. Finally, we run a Kolmogorov-Smirnov (KS) test using `scipy.stats.ks_2samp` to test the null hypothesis that the MDF we measure

for CVn II and the MDF from [166] are drawn from the same underlying distribution. The resulting p-value for the test is 0.11, suggesting that there are insufficient grounds to reject this null hypothesis, and it is possible for these MDFs to share the same underlying distribution.

The center column compares our metallicities for Grus I against the literature. [55] identified 8 members of Grus I using Magellan/IMACS spectroscopy and measured radial velocities and metallicities from the CaT feature. Of the 3 stars that we have in common with that study, two of them have CaT metallicity measurements. They are shown in the top panel. One star agrees within $< 1.5\sigma$ ([Fe/H] $= -2.5$), while the other is ~ 1 dex more metal-poor in [55]. C-enhancement could contribute to this discrepancy by adding absorption into the $F395N$ filter that would make our measurement of this star more metal-rich, but there are currently no known C-enhanced stars in Grus I. [149] studied two of the brightest stars in Grus I using high-resolution Magellan/MIKE spectroscopy. However, these stars are saturated in the archival *HST* broadband imaging, and cannot be compared.

In the bottom panel, we compare our MDF against those from [149] and [55]. [55] infer $\langle$[Fe/H]$\rangle = -2.62 \pm 0.11$ and were only able to place an upper limit on $\sigma_{\rm [Fe/H]}$ of 0.44 dex. We measure $\langle$[Fe/H]$\rangle = -2.62^{+0.14}_{-0.15}$, which is in 1-sigma agreement with [55]. Our $\sigma_{\rm [Fe/H]}$ measurement of $0.61^{+0.12}_{-0.11}$ is larger than what [55] found, though our sample is also significantly larger and has better populated tails. Taking both distributions at face value, the KS test produces a p-value of 0.06, suggesting that these MDFs may share the same underlying distribution.

In the right column, we compare our findings for Dra II against those from [184]. [184] studied 12 Dra II stars using the Pristine narrow-band CaHK filter. We have 7 stars in common with [184].

The top panel shows that our well-constrained metallicity measurements are in better than 1σ agreement with the measurements from [184]. There are three stars for which we can only provide an upper limit, and which are more metal-rich than -3.0 in the [184] study. We note that [184] impose a metallicity floor on their measurements at [Fe/H] $= -3.0$, limiting this comparison.

In the bottom panel of the Dra II column, we compare our MDF to the one derived by [184]. [184] measure $\langle$[Fe/H]$\rangle = -2.7 \pm 0.1$ dex and place an upper limit on $\sigma_{\rm [Fe/H]}$ of 0.24. Their $\langle$[Fe/H]$\rangle$ measurement is in 1σ agreement with ours. Additionally, we also resolve $\sigma_{\rm [Fe/H]}$ because our MDF spans a wider range. The floor of -3.0 adopted by [184] complicates their ability to resolve $\sigma_{\rm [Fe/H]}$.

The corresponding KS test yields a p-value of 0.09, suggesting similarity between our MDF for Dra II and the one from the literature

We refer the reader to §3.11 for the full set of 1-1 comparisons between our measurements and those from the literature across all the UFDs in this study.

3.6 Results

We undertake an exhaustive comparison of our MDFs to those previously published in the literature for the same galaxies. For completeness, here we list the papers used for each galaxy's literature values and refer to the face value results from these papers in the following sections: Eri II ([180], [202]; CVn II ([166]; Hya II ([161]); Ret II ([275], [168], [313], [152], [151]); Hor I ([168], [228]); Grus I ([149], [55]); Ret III ([94]); Wil 1 ([328]); Phe II ([94]); Eri III (none); Tuc V ([274]); Seg 1 ([107], [232], [279], [93]); Dra II ([184]). We present a summary of our direct comparisons to the literature in §3.11.

MDFs for Individual Galaxies

Eri II

Eri II ($M_V = -7.1$, $L = 10^{4.8}\ L_\odot$) was first discovered in [23] and [167]. Since its discovery, [180] identified 28 RGB members within 8 arcmin of Eri II using Magellan/IMACS spectroscopy and measured metallicities for 16 of them using the CaT equivalent width calibration. They measure $\langle$[Fe/H]$\rangle = -2.38 \pm 0.13$ and $\sigma_{\rm [Fe/H]} = 0.47^{+0.12}_{-0.09}$. [202] derived metallicities for 46 RR Lyrae stars in Eri II; their metallicity inference method is calibrated to the $\langle$[Fe/H]$\rangle$ measured by [180], and they report $\sigma_{\rm [Fe/H]}$ of 0.2 dex. As the authors remark, their smaller inferred $\sigma_{\rm [Fe/H]}$ is expected because the most metal-poor and metal-rich stars in a galaxy's MDF would not end up in the instability strip for RR Lyraes.

Due to its brightness and to the abundance of available literature references, we analyzed this galaxy in the first paper of our program in [96] to verify the efficacy of CaHK for recovering the MDFs of UFDs. In [96], we report metallicities for 60 resolved RGB stars in Eri II, measure $\langle$[Fe/H]$\rangle = -2.50 \pm 0.07$ and $\sigma_{\rm [Fe/H]} = 0.42 \pm 0.06$. In this work, we re-analyze Eri II following the procedure outlined in previous sections, which also newly includes a treatment of systematic uncertainties. Selecting along the RGB of Eri II, we obtain a sample of 75 stars for this analysis. We end up with a larger sample size because the $F606W - F814W$ CMD in which we made our member selection is higher S/N than the $F475W - F814W$ CMD used for member selection in [96]. The resulting MDF spans a similar range to that from our previous study.

From these stars, we measure $\langle$[Fe/H]$\rangle = -2.63^{+0.06}_{-0.06}$ and $\sigma_{\rm [Fe/H]} = 0.26^{+0.08}_{-0.09}$. Both the mean metallicity and the metallicity dispersion are lower than the values inferred from [96] by over 1σ. This is because the MIST models used for the analysis in this paper is scaled to the [116] solar abundances, while the MIST models used in [96] are scaled to the [13] solar abundances.[6] The metallicity measurements made using the [116] scaled models are on average more metal-poor by $0.1 \sim 0.2$ dex. This difference accounts for the change in $\langle$[Fe/H]$\rangle$. The lower $\sigma_{\rm [Fe/H]}$ is due to a larger fraction of EMP stars in our sample, which contribute to a smaller dispersion measurement because of the 0.5 dex systematic uncertainty floor.

CVn II

CVn II ($M_V = -5.1$, $L = 10^{4.0}$ $L_\odot$) was originally discovered in SDSS by [26] and subsequently studied spectroscopically by [278], [166] and [307]. From a sample of 14 stars, [166] measure $\langle$[Fe/H]$\rangle = -2.2 \pm 0.05$ dex and $\sigma_{\rm [Fe/H]} = 0.59$ dex.

From a sample of 40, we measure a metallicity of $-2.98^{+0.12}_{-0.12}$ and $\sigma_{\rm [Fe/H]} = 0.55^{+0.12}_{-0.10}$. Our mesaurement of $\langle$[Fe/H]$\rangle$ places CVn II as one of the most metal-poor UFDs known to-date.

As detailed in §3.5, our $\sigma_{\rm [Fe/H]}$ measurement is in good agreement with the spectroscopic study, but we measure a lower $\langle$[Fe/H]$\rangle$ due to more low-metallicity stars in our sample. Differences in $\langle$[Fe/H]$\rangle$ appear to be driven by our larger fraction of EMPs: 38% of our stars are EMP, versus 20% in the [166] sample. One possibility is that the small sample of Kirby et al. is missing EMPs, leading to a higher $\langle$[Fe/H]$\rangle$ estimate. Alternatively, if half of our EMPs are actually more metal-rich by 0.5 dex, it would bring our mean metallicities into better agreement.

Hya II

Hya II ($M_V = -4.9$, $L = 10^{3.9}$ $L_\odot$) was discovered by [195] in the Survey of the MAgellanic Stellar History (SMASH) conducted using the DECam instrument on the Blanco telescope. [161] followed up on this discovery by observing Hya II using Keck/DEIMOS, targeting the CaT lines. They identified 13 members of Hya II, and among that subset were able to measure metallicities for 5 of those stars. They measured for Hya II $\langle$[Fe/H]$\rangle = -2.02 \pm 0.08$, and $\sigma_{\rm [Fe/H]} = 0.40^{+0.48}_{-0.26}$.

We present the MDF of Hya II, constructed from 31 RGB stars, in Figure 3.10. The stars span a metallicity from -4.0 to -1.5, and the bulk of them are at around

[6] C. Conroy, A. Dotter; private communication.

a metallicity of −3.0. From this sample, we measure $\langle[\mathrm{Fe/H}]\rangle = -3.05^{+0.12}_{-0.13}$ and $\sigma_{[\mathrm{Fe/H}]} = 0.47^{+0.13}_{-0.12}$. Compared to the measurements from [161], our $\sigma_{[\mathrm{Fe/H}]}$ are in 1-sigma agreement, but our $\langle[\mathrm{Fe/H}]\rangle$ is lower than that study by about ~ 0.7 dex because our sample is dominated by stars below −2.5. We have 7 stars in common with the sample studied by [161], and none of them are foreground interlopers.

We also note the star in our sample that is at [Fe/H] ~ -1.5, setting it apart from the rest of the stars in our sample. We do not have data to verify conclusively whether it may be an outlier, so instead we recompute the Gaussian MDF excluding that star to infer $\langle[\mathrm{Fe/H}]\rangle = -3.08^{+0.11}_{-0.12}$ and $\sigma_{[\mathrm{Fe/H}]} = 0.33^{+0.12}_{-0.13}$. As expected, this new calculation results in a lower $\sigma_{[\mathrm{Fe/H}]}$, but this new value is still in 1σ agreement with the value computed from using the full sample. Since the uncertainty on $\sigma_{[\mathrm{Fe/H}]}$ from [161] is nearly 0.5 dex on the upper end, this new calculation also does not represent a significant improvement in agreement from the calculation made using the full sample. Additionally, the removal of the most metal-rich star in our sample worsens the discrepancies between the $\langle[\mathrm{Fe/H}]\rangle$ measurements. Most notably, we measure the MDF from 30 stars whereas [161] measured the MDF from 5, and our expanded sampling may explain the bulk of these discrepancies.

Ret II

Ret II ($M_V = -4.0$, $L = 10^{3.5}\ L_\odot$) was discovered in the DES by [23] and [167]. Since then, it has been a dwarf galaxy of great interest to the community because its stars contain evidence of a rare r-process enrichment event ([152], [245]). The most recent study on Ret II, [151], identified 32 member stars of the satellite using VLT/GIRAFFE and Magellan/M2FS spectroscopy and aimed to measure the abundances of the r-process element Barium. As part of this study, they provided constraints on the metallicities of 29 stars in that sample. From the 13 stars for which they were able to constrain metallicities beyond an upper limit, they measure $\langle[\mathrm{Fe/H}]\rangle = -2.64 \pm 0.11$ and $\sigma_{[\mathrm{Fe/H}]} = 0.32^{+0.10}_{-0.07}$.

We identify 76 candidate members in Ret II along the MSTO and MS. Using the catalog of [275], we remove one star whose velocity is inconsistent with Ret II membership. From the remaining 76 stars, which span a wide range in metallicity, we measure $\langle[\mathrm{Fe/H}]\rangle = -2.64^{+0.1}_{-0.11}$ and $\sigma_{[\mathrm{Fe/H}]} = 0.72^{+0.09}_{-0.08}$. Our $\langle[\mathrm{Fe/H}]\rangle$ measurement is in agreement with [151] and earlier works on the dwarf ([168], [275], [312]). However, we resolve a larger $\sigma_{[\mathrm{Fe/H}]}$.

Direct comparison with existing metallicities is challenging. Due to saturation effects in our photometry, our sample lacks substantial overlap with the [151] sam-

ple. We have three stars in common with that study, with two stars of that subset constrained only by an upper limit in [151]. The star for which the measurement is constrained is in agreement to 2σ, and the upper limits point in the correct direction towards agreement.

Our large metallicity dispersion in Ret II is driven by the larger number of stars in the tails of the MDF than what [151] report. Although the uncertainties on the metallicities of these stars are large (i.e., we adopt a 0.3 dex systematic uncertainty, see §3.10), these stars still contribute to a higher metallicity dispersion measurement as compared to the literature. Because this dispersion is so much larger than what is reported by spectroscopic data, we undertake further scrutiny to see if any systematic effects in our analysis, or to Ret II in particular, can reconcile the difference.

First, we consider the possibility of foreground contamination. The MW halo has very few EMP ([Fe/H] < -3.0) stars (e.g., [66]), which suggests foreground is unlikely the source of a large metal-poor component.

Instead, we consider the possibility that our large dispersion may result from substantial contamination from higher metallicity MW foreground stars. Figure 3.15 illustrates this possibility. Here, we plot the simulated TRILEGAL MW foreground in the direction of Ret II. We find that, on average, one foreground star passes our isochrone and spatial cuts. A single star does not significantly alter the dispersion measurement.

The TRILEGAL model also suggests that if foreground is significant, it should be present in other areas of the CMD, i.e., not just those that pass our isochrone cut. For Ret II, the CMDs do not exhibit large populations of objects outside the RGB and MS of Ret II, further suggesting that foreground contamination is not significant. A clear example of a galaxy with a larger degree of foreground contamination is Seg 1, for which there are many objects on either side of the actual galaxy RGB and MS.

Second, we consider the possibility that there may be some unknown MW substructure along the line-of-sight that is not accounted for in the smooth MW halo models of TRILEGAL. Such a contaminating substructure would have to be able to account for a large fraction of the ~ 20 MR and/or MP stars observed in the tails of the MDF. Additionally, it would have to be concentrated almost entirely along the MS of Ret II. To-date, there are no currently-known substructures in the vicinity of Ret II from wider-field spectroscopic studies of Ret II ([312], [275], [151]), as well as from photometric imaging ([82], [224]). It is unlikely that a previously-undiscovered stellar substructure would be first detected in a narrow HST pointing compared to other observations.

Third, we consider the possibility that our dispersion measurements are inflated by lower S/N stars. That is, we allow for the possibility that some unaccounted-for systematic effects in photometry of the the faint stars has biased our metallicity

determinations.[7] To explore this effect, we remove faint stars in our sample with $m_{F475W} > 22.5$ ($M_{F475W} > 5$) and re-fit our MDF with the remaining 24 stars, finding $\langle$[Fe/H]$\rangle = -3.07 \pm 0.19$ and $\sigma_{\rm [Fe/H]} = 0.70^{+0.17}_{-0.15}$. This cut disproportionately removes the MR stars, which, in part is due to a known effect of magnitude limited cuts (i.e., MR stars are fainter at a fixed magnitude owing to increased atmospheric opacity; [191]). As a result, we measure a lower mean for this revised sample. The resulting dispersion is still large and in agreement with the dispersion inferred using our full sample.

Finally, we consider that unaccounted-for impacts of binarity are inflating our dispersion measurements. Our investigation of the impact of binarity in §3.10 suggests that we may inflate the metallicity of an unresolved binary star by up to 0.2 dex by fitting them with single stellar models. We consider the upper limit of binarity on our MDF by measurement by assuming that all of our stars that are more MR than -2.0 have been affected by the maximum possible impact of binarity– i.e., all 20 of these stars have a ~ 0.5 $M_{\odot}$ solar mass companion (see Fig 3.16). We subtract 0.2 dex from their metallicity measurements and re-compute our Gaussian fit, finding $\langle$[Fe/H]$\rangle = -2.69 \pm 0.1$ and $\sigma_{\rm [Fe/H]} = 0.63 \pm 0.1$. The resulting mean and dispersion remain in agreement with the values inferred using our full sample.

In summary, all of our tests retain the large dispersion inferred using the original sample. At worst, they implausibly shift the mean out of agreement with the mean measured the original sample and from the literature. We do not claim to have resolved the tension with the literature, but at this time there is no obvious solution to resolving these discrepancies. We welcome spectroscopic follow-up studies by the community to improve membership selection and refine these measurements, and provide coordinates and magnitudes for all the stars in Ret II used to derive its MDF in Table 3.4.

Hor I

Hor I ($M_V = -3.8$, $L = 10^{3.4}$ $L_{\odot}$) was discovered in DES data by [23] and first followed up spectroscopically by [168] using VLT/GIRAFFE. In that study, they identified 5 candidate members. From those stars, they report $\langle$[Fe/H]$\rangle = -2.76 \pm 0.1$ and $\sigma_{\rm [Fe/H]} = 0.17^{+0.20}_{-0.03}$, and detect alpha enhancement of $[\alpha/{\rm Fe}] = 0.30 \pm 0.07$. [228] later observed 3 of these stars using Magellan/MIKE and performed a detailed chemical abundance analysis. The stars they observed have a low average metallicity of [Fe/H] ~ -2.6, and low alpha-enhancement at $[\alpha/{\rm Fe}] \sim 0.0$.

[7] See §3.12 for additional discussion around this context.

We present the MDF of Hor I, measured from 27 RGB stars, in Figure 3.10. The stars in the MDFs span a wide range of metallicity, with some potentially being EMP stars, to stars as metal-rich as ~ -1.0 dex. The bulk of the stars in Hor I are between -3.0 and -2.0.

The stars observed in the aforementioned studies fall beyond our HST footprint, so we cannot make direct comparisons of the measurements. Instead we compare the broad features of metallicity measurement results. Similar to the aforementioned studies, we find a low $\langle$[Fe/H]$\rangle$ for Hor I of $-2.79^{+0.12}_{-0.13}$. We also resolve $\sigma_{\rm [Fe/H]} = 0.56^{+0.11}_{-0.09}$. We note that there is a star in the MDF of Hor I more metal-rich than ~ -1.5 dex that could be an interloper, but absent of detailed kinematic and astrometric data, it is difficult to ascertain for sure that it is not a member of Hor I. We instead re-compute the Gaussian MDF excluding these stars to infer $\langle$[Fe/H]$\rangle = -2.84^{+0.11}_{-0.12}$ dex and $\sigma_{\rm [Fe/H]} = 0.41^{+0.11}_{-0.10}$ dex. As expected, the removal of this star preserves the metal-poor nature of Hor I. $\sigma_{\rm [Fe/H]}$ also decreases as a result, but we still clearly resolve a metallicity spread in the dwarf.

Grus I

Grus I ($M_V = -3.5$, $L = 10^{3.3}$ $L_\odot$) was discovered by [167] in the DES survey. At the time of discovery, its classification was unknown. [149] studied the chemical abundances of two stars in Grus I and used the deficiency in neutron capture elements in those two stars to classify Grus I as a dwarf galaxy. [55] was able to observe additional members of Grus I using Magellan/IMACS spectroscopy to measure its metallicity and velocity dispersion. They were unable to resolve $\sigma_{\rm [Fe/H]}$, but the measured velocity dispersion of $\sigma_{rv} = 2.5^{+1.3}_{-0.8}$ km s^{-1} translates to a large dynamical mass-to-light ratio for Grus I and informs its classification as a dwarf galaxy.

In §3.5, we presented a detailed comparison between our Grus I MDF measurement and those from [55]. We measure $\langle$[Fe/H]$\rangle = -2.62^{+0.14}_{-0.15}$ and $\sigma_{\rm [Fe/H]} = 0.61^{+0.12}_{-0.11}$. Our $\langle$[Fe/H]$\rangle$ measurement is consistent with the [55] study, but we were able to resolve $\sigma_{\rm [Fe/H]}$ whereas that study could only provide an upper limit. Our results further support the conclusion that Grus I is a dwarf galaxy.

Ret III

Ret III ($M_V = -3.3$, $L = 10^{3.2}$ $L_\odot$) was discovered in DES by [82], and followed up spectroscopically by [94] using VLT/FLAMES targeting the CaT features. From that study, [94] found 3 likely members in Ret III, and used them to measure

$\langle$[Fe/H]$\rangle = -2.81 \pm 0.09$ and $\sigma_{\rm [Fe/H]} = 0.35^{+0.21}_{-0.09}$. They were unable to resolve a velocity dispersion, putting an upper limit on the value at 31.2 km s^{-1}.

We identify 18 RGB stars in Ret III. From this sample, we measure $\langle$[Fe/H]$\rangle = -2.46^{+0.12}_{-0.15}$ and $\sigma_{\rm [Fe/H]} = 0.31^{+0.2}_{-0.18}$. Our $\sigma_{\rm [Fe/H]}$ measurement is in good agreement with the Fritz et al. measurement, but we infer a larger $\langle$[Fe/H]$\rangle$.

We also have two stars in common with the [94] study, all of which were deemed spectroscopic members. For star 0 in our sample, we measure a metallicity of [Fe/H] $= -2.38^{+0.04}_{-0.03}$ (stat.) $\pm$ 0.2 (syst.), compared to their measurement of $-3.24 \pm$ 0.15. For star 1 in our sample, we measure [Fe/H] $= -2.07^{+0.04}_{-0.04}$ (stat.) $\pm$ 0.2 (syst.), compared to their measurement of -2.32 ± 0.15. Our measurements for star 0 and star 1 are larger than the [94] measurements by $> 3\ \sigma$ and $\sim 2\ \sigma$ respectively. The [94] measurements were derived from spectral synthesis methods that assume [α/Fe]$= +0.5$, which is more enhanced than our assumption, but this is not enough to fully account for discrepancies. We discuss these comparisons further in §3.11.

Wil 1

Wil 1 ($M_V = -2.9$, $L = 10^{3.1}\ L_\odot$) was discovered by [326] as one of the first faint MW satellites known to the community. Similar to Seg 1, Wil 1 was one of the stellar associations whose classification as either a star cluster or a dwarf galaxy has been the subject of ongoing debate.

The most comprehensive spectroscopic study of Wil 1 done to-date was by [328] using Keck/DEIMOS spectroscopy. They identified 45 candidate members of Wil 1 and among 40 of those are high-confidence. Their stars span the bright RGB of Wil 1 down to the main sequence. Although they find an irregular kinematic distribution for Wil 1, they detect evidence of a large metallicity spread in Wil 1 from metallicity measurements of the two RGB stars in their sample, with one star at [Fe/H] $= -1.73 \pm 0.12$, and the other at [Fe/H] $= -2.65 \pm 0.12$.

We crossmatch our sample against that from [328] and find that we have 10 stars in common. Of the 10 stars we have in common with their study, one was identified as a probable nonmember in Wil 1.

We identify 68 stars in Wil 1 on the MSTO and MS. Our stars span a wide range of metallicity from -4.0 to -1.0. We measure $\langle$[Fe/H]$\rangle = -2.53^{+0.11}_{-0.11}$, and $\sigma_{\rm [Fe/H]} = 0.65^{+0.10}_{-0.09}$. A significant fraction of the stars we find are at metallicities above -2.0 (31%). With a sample size of over an order magnitude larger, we confirm the large metallicity range suggested by measurements of the two stars from [328]. The large metallicity dispersion we recover supports results from mass-segregation studies that Wil 1 is a dwarf galaxy [22].

Phe II

Phe II ($M_V = -2.7$, $L = 10^{3.0}\ L_\odot$) was discovered in the DES footprint by [23] and [167], and subsequently followed up spectroscopically by [94] using VLT/FLAMES spectroscopy targeting the CaT features. From that study, the authors identify 6 likely members, and 5 whose membership they are certain of. From the 5 members, they measure $\langle[\mathrm{Fe/H}]\rangle = -2.51^{+0.19}_{-0.17}$ and $\sigma_{[\mathrm{Fe/H}]} = 0.33^{+0.29}_{-0.16}$. They also measure a radial velocity dispersion of $\sigma_v = 11.0^{+9.4}_{-5.3}$ km s^{-1}. From these measurements resolving both a metallicity dispersion as well as a large velocity dispersion (and therefore a large mass-to-light ratio), the authors conclude that Phe II is a dwarf galaxy.

We identify 10 RGB stars in Phe II, one of which we have in common with [94]. The star we have in common with that study is a kinematic member of Phe II. Our measurement for that star is [Fe/H] $= -2.23 \pm 0.04$ (stat.) ± 0.2 (sys.), while [94] measure for it a metallicity of [Fe/H] $= -2.65 \pm 0.15$. Our measurements for this star agree within 2σ.

From our overall sample, we measure $\langle[\mathrm{Fe/H}]\rangle = -2.36^{+0.18}_{-0.16}$ and $\sigma_{[\mathrm{Fe/H}]} = 0.41^{+0.22}_{-0.17}$. These measurements agree with those from [94] at the 1-sigma level. Alongside the absence of mass segregation detected for Phe II stars [22], our results support the conclusion that Phe II is a dwarf galaxy.

Eri III

Eri III ($M_V = -2.1$, $L = 10^{2.8}\ L_\odot$) was simultaneously discovered by [23] and [167] in the DES survey. To-date, it has not been observed by spectroscopy, but [65] targeted it for follow-up Gemini imaging to derive its structural properties. With a half-light radius of $r_h = 8.3^{+0.9}_{-0.8}$ pc, and a magnitude of $M_V = -2.1$, the categorization of Eri III, like many recently-discovered satellites, is ambiguous from structural parameters alone.

We identify 13 candidate RGB members in Eri III and present the resulting MDF in Figure 3.10. The stars in Eri III span a wide range of metallicities, from -3.0 to -1.2. Using these measurements, we infer $\langle[\mathrm{Fe/H}]\rangle = -2.03^{+0.16}_{-0.18}$ and $\sigma_{[\mathrm{Fe/H}]} = 0.49^{+0.22}_{-0.18}$. Since we resolve a non-zero $\sigma_{[\mathrm{Fe/H}]}$ for this satellite, we classify it as a dwarf galaxy. [22] is unable to resolve mass-segregation in Eri III above 3σ level, supporting our classification of Eri III from the metallicity dispersion. Spectroscopic follow-up to determine kinematic properties and membership for this satellite would help confirm or refute this categorization.

Tuc V

Tuc V ($M_V = -1.6$, $L = 10^{2.6}\ L_\odot$) was first discovered by [82] in the DES footprint. [65] targeted Tuc V for follow-up imaging, but did not find evidence in the vicinity of Tuc V of a bound stellar association. From this imaging, they suggest that Tuc V may be a chance overdensity in the SMC halo due to its proximity, or a dissolving star cluster.

Since then, [274] studied Tuc V using Magellan/IMACS spectroscopy in the CaT region and identified 3 candidate members of Tuc V. They were able to measure CaT metallicites for two of the candidate members, finding $\langle[\mathrm{Fe/H}]\rangle = -2.16 \pm 0.23$. They were unable to resolve $\sigma_{[\mathrm{Fe/H}]}$.

As shown in the CMD figures (Figures 3.1, 3.2), we clearly see a stellar sequence in our imaging of the Tuc V field, including a defined MSTO. We identify 6 stars along the RGB of Tuc V and from these 6 stars, measure $\langle[\mathrm{Fe/H}]\rangle = -2.41^{+0.26}_{-0.34}$ and $\sigma_{[\mathrm{Fe/H}]} = 0.61^{+0.44}_{-0.28}$, thereby resolving a nonzero metallicity dispersion at the 2-sigma level. We therefore classify Tuc V as a dwarf galaxy, supporting the conclusion from the absence of mass-segregation in this satellite as measured by [22].

Seg 1

Seg 1 ($M_V = -1.3$, $L = 10^{2.5}\ L_\odot$) was one of the first-discovered UFDs, uncovered by [26] in SDSS data. At the time of discovery, it was among the faint satellites that ushered in a new paradigm in dwarf galaxy studies, where structural parameters alone became insufficient to determine a stellar association's classification as either star cluster or galaxy. Follow-up spectroscopic studies to determine its classification are [107], [232], [279], and [93]. [279] conducted a complete spectroscopic study of stars in the field of Seg 1 down to 22 magnitude in the SDSS r band, encompassing the RGB and the MSTO. [93] performed high-resolution chemical abundance analysis of 6 RGB stars in Seg 1, adding their sample to the 1 other star analyzed in the same manner by [232], and analyze this data in context of Seg 1 history. The metallicities of the 7 stars studied and compiled by [93] range from -3.8 to -1.4.

We crossmatch our sample against the [279] sample and found that we have 13 stars in common from our initial CMD selection among the main sequence. Of the 13 stars, 6 were ruled out as kinematic nonmembers by [279]. Of the 6 nonmembers, 4 have characteristic velocities of Milky Way stars, and 2 belonged to the 300S stellar stream in the vicinity of the dwarf ([118], [100]). Since the observed Seg 1 stars are on the main sequence where the CaT calibration does not extend, we do not have metallicity measurements from this study for comparison.

From 12 stars, we measure for Seg 1 $\langle$[Fe/H]$\rangle = -2.36^{+0.23}_{-0.25}$ and $\sigma_{\rm [Fe/H]} = 0.65^{+0.26}_{-0.21}$. The stars in our sample also span the same metallicity range as the stars from [93]. We also have one star in common with [93], which we discuss in §3.10 in the context of assessing the impact of carbon enhancements. [93] identified that star as the most metal-rich known in Seg 1, with [Fe/H] $= -1.42 \pm 0.24$ and also carbon enhancement with [C/Fe] $= 1.44 \pm 0.2$. In our work, we find that this star has [Fe/H] $= -1.86^{+0.11}_{-0.12}$ (stat.) $\pm$ 0.3 (syst.); these measurements are in agreement within $\sim 1.5\ \sigma$.

Dra II

Dra II ($M_V = -0.8$, $L = 10^{2.3}\ L_\odot$) was discovered by [170] in the Pan-STARRS survey. It is the faintest galaxy in our sample and has no RGB stars. We describe its MDF inference in detail in §3.5.

At the time of its discovery, its classification as either a star cluster or a galaxy was uncertain from structural parameters alone. To resolve this uncertainty, [184] observed Dra II using the Pristine narrow-band photometry and Keck/DEIMOS spectroscopy to obtain metallicity and kinematic information. They measure a low $\langle$[Fe/H]$\rangle$ for Dra II (-2.7 dex), a low $\sigma_{\rm [Fe/H]}$ (< 0.24 dex), and place an upper limit on the velocity dispersion of Dra II at $\sigma_v < 5.9$ km s^{-1}. Coupled with an orbital history for Dra II that takes it within 25 kpc of the Galactic Center, [184] suggest that Dra II is a potentially disrupting dwarf galaxy.

More recently, as part of a broader study, [22] measure the degree of stellar mass segregation in Dra II. They find $R_{Bright}/R_{Faint} = 0.78 \pm 0.07$, meaning that brighter, more massive stars in the satellite are more centrally concentrated than fainter, less massive ones.[8] Since mass segregation is an expected feature in star clusters, they conclude that Dra II is a star cluster.

Our analysis reveals that Dra II is unambiguously a dwarf galaxy, based on its large metallicity spread. Specifically, we find $\langle$[Fe/H]$\rangle = -2.72^{+0.10}_{-0.11}$ and $\sigma_{\rm [Fe/H]} = 0.40^{+0.12}_{-0.12}$. Compared to [184], our $\langle$[Fe/H]$\rangle$ is similar, but our dispersion is much larger. We discuss reasons for this difference in §3.5. There are no clear systematics in our data that would lead to such a large spread. Conversely, we do not see any plausible way to reconciling the observed CaHK data with the lack of $\sigma_{\rm [Fe/H]}$ that is expected for GCs. The remaining mystery is how to interpret the inferred mass segregation with a large metallicity spread. Additional kinematic information to 1)

[8] R_{Bright} and R_{Faint} respectively refer to the radii of bright and faint stars in the satellite. A system with no mass segregation, e.g. dwarf galaxies, would have R_{Bright}/R_{Faint} consistent with 1.

refine velocity dispersion measurements and 2) confirm dwarf membership of the MP and MR stars in Dra II, may help to bring clarity to the true nature of this enigmatic object.

Broad Characterization of MDFs Across the Sample

Figure 3.8 shows broadband CMDs of our entire sample, with the stars that we use for our MDF determinations color-coded by their F395N S/N. The sample displayed in this figure has been cleaned for contamination using available kinematic data, which we detail in §3.6. We verify that all stars that we select in $F606W - F814W$ also fall along the stellar population sequence in $F475W - F814W$. For stars that fall on the edge of the selection box, we find that their metallicities are not outliers compared to the rest of the distribution, and therefore retain them in the sample. The galaxies with the largest sample sizes are Ret II and Wil 1, which respectively have 76 and 68 stars from the lower RGB and MSTO. The galaxy with the smallest sample sizes are Phe II and Tuc V at 10 and 6 stars respectively.

Figure 3.9 shows the stars for each galaxy in CaHK color space. For each galaxy, we overplot $[\alpha/\mathrm{Fe}] = +0.4$ MIST mono-metallic isochrones for either RGB or MS, appropriately selected for each galaxy. For most of our galaxies, the sample of members fall along the RGB and lower RGB, so those corresponding tracks are presented in their respective panels. The exceptions to this are Ret II, Wil 1, Seg 1 and Dra II, where the sample is dominated by MSTO and lower MS stars. For bluer $F475W - F814W$ colors (≤ 1.4), the CaHK tracks for RGB and MS evolutionary phases look similar and using either set of tracks would produce comparable MDF measurements. On the redder end, the CaHK tracks for MS stars are more closely spaced, but few of our stars fall in that color regime. Overall, visual inspection alone shows that each galaxy hosts stars of multiple, distinct metallicities.

Figure 3.10 shows MDFs for each galaxy resulting from applying the metallicity and MDF fitting methodologies described in §3.4. In alignment with the intuition guided by the stars' positions on the CaHK color plots in Figure 3.9, all UFDs have a wide range of metallicities, with stars for which we indicate upper limits of $\lesssim -3.0$ up to stars as metal-rich as -1. Some MDFs are broad and flat (Hya II, Ret II, Grus I, Seg 1), while others are clearly peaked (Eri II, Hor I, Phe II, Dra II). The majority of the MDFs display evidence of metal-poor tails, although the characterization of their full extent is limited by the edge of our metallicity grid. We also compute additional summary statistics to quantify deviations from Gaussianity, and are unable to resolve significant departures from Gaussianity for majority of our MDFs. We present these results in §3.13.

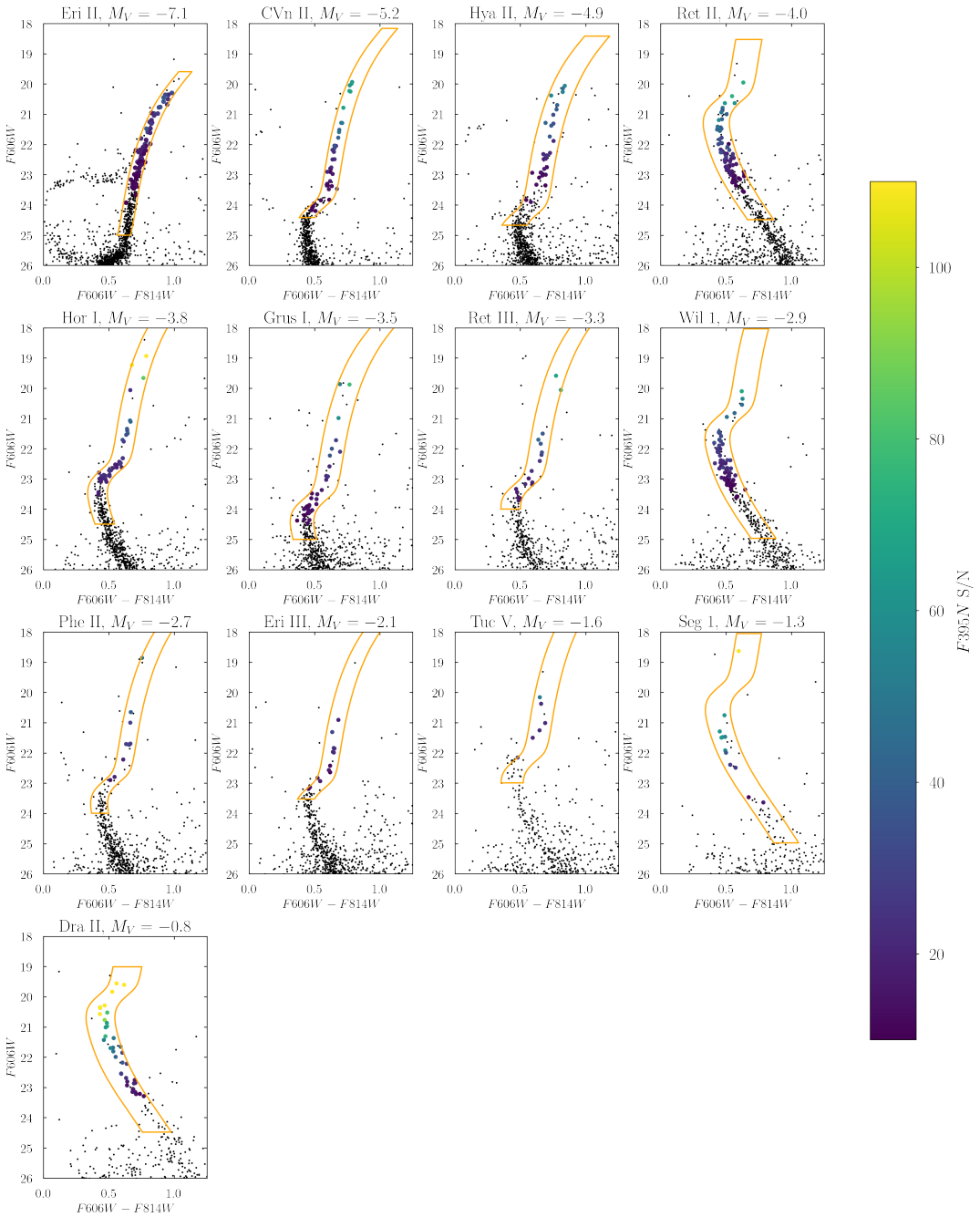


Figure 3.8: A gallery of $F606W - F814W$ CMDs with membership selection indicated by the orange boxes drawn around the RGB. After making this initial selection, we crossmatch against literature radial velocity data where available to remove foreground interlopers. Stars used to infer MDFs are color-coded with $F395N$ S/N > 10.

The left panel of Figure 3.11 shows the composite MDF from our study, derived by stacking the MDFs of all the individual UFDs. We measure metallicities for 463 stars across 13 UFDs, and disaggregate the composite MDF by contributions from each galaxy. For all of these measurements, we measure a mean of -2.66 ± 0.04 and sigma of 0.56 ± 0.03. We discuss comparisons with composite measurements from the literature in §3.7, and summarize our MDF measurements for individual UFDs in Table 3.2.

As part of validating our measurements, we compare our measurements with those in the literature where available. We discuss comparisons within individual UFDs in §3.6. In §3.11, we provide a summary figure of direct literature comparisons as Fig 3.19, and discuss comparisons between specific methods in greater detail. In summary, our measurements are in agreement with literature measurements to with $\sim$1.5 sigma. Given the heterogeneity of literature measurements, we consider this an affirming result of the fidelity of CaHK metallicities.

In §3.14, we present the table of measurements in Table 3.4, reporting both the random uncertainties from photometry, and from systematic uncertainties that we determined following our procedure in §3.10. We also identify 112 EMP ([Fe/H] $<$ -3.0) star candidates, with 5 of them being stars that are low S/N, but whose photometry place them bluewards of the CaHK grid. On the other end of the MDF, we identify 86 stars that are more metal-rich than [Fe/H] $= -2.0$. We provide these stars in Table 3.5 and 3.6 respectively, also in §3.14.

Note. A summary of our MDF measurements. We list $\langle$[Fe/H]$\rangle$ and $\sigma_{\rm [Fe/H]}$ inferred from the UFDs in our sample, the number of stars used to make the measurement, and the number of stars of interest at the extreme ends of the UFD's MDF. We refer the reader to Section 5 for detailed discussions on the determination of $\langle$[Fe/H]$\rangle$ and $\sigma_{\rm [Fe/H]}$, and comparisons where available to previous studies.

3.7 Discussion

Comparison to the Literature

The right panel of Figure 3.11, shows a composite MDF (red) from the 463 stars collected from all UFDs in our sample. For comparison, we overplot with the maroon line the composite MDFs for *all* existing literature stellar metallicity measurements in the same UFDs. The literature sample consists of $\sim$ 110 stars and includes stars not in our sample (e.g., at larger radii than the *HST* footprint). In the same panel, we also show with a gray line literature metallicity measurements for *all* UFDs around

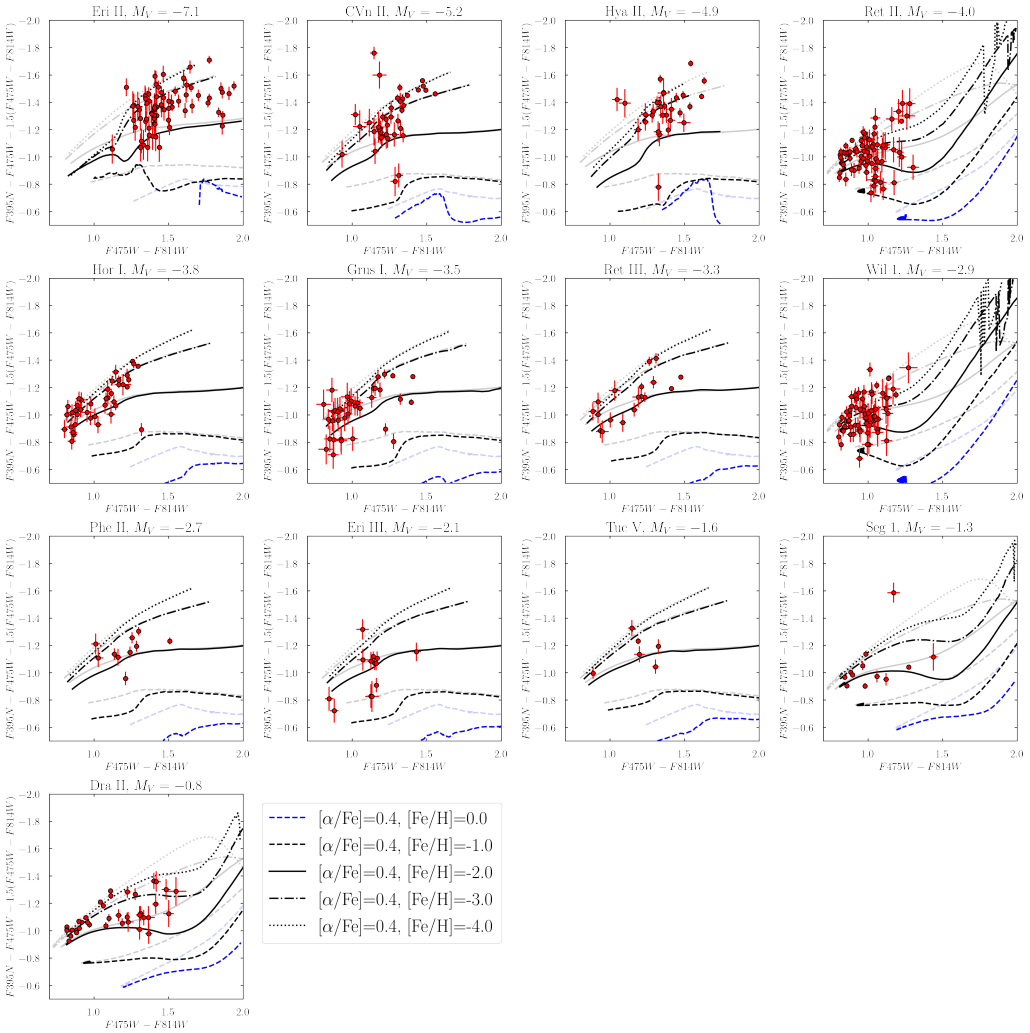


Figure 3.9: A gallery of CaHK diagrams for each UFD, ordered by decreasing luminosity. We have overplotted the MIST alpha-enhanced ([α/Fe] = +0.40) CaHK tracks for RGB stars in most cases and MS tracks for Ret II, Wil 1, Seg 1, and Dra II, which are dominated by MS and MSTO stars. The tracks have been convolved with ASTs run for each galaxy. These tracks are solely for illustrative purposes to demonstrate the impact of ASTs, and actual tracks used for fitting individual stars may look different due to the process described in §3.4. It is clear from the distribution of stars that each galaxy hosts stars over a wide range of metallicities.

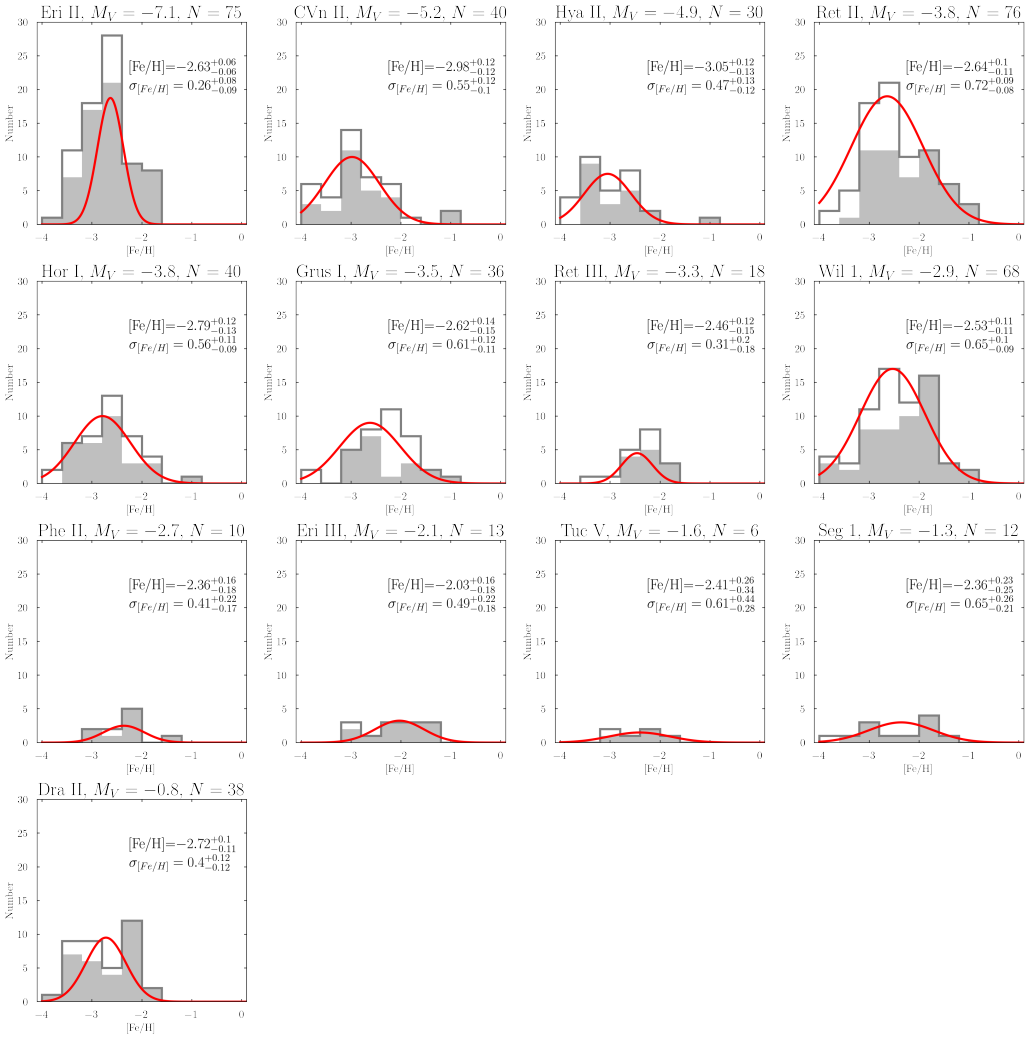


Figure 3.10: A gallery of MDFs for each galaxy based on our CaHK fitting. Metallicity bin sizes are 0.4 dex wide, which is comparable to typical stellar metallicity uncertainties. Well-constrained fits are indicated by shaded grey regions, whereas poorly constrained fits- largely upper limits- are shown as open histograms. We overplot the MDFs with the best-fit Gaussian (red). With the exception of Ret III, we resolve $\sigma_{[\mathrm{Fe/H}]}$ above at least the 2σ level for our UFD sample.

Table 3.2: Summary of MDF Measurements

Galaxy	M_v (mag)	$\langle$[Fe/H]$\rangle$ (dex)	$\sigma_{\rm [Fe/H]}$ (dex)	$N_{\rm stars}$	$N_{\rm [Fe/H]<-3.0}$	$N_{\rm [Fe/H]>-2.0}$
Eridanus II	-7.1	$-2.63^{+0.06}_{-0.06}$	$0.26^{+0.08}_{-0.09}$	75	17	8
Canes Venatici II	-5.2	$-2.98^{+0.12}_{-0.12}$	$0.55^{+0.12}_{-0.10}$	40	15	3
Hydra II	-4.9	$-3.05^{+0.12}_{-0.13}$	$0.47^{+0.13}_{-0.12}$	30	15	1
Reticulum II	-4.0	$-2.64^{+0.1}_{-0.11}$	$0.72^{+0.09}_{-0.08}$	76	17	20
Horologium I	-3.8	$-2.79^{+0.12}_{-0.13}$	$0.56^{+0.11}_{-0.09}$	40	10	5
Grus I	-3.5	$-2.62^{+0.14}_{-0.15}$	$0.61^{+0.12}_{-0.11}$	36	5	10
Reticulum III	-3.3	$-2.46^{+0.12}_{-0.15}$	$0.31^{+0.2}_{-0.18}$	18	2	3
Willman 1	-2.9	$-2.53^{+0.11}_{-0.11}$	$0.65^{+0.10}_{-0.09}$	68	13	21
Phoenix II	-2.7	$-2.36^{+0.18}_{-0.19}$	$0.41^{+0.22}_{-0.17}$	10	1	1
Eridanus III	-2.1	$-2.03^{+0.16}_{-0.18}$	$0.49^{+0.22}_{-0.18}$	13	0	6
Tucana V	-1.6	$-2.41^{+0.26}_{-0.34}$	$0.61^{+0.44}_{-0.28}$	6	1	1
Segue 1	-1.3	$-2.36^{+0.23}_{-0.25}$	$0.65^{+0.26}_{-0.21}$	12	2	5
Draco II	-0.8	$-2.72^{+0.10}_{-0.11}$	$0.40^{+0.12}_{-0.12}$	38	14	2

the MW, including those for galaxies not in our sample.

There are several key takeaways from Figure 3.11. The first is the drastic increase in sample size. Compared to the literature, in our sample of 13 UFDs, we increase the number of stellar metallicity measurements by nearly a factor of ~ 5. In almost all of our galaxies, we at least double the number of stars with metallicity measurements, with the exception of Seg 1. For Ret III, Wil 1, Eri III, and Tuc V in which previous efforts yielded less than 3 stars with metallicity measurements per galaxy, our work provides large enough samples to measure robust metallicity spreads. The largest gain is for Wil 1: The 68 stars in our study represents a dramatic improvement over [328], in which only 2 of its RGB stars had metallicity measurements.

Second, we significantly increase the total number of stars in all UFDs with reliable metallicity determinations. Compared to the literature MDF, drawn from 26 galaxies [277], we double the total number of stars with metallicites; only a small fraction of our data overlaps with existing measurements, as discussed in previous sections.

This larger sample has some implications for MDF interpretation. For example, there are some modest differences in the mean and scatter in our MDF versus the previous composite literature MDF. For all of our measurements, we find a mean of -2.66 ± 0.04 and sigma of 0.56 ± 0.03. If we only include well-constrained fits, which disproportionately exclude our EMP star candidates, we find a higher mean

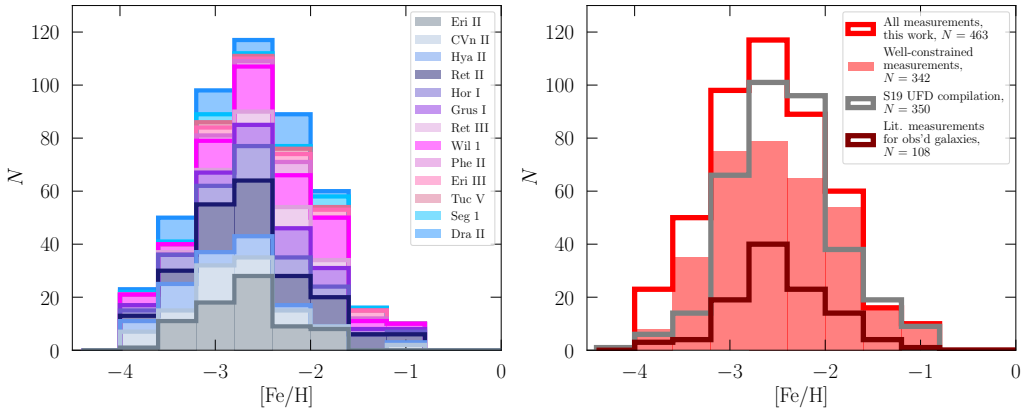


Figure 3.11: The composite MDF for all UFDs in our sample, shown against select UDF MDFs from the literature. **Left:** The breakdown of the composite MDF by contribution from each UFD in our sample. **Right:** Our MDF (red) compared to the literature. The maroon line is the composite MDF made from all literature measurements available for the same galaxies in our sample, including stars not observed by our program. Our program increases the number of stellar metallicities in these galaxies by nearly a factor of 5. The gray line is the composite UFD MDF made from all available UFD stellar metallicity measurements, compiled by [277]. Our work more than doubles the number of metallicities in all UFDs. There is a significant increase in the number of EMP star candidates in these systems compared with previous studies. In all cases, our work demonstrates the excellent ability for space-based CaHK narrow-band imaging to significantly expand the number of UFD stars with metallicity measurements.

of -2.38 ± 0.03 and a smaller scatter of 0.40 ± 0.03. In comparison, the literature values are mean of -2.41 ± 0.03 and sigma of 0.49 ± 0.02.

These differences are driven by pronounced differences in the tails of the composite MDFs. On the metal-poor end, we identify 112 stars as EMP ([Fe/H] < -3.0) candidates. These candidates make up 24% of all stars in our sample. This is a much larger fraction than the literature values both in the same galaxies (12%) and across all UFDs (14%, [277]). Due to limitations of the current CaHK methodology (e.g., our grid sharply ends at [Fe/H]$= -4.0$), it is plausible that not all of these candidates are *bona fide* EMP stars. Removing the 5 low S/N stars that fall beyond our metallicity grid decreases our EMP star fraction to 23%. Within the Galaxy, spectroscopic follow up of the Pristine-identified EMPs had only a 20% success rate

(i.e., 80% were not EMPs; [329], [2]). Our observational situation is markedly different than a broad survey of the MW: we have targeted the central regions of UFDs, coherent objects with known distances, and use CMD selection to limit interlopers. While there may be possible foreground contaminants in excess of our estimates (see §3.9), the contamination rate is likely to be small. Thus, the main source of uncertainty is in the coarse performance of CaHK techniques for EMPs. Spectroscopic follow up will be important, but may not be possible until ELTs are online owing the faintness of most stars in our sample.

At the other extreme, we find 19% of our sample (86 stars) is more metal-rich than [Fe/H] $= -2.0$. The fraction of similarly metal-rich stars in the literature MDFs are 18% for the same UFDs as in our sample and 19% for all UFDs [277]. Thus, our MR star fraction is in agreement with the literature. We have confidence in our MR star measurements because the performance of CaHK is more precise for more enriched stars, and we expect a small number of contaminants given our observational strategy. There is no broad consensus for whether UFDs should host such metal-rich stars, with some suggesting that they are unlikely to be actual member stars (e.g., [94]). However, there are enough clear examples of spectroscopically confirmed metal-rich stars in UFDs (e.g., CVn II, Wil I, Seg 1) to reinforce the reasonability of our findings.

A final, and particularly important point, is that of homogeneity. The literature composite MDFs shown in Figure 3.11 are drawn from over a dozen different studies of which rely on many different spectroscopic observations (e.g., wavelength range, S/N, resolution), metallicity inference techniques (e.g., full spectral synthesis, CaT), and underlying assumptions (e.g., line lists). As highlighted in [256], these types of differences lead to ~ 0.3 dex variations in the [Fe/H] values for RGB stars in the MW GC M15, underscoring the importance of homogeneous measurements. Thus, a key product of this work is that all of the metallicity determinations are self-consistent, on the same scale, and have uniformly determined uncertainties. The net result is that not only have we greatly increased the sample of stellar metallicities in UFDs, we have also provided clear evidence for a metallicity floor, large internal dispersions, etc. that are free of study-to-study systematics.

The Faint End of the Dwarf Galaxy Mass-Metallicity Relation

Figure 3.12 shows our results in the context of the known mass-metallicity relation for dwarf galaxies. We find that across three orders of magnitude in luminosity from 10^2 to $10^5 L_\odot$, there is no mass-metallicity relation for UFDs. Rather, their

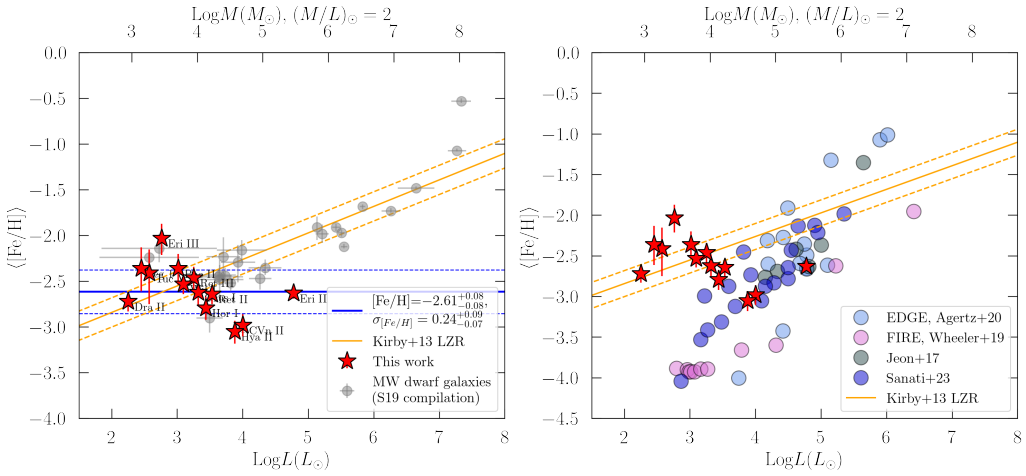


Figure 3.12: The mass-metallicity relation for dwarf galaxies, updated with results from this work. **Left:** We add our $\langle$[Fe/H]$\rangle$ measurements to the $\langle$[Fe/H]$\rangle$ measurements of other Milky Way dwarf galaxies, using the table compiled by [277]. Our results show a clear floor in the mass-metallicity relation in the UFD regime. We characterize this putative floor using only our measurements, assuming that the floor can be described by a Gaussian mean and scatter, placing the mean of the floor at [Fe/H]$= -2.61 \pm 0.08$ dex. **Right:** Our $\langle$[Fe/H]$\rangle$ measurements compared to those from select cosmological simulations. While simulations can broadly reproduce the mass-metallicity relation for the more luminous dwarf galaxies, they currently struggle to enrich less-luminous dwarf galaxies to the same level as we observe.

mean metallicities are scattered about [Fe/H] $= -2.6$. Early spectroscopic studies had already hinted at such an empirical result, but confidence in this feature was uncertain due to small sample sizes used to make measurements in individual UFDs, as well as hard-to-quantify systematic differences between metallicity measurements made using various techniques ([277]).

Our large sample of homogeneous metallicities over a range of UFDs definitively shows a break in the relation compared to that for larger galaxies. We quantify the nature of this feature by conducting a linear fit to the mean metallicities of our measurements, following the procedure laid out in [133]. The resulting slope of the line in units of [Fe/H]/Log$_{10}$ $L_\odot$ is -0.17 ± 0.11, with an intercept of -2.06 ± 0.38 dex. The value of this slope is consistent with zero, and in any case, is discrepant from the positive slope of the relation for more luminous dwarfs.

While this feature was previously thought of as a "floor" in the relation in early

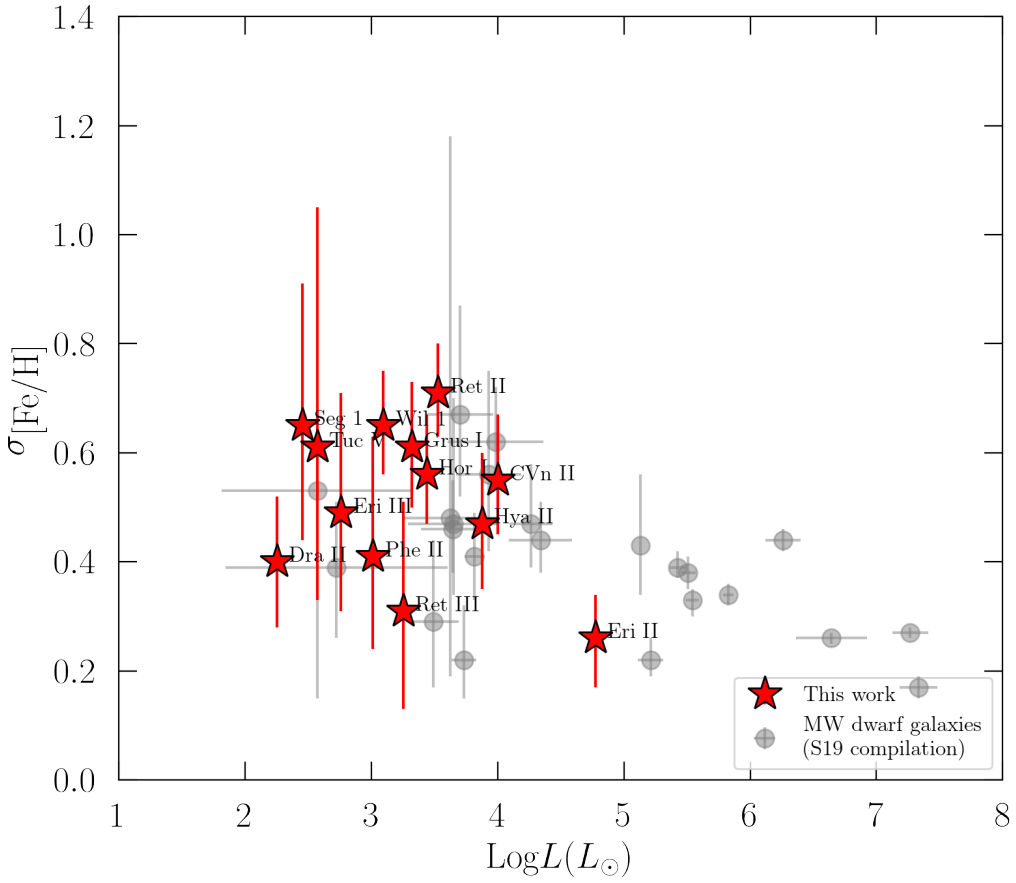


Figure 3.13: We compare our $\sigma_{[Fe/H]}$ measurements, made assuming a Gaussian characterization of the MDF, to the $\sigma_{[Fe/H]}$ measurements of other Milky Way dwarf galaxies (compiled by [277]). Our results confirm the large internal metallicity variations in these systems.

theoretical works attempting to reproduce it (e.g., [322]), we instead conceptualize the $\langle$[Fe/H]$\rangle$ of the UFD population as a normal distribution centered around [Fe/H] $= -2.61 \pm 0.08$ with $\sigma_{\rm [Fe/H]} = 0.24^{+0.09}_{-0.06}$ dex (Figure 3.12). We also make the same Gaussian fit to the [277] compilation of mean metallicities for systems with less than 10^5 $L_\odot$, finding a mean of -2.40 ± 0.06 and a dispersion of 0.21 ± 0.06. The mean metallicity are in agreement to within 2σ, and the dispersion is in good agreement. Under this framework, galaxies such as Eri III and Hya II are two-σ deviations from the distribution. The scatter that we observe about this distribution also traces UFDs' known sensitivity to the stochasticity of baryonic processes.

The galaxy mass-metallicity relation is the observational synthesis of the baryonic physics driving galaxy formation across all scales. Previously, the dwarf galaxy mass-metallicity relation established by [166] was shown to be universal across galaxies of different morphological types and environments in the Local Group, and could be somewhat matched with mass-metallicity relations from other techniques that extend to galaxies as massive as 10^{12} $M_\odot$. The canonical interpretation of this phenomenon is that more massive galaxies are better able to retain SNe enrichment products to form successive generations of stars compared to their fainter counterparts. That UFDs no longer display the same trends suggests that this picture of galaxy evolution requires additional refinement for the faintest end of the luminosity function.

In the right panel of Figure 3.12, we compare the dwarf galaxy data against simulated ultra-faints from the independent simulations of [143], [322], [1], and [252]. While simulations have begun to reproduce the mean metallicities of UFDs more luminous than 10^4 $L_\odot$, fainter UFDs still remain a theoretical challenge to simulate.

The mean metallicities of UFDs are shown to be particularly sensitive to the details of feedback implementation, where increasingly strong feedback mechanisms suppresses subsequent enrichment and star formation and produces low mean metallicities [1]. In the case of FIRE-2 simulations, which implements strong feedback, many of the lowest-luminosity UFDs never enrich beyond the initialized metallicity floor [322], as shown by the lower-luminosity FIRE UFDs in Fig 3.12 at [Fe/H] $= -4.0$. So far, there have been numerical experiments varying parameters such as star formation, radiative transfer, SNe energies ([1], [252]), metallicity-dependence of Type Ia SNe DTDs [103], and top-heaviness and stochastic sampling of the IMF ([10], [242] respectively), in order to explore the parameter space of physics that elevate enrichment levels in UFDs. Overall, this area of study is still ongoing.

One notable discrepancy between current UFD simulations and the UFDs that we have observed is the impact of environment. While the simulations quoted thus far evolve UFD halos in isolation, all of the UFDs in our sample are present-day satellites either of the MW or the Magellanic clouds. Environment can matter be-

cause the presence of a nearby, more massive host could provide pre-enriched gas and introduce additional metals into the UFD's internal ecosystem (e.g., [143]). Additionally, reionization is thought to play a central role in truncating the star formation of UFDs (e.g., [41]), and a galaxy's environment becomes a proxy for uneven distance and exposure from reionizing sources (e.g., [69]).

On the other hand, studies of UFD infall times based on *Gaia* proper motions and simulation analogs suggest that the majority of them fell into the Milky Way after forming all of their stars ([87], [244], [11]). In that case, perhaps the immediate Milky Way environment would not be relevant for interpreting their present-day MDFs. Additionally, some galaxies within our sample are also satellites of the LMC prior to falling into the Milky Way (e.g., [238]), and early studies already suggest that they may have experienced different chemical enrichment pathways and SFHs compared to MW satellites ([147], [250]). Detailed orbital histories of Local Group satellites and, subsequently, a more complete account of Local Group assembly history at high redshifts, would also be constructive for disentangling competing physics that contribute to UFD formation.

In Figure 3.13, we present $\sigma_{\rm [Fe/H]}$ of UFDs as a function of luminosity and in comparison with data from other LG dwarfs. Our data show that UFDs span a range of $\sigma_{\rm [Fe/H]}$, from ~ 0.3 dex to ~ 0.7 dex. This empirical result was also hinted at in prior studies, and our dataset enables its confirmation. The interpretation of UFD $\sigma_{\rm [Fe/H]}$ is an active area of investigation, and potential physical mechanisms responsible include the stochasticity of chemical enrichment processes and metal-mixing (e.g., [93], [85]).

The Prevalence of Metal-Rich Stars

Our sample contains a higher fraction of stars more MR than [Fe/H] > -2.0 than previously discovered in the literature. Here, we discuss some of the implications of and potential concerns with this discovery.

As discussed in §3.9 and §3.6, based on foreground modeling and the narrow FoV of our observations, we do not expect foreground to be a major source of MR stars in our sample. At the same time, we acknowledge the possibility that our sample may be affected by foreground in excess of our estimates, e.g., there is a non-zero probability that other yet-to-be-discovered MW substructures spatially overlap with our HST fields. To address this small, but non-zero, possible impact on our results, we take the very conservative approach of recomputing the MDFs with and without MR stars for individual UFD cases where this may be a concern (e.g. they are outliers compared to the rest of the sample; see §3.6). However, because it seems unlikely

that all MR stars in all our UFDs are MW interlopers, we choose to be inclusive in our membership sample. Accordingly, we provide these MR stars in Table 3.6 and welcome follow-up studies by the community to refine membership and undertake other studies of these stars (e.g., detailed abundance patterns).

To-date, the broad consensus for the abundance of MR ([Fe/H] > -2.0) stars in UFDs is not well-established. However, there also are known cases of spectroscopically confirmed MR stars in UFDs (e.g., CVn II, Wil 1, and Seg 1). As a result, we also remark on the astrophysical implications of our findings. MR stars are quite important for detailed interpretations of chemical evolution in UFDs: the shape of the metal-rich end of a galaxy's MDF is driven by the equilibrium between gas enrichment processes and accretion of pristine gas, as well as the rapidity of star formation truncation (e.g., [142], [257]). The detailed abundance patterns of metal-rich stars may also provide insight into enrichment mechanisms and/or number of enrichment event that preceded their formation (e.g., [92]).

If the dwarf galaxy mass-metallicity relation could be extrapolated down to the UFD regime [166], then the expectation prior to this work is that UFDs should indeed be composed primarily of metal-poor stars. However, as discussed in §3.7, our results have shown that the faintest UFDs deviate from this expectation. These observations suggest that different galaxy formation physics and enrichment processes dominate in the UFD regime, and additional theoretical investigations are needed to ascertain the extent to which UFDs can enrich stars beyond [Fe/H] $= -2.0$.

Metallicities for a Large Sample of Ancient Stars

A main challenge in EMP studies in the MW is a lack of precise ages. EMPs are typically found in the field and age dating techniques rely on fitting single-stars to isochrones, which can produce very precise, but inaccurate ages, or, in some cases, nuclear cosmochronolgy (i.e., isotopic age dating), which has large uncertainties (see e.g., [37] for a detailed discussion).

While it would seem that lower metallicity stars in the MW formed at older ages, theory paints a more complicated picture. Cosmological simulations of the Milky Way have already suggested that stellar age and metallicity are not monotonic relations (e.g., [290], [17]). For example, these studies show that stars as metal-rich as [Fe/H] ~ -1.0 could have formed as early as within the first 1 Gyr of the Galaxy's lifetime alongside stars as metal-poor as [Fe/H] ~ -4.0. A star with [Fe/H] ~ -2.5 could have formed as long ago as 13 Gyr or as recently as 7 Gyr ago. As a result, due to the complexity of the Milky Way's stellar populations (see, e.g., [117], [204], [158], [263] for corroborating observations), ages are challenging to infer based on metallicity alone.

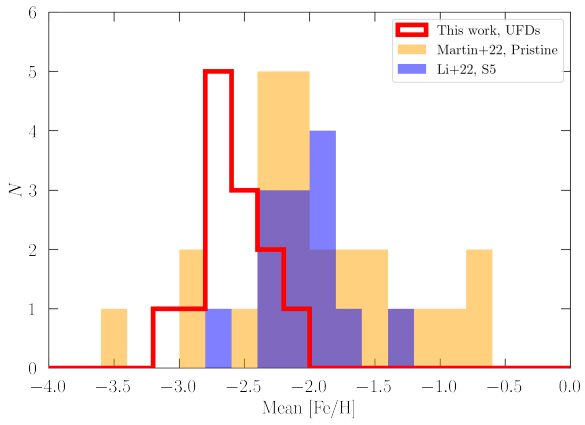


Figure 3.14: The mean metallicities of our UFDs compared to those of recent streams characterized by S5 [183] and Pristine [199]. The distributions are noticeably different, suggesting UFDs are not the main progenitors of the currently known MW stream population.

In contrast, UFDs have well-constrained ages. By fitting the MSTO of deep optical CMDs, numerous studies have shown that UFDs that orbit the MW formed the majority of their stars during or prior to the epoch of reionization (e.g., [41], [319], [101], [280], [250], [281]). Consequently, the metallicites and MDFs we measure all arise from stars that formed within the first billion years of the Universe. Chemical evolution modeling can provide insights into the physical mechanisms by which such small galaxies can create such large metallicity spreads so rapidly in the early Universe (e.g., [257], [4]). We will pursue a similar investigation with our current sample in the next paper in this series.

Hierarchical Structure Formation

The formation of larger galaxies from the hierarchical mergers of their smaller counterparts has been a long-standing tenet of ΛCDM cosmology (e.g., [272], [323]). An increasingly common scenario in the literature is that the observed signatures of accretion are dominated by larger galaxies (e.g., LMC-sized) over small UFD-like systems (e.g., [67], [72], [127], [27], [229]), though the discovery of numerous fainter streams and substructures [e.g., 182, 273, 183, 139] may provide a more granular perspective and reveal the contribution of fainter galaxies.

Figure 3.14, shows the distribution of mean metallicities of our satellites compared

to the stellar streams recently characterized by S5 [183] and Pristine [199]. The mean metallicities of our galaxies are centered at $\langle$[Fe/H]$\rangle \sim -2.6$ and range from $\langle$[Fe/H]$\rangle = -3.0$ to $\langle$[Fe/H]$\rangle = -2.0$. In contrast, the streams observed by S5 and Pristine tend to be more enriched, and span a larger range of metallicities. For both comparison studies, the teams were unable to resolve $\sigma_{\rm [Fe/H]}$ in their streams, suggesting that they were of globular cluster origin. These preliminary comparisons suggest that the UFDs we observe are a distinct class of objects from the newer streams that are being discovered in the MW.

From a theoretical perspective, [40] explored the possibility of recovering completely tidally disrupted UFDs by searching for clustering in dynamical action space. Overall, they found that the prospects are slim because the signal of UFD remnants are weak compared to the background. These results affirm the emerging picture based on our metallicity measurements, that UFDs do not have similar properties as currently-known MW streams and their progenitors. It is however possible that our current understanding of the UFD stream composition in the MW is limited by selection effects and absence of available information in current stream-finding efforts. [40] note that additional chemical abundance information such as metallicity and/or r-process elements may improve the efficacy of such searches, in which case, the results of our study can assist in future efforts by establishing a baseline for the expected chemical profile of UFDs.

3.8 Conclusion

We present metallicity measurements of ~ 500 stars across 13 UFDs, measured from *HST* narrow-band imaging in the $F395N$ filter. Our dataset doubles the number of available metallicities by a factor of five among the just UFDs in our study, and double the number of available metalliciites across all UFDs. We use these stellar metallicities to measure the MDFs of these 13 systems.

We summarize the key results enabled by our study:

1. HST $F395N$ narrow-band imaging can recover UFD MDFs to the same level of fidelity as numerous other metallicity measurement methods currently used by the community.

2. Our results are the largest homogeneous set of stellar metallicities measured in UFDs to-date.

3. With this vastly expanded sample size, we are able to robustly resolve non-zero metallicity dispersions for all 13 of our targets. For Eri III, we confirm its status as a UFD (as opposed to a GC) for the first time.

4. The composite MDF of the UFDs has $\langle$[Fe/H]$\rangle = -2.66 \pm 0.04$ dex and a dispersion of 0.56 ± 0.03. Individually, our UFDs span a range of $\langle$[Fe/H]$\rangle$ from ~ -3.0 to ~ -2.0, and dispersions ranging from ~ 0.3 to ~ 0.7. With $\langle$[Fe/H]$\rangle \sim -3.0$ as measured by our study, CVn II and Hya II are the most metal-poor UFDs known to-date.

5. We identify stars on the extreme ends of the UFD MDFs ([Fe/H] < -3.0 and [Fe/H] > -2.0) that would be promising candidates for detailed spectroscopic follow-up studies to confirm their metallicities and origins. Respectively, these stars make up 24% and 19% of our sample. The EMP fraction we measure is larger than the literature value across all known UFDs of 14%, and the MR star fraction is in agreement with the literature fraction of 19%.

6. We quantify the metallicity floor in the dwarf galaxy mass-metallicity relation as a distribution centered on [Fe/H] $\sim -2.61 \pm 0.08$ with a dispersion of $0.24^{+0.09}_{-0.06}$ dex that ranges across three orders of luminosity in the UFD regime, from 10^2 to 10^5 $L_\odot$.

7. We provide the largest set of stellar metallicity measurements for a population of stars which, owing to HST SFH studies of UFDs, are known to have overwhelmingly have formed within 1 Gyr of the Big Bang. This is in contrast to metal-poor stars in the MW, for which age uncertainties can be several Gyr owing to the complex formation history of the MW.

8. The mean metallicities of our UFD sample are different from the mean metallicites of many known streams in the MW, reinforcing the idea that surviving UFDs do not make up the vast majority of MW halo substructure that can be detected at present.

9. Our well-populated and homogeneous MDFs pave the way for detailed interpretation of the physics of UFD formation, with recent works like [257] providing an analytic framework for such studies moving forward.

Our study demonstrates the power for *HST* narrow-band imaging to amass a large sample of standardized metallicity measurements and enable science cases in UFDs that have not been previously pursued due to sparse and heterogeneous datasets. This observational technique, as well as analogous techniques from the ground (e.g.,

[119], [56], [188]) will continue to play a pivotal role in measuring metallicities of faint stars in distant galaxies that are anticipated to be uncovered by next-generation photometric surveys.

3.9 Foreground Contaminants

Our MDFs may suffer from some degree of MW foreground contamination. Unlike spectroscopy, we are unable to readily identify most contaminants (i.e., via kinematic selection). However, in contrast to spectroscopic studies, we intentionally target the inner regions of UFDs (i.e., within 1 r_h), for which the contamination fraction is expected to be lower than many ground-based surveys that extend to much larger areas.

To estimate the effect of foreground interlopers, we adopt a statistical approach. For each UFD, we use the TRILEGAL MW model [304] to query all simulated stars within 0.5 deg^2 of the center of each galaxy. We query such a large on-sky area to adequately sample the distribution generated from the model. TRILEGAL outputs simulated stars in the filters and with known physical parameters (e.g., metallicity) which we use to evaluate the expected contamination fraction.

We estimate the expected number of foreground contaminants in our data by (i) using the ratio of model area to WFC3 field of view and (ii) requiring the possible contaminants fall into our member-selection region on the CMD of each galaxy. The result for most galaxies is that we expect at most 1 foreground contaminant. The combination of the small WFC3 field-of-view, focus on the central regions of the galaxies, and CMD-based selection criteria ensure that we are predominantly including UFD member stars in our MDFs.

Figure 3.15 illustrates this process using the foreground model in the direction of Reticulum II (Ret II). The left panel shows the TRILEGAL CMD of the queried foreground model within 0.5 deg^2, with the stars color-coded by metallicity. The center panel shows the stars that remain from the same isochrone cut that we use to select Ret II members. The right panel illustrates the expected impact of foreground contamination when scaling the number of expected stars that pass the isochrone cut by the WFC3 field of view.

This is only an estimate, as in some case, UFDs may have contamination in excess of the smooth TRILEGAL model (e.g., due to MW substructure in the case of Segue 1). In such cases, we are able to use some stellar kinematics to further clean our sample. We discuss these cases individually in §3.6. In general, the odds that our targeted HST observations fall onto another substructure with stars that

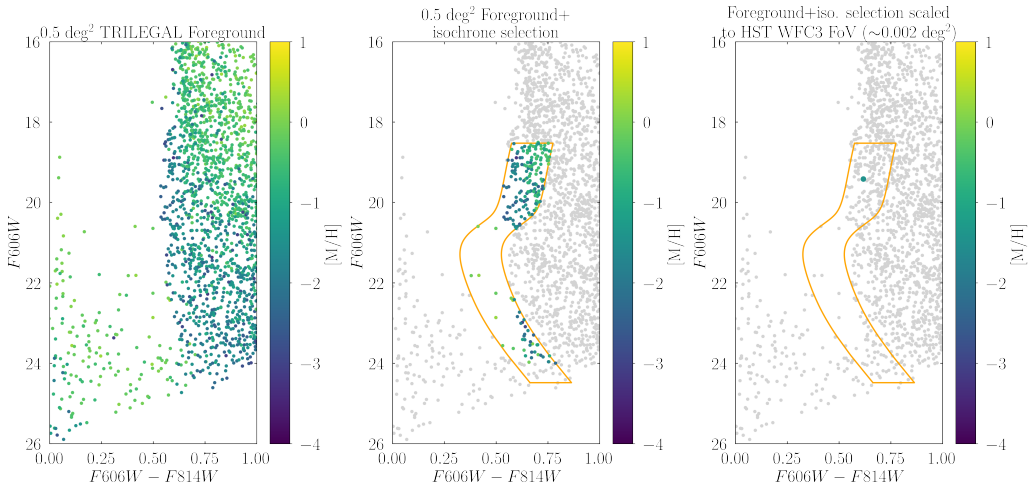


Figure 3.15: The potential impact of foreground contamination on our results illustrated using Reticulum II. **Left:** CMD of the TRILEGAL foreground model [304] by querying 0.5 deg^2 centered around Ret II, color-coded by metallicity. **Middle:** Remaining MW foreground stars (colored) from applying the same isochrone cut used to select Ret II members. **Right:** Impact of foreground contamination when scaling down number of expected interlopers by the WFC3 FoV. We typically expect ~ 1 MW interloper in our final stellar sample. The nature of our observations and selection criteria combine to make foreground contamination minimal.

satisfy all our selection criteria are generally quite small. Accordingly, we find that interlopers are unlikely to significantly alter our MDFs.

3.10 Systematic Uncertainties in Individual Star Metallicities

There are several plausible physics effects that could affect our metallicity estimates beyond what is discussed in the main paper. Here, we describe these effects and estimate their possible contribution to our metallicity and MDF determinations.

The Impact of α Enhancements

UFDs are known to host stars with different degree of α-enhancement [277]. The effect on CaHK-based metallicities is modest, as shown in [96]. There, we demonstrated that using MIST models with different levels of α-enhancements (0.4 dex vs. 0.0 dex) shift the inferred stellar metallicity by no more than ~ 0.2 dex.

Light-Element Abundance Variations

Lighter element abundance variations can affect absorption around the Ca H&K lines. Notably, enhancements in C and N can introduce contaminating absorption into the near-UV region of the Ca H&K lines (e.g., Fig. 2 from [291]).

C is an element of particular concern, as nearly half of known metal-poor ([Fe/H] < -3 stars in the MW show carbon enhancements (e.g., [92]). Carbon enhancement can introduce additional absorption around the Ca H&K lines, potentially polluting the CaHK narrowband measurement (see Figure. 2 of [291]). The expected impact is that a carbon enhanced star would have a higher inferred CaHK-based metallicity than its true metallicity (i.e., there would be more absorption in the $F395N$ band). As [291] show, modest carbon enhancements do not drastically affect the CaHK band. Quantifying the impact of carbon on every star in our sample is a complicated process and is beyond the scope of this paper. Instead, we use an example case to illustrate the impact of strong carbon enhancement on our inferred metallicites and MDFs.

One star in our entire sample is known to be carbon enhanced from high resolution spectroscopy. This star, J100714+160154 in Segue 1, was determined by [93] to have [Fe/H]$= -1.42 \pm 0.24$, and, notably, a carbon enhancement of [C/Fe]$= +1.44 \pm 0.2$. In this paper, we find a value of [Fe/H] $= -1.86^{+0.11}_{-0.12}$(stat.) $\pm$ 0.3(syst.), indicating they are in consistent within 1.2 σ. Though it is only a single example, it does show that even a very strong carbon enhancement does not change the metallicity significantly beyond the bounds of our 1σ uncertainties.

For all other stars in our sample, we perform a coarser check on the impact of carbon. Since line blanketing from carbon enhancement affects the near-UV spectral region covered by the $F475W$ filter, we should expect that a carbon-enhanced star would appear redder in $F475W - F814W$ than compared to expectations. In contrast, $F606W - F814W$ colors should be comparatively unaffected because there are few carbon features in the $F606W$ filter. We do not find a strong trend in our sample. Though it is likely that a modest fraction of our stars have some degree of carbon enhancement, we believe it is unlikely that they are affecting our MDFs beyond the reported uncertainties.

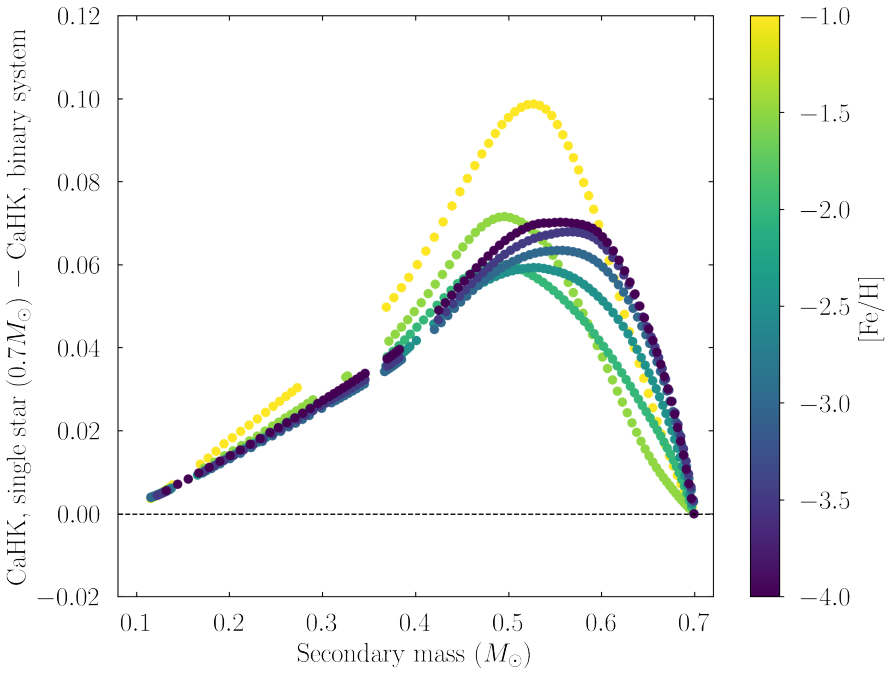


Figure 3.16: The effect of unresolved binaries on the CaHK color. The y-axis shows the difference in CaHK color between a single MS star at 0.7 $M_\odot$ and a binary system composed of a 0.7 $M_\odot$ MS star with companions from 0.1 $M_\odot$ to 0.7 $M_\odot$, for different metallicities spanned by our CaHK color grid. The impact of binary stars on our metallicities is small-to-modest compared to other sources of uncertainty.

Binary stars

At least one third of low-mass main sequence stars are accompanied by a companion(s) [83]. In our sample, Ret II, Wil 1, Seg 1, and Dra II are primarily characterized by stars on the lower main sequence (Figure 3.1), a place in which unresolved binaries have the largest photometric impacts. The broadness of their lower MS is suggestive of binary companions. Using the method detailed below, we estimate the impact of unresolved binaries on CaHK-based metallicities to be small, thus we do not *a priori* exclude any potential unresolved binaries from our sample.

We estimate the effects of binaries by calculating synthetic photometry of single and binary stars. Specifically, we simulate a binary system with a primary mass of 0.7 $M_\odot$, a typical stellar mass in our sample, and accompanied by a lower-mass companion star of varying masses, down to the lowest mass limit available from the

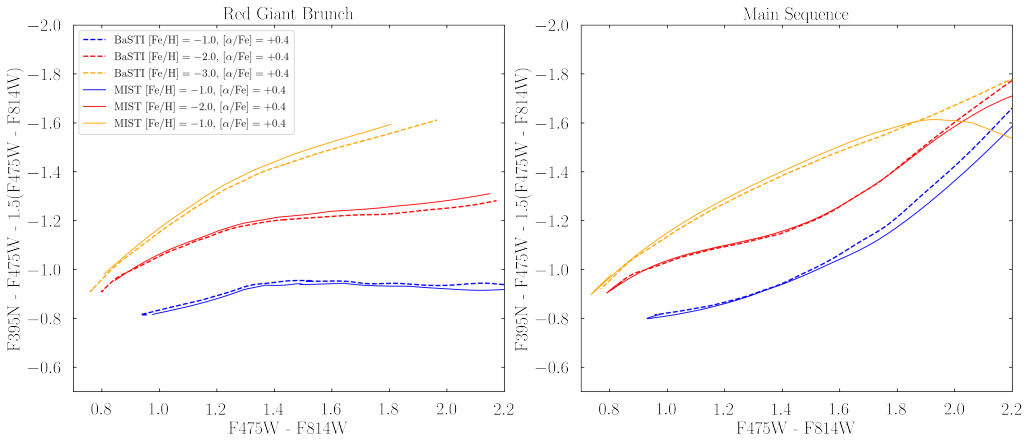


Figure 3.17: Comparing MIST and BaSTI stellar evolution models in CaHK space for α-enhanced, 13 Gyr RGB (left) and MS (right) stars.

MIST isochrones (0.1 $M_{\odot}$). We assume that both stars have the same metallicity, and conduct this calculation for metallicities from [Fe/H] = −1.0 to −4.0. We also assume that light from both stars are visible, which means that the deviations from CaHK for a single-star system that we calculate are upper limits on the magnitude of the effect.

Figure 3.16 illustrates the impact of a binary companion on the CaHK color. The presence of an unresolved companion makes a star appear more metal-poor (i.e., bluer) in CaHK space. This effect is more pronounced for stars that are more metal-rich. For stars with [Fe/H] > −1.5, the impact of a binary companion can shift it away from the CaHK track by up to 0.1 mag, which translates into a metallicity shift of $\sim$ 0.2 dex. For lower metallicites, the effect is $\sim$ 0.1 dex. The assumptions in this calculation means that these numbers describe the upper limit of the impact of binarity. The impact of unresolved binaries is modest compared to our overall uncertainty budgets, indicating that unresolved binaries are not a major uncertainty on our stellar metallicities.

Uncertainties in Stellar Evolution Modeling

There are uncertainties intrinsic to stellar evolution modeling and the generation of stellar atmospheres that can affect the placement and curvature of CaHK color tracks. In Figure 3.17, we compare the MIST tracks used in our work to the tracks

from the Bag of Stellar Tracks and Isochrones (BaSTI; [129], [241]) across the range of metallicities common to both models.

For RGB stars, the tracks are offset by up to 0.05 mag at $F475W-F814W \sim 2.0$, and < 0.02 mag at $F475W - F814W \sim 1.0$. This translates to up to ~ 0.2 dex systematic difference in metallicity, and the difference diminishes at bluer colors. For MS stars, the tracks are offset by less than 0.02 mag between $F475W - F814W \sim 0.8$ to $F475W - F814W \sim 1.5$, which translates to at most 0.2 dex systematic difference in metallicity. These systematic differences are well within the statistical and systematic uncertainties we adopt for our measurements.

Quantifying Systematic Uncertainties

While a detailed investigation of the physics contributing to CaHK metallicity uncertainties is beyond the scope of this work, we do attempt to quantify their impact. We begin by discussing the EMP end of our measurements ([Fe/H] < -3). Towards lower metallicities, CaHK loses its discriminating power, as shown in the CaHK tracks in Figure 3.9. The EMP star search from the Pristine survey using CaHK photometry has yielded success rates of about $\sim 20\%$ for stars with [Fe/H] < -3 ([329], [308]).

Additionally, there are known issues with the MIST/MESA isochrones for metal-poor stars.[9] Given that refining the models of metal-poor stars is an active area of research [156], we adopt a systematic error floor of ~ 0.5 dex for all stars whose metallicity measurements are below -3.

For stars at more intermediate metallicities, we quantify the impact of systematics by attempting to recover the MDF of M92, a metal-poor globular cluster with $\langle$[Fe/H]$\rangle$ on par to those expected for UFDs ($\langle$[Fe/H]$\rangle = -2.2$) and no known metallicity dispersion, [Ca/Fe]$= 0.10 \pm 0.05$ with a dispersion consistent with zero[10], [Mg/Fe]$= 0.14 \pm 0.04$ with a dispersion of $0.22^{+0.03}_{-0.02}$, and [C/Fe]< 0 [215]. We retrieve archival $F395N$ narrow-band imaging for M92 taken by HST program GO-11729 (PI: Holtzman) and reduce it alongside short ($\sim$ 10s) $F475W$ and $F814W$ archival exposures from HST programs GO-10505 (PI: Gallart) and GO-12116 (PI: Dalcanton).

From the resulting catalog, we select stars with $F395N$ S/N> 100. The resulting M92 data begin below the horizontal branch and extend down to the MSTO. We present the data in Figure 3.18. The stars do not follow a perfectly narrow track,

[9]For stars at lower metallicities, temperatures inferred from isochrone mapping tended to be hotter by up to $\Delta T_{eff} = +500$ K compared to spectroscopic methods (e.g., [219], [159]).

[10]Using the data from [215], we compute mean and dispersion for additional elements following the procedure in §3.4.

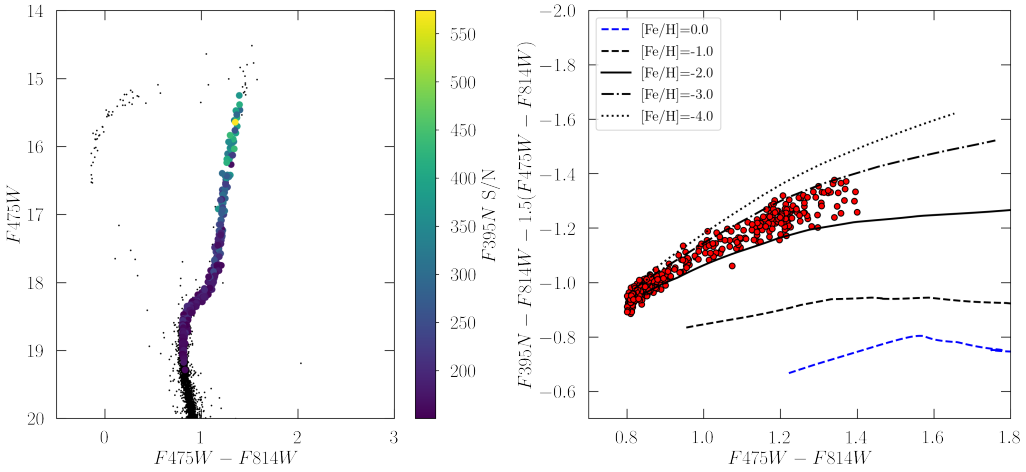


Figure 3.18: HST data of the M92 GC, a mono-metallic population, that we use to determine systematic uncertainties for our metallicity measurements. (left) CMD of M92 in $F475W - F814W$. (right) The position of M92 members on CaHK diagram. The majority of these stars lie between the [Fe/H] = −3 and [Fe/H] = −2 tracks.

but they lie overwhelmingly between the [Fe/H] = −3 and [Fe/H] = −2 tracks. With our S/N selection criteria, any scatter observed in the placement of M92 members in CaHK should be driven largely by abundance variations and other modeling uncertainties.

Using this data, we aim to find the minimum individual metallicity measurement uncertainty that would result in the inferred metallicity dispersion of M92 to be zero. As part of this exercise, we split the samples by stellar evolution phase, which also functions as a proxy for temperature: stars on the MSTO are hotter than their counterparts on the RGB. For hotter stars, the CaHK mono-metallic tracks begin to converge and make it more difficult to discern metallicities.

For each star, we assign it a metallicity based on its location on a grid of interpolated MIST [α/Fe]= +0.20 models.[11] We then assign a measurement uncertainty to each star and infer the metallicity dispersion of M92 following the procedure outlined in §3.4. For stars on the lower RGB, we find that a minimum measurement uncertainty of 0.2 dex is necessary to reduce the metallicity dispersion of M92 to be consistent with zero. For stars on the MSTO, a minimum measurement uncertainty

[11] Although we use [α/Fe]= +0.20 models for this exercise, they look very similar to [α/Fe]= +0.40 models in CaHK color space.

of 0.3 dex is necessary.

Impact of Systematic Offset on Paper Conclusions

In §3.11, we make direct comparisons to literature measurements where available, but interpretation of discrepancies and offsets are ultimately complicated by small sample sizes and a diversity of metallicity inference methods. Here we consider the robustness of the key results of our paper to systematic shifts in metallicity. These shifts can be caused, for example, by using different stellar evolution models, scaling our measurements to different solar abundances, and/or assuming different levels of α enhancement, all of which are not standardized among literature measurements.

If a MP offset was applied to our measurements:

- The overall level of the luminosity-metallicity relation for UFDs would be lowered across our sample, but the break in the LZR would remain. For the mean metallicities to begin approaching agreement with simulations, an offset of 0.5 dex at minimum would be required. Such an offset would bring our results out of agreement with literature values.
- We would expect less MR stars in our sample, bringing the MR star fraction out of agreement with the literature.
- Our distribution of mean metallicities will deviate further from the MW streams population from [199] and [183], and it is unlikely that the range of UFD mean metallicities will broaden enough to be comparable to results from stream searches.

If a MR offset was applied to our measurements:

- The overall level of the luminosity-metallicity relation for UFDs would be raised across our sample, thereby exacerbating the problem of under-enriching UFDs in simulations.
- Accordingly, we would expect more MR stars in our sample, leading to tension with spectroscopic results.
- Our distribution of mean metallicities will fall closer to the peak of the MW streams population from [199] and [183], but it is still unlikely that the range of UFD mean metallicities will broaden enough to be comparable to results from stream searches.

Overall, these offsets would not affect the main results of the paper.

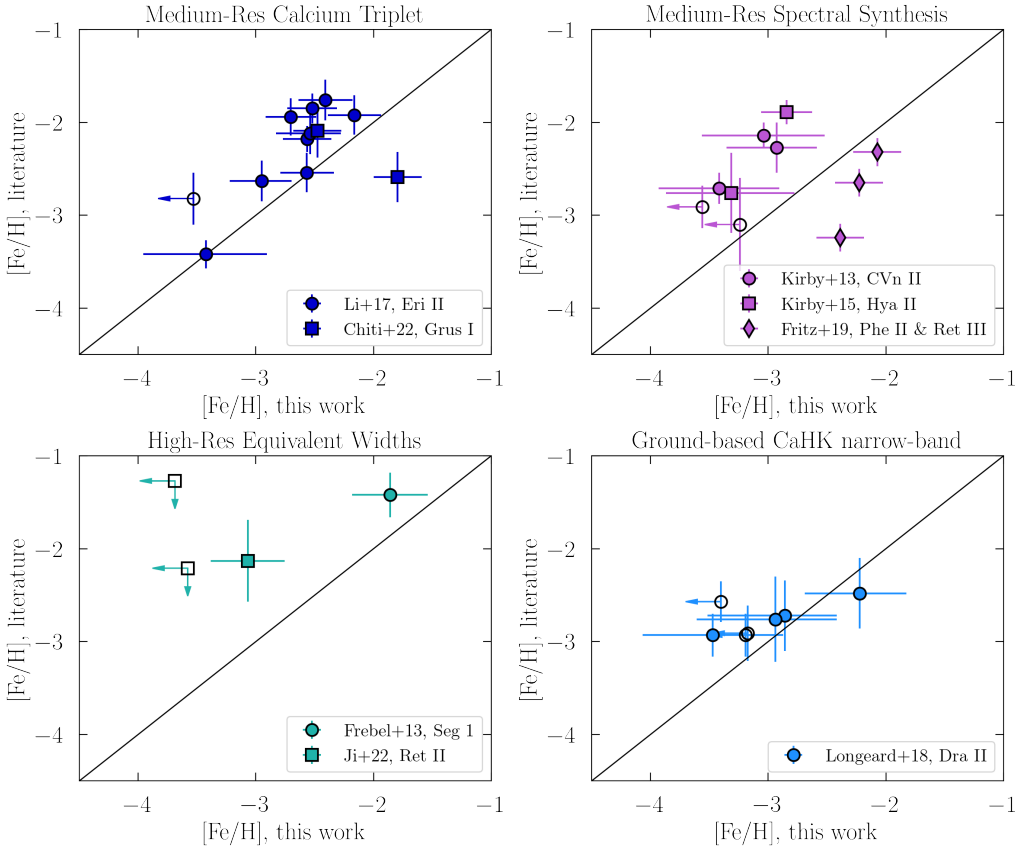


Figure 3.19: Comparisons between our measurements and those from the literature, between different measurement methods. The vast majority of literature metallicity measurements come from medium-resolution studies, particularly those leveraging the calcium triplet metallicity calibration. The ground-based CaHK narrow-band measurements are from the Pristine study of Dra II [184].

3.11 Comparisons to Literature Methods

In Figure 3.19, we compare metallicity measurements from this work to stars with metallicities in the literature derived from different techniques.

The upper left panel of Figure 3.19 shows a comparison between our metallicities and those derived using the [50] CaT equivalent widths calibration. The galaxies whose data are used for this comparison are Eri II (Magellan/IMACS, [180]) and Grus I (Magellan/IMACS, [55]). This comparison shows about 0.3 dex systematic

offset and agree reasonably well (within $\sim 1.5\sigma$). Uncertainties between the two methods are generally comparable in size. The [50] calibration is anchored by Galactic globular and open clusters for metallicities between -2.33 and $+0.47$, and below that metallicity range, the calibration was anchored by known metal-poor galactic field stars known at the time of writing. This calibration sample includes both solar-scaled and α enhanced stars, and though not factored into the calibration, it is acknowledged in the paper that the CaT equivalent widths, and therefore the inferred metallicity, has a secondary dependence on Ca abundances. The scatter in the comparison may be due to differences in assumed α abundances as well as additional systematic effects.

The upper right panel of Figure 3.19 shows a comparison of our metallicities to those derived using spectral synthesis methods of medium-resolution spectra. The galaxies represented in this panel are CVn II (Keck/DEIMOS, [166], later analyzed by [307]), Hya II (Keck/DEIMOS, [161]), Ret III and Phe II (VLT/FLAMES, [94]). The metallicity measurements from [166] and [161] tend to be more metal-rich than our measurements (falling above the 1-1 line) by ~ 0.6 dex, though the overall the samples agree within 1σ.

On average, the measurements of [94] tend to be more metal-poor than our measurements by ~ 0.5 dex (i.e., they fall below the one-to-one line). Where the Kirby et al. studies do not assume α-enhancement, the [94] measurements assume [α/Fe]$= +0.5$, which is slightly enhanced relative to the models that we use. In CaHK color space, we found that additional α enhancement makes a star appear more metal-poor, and this may account for some of the discrepancy that we observe. Some of the technical details in [94] are not entirely clear to us, making it a little challenging to determine what other factors might lead to the observed discrepancies.

The lower left panel of Figure 3.19 shows a comparison of our metallicities to those derived using equivalent widths of high-resolution spectroscopy. The galaxies in this sample are Seg 1 (Magellan/MIKE, [93]) and Ret II (Magellan/M2FS and FLAMES/GIRAFFE, [151]). As discussed in previous sections, our metallicity measurement for the star that we have in common with [93] is in good agreement at [Fe/H] ~ -1.5. The remaining stars in this panel are from [151]. For the single star that is not an upper limit, the two methods are in agreement at $\sim 1.5\sigma$. The spectra of this star suggests [Ca/Fe] $= -0.25 \pm 0.48$ and an unknown α-enhancement. Knowledge of the latter could bring them into better agreement. [151] was only able to place upper limits on the metallicities of the other two stars, and our metallicities are consistent with these upper limits.

Finally, the bottom right panel of Figure 3.19 shows ground-based CaHK Pristine measurements from Dra II [184] compared to our CaHK measurements. The level of agreement is good, given the uncertainties. Though our uncertainties are much larger

than [184], this is because we adopt a more conservative treatment of systematic uncertainties, as described in §3.10. Our random uncertainties for these stars are 0.3 dex, which are comparable to what [184] report.

Due to calibration limits, [184] also placed a metallicity floor on their measurements at [Fe/H] = −3.0. Because we use synthetic model grids that extend to [Fe/H] = −4.0, we are able to report more metal-poor values, as opposed to upper limits. Though limited in sample size, this comparison affirms the metal-poor nature of Dra II and demonstrates reasonable consistency between ground-based and space-based CaHK narrowband metallicities.

3.12 Metallicity Measurements as a Function of Stellar Evolutionary Phase and Brightness

As a diagnostic of the reliability of our measurements, we investigate whether there are systematic effects in metallicity measurements as a function of stellar evolutionary phase and/or apparent brightness that may be affecting our mean and dispersion measurements. We present all of the measurements that we use for the Gaussian MDF inference fit (see §3.4 for the procedure on their treatment) in Figure 3.20.

In the top panel, we plot our measurements as a function of absolute magnitude, where absolute magnitude is a proxy for stellar evolutionary phase. There is no apparent systematic trend in metallicity as a function of absolute magnitude across our sample, and the larger scatter for MS stars can be attributed to their larger systematic uncertainties as determined in §3.10, as well as the lower S/N of the fainter stars. Similarly, there is no apparent systematic trend in metallicity as a function of apparent magnitude, and the larger scatter in metallicity measurements for fainter stars is in line with expectations for measurements made using lower S/N data.

3.13 Additional MDF Summary Statistics

To assess deviations from Gaussianity, in this section we present the 16th percentile, median, and 84th percentile measurements for our MDFs, as well as the skew and kurtosis. We compute these quantities by first assuming Gaussian uncertainties on our individual measurements following the procedure outlined in §3.4 to generate 10000 Monte Carlo realizations of our MDF, and then deriving summary statistics and their uncertainties from these realizations. In all cases, the median we recover is in 1σ agreement with the Gaussian mean. For the cases of Wil 1, Ret II, and Dra II,

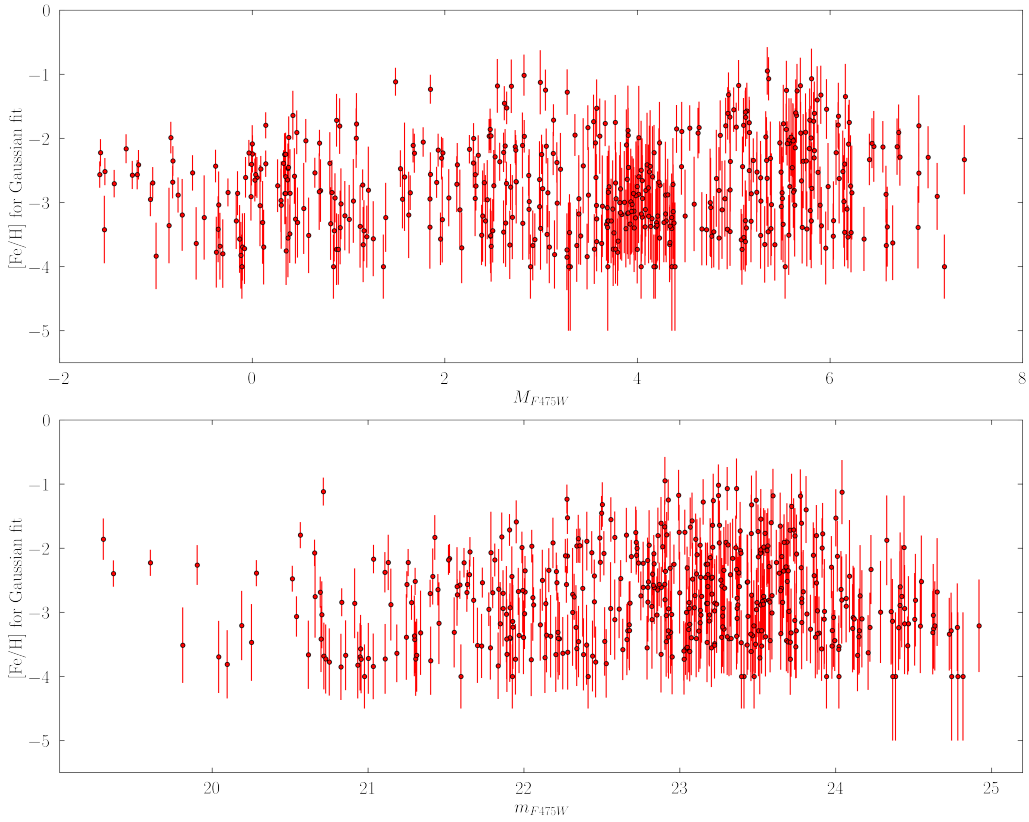


Figure 3.20: Stellar metallicities used for fitting the mean and dispersion (§3.4) of our MDFs as a function of brightness across our entire sample of galaxies. The measurements shown here are specifically for the process of fitting the MDFs, and may not fully reflect the final reported measurements (e.g., asymmetric uncertainties, upper limit constraints). The uncertainties shown here also take into account the systematic uncertainties we adopt as discussed in §3.10, and statistical uncertainties for our brighter stars are often smaller. **Top:** Metallicity measurements as a function of absolute magnitude, where absolute magnitude is a stand-in for stellar evolutionary phase. **Bottom:** Metallicity measurements as a function of apparent magnitude.

we resolve a kurtosis above at least the 2σ level, suggesting that their MDFs have weaker tails compared to a standard Gaussian. In all other cases, we are unable to resolve significant deviations from Gaussianity. We present these measurements in Table 3.3.

Table 3.3: Additional MDF Summary Statistics

Galaxy	M_v (mag)	$N_{\rm stars}$	16th Percentile MDF (dex)	Median (dex)	84th Percentile (dex)	Skew	Kurtosis
Eridanus II	−7.1	75	$-3.50^{+0.12}_{-0.12}$	$-2.70^{+0.07}_{-0.07}$	$-2.12^{+0.08}_{-0.08}$	$-0.3^{+0.2}_{-0.2}$	$-0.1^{+0.5}_{-0.4}$
Canes Venatici II	−5.2	40	$-3.88^{+0.15}_{-0.15}$	$-3.09^{+0.13}_{-0.14}$	$-2.23^{+0.13}_{-0.13}$	$0.3^{+0.3}_{-0.3}$	$0.0^{+0.8}_{-0.5}$
Hydra II	−4.9	30	$-3.93^{+0.17}_{-0.18}$	$-3.16^{+0.14}_{-0.15}$	$-2.46^{+0.14}_{-0.13}$	$0.1^{+0.4}_{-0.5}$	$0.2^{+1.1}_{-0.7}$
Reticulum II	−4.0	77	$-3.73^{+0.12}_{-0.12}$	$-2.74^{+0.12}_{-0.19}$	$-1.61^{+0.12}_{-0.11}$	$0.1^{+0.2}_{-0.2}$	$-0.8^{+0.2}_{-0.1}$
Horologium I	−3.8	40	$-3.72^{+0.16}_{-0.17}$	$-2.88^{+0.14}_{-0.14}$	$-2.06^{+0.15}_{-0.14}$	$0.1^{+0.3}_{-0.3}$	$-0.4^{+0.5}_{-0.3}$
Grus I	−3.5	36	$-3.66^{+0.20}_{-0.20}$	$-2.80^{+0.15}_{-0.16}$	$-1.86^{+0.17}_{-0.17}$	$0.0^{+0.3}_{-0.4}$	$-0.3^{+0.7}_{-0.4}$
Reticulum III	−3.3	18	$-3.46^{+0.26}_{-0.28}$	$-2.49^{+0.14}_{-0.15}$	$-1.94^{+0.17}_{-0.14}$	$-0.4^{+0.4}_{-0.4}$	$-0.5^{+0.7}_{-0.5}$
Willman 1	−2.9	68	$-3.64^{+0.14}_{-0.13}$	$-2.55^{+0.13}_{-0.13}$	$-1.57^{+0.12}_{-0.11}$	$-0.1^{+0.2}_{-0.2}$	$-0.8^{+0.3}_{-0.2}$
Phoenix II	−2.7	10	$-3.01^{+0.23}_{-0.27}$	$-2.39^{+0.14}_{-0.14}$	$-1.99^{+0.16}_{-0.15}$	$-0.4^{+0.6}_{-0.6}$	$-0.3^{+1.0}_{-0.6}$
Eridanus III	−2.1	13	$-2.77^{+0.28}_{-0.33}$	$-2.05^{+0.14}_{-0.14}$	$-1.84^{+0.18}_{-0.16}$	$-0.6^{+0.4}_{-0.4}$	$-0.2^{+1.0}_{-0.6}$
Tucana V	−1.6	6	$-3.15^{+0.30}_{-0.44}$	$-2.43^{+0.18}_{-0.16}$	$-1.98^{+0.17}_{-0.15}$	$-0.5^{+0.5}_{-0.5}$	$-0.8^{+0.8}_{-0.6}$
Segue 1	−1.3	12	$-3.30^{+0.29}_{-0.30}$	$-2.29^{+0.20}_{-0.22}$	$-1.69^{+0.17}_{-0.17}$	$-0.6^{+0.4}_{-0.4}$	$-0.7^{+0.9}_{-0.5}$
Draco II	−0.8	38	$-3.68^{+0.13}_{-0.17}$	$-2.75^{+0.13}_{-0.13}$	$-2.04^{+0.12}_{-0.12}$	$-0.3^{+0.2}_{-0.3}$	$-0.7^{+0.5}_{-0.3}$

Note. Additional summary statistics for our MDFs. We list the 16th, 50th, and 84th percentiles, as well as the skew and kurtosis measured from our MDFs.

3.14 Tables of Metallicity Measurements

Table 3.4: Metallicity Measurements of All Stars

UFD	Star	R.A. (deg)	Decl. (deg)	F814W (mag)	F606W (mag)	F475W (mag)	F395N (mag)	V/I (mag)	$C_{a}HK$ (mag)	[Fe/H] (dex)
Eri II	0	56.099955	−43.545433	19.311 ± 0.000	20.292 ± 0.001	21.248 ± 0.003	22.634 ± 0.033	1.937 ± 0.003	−1.520 ± 0.033	$-2.56^{+0.04}_{-0.05}$ (stat.) ±0.2 (syst.)
Eri II	1	56.111058	−43.523014	19.397 ± 0.001	20.351 ± 0.001	21.301 ± 0.002	22.692 ± 0.048	1.904 ± 0.002	−1.465 ± 0.048	$-2.52^{+0.06}_{-0.07}$ (stat.) ±0.2 (syst.)
Eri II	2	56.114817	−43.526851	19.423 ± 0.001	20.354 ± 0.001	21.257 ± 0.002	22.680 ± 0.034	1.834 ± 0.002	−1.328 ± 0.034	$-2.22^{+0.06}_{-0.07}$ (stat.) ±0.2 (syst.)
Eri II	3	56.123845	−43.529984	19.526 ± 0.001	20.444 ± 0.001	21.298 ± 0.002	22.246 ± 0.029	1.772 ± 0.002	−1.710 ± 0.029	$-3.42^{+0.14}_{-0.14}$ (stat.) ±0.2 (syst.)
Eri II	4	56.086611	−43.541012	19.548 ± 0.001	20.498 ± 0.001	21.398 ± 0.003	22.672 ± 0.044	1.850 ± 0.003	−1.501 ± 0.044	$-2.71^{+0.09}_{-0.08}$ (stat.) ±0.2 (syst.)
Eri II	5	56.088979	−43.505809	19.660 ± 0.001	20.577 ± 0.001	21.522 ± 0.003	23.008 ± 0.030	1.862 ± 0.003	−1.397 ± 0.030	$-2.16^{+0.08}_{-0.11}$ (stat.) ±0.2 (syst.)
Eri II	6	56.084220	−43.536364	19.729 ± 0.001	20.674 ± 0.001	21.588 ± 0.004	22.902 ± 0.047	1.859 ± 0.004	−1.475 ± 0.047	$-2.57^{+0.09}_{-0.08}$ (stat.) ±0.2 (syst.)
Eri II	7	56.060979	−43.526336	19.866 ± 0.001	20.758 ± 0.001	21.637 ± 0.004	22.861 ± 0.030	1.771 ± 0.004	−1.433 ± 0.030	$-2.57^{+0.11}_{-0.11}$ (stat.) ±0.2 (syst.)
Eri II	8	56.110605	−43.545527	19.888 ± 0.001	20.770 ± 0.001	21.650 ± 0.003	22.898 ± 0.034	1.762 ± 0.003	−1.395 ± 0.034	$-2.41^{+0.11}_{-0.11}$ (stat.) ±0.2 (syst.)
Eri II	9	56.075786	−43.519993	20.126 ± 0.001	20.969 ± 0.001	21.775 ± 0.003	22.740 ± 0.034	1.649 ± 0.003	−1.508 ± 0.034	$-2.95^{+0.18}_{-0.16}$ (stat.) ±0.2 (syst.)

Note. Metallicity measurements for all stars in our sample. Statistical uncertainties on the metallicity measurements originate from photometric uncertainties, and systematic uncertainties are assigned following the investigation in §3.10. (This table is available in its entirety in machine-readable form.)

Table 3.5: Extremely Metal-poor Star Candidates

UFD	Star	R.A. (deg)	Decl. (deg)	F814W (mag)	F606W (mag)	F475W (mag)	F395N (mag)	V/I (mag)	$C_{a}HK$ (mag)	[Fe/H] (dex)
Eri II	3	56.123845	−43.529984	19.526 ± 0.001	20.444 ± 0.001	21.298 ± 0.002	22.246 ± 0.029	1.772 ± 0.002	−1.710 ± 0.029	$-3.42^{+0.14}_{-0.14}$ (stat.) ±0.5 (syst.)
Eri II	12	56.096139	−43.523451	20.193 ± 0.001	21.038 ± 0.001	21.835 ± 0.003	22.640 ± 0.048	1.642 ± 0.003	−1.658 ± 0.048	<-3.53
Eri II	13	56.085980	−43.552250	20.368 ± 0.001	21.193 ± 0.001	21.969 ± 0.003	22.798 ± 0.041	1.601 ± 0.003	−1.573 ± 0.041	$-3.36^{+0.38}_{-0.35}$ (stat.) ±0.5 (syst.)
Eri II	17	56.084077	−43.509971	20.484 ± 0.001	21.308 ± 0.001	22.104 ± 0.003	23.007 ± 0.042	1.620 ± 0.003	−1.527 ± 0.042	$-3.20^{+0.28}_{-0.33}$ (stat.) ±0.5 (syst.)
Eri II	18	56.078614	−43.541732	20.651 ± 0.001	21.468 ± 0.001	22.249 ± 0.004	23.067 ± 0.055	1.598 ± 0.004	−1.579 ± 0.055	$-3.64^{+0.27}_{+0.23}$ (stat.) ±0.5 (syst.)
Eri II	20	56.114148	−43.547555	20.791 ± 0.001	21.587 ± 0.001	22.334 ± 0.004	23.168 ± 0.035	1.543 ± 0.004	−1.480 ± 0.035	$-3.23^{+0.33}_{-0.43}$ (stat.) ±0.5 (syst.)
Eri II	22	56.070042	−43.529300	21.053 ± 0.001	21.798 ± 0.001	22.460 ± 0.003	22.979 ± 0.044	1.407 ± 0.003	−1.592 ± 0.044	<-3.24
Eri II	23	56.076370	−43.538978	21.064 ± 0.001	21.848 ± 0.002	22.527 ± 0.005	23.117 ± 0.063	1.463 ± 0.005	−1.605 ± 0.063	<-3.35
Eri II	25	56.100176	−43.539428	21.215 ± 0.001	21.990 ± 0.002	22.666 ± 0.005	23.371 ± 0.046	1.451 ± 0.005	−1.472 ± 0.046	$-3.29^{+0.38}_{-0.41}$ (stat.) ±0.5 (syst.)
Eri II	32	56.092274	−43.523353	21.449 ± 0.001	22.198 ± 0.002	22.913 ± 0.005	23.675 ± 0.062	1.464 ± 0.005	−1.434 ± 0.062	$-3.05^{+0.50}_{-0.28}$ (stat.) ±0.5 (syst.)

Note. Extremely metal-poor ([Fe/H]< -3.0) star candidates identified in our work. (This table is available in its entirety in machine-readable form.)

Table 3.6: Metal-rich ([Fe/H] > -2.0) Stars

UFD	Star	R.A. (deg)	Decl. (deg)	F814W (mag)	F606W (mag)	F475W (mag)	F395N (mag)	VI (mag)	CaHK (mag)	[Fe/H] (dex)
Eri II	11	56.105741	−43.529386	20.129 ± 0.001	20.954 ± 0.001	21.987 ± 0.003	23.548 ± 0.063	1.858 ± 0.003	−1.226 ± 0.063	$-1.99^{+0.14}_{-0.14}$ (stat.) ±0.2 (syst.)
Eri II	48	56.106782	−43.547699	21.819 ± 0.002	22.560 ± 0.002	23.211 ± 0.006	24.147 ± 0.100	1.392 ± 0.006	−1.152 ± 0.100	$-1.99^{+0.27}_{-0.25}$ (stat.) ±0.2 (syst.)
Eri II	49	56.102513	−43.533665	21.817 ± 0.002	22.565 ± 0.002	23.254 ± 0.006	24.338 ± 0.107	1.437 ± 0.006	−1.072 ± 0.107	$-1.64^{+0.31}_{-0.37}$ (stat.) ±0.2 (syst.)
Eri II	53	56.095432	−43.523738	21.883 ± 0.002	22.611 ± 0.002	23.295 ± 0.006	24.267 ± 0.103	1.412 ± 0.006	−1.146 ± 0.103	$-1.91^{+0.23}_{-0.29}$ (stat.) ±0.2 (syst.)
Eri II	63	56.091969	−43.509073	22.349 ± 0.002	23.058 ± 0.003	23.707 ± 0.008	24.673 ± 0.102	1.358 ± 0.008	−1.071 ± 0.102	$-1.72^{+0.32}_{-0.34}$ (stat.) ±0.2 (syst.)
Eri II	64	56.078675	−43.556979	22.408 ± 0.002	23.116 ± 0.003	23.739 ± 0.009	24.647 ± 0.108	1.331 ± 0.009	−1.089 ± 0.108	$-1.81^{+0.38}_{-0.38}$ (stat.) ±0.2 (syst.)
Eri II	68	56.089733	−43.506056	22.603 ± 0.002	23.310 ± 0.004	23.915 ± 0.008	24.814 ± 0.102	1.312 ± 0.008	−1.069 ± 0.102	$-1.78^{+0.35}_{-0.39}$ (stat.) ±0.2 (syst.)
Eri II	69	56.113460	−43.540911	22.595 ± 0.002	23.296 ± 0.003	23.912 ± 0.008	24.771 ± 0.090	1.317 ± 0.008	−1.116 ± 0.090	$-1.99^{+0.31}_{-0.41}$ (stat.) ±0.2 (syst.)
CVn II	21	194.302909	34.324379	22.284 ± 0.003	22.902 ± 0.003	23.597 ± 0.029	24.701 ± 0.083	1.313 ± 0.029	−0.866 ± 0.088	$-1.18^{+0.40}_{-0.44}$ (stat.) ±0.2 (syst.)
CVn II	26	194.310078	34.320700	22.754 ± 0.004	23.354 ± 0.004	24.041 ± 0.030	25.150 ± 0.103	1.287 ± 0.030	−0.822 ± 0.107	$-1.13^{+0.44}_{-0.48}$ (stat.) ±0.2 (syst.)

Note. Metal-rich ([Fe/H] > -2.0) stars identified in our work.
(This table is available in its entirety in machine-readable form.)

Chapter 4

Stellar Metallicities and Gradients in the Isolated, Quenched Low-Mass Galaxy Tucana

4.1 Overview

We measure the metallicities of 374 red giant branch (RGB) stars in the isolated, quenched dwarf galaxy Tucana using Hubble Space Telescope (HST) narrow-band (F395N) Calcium H & K (CaHK) imaging. Our sample is a factor of ~ 7 larger than what is available from previous studies. Our main findings are: (i) A global metallicity distribution function (MDF) with $\langle[\mathrm{Fe/H}]\rangle = -1.55^{+0.04}_{-0.04}$ and $\sigma_{[\mathrm{Fe/H}]} = 0.54^{+0.03}_{-0.03}$; (ii) A metallicity gradient of -0.54 ± 0.07 dex R_e^{-1} (-2.1 ± 0.3 dex kpc^{-1}) over the extent of our imaging (~ 2.5 R_e), which is steeper than literature measurements. Our finding is consistent with predicted gradients from the publicly-available FIRE-2 simulations, in which bursty star formation creates stellar population gradients and dark matter cores; (iii) Tucana's bifurcated RGB has distinct metallicities: a blue RGB with $\langle[\mathrm{Fe/H}]\rangle = -1.78^{+0.06}_{-0.06}$ and $\sigma_{[\mathrm{Fe/H}]} = 0.44^{+0.07}_{-0.06}$, and a red RGB with $\langle[\mathrm{Fe/H}]\rangle = -1.08^{+0.07}_{-0.07}$ and $\sigma_{[\mathrm{Fe/H}]} = 0.42^{+0.06}_{-0.06}$; (iv) At fixed stellar mass, Tucana is more metal-rich than MW satellites by ~ 0.4 dex, but its blue RGB is chemically comparable to the satellites. Tucana's MDF appears consistent with star-forming isolated dwarfs, though MDFs of the latter are not as well-populated; (v) $\sim 2\%$ of Tucana's stars have [Fe/H] < -3 and 20% [Fe/H] > -1. We provide a catalog for community spectroscopic follow-up.

This chapter has been adapted from Fu, Weisz et al. (2024), which was published

in the Astrophysical Journal. This chapter was coauthored by the following individuals, and is included in this dissertation with their permission: Daniel R. Weisz, Else Starkenburg, Nicolas Martin, Francisco J. Mercado, Alessandro Savino, Michael Boylan-Kolchin, Patrick Côté, Andrew E. Dolphin, Mario L. Mateo, Jenna Samuel, Nathan R. Sandford.

4.2 Introduction

Environment plays a pivotal role in regulating dwarf galaxy star formation. This theoretical understanding emerges from the empirical morphology-density relation that has been established over decades' worth of observations (e.g., [81], [111], [32], [203], [34], [105]), where star-forming (e.g. gas-rich and/or with Hα emission) dwarf galaxies are found in the field far from massive hosts, and quenched (e.g. gas-deficient) dwarf galaxies tend to be satellites.

As part of the same theoretical and empirical landscape, quenched, low-mass field dwarf galaxies, exceptions to the rule, are quite rare. The origins of the few that *do* exist are not well-understood. Hypotheses thus far have ranged from classifying them as backsplash galaxies that interacted with a more massive host in the distant past (e.g., [298], [259]), to being the product of complicated interactions from a reionizing UV background [240], to forming instead from interactions with the cosmic web [29], but detailed studies are needed to assess the validity and prevalence of various processes.

Alongside the Cetus dSph, the Tucana dSph is one of two quenched field dwarf galaxies known in the Local Group, with present-day distances of $\sim$ 877 and $\sim$ 1345 kpc from the MW and M31 respectively [173], and sufficiently nearby for resolved stellar population studies. Its distance from either of the LG spiral galaxies suggests that it may have evolved largely independently of a more massive host, and therefore is not subject to processes such as ram pressure stripping and tidal fields. Aside from its rare status as a quenched field dwarf galaxy, Tucana is also peculiar among analog dwarf galaxies, as its color-magnitude diagram (CMD) contains multiple distinct morphological overdensities (e.g., bifurcated red giant branch, horizontal branch) that are not as conspicuous in other LG dwarf galaxies with even more extended SFHs (e.g., [217], [264]).

In all of these cases, the stellar metallicity distribution function (MDF) of a galaxy is essential to studies decoding the astrophysics driving its present-day features (e.g., pre-enrichment, gas accretion). Detailed observations have been conducted in more LG dwarf galaxies (e.g., [166], [313], [235], [302]), but similarly detailed studies have been challenging in distant dSphs such as Tucana due to few stars sufficiently bright

for efficient spectroscopic observations. The three spectroscopic studies of Tucana to-date, [91, VLT/FORS2], [115, VLT/FLAMES+GIRAFFE], and [296, henceforth T20, VLT/FORS2], have yielded 52 stars with metallicity measurements down to $g \sim 23.5$ mag. Additional stellar metallicity measurements in Tucana are needed to fully sample its MDF (e.g., extent of the tails, skewness) and accurately infer the astrophysical picture during its star-forming epoch. One approach to expand the sample, which we take in this paper, is to measure metallicities of even fainter stars using a well-tested photometric metallicity method.

Photometric metallicity measurements based on observations of the metallicity-sensitive, near-UV Ca H&K lines have been a longstanding technique used in studies of resolved stellar populations (e.g., [293], [24], [155], [247]). This technique has also seen increasing use in recent years to conduct studies of LG dwarf galaxies and the Milky Way (e.g., [291], [56], [119], [188], [97], [200]). Building off this legacy, we have conducted an HST imaging program to measure photometric metallicities in RGB stars of Tucana as faint as F475W$\sim$25 mag in order to measure a well-populated MDF, establish empirical trends (e.g., gradients), and provide insight into its formation pathways.

This paper is organized as follows. In §4.3, we present our observations and our stellar member selection process. In §4.4, we describe our methods for measuring individual metallicities as well as MDF summary statistics. In §4.5 we present our MDF measurement results, as well as spatial metallicity trends and metallicity as a relation to stellar populations. In §4.6, we discuss the implications of our results. We conclude in §4.7.

4.3 Observations

Observations and Data Reduction

We obtain new WFC3/UVIS $F395N$ imaging for Tucana as part of HST GO-16226 (PI: Fu), which has targeted both Cetus and Tucana. Imaging for Tucana was taken between July 27, 2022 and July 31, 2022 over the course of 12 orbits. We integrated the narrow-band filter for a total of 32,268s, with the target depth of achieving $S/N > 10$ at the horizontal branch (HB), $F475W \sim 25$ mag. We perform dithers to remove hot pixels and reject cosmic rays, following the dither pattern from HST GO-10505 (PI: Gallart). We also require that the main science field overlap with archival broadband $F475W$ and $F814W$ imaging from HST GO-10505Our metallicity inference technique is analogous to those used by the *Pristine* narrow-band CaHK MW survey (e.g., [291], [200]), and we require additional broadband filters to

provide temperature information. In the *Pristine*-like color space constructed using *HST* filters, $(F475W - F814W)$ vs. $F395N - F475W - 1.5 * (F475W - F814W)$, stars of different metallicity cleanly separate (e.g. [96], [97]) and enable our principal science case. Additionally, we impose orientation requirements so that our parallel ACS/WFC exposures, taken in $F475W$ and $F814W$, overlap with parallel fields targeted in HST GO-10505. The parallel fields were designed to target scientifically valuable areas in Tucana's galactic halo; we defer analysis of data for this ancillary science case to a future publication.

We perform point-spread function (PSF) photometry simultaneously on individual $F395N$, $F475W$, and $F814W$ `flc` images using DOLPHOT ([78], [76]). We then apply a quality cut on the catalog by requiring $S/N > 5$, $\text{sharp}^2 < 0.3$ and crowd < 1 in $F475W$ and $F814W$. We only cull our catalogs using the broadband filters, as they are deeper and therefore more efficient in selecting quality sources.

Figure 4.1 shows the footprint of our WFC3 imaging compared to the on-sky extent of the galaxy. Small black dots are stars that pass the culling criteria. The blue star shows the center of the galaxy, and the red ellipses trace 1, 2, and 3 R_e of the galaxy (Table 4.1). Our photometry span ~ 2.5 R_e of the galaxy, allowing us to characterize its spatial metallicity properties in addition to a global MDF (see §4.5).

The left panel of Figure 4.2 shows the resulting broadband CMD for Tucana, constructed from stars that pass the above cuts. Stars with $F395N S/N > 3$ are color-coded by their respective narrow-band S/N. The right panel shows the narrow-band CMD of Tucana, overplotted with average narrow-band photometric uncertainties as a function of $F395N$. The high concentration of stars running along the diagonal line faintward of $F395N \sim 25.75$ mag are HB stars.

Member Selection

We determine our sample of Tucana member stars by first selecting stars whose colors are consistent with being on the RGB. Most of our stars are too faint to be observed spectroscopically, so we rely primarily on photometric criteria to select the large majority of our sample. In general, we do not expect contamination to have a major impact on our results: Due to the small HST WFC3 field of view, we do not expect enough MW halo stars to fall within it to significantly impact our final measured MDFs [97]. Additionally, there are no known MW substructures in the vicinity of Tucana found in spectroscopic surveys of the same region of the sky ([91], [115], [296]) that could introduce contamination at a level above the background expectations from the MW halo.

One selection effect in our data is that at a given magnitude, we will tend to preferentially lose metal-rich (MR) stars in a simple S/N quality cut because more

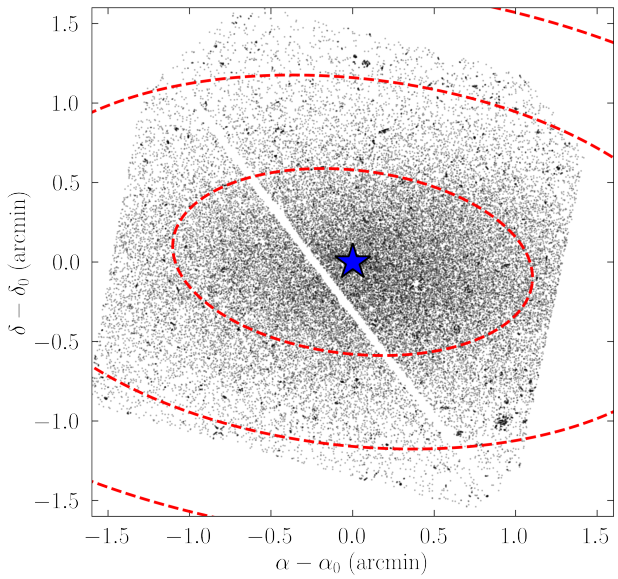


Figure 4.1: FoV of our HST WFC3 $F395N$ imaging compared to the center (blue star) and the 1, 2, and 3 half-light radii contours of Tucana (red ellipses). Small black points are stars which pass our S/N selection criteria. Our data enable stellar metallicity measurements within ~ 2.5 R_e of the galaxy, allowing us to measure a global MDF as well as characterize spatial metallicity trends.

MR stars tend to have lower S/N in $F395N$ as a result of more absorption in the filter. This is similar to the fixed magnitude effect for spectra, e.g. as discussed by [191] in the context of the LMC. We also observe this impact in the left panel of Figure 4.2, where, for example, at $F475W \sim 24$, stars on the bluer side of the RGB (which tend to be more metal-poor) have higher S/N than stars on the redder side of the RGB. Thus, for the S/N quality cut, we require that stars in our sample have S/N greater than 7 in $F395N$ as opposed to the criteria of 10 used in previous Ca H&K narrow-band studies (e.g., [97]). This selection criterion allows us to include most stars brighter than $F475W \sim 24$ mag.

For brighter stars in the resulting sample, we then do an additional level of membership vetting by cross-matching our catalog with the datasets analyzed in [296], which include a re-analysis of Tucana observations from [91] and [115]. None of the overlapping stars that our catalog has with the spectroscopic studies were ruled out as Tucana radial velocity non-members.

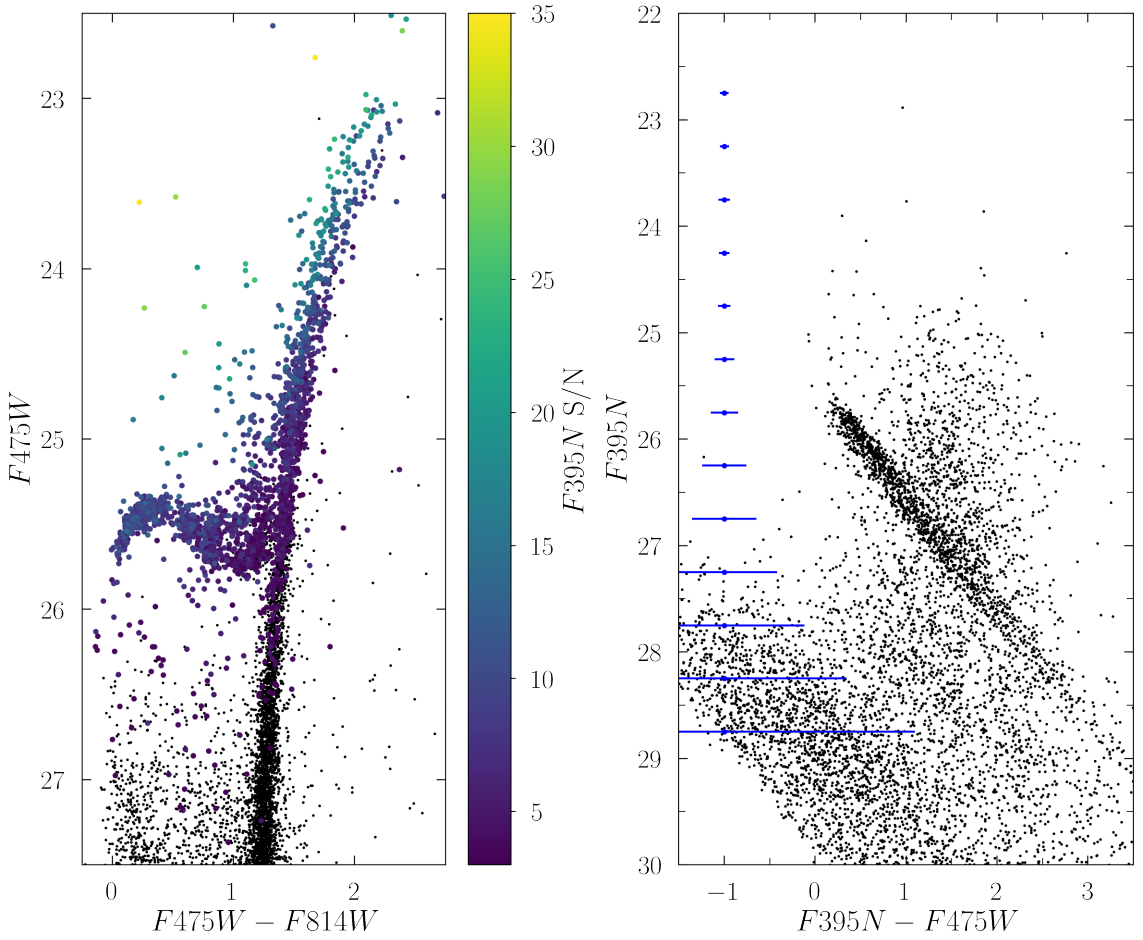


Figure 4.2: **Left:** The broadband CMD of Tucana. To demonstrate the depth of the narrow-band data, we color code stars with $F395NS/N > 3$ by their narrow-band S/N value. Our data reach $F395NS/N \sim 10$ at about $F475W$ 24.5 mag, enabling stellar metallicity measurements for stars at least 1 mag fainter than the brightness limit of studies from current ground-based instruments. **Right:** Narrow-band $F395N$ CMD of Tucana. The blue error bars show the typical uncertainty as a function of $F395N$. Uncertainties in $F395N - F475W$ color are driven by uncertainties in $F395N$. The high concentration of stars running along the diagonal line faintward of $F395N \sim 25.75$ mag are HB stars. Stars above the diagonal line are the bright RGB stars that ultimately comprise our analysis sample.

Table 4.1: Tucana Characteristics

Parameter	**Value**	**Reference**
R.A. (deg)	340.45667	[173]
decl. (deg)	-64.41944	[173]
Ellipticity	0.48 ± 0.03	[261]
P.A. (deg)	97 ± 2	[261]
R_e (arcmin)	0.8 ± 0.1	[261]
Luminosity (Log $L_\odot$)	5.58 ± 0.01	[227]
$E(B-V)$	0.0268	[267]
$(m-M)_0$	24.73 ± 0.03	[227]
$D_\odot$ (kpc)	886 ± 13	[227]
R_e in WFC3 FoV	3.38	This work
F475W exp. time (s)	34,560	This work
F814W exp. time (s)	30,976	This work
F395N exp. time (s)	32,268	This work

Note. Observational characteristics of Tucana. Information below the horizontal line describes the HST observations used in this work. We use broadband imaging from HST GO-10505 (PI: Gallart). All the HST images used for this work can be found at the following MAST DOI: `10.17909/8974-w227`.

Artificial Star Tests

We assess the photometric uncertainties for stars in our sample by running artificial star tests (ASTs). ASTs involve inserting stars of known magnitudes (i.e., in $F395N$, $F475W$, and $F814W$) into the corresponding *HST* `flc` images, and attempting to recover their measurements using the same DOLPHOT PSF-fitting procedure used to obtain the original photometric reduction. By running large numbers of ASTs, we build up the statistics necessary to calculate the photometric uncertainty (scatter between the difference in recovered and input magnitudes) and bias (systematic offsets in the difference in recovered and input magnitudes). As we measure metallicities for individual stars, we do not leverage the completeness information in the ASTs that are used for population-level inferences in e.g. SFH studies.

Following [97], we generate ASTs for each potential member star in Tucana that passes our initial color cut. We center the ASTs for each star within 0.2 mag of its $F475W$ magnitude, and require that the input ASTs fall within the color space of $0.7 < F475W - F814W < 2.5$ and $-2.0 < CaHK < -0.2$. The 10,000 ASTs we run

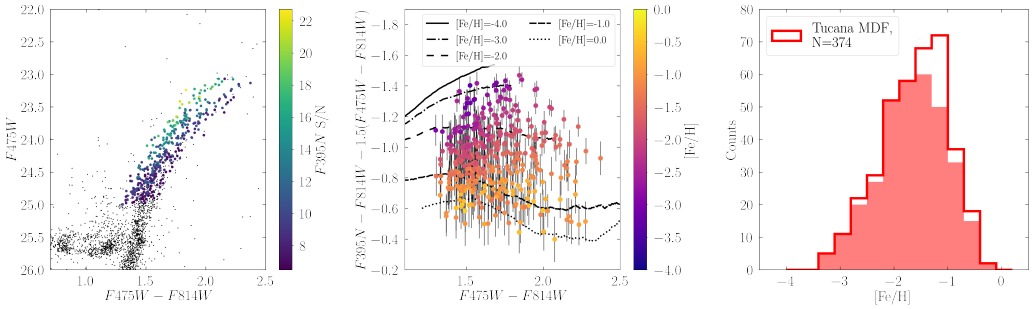


Figure 4.3: **Left:** Selection of Tucana stars along RGB and their $F395N$ S/N. **Center:** Location of member stars on *Pristine*-like CaHK space. Overplotted are mono-metallic CaHK tracks convolved using the AST error profile of a star at $F475W = 24.14$, the median brightness of stars in our sample. The stars are color-coded by their inferred metallicity, which can also be upper limits on the metal-poor (MP) end and lower limits on the metal-rich (MR) end. Reasons why the color-coding of the stars does not perfectly follow the trend implied by the mono-metallic tracks can be attributed to the reporting of measurement limits for $\sim 50\%$ of stars more MR than [Fe/H] $= -1.0$ (e.g. §4.5), as well as the varied S/N of stars blueward of $F475W - F814W = 2.0$, which span about 2 magnitudes in brightness. **Right:** Resulting MDF of Tucana. Empty histograms represent stars for which we were only able to constrain either an upper limit (on the MP end) or a lower limit (on the MR end). Our data has enabled metallicity measurements for 374 stars down to $F475W \sim 25$ mag.

are distributed to cover all the models in the *Pristine*-like Ca H&K color space that we will use to measure individual metallicities.

In §4.4, we discuss how we incorporate the results of the ASTs into our individual metallicity inference procedure.

4.4 MDF Measurements

Individual Metallicity Measurements

Our metallicity measurement method largely follows that from [97]. For fitting the Ca H&K data of individual stars in our sample, we adopt a fitting technique that is statistically similar to the long-established CMD star formation history modeling approach [75]. Here, we briefly describe this process, and provide updates made to

the method to better describe the case of a galaxy with a SFH more extended than a UFD.

We first construct the equivalent of a Hess diagram (i.e., a density map) in the *Pristine*-like color space shown in the center panel of Figure 4.3 using bins of 0.025 by 0.025 mag. We then convolve our synthetic stellar population models, which have a range of metallicities, by the uncertainty and bias profile as set by our ASTs. Afterwards, we infer stellar metallicities by using a Poisson likelihood function to compare the overlap of an individual star's CaHK color-color properties with that of model CaHK tracks of various metallicities that have been corrected for observational effects following the results of the ASTs.

One notable departure from the [97] method is that here we account for the impact of varying [α/Fe] over the range of metallicities considered. In dwarf galaxies of comparable luminosity to Tucana, the expectation is that there will be variations in [α/Fe] due to its extended SF ([217], [264]): specifically, the decline of [α/Fe] values at higher metallicities due to the delayed onset of Type Ia SNe (e.g., [299], [110]). We address these issues in our choice of priors for the metallicity inference process.

We begin by using soon-to-be-released v2 models from the MESA Stellar Isochrones and Tracks (MIST) isochrone suite ([79], [58]). We choose this set of models over other available models because their grid calculates models for the largest range of metallicities ([Fe/H] = -4.0 to $+0.5$) and over a range of [α/Fe] enhancements ([α/Fe] = $+0.0$ to $+0.4$). We obtained metallicity grids generated for populations with [α/Fe] = $+0.0$, [α/Fe] = $+0.2$, and [α/Fe] = $+0.4$ to capture the range of α enhancements observed in dwarf galaxies (e.g., [301]). The spacing between the metallicity models is 0.05 dex and range from [Fe/H] = -4.0 up to [Fe/H] = $+0.0$.[1] We then convolve these synthetic models through observational effects, which are (1) dust corrections using the extinction values from [267] and filter-specific coefficients from MIST, and (2) bias and error effects as characterized by the results of our ASTs described in §4.3.

To compare the Hess-like diagram of individual stars to our resulting models, we adopt a Poisson likelihood function with the form:

$$\log L = \sum_{m_i \neq 0} d \ln m_i - m_i - \ln(d_i!), \tag{4.1}$$

[1]MIST generates models up to [Fe/H] = $+0.5$, but past [Fe/H] = $+0.0$, the CaHK models are unable to distinguish between stars of different metallicity. We therefore truncate our grid at $+0.0$. In practice, we can only obtain lower limit constraints for stars that fall at this boundary.

where m_i are the number of counts in the model bin, and d_i is the data in each bin.

Since there are no constraints on [α/Fe] abundances in Tucana from currently-available spectroscopy, we adopt priors to account for the impact of varying [α/Fe] across metallicity by referring to observed trends for classical dwarf galaxies (e.g., [301]). Our priors are as follows: (1) For metallicity measurements below [Fe/H] $<$ -2.0, we assume [α/Fe] $= +0.4$. (2) For metallicity measurements above [Fe/H] $>$ -1.0, we assume [α/Fe] $= +0.0$. (3) For the intermediate range between -2 $<$ [Fe/H] < -1, we use the [α/Fe] $= +0.2$ models to infer metallicities. This choice is to approximate the knee-to-ankle transition observed in [α/Fe] vs. [Fe/H], although at fixed [Fe/H], there is also a scatter in [α/Fe] of $\sim$ 0.2 dex. As quantified in [96], the difference between inferring individual metallicities assuming [α/Fe] $= +0.4$ vs. [α/Fe] $= +0.0$ is to shift the measurement by about 0.2 dex in the metal-rich direction with lower [α/Fe], so the systematic measurement uncertainty we adopt accounts for uncertainty for scatter in [α/Fe] at fixed metallicity and uncertainty in the form of the α-metallicity relation. In Appendix 4.8, we explore the impact that assuming a different form for the α-to-Fe knee pattern has on our resulting MDF.

We then sample the resulting posterior distribution using `emcee` [90]. We initialize 50 walkers and run the chain for 10,000 steps, with a burn-in time of about 50 steps per star. We monitor convergence using the Gelman-Rubin statistic (GR; [109])

Subsequent inferences to calculate MDF summary statistics and metallicity trends (e.g., §4.5) assume symmetric, Gaussian uncertainties on individual star metallicity measurements. In reality, this is not the case because the spacing between mono-metallic CaHK tracks are uneven and because there are stars for which we can only constrain lower or upper limits (e.g., see Figure 4.4). We thus follow the methods in [97] to make the following adjustments to our measurements for population-level inferences:

For stars whose posterior distributions are well-constrained enough to measure median and 68% confidence interval uncertainties, we average the uncertainties and add them in quadrature with the 0.2 dex systematic metallicity uncertainty for RGB stars quantified in [97] to arrive at the final measurement.

For posterior distributions that only constrain either a lower or an upper limit, we adopt measurements that are defined by the median and the 68% confidence interval of the posterior distributions. For stars with upper limits below -3 (i.e., an extremely metal-poor star candidate), we add uncertainties in quadrature with a systematic uncertainty of 0.5 dex to account for the reduced sensitivity of CaHK at low metallicities, though these stars are rare in our sample to begin with. For all other cases, we add the uncertainties in quadrature with their corresponding systematic uncertainty, which is already likely to be small in comparison to the

posterior distribution-defined uncertainties.

MDF Summary Statistics

In this section, we describe the procedure for calculating summary statistics of Tucana's MDF for comparison to the literature.

First, we measure the mean and dispersion of the MDF of Tucana by assuming that it is characterized by a single Gaussian distribution. We follow community convention by inferring the MDF using a two-parameter Gaussian likelihood function used by [311] and subsequent studies of Local Group dwarf galaxies (e.g. [180], [274]):

$$\begin{aligned} \log L = &-\frac{1}{2}\sum_{i=1}^{N}\log(\sigma^2_{\mathrm{[Fe/H]}} + \sigma^2_{\mathrm{[Fe/H]},i}) \\ &-\frac{1}{2}\sum_{i=1}^{N}\frac{(\mathrm{[Fe/H]}_i - \langle\mathrm{[Fe/H]}\rangle)^2}{\sigma^2_{\mathrm{[Fe/H]}} + \sigma^2_{\mathrm{[Fe/H]},i}}, \end{aligned} \tag{4.2}$$

where $\langle\mathrm{[Fe/H]}\rangle$ and $\sigma_{\mathrm{[Fe/H]}}$ are the mean metallicity and metallicity dispersion of the galaxy, and $\mathrm{[Fe/H]}_i$ and $\sigma_{\mathrm{[Fe/H]},i}$ are the metallicity and metallicity uncertainty for an individual star.

We adopt a uniform prior on the mean and require it remain within the range set by the most metal-poor and metal-rich stars in Tucana. We also require that the dispersion be greater than or equal to 0. We use `emcee` to sample the posterior distribution, initializing 50 walkers for 10,000 steps. The autocorrelation time is about 50 steps, and we use the corresponding GR statistic to assess convergence.

Next, we compute statistics that quantify higher-order features of the MDF, such as skew and kurtosis, by employing a Monte Carlo method. Similar to the procedure for measuring the mean and dispersion, we assume Gaussian uncertainties on individual metallicity measurements. We use this uncertainty profile to construct 10,000 realizations of the MDF, from which we measure skew and kurtosis. The final measurements we report correspond to the median of the distribution of skew and kurtosis measurements, with lower and upper uncertainties respectively set by the 16th and 84th percentile.

4.5 Results

In this section, we present the results of our MDF measurements. The center panel of Figure 4.3 presents the position of our member stars in CaHK-space, color-coded

by their inferred metallicity. The right panel of the same figure presents the overall MDF. Table 4.2 presents the MDF summary statistics, along with the sections in which they are discussed. We begin our presentation of the results by discussing individual measurements in §4.5 and remark on the overall shape of our MDF in §4.5. In §4.5, we present our measurement of radial metallicity trends in Tucana, and in §4.5, we present the distribution of our metallicity measurements along Tucana's bifurcated RGB. We present our individual measurements as part of Appendix 4.10 in Tables 4.4, 4.5, and 4.6, corresponding to the entire sample, the EMP ([Fe/H] $<$ -3.0) star candidates, and MR ([Fe/H] > -1.0) stars respectively.

Individual Measurements

The center panel of Figure 4.3 presents the distribution of stars in our sample in CaHK color space, color-coded by their final inferred metallicity, some of which reflect upper (on the MP end) or lower (on the MR end) limits. Overplotted are a set of representative AST-convolved CaHK mono-metallic tracks for a star at $F475W \sim 24.14$, which is the median brightness of stars in our sample. Following the intuition guided by the tracks, the metallicity of stars increases with redder CaHK, but there are some discrepancies to this trend on the MR end of the MDF. This is because stars bluer than $F475W - F814W = 2.0$ occupy a range of luminosities that is not monotonic in CaHK space. As described in [97], the bias effects captured by the ASTs are larger for faint stars, and as a result, a faint star would have an inferred metallicity that is more MP than the inferred metallicity of a brighter star occupying a similar position in CaHK color space.

Figure 4.4 shows examples of individual metallicity posterior distributions to illustrate the nature of our measurements. We have selected three stars that represent the range of posteriors in our fits. As in [97], most posterior distributions are well within the metallicity limits bounded by our grid and have well-defined peaks. An example is shown in the top right panel of Figure 4.4. Stars with constrained posterior distributions are often at intermediate metallicities ranging from [Fe/H] $= -2.5$ to [Fe/H] $= -1.0$.

Some posterior distributions are truncated at either the MR or the MP end, corresponding to the respective limits of our metallicity grids. We designate measurements as constrained if there is a clear peak in the posterior distribution and if the 1σ photometric uncertainties of the star fall within the grid. These types of truncated posterior distributions are similar to the ones presented in Figure 5 of [97], so we do not include them here.

Finally, there are stars on the extremes of the MDF for which we can only constrain either a lower or an upper limit. These stars are at the edge of our grid, and

Table 4.2: Tucana MDF Characteristics

Feature	**Parameter**	**Value**	N	**Reference in Thesis**
Overall MDF	[Fe/H]	$-1.55^{+0.04}_{-0.04}$	374	§4.5
	$\sigma_{\rm [Fe/H]}$	$0.54^{+0.03}_{-0.03}$	···	···
	Skew	$-0.16^{+0.11}_{-0.11}$	···	···
	Kurtosis	$-0.02^{+0.28}_{-0.21}$	···	···
Gradient within $2.5\,R_e$	$\nabla_{\rm [Fe/H]}$ (dex R_e^{-1})	-0.54 ± 0.07	374	§4.5
	$\nabla_{\rm [Fe/H]}$ (dex arcmin^{-1})	-0.57 ± 0.1	···	···
	$\nabla_{\rm [Fe/H]}$ (dex kpc^{-1})	-2.1 ± 0.3	···	···
Inner R_e	[Fe/H]	$-1.35^{+0.05}_{-0.05}$	203	§4.5
	$\sigma_{\rm [Fe/H]}$	$0.51^{+0.04}_{-0.04}$	···	···
	Skew	$-0.2^{+0.15}_{-0.16}$	···	···
	Kurtosis	$-0.04^{+0.44}_{-0.31}$	···	···
$1\,R_e < R < 2\,R_e$	[Fe/H]	$-1.77^{+0.05}_{-0.05}$	160	§4.5
	$\sigma_{\rm [Fe/H]}$	$0.45^{+0.05}_{-0.05}$	···	···
	Skew	$-0.02^{+0.18}_{-0.19}$	···	···
	Kurtosis	$0.06^{+0.41}_{-0.30}$	···	···
$2\,R_e < R \lesssim 2.5\,R_e$	[Fe/H]	$-2.22^{+0.21}_{-0.22}$	11	§4.5
	$\sigma_{\rm [Fe/H]}$	$0.54^{+0.27}_{-0.28}$	···	···
	Skew	$-0.19^{+0.44}_{-0.44}$	···	···
	Kurtosis	$-0.80^{+0.68}_{-0.43}$	···	···
Red RGB	[Fe/H]	$-1.08^{+0.07}_{-0.07}$	69	§4.5
	$\sigma_{\rm [Fe/H]}$	$0.42^{+0.06}_{-0.06}$	···	···
	Skew	$0.08^{+0.18}_{-0.18}$	···	···
	Kurtosis	$-0.70^{+0.34}_{-0.23}$	···	···
	$\nabla_{\rm [Fe/H]}$ (dex R_e^{-1})	-0.42 ± 0.14	···	···
Blue RGB	[Fe/H]	$-1.78^{+0.06}_{-0.06}$	103	§4.5
	$\sigma_{\rm [Fe/H]}$	$0.44^{+0.07}_{-0.06}$	···	···
	Skew	$0.21^{+0.21}_{-0.20}$	···	···
	Kurtosis	$0.02^{+0.39}_{-0.31}$	···	···
	$\nabla_{\rm [Fe/H]}$ (dex R_e^{-1})	-0.62 ± 0.11	···	···

Note. Summary of metallicity properties of Tucana' s MDF from this work. For each property, we include the number of stars used in the calculation and the sections where these results are presented and discussed. The number of stars in the blue and red RGBs do not add up to the total number of stars in our sample because we include an additional magnitude cut in our selection.

their uncertainties overlap with their respective extreme ends of the grid to permit constraint using the MCMC procedure. We include examples of lower and upper limit posterior distributions in the lower left and lower right panels of Figure 4.4 respectively.

In general, posterior distributions at the MR end tend to be broader than the posterior distributions for measurements at intermediate metallicities due to (1) The MR stars having lower S/N on average than the MP stars at a given magnitude, and (2) The CaHK tracks having less discriminatory power over different metallicities past [Fe/H] $= -0.5$.

Next, we compare our measurements to literature metallicities from T20. T20 is the most comprehensive spectroscopic study of Tucana so far. They obtain new observations of Tucana using VLT/FORS2, targeting the near-IR range covering the Ca II triplet lines, and derive metallicities based on the [289] CaT EW calibration. Alongside their new data, they also analyze previous spectra of Tucana RGB stars from [91] (VLT/FORS2) and [115] (VLT/FLAMES/GIRAFFE). Metallicity measurements were made from the new dataset of [296], referred to in the paper as P91, and from the [91] dataset, referred to in the paper as P69. Between the P91 and P69 datasets, we have the largest number of stars in common with the P91 data because its observations are more centrally concentrated on Tucana and have more overlap with our FoV.

We present our comparisons with T20 in Figure 4.5. The left panel shows where our stars are located on the HST CMD within our WFC3 FoV, as well as where the stars have also been observed with spectroscopy. The center panel of Figure 4.5 shows 1-1 comparisons between our measurements and those of T20. In total, we have 35 stars in common with this study, with 24 that have metallicity measurements for which we can make direct comparisons. Among the 24 stars, one is a variable star, rendering its CaHK metallicity unreliable[2], so we exclude it from comparison. In total we have 23 stars for metallicity comparisons with T20. The measurements show a strong correlation and are in agreement at $\sim 1\ \sigma$ for constrained measurements (filled circles).

To more broadly understand the reliability of CaHK, we now combine all HST CaHK measurements with the literature in Figure 4.6. We compare photometric stellar metallicity measurements using *HST* narrow-band CaHK imaging (UFDs Eri II and Grus I, [96], [97]; Tucana, this work) against measurements of the same stars made using the CaT EW calibration from ground-based spectroscopy (e.g., [180],

[2][200] and references therein discuss how the metallicity of a star can be erroneously inferred if the photometry used to calculate its CaHK color index are taken at different points in its variable phase. As available data are insufficient for characterizing the variability cycle of this star, resolving this issue is beyond the scope of our work.

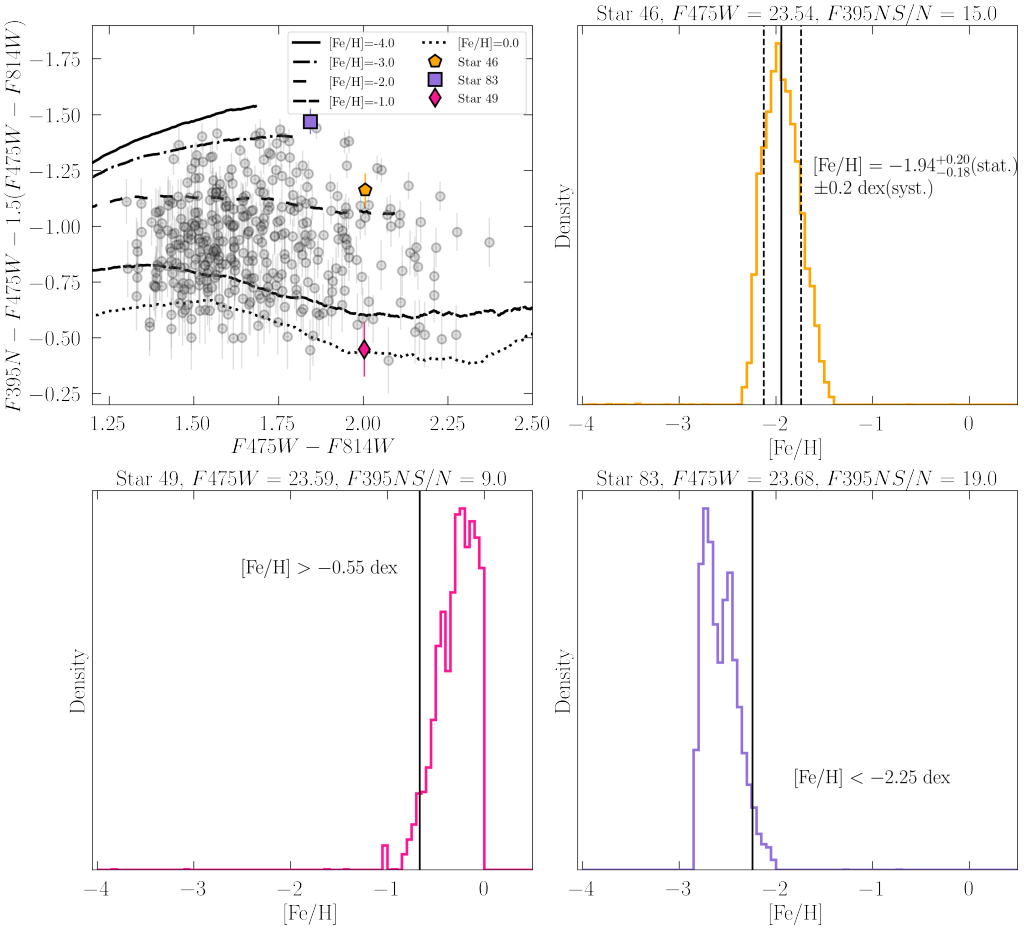


Figure 4.4: Example posterior distributions for examples of stars with a well-constrained measurement (90% of our sample), an upper limit constraint (1% of our sample), and a lower limit constraint (9% of our sample), and their corresponding positions in CaHK color-color space, as well as their corresponding summary statistic. The AST-convolved tracks plotted here are the same as the ones in Figure 4.3.

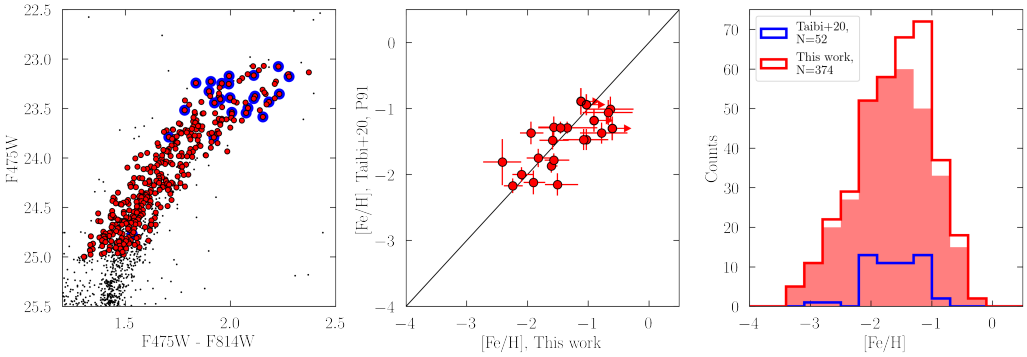


Figure 4.5: Comparing our metallicity measurements to the most comprehensive ground-based CaT EW spectroscopic study of Tucana to-date [296, VLT/FORS2]. **Left:** HST broadband CMD that shows our stars (red), the stars we have in common with [296] (blue). **Center:** One to one comparison of our metallicity measurements with the measurements that we have in common with [296]. **Right:** Overall MDF comparisons between our metallicity measurements with the MDF from [296]. Our imaging technique permits recovery of metallicities at a similar level of fidelity to state-of-the-art ground-based spectroscopic calibrations, with vastly better sampling along the LF of Tucana to fill out the tails of the MDF.

[296], [55]), with the usual caveats that the CaT methods shown here are heterogeneous (e.g., different calibrations, data quality). Additionally, our CaHK measurement uncertainties reported here also account for systematic uncertainty introduced, e.g., by model and abundance uncertainty ([97]), whereas the measurements reported from CaT EW measurements in these studies include only statistical uncertainties, not ones that may be introduced from different CaT EW calibrations (e.g. [289], [50]).

In any case, these measurements show remarkably broad agreement over a large range of metallicities with the long-standing CaT EW method for measuring stellar metallicities in RGB stars of LG dwarf galaxies. Among the constrained measurements, there is no systematic offset, and they are on average within $\sim 1.2\ \sigma$ agreement; the intrinsic dispersion in this relation is $\sim 0.3\ \sigma$. A clear takeaway from this comparison is that CaHK imaging provides a robust approach to constructing a large samples of reliable, resolved star metallicities at magnitudes that are often inaccessible to any other current facility. We provide all of our individual measurements in Table 4.4.

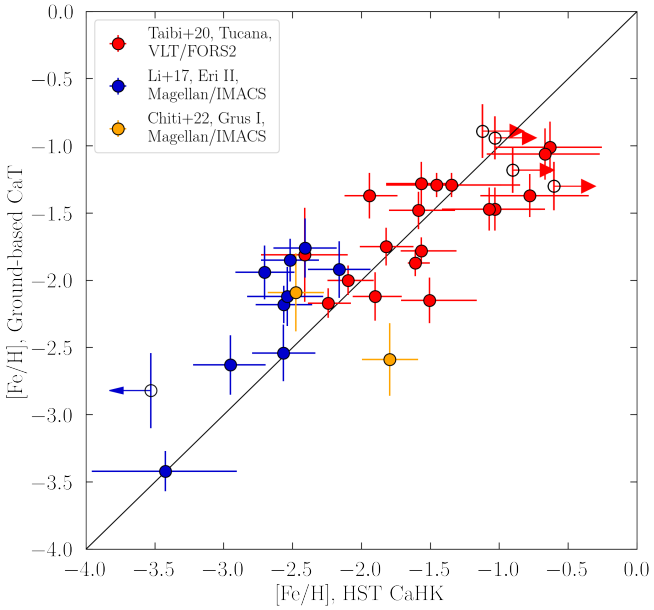


Figure 4.6: Comparing metallicity measurements made using *HST* CaHK narrow-band photometry (UFDs Eri II, Grus I, [96], [97]; Tucana, this work) against those made using ground-based spectroscopy relying on the CaT EW calibration ([180], [296], [55]). We include a one-to-one line for visual reference. The measurements show remarkable agreement, and demonstrate that CaHK narrow-band imaging is a competitive method for measuring stellar metallicities compared with the most commonly-used method for Local Group dwarf galaxies.

Overall MDF

We present our global MDF of Tucana in the right panel of Figure 4.3, constructed from 374 stars. The MDF spans a metallicity range from [Fe/H] = −3.5 to [Fe/H] = −0.5. 60% of the stars are between [Fe/H] = −2.0 and [Fe/H] = −1.0. We identify 8 stars with [Fe/H] < −3.0 as extremely metal-poor (EMP) star candidates. On the MR end, [Fe/H] > −1.0, we identify 76 stars, with 37 of them being lower limits. The MDF may be slightly skew negative as it visually appears to have a slightly longer MP tail, though this may also be in part due to larger uncertainties for MP stars. We present our EMP candidates and MR stars in Tables 4.5 and 4.6, respectively.

Table 4.2 quantifies basic properties of the MDF. For the global MDF, we measure $\langle[\mathrm{Fe/H}]\rangle = -1.55^{+0.04}_{-0.04}$ and $\sigma_{[\mathrm{Fe/H}]} = 0.54^{+0.03}_{-0.03}$. We measure a skew and kurtosis

of $-0.16^{+0.11}_{-0.11}$ and $-0.02^{+0.28}_{-0.21}$ respectively. The skew is mildly negative, confirming visual impressions, but is consistent with zero at $\sim 1.5\sigma$. The kurtosis is consistent with zero, which is also consistent with a clear single peak. Overall, the MDF is well-described by a Gaussian distribution.

The blue histogram in the right panel of Figure 4.5 shows the MDF reported by T20. From 52 RGB stars, T20 measure $\langle$[Fe/H]$\rangle = -1.58$ dex and $\sigma_{\rm [Fe/H]}$(intrinsic) = 0.39 dex. Using their measurements, we re-infer their MDF properties following the procedure in §4.4, obtaining $\langle$[Fe/H]$\rangle = -1.64 \pm 0.06$ dex and $\sigma_{\rm [Fe/H]} = 0.41 \pm 0.05$ dex. Our mean metallicity is in agreement with the T20 MDF, but we measure a larger metallicity dispersion. On the MP end, 2% of our stars are MP, whereas T20 do not find any stars with [Fe/H] < -3.0. On the MR (> -1.0) end, 20% of our stars are MR, while 4% (2 stars) from the MDF of T20 are MR. Stars between [Fe/H] $= -2.0$ and [Fe/H] $= -1.0$ make up 79% percent of the T20 sample, whereas they are a smaller fraction of our MDF.

We find a larger dispersion than T20 because the CaHK method provides a larger, more complete sampling of the MDF. It allows us to measure metallicities for a nearly complete sample of stars to a faint magnitude limit ($F475W \sim 24$). No current spectroscopic facility can reach such faint stars, and most spectroscopic observations are challenged by selection effects (e.g., slitmask placement). This MDF comparison illustrates one of the strengths of photometric metallicities.

Radial Trends in Metallicity

The spatial extent probed by our imaging ($\sim$ 500 pc; $\sim 2.5\ R_e$) and large sample of metallicities allows us to investigate radial trends. Figure 4.7 shows the spatial distribution of stellar metallicites in Tucana. It is visually apparent that stars in the center of Tucana are higher metallicity than those in the outskirts.

We reinforce this impression by plotting metallicities for each star as a function of radius, along with fits to the data, in Figure 4.8. We quantify the strength of this gradient first by fitting a line to individual stellar metallicities as a function of elliptical R_e from the center. Following the procedure outlined in [133], we adopt their likelihood function, which assumes Gaussian uncertainties on our measurements. Our parameters of interest are the slope $\nabla_{\rm [Fe/H]}$ and intercept $\rm [Fe/H]_0$. Additionally, we marginalize over an additional parameter f which quantifies the fractional underestimation of measurement uncertainty. We assume uniform priors for the slope ($-5 < \nabla_{\rm [Fe/H]} < 0.5$ dex arcmin^{-1}), intercept ($-4 <$ [Fe/H]$_0 < 0.0$) dex, and the logarithmic fractional uncertainty ($-10.0 < \log f < 1.0$). We sample the result-

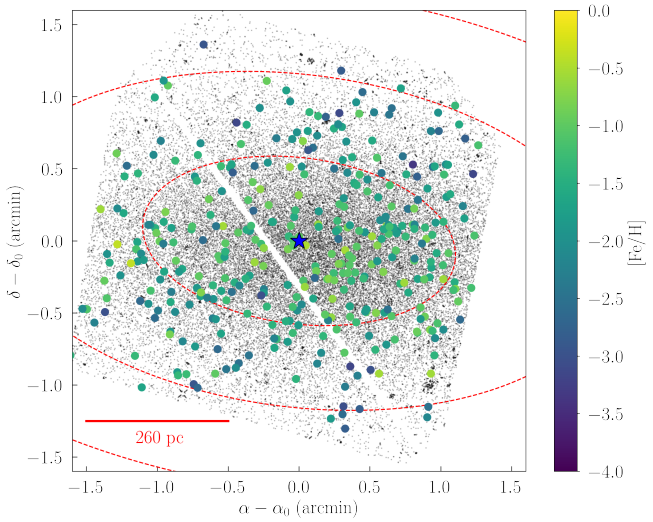


Figure 4.7: The spatial distribution of our CaHK-based stellar metallicities for Tucana. Overplotted are the elliptical half-light radii at 1 R_e, 2 R_e and 3 R_e. Visually, it's clear that the central region of Tucana has more MR stars and the outer regions have more MP stars.

ing posterior distribution using `emcee`. We run 32 walkers for 10,000 steps, with a burn-in time of 50 steps. We monitor convergence using the GR statistic.

Using the entire dataset, we measure a metallicity gradient across 2.5 R_e of Tucana of $\nabla_{\rm [Fe/H]} = -0.54 \pm 0.07$ dex R_e^{-1}. For completeness, we also fit a gradient as a function of angular distance from the galaxy, which assumes circular radii from the center. We find a gradient of $\nabla_{\rm [Fe/H]} = -0.57 \pm 0.1$ dex arcmin^{-1}, which translates in physical units to -2.1 ± 0.3 dex kpc^{-1}. We report the gradient in units of kpc to maintain consistency with how gradients in the literature have been reported [295], but because the resulting value is large, its interpretation requires additional orienting remarks. In particular, since the radial extent of Tucana probed by our data is $\sim$ 500 pc, we caution against interpreting the gradient by extrapolating beyond what is covered by the data (e.g., it may flatten out at larger radii). Within the extent of our radial coverage, the value of the gradient is consistent with the statement that the difference between the center and 2.5 R_e of Tucana is $\sim$ 1 dex, which we see borne out visually in Figure 4.8.

In Appendix 4.9, we present the correlation plot for the gradient fit using elliptical R_e, which we report as the main result for this paper. In Appendix 4.9, we present

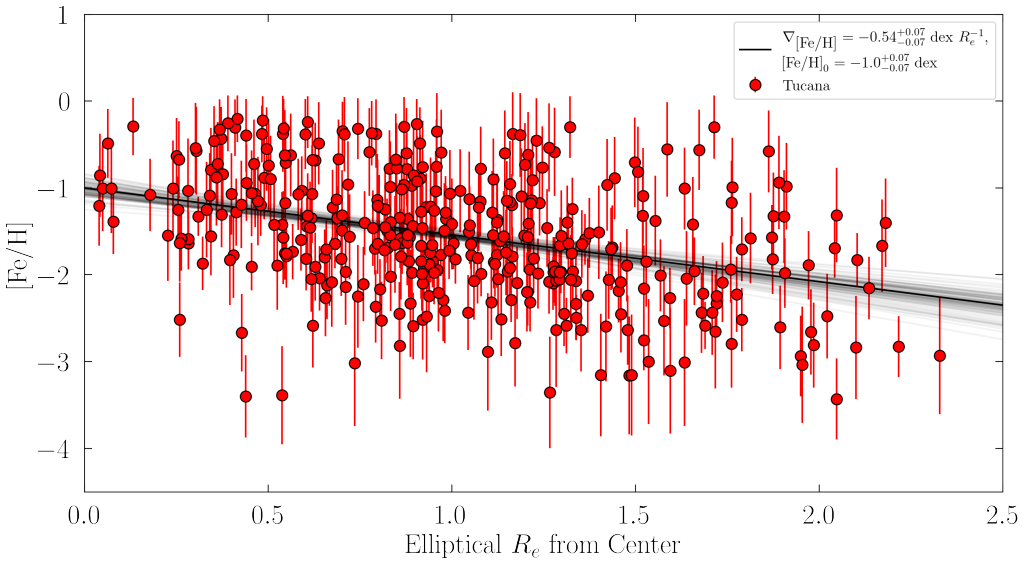


Figure 4.8: Result of fitting a linear model to our Tucana data as a function of elliptical R_e from its center. From our well-sampled MDF, which gives clear shape to the MP and MR tails, we are able to robustly recover a metallicity gradient.

the linear fit and corresponding correlation plots for the inference assuming circular arcmin, which are comparable to the gradient measured using elliptical R_e.

Our large sample size also allows us to measure MDFs in spatial bins across Tucana. We compute the MDFs, and associated summary statistics, for the MDFs in three spatial bins: < 1 R_e, between $1 - 2$ R_e, and from> 2 R_e to the spatial limit of our imaging. We compute mean metallicity, dispersions, skew, and kurtosis for the MDF following the procedure outlined in §4.4. The mean metallicity decreases as a function of increasing radius, with $\langle[Fe/H]\rangle = -1.35^{+0.05}_{-0.05}$, $-1.77^{+0.05}_{-0.05}$, and $-2.22^{+0.21}_{-0.22}$ across the three respective bins. The metallicity dispersions in all three bins have a similar value of ~ 0.5 dex. We also compute the skew and kurtosis, though both are consistent with zero at $< 2\sigma$.

Metallicities Along the Split RGB

Distinct stellar populations have long been noted in Tucana as overdensities in various features of its CMD. [121] and [217] note distinct populations in the RGB bump of Tucana, with the latter remarking that similar features are not observed in Cetus,

a dSph with similar environmental and SFH properties. [264] similarly note multiple CMD overdensities in the HB of Tucana, pointing to the presence of distinct populations.

As highlighted in Figure 4.9, these features manifest among the brightest stars in Tucana as a visual bifurcation in the RGB. We characterize the metallicity properties of the respective bifurcations by selecting RGB stars that are brighter than $F475W \sim 24.2$ mag. Above this magnitude, the separation is most visually apparent, and we avoid the completeness issues with the preferential exclusion of metal-rich stars towards the fainter end of our sample. We then fit the MDFs of each RGB following the procedure described in §4.4. The resulting MDFs with their summary statistics are shown in the right panel of Figure 4.9. For the blue RGB MDF, we measure $\langle[\mathrm{Fe/H}]\rangle = -1.78^{+0.06}_{-0.06}$ and $\sigma_{[\mathrm{Fe/H}]} = 0.44^{+0.07}_{-0.06}$. For the red RGB MDF, we measure $\langle[\mathrm{Fe/H}]\rangle = -1.08^{+0.07}_{-0.07}$ and $\sigma_{[\mathrm{Fe/H}]} = 0.42^{+0.06}_{-0.06}$. Our measurements unambiguously show that metallicity is at least partially responsible for the RGB split.

Additionally, we also investigate the spatial chemical properties of stars in the respective bifurcations, and present the results in Figure 4.10. Even by eye, it is apparent that stars in the metal-rich red RGB are more centrally concentrated than the bluer RGB. This result tracks with our metallicity gradient fit to the entire MDF sample. We also fit the metallicity gradient to stars in the respective bifurcations following the same procedure from §4.5. For the blue RGB, we recover $\nabla_{[\mathrm{Fe/H}]} = -0.62 \pm 0.11$ dex R_e^{-1}, and for the red RGB, we recover $\nabla_{[\mathrm{Fe/H}]} = -0.42 \pm 0.14$ dex R_e^{-1}. We present corresponding correlation plots in §4.9

4.6 Discussion

Improved MDF Statistics for Tucana and the Power of CaHK

As presented in §4.5, we measure for Tucana $\langle[\mathrm{Fe/H}]\rangle = -1.55^{+0.04}_{-0.04}$ and $\sigma_{[\mathrm{Fe/H}]} = 0.54^{+0.03}_{-0.03}$. These measurements are in good overall agreement with the literature values of T20, though with higher precision because we are able to use 374 stars, which is a factor of ~ 7 larger than existing CaT spectroscopic measurements. Our mean metallicity measurement is consistent with Tucana's expected location on the dwarf galaxy mass-metallicity relation [166]. Our expanded sample size enables us to measure a slight negative skew for our MDF, indicating a longer MP tail for Tucana, but both our skew and kurtosis measurements are consistent with the MDF

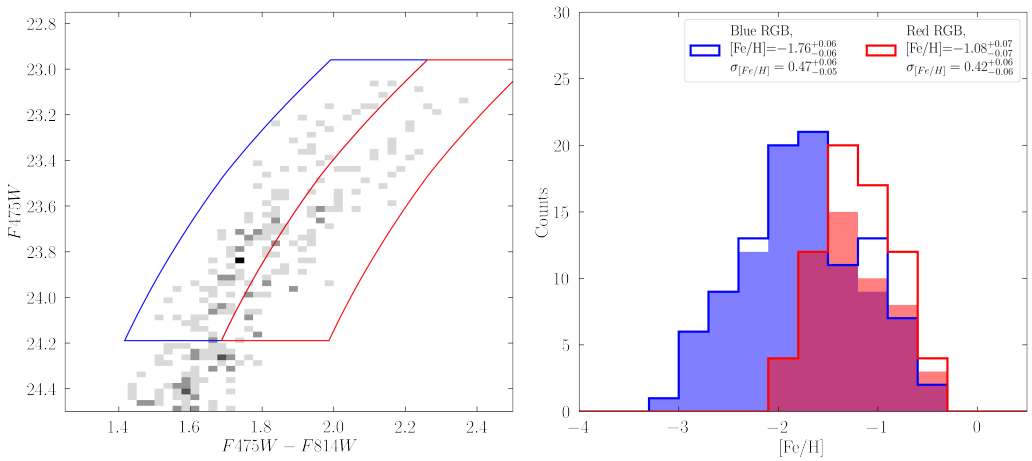


Figure 4.9: MDFs of stars along the respective bifurcations of Tucana's RGB. **Left:** Hess diagram of Tucana stars analyzed in this work, color-coded by the boxes used to select stars on the blue and red bifurcations of the RGB. We select stars above a certain magnitude range to ensure better completeness for our comparison. **Right:** Comparing the MDFs of stars that fall on the blue and red branches of the bifurcation respectively. Empty histograms on the metal-poor and metal-rich ends of the MDF respectively denote upper and lower limits. The metallicity difference between stars on the two branches is apparent even by eye, and the corresponding summary statistics in the legend quantify these differences: the MDF of the blue RGB is more MP than the MDF of the red RGB by ~ 0.7 dex.

of Tucana deviating little, if at all, from Gaussianity. In Appendix 4.8, we show how these results largely hold assuming different [α/Fe] vs. [Fe/H] relationships.

On the MP end of the MDF, we identify 8 EMP star candidates in Tucana, comprising 2% of our sample. This is consistent with observations of other dwarf galaxies in the Local Group, whose MDFs are generally characterized by a sparse MP tail below [Fe/H] < -3.0 (e.g., [176], [288], [177], [130], [119]). EMP stars are scientifically interesting for their ability to trace the chemical enrichment pathways of the first stars [92], and the low-metallicity dSphs have, due to their relatively simpler SFHs compared to the MW, long been a promising site for EMP searches. We include our EMP candidates in Table 4.5 as priority targets for spectroscopic follow-up.

On the MR end of the MDF, we identify 76 MR ([Fe/H] > -1.0) stars in Tucana, with 37 of them being lower limit constraints. These measurements are not well-

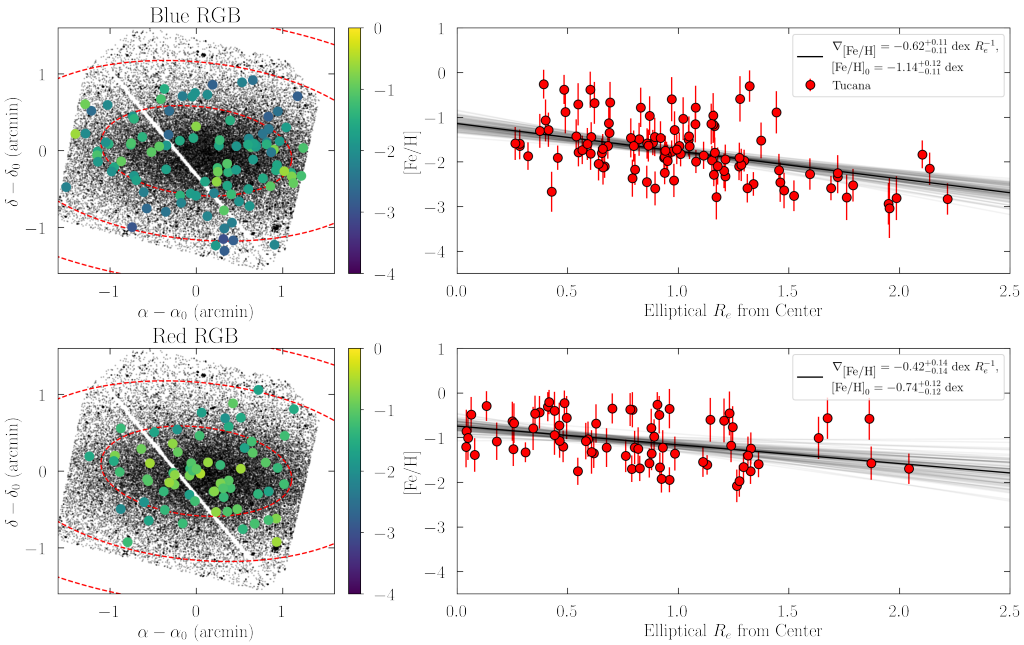


Figure 4.10: Spatial properties of stars along the respective bifurcations of Tucana's RGB. The left panels of each row present the spatial distribution of stars in each bifurcation, color-coded by their metallicity. The right panels of each row present stellar metallicities as a function of elliptical half-light radii, and the corresponding metallicity gradient fit. Stars in the more metal-rich red RGB are more centrally concentrated than stars in the blue RGB. We recover a steeper metallicity gradient for stars along the blue RGB than for stars along the red RGB.

constrained because they are low S/N, and because the discriminating power of the Ca H&K narrow-band filter diminishes at high metallicity. The shape of the MR tail in a dwarf galaxy's MDF is crucial for modeling its chemical evolution (e.g., [257]) and is therefore also of interest for detailed follow-up. We provide a table of these stars in Table 4.6 and invite the community for spectroscopic follow-up in the era of ELTs.

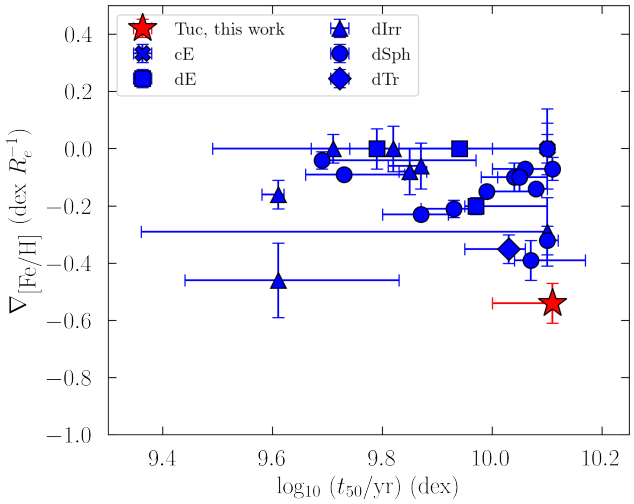


Figure 4.11: Comparing the metallicity gradient in Tucana from our work with gradients of LG dwarf galaxies across a range of morphological type measured with spectroscopy [295]. The gradient of Tucana is one of the significant ones known among LG dwarfs. Additionally, while the spectroscopic gradients do not show a clear relation with t_{50} (median stellar age), we demonstrate in Figure 4.12 that our gradient measurement for Tucana is consistent with predictions from cosmological simulations that posit feedback as the primary mechanism for gradient formation in isolated dwarf galaxies [214].

Radial Trends in Metallicity

Comparison to Literature Gradients

Based on the spatial concentration of different populations of HB stars, [264] suggested that population gradients should be expected in Tucana. However, T20 was unable to definitively resolve differences in metallicity between the inner parts and the outskirts of the galaxy. They fit their data using an error-weighted least squares method to infer a metallicity gradient of $\nabla_{\rm [Fe/H]} = -0.16 \pm 0.09$ dex arcmin^{-1} for Tucana members within ~ 2.5 R_e of the galaxy. These numbers translate into -0.13 ± 0.07 dex R_e^{-1} and -0.6 ± 0.4 dex kpc^{-1}.

Due to differences in the treatment of the linear fitting procedure, as well as galaxy parameters used to convert the gradients into different physical units, we re-fit a line to the T20 data following the procedures outlined in §4.5 to ensure a direct

comparison to our measurements and gradient determinations. For the T20 data we find $\nabla_{\rm [Fe/H]} = -0.10 \pm 0.11$ dex arcmin^{-1}, translating to -0.08 ± 0.09 dex R_e^{-1} and -0.38 ± 0.44 dex kpc^{-1}, which are slightly different, but consistent with the T20 results. Our re-fit still describes the same qualitative result: the spectroscopic data do not robustly resolve a metallicity gradient in the dwarf, which is not consistent with the gradient we measure from the larger CaHK sample.

Figure 4.11 compares our metallicity gradient measurements to those from the analysis of archival spectroscopic data carried out by [295] in t_{50} vs. $\nabla_{\rm [Fe/H]}$ space for a larger set of LG dwarf galaxies. The t_{50} values for other LG dwarf galaxies come from a combination of the [319] compilation, published results from the LCID project (Cetus, [216]; Tucana, [216]; Leo A, [61]; Phoenix), and several additional studies (WLM, [3]; Sextans, [31]; And II, [282]). Individual metallicity measurements used in [295] were derived using either spectral fitting of Fe I lines or from using the CaT calibration. The number of stars used to make metallicity gradient measurements in LG dwarfs ranges from ~ 50 to ~ 300.

Our metallicity gradient in Tucana is steeper than previous measurements. In fact, it is one of the steepest gradients measured in any LG dwarf galaxy to date. We now consider several aspects of our analysis that could affect the robustness of this result.

First, as shown by Figures 4.5 and 4.6, our individual metallicities are consistent with the CaT-based values across the full range of metallicities. Thus, it is unlikely that any systematic in our measurement is the primary driver of a steep gradient.

Second, we assess the impact of selection effects on our measurements. One selection effect impacting our overall analysis is that towards fainter magnitudes, we preferentially lose MR stars in our sample. This is because at a given brightness, MR stars have lower S/N in $F395N$ due to increased absorption in the Ca H&K features. The effect is similar to the one described in [191]. To mitigate the impact of this effect in our metallicity gradient inference, we re-measure our metallicity gradient with only stars that are brighter than $F475W$ of 24 mag, where we have higher levels of completeness along the RGB. The resulting gradient is on the order of -0.8 dex arcmin^{-1}, which is larger in magnitude than the measurement made using the full sample. Thus it is unlikely that this particular selection effect is inflating our metallicity gradient measurement.

Third, we consider that the discrepancies may result from the uncertain nature of spectroscopic selection effects, which comprise the vast majority of dwarf galaxy metallicity gradient measurements in the literature thus far. In particular, it seems plausible that the empirical picture of gradients has been limited by spectroscopic selection effects, some of them complex (e.g., the placement of stars on masks for

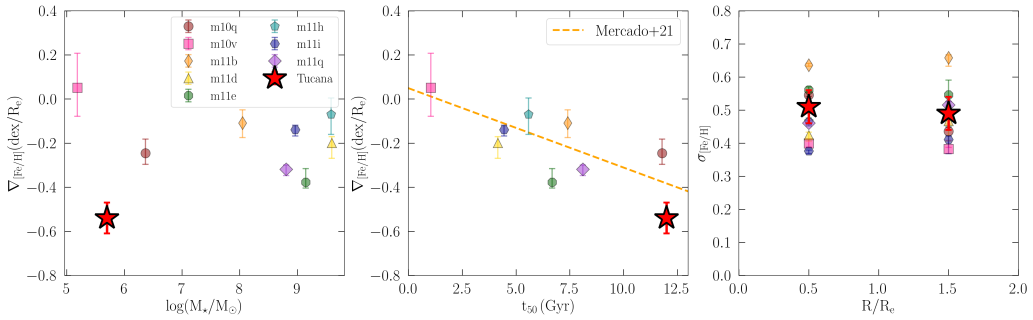


Figure 4.12: Comparing our metallicity gradient measurement for Tucana with those from the FIRE-2 simulations (e.g., [214]), which posit that metallicity gradients in isolated dwarf galaxies are driven by feedback-induced breathing modes [16]. **Left:** Comparing our gradient measurement and gradients from simulations as a function of stellar mass. The weak correlation between stellar mass and gradient strength is an emerging consensus among simulations, and we present this panel largely for completeness reasons. **Center:** Comparing our gradient measurement and gradients from simulations as a function of t_{50} (Gyr). The orange dotted line is the relation between t_{50} and gradient strength as found by [214]. Our gradient measurement for Tucana is consistent with this theoretical relation. **Right:** Examining trends in metallicity dispersion as a function of R_e. The radial dispersion trend in Tucana is consistent with those from simulations.

MOS spectroscopy). It becomes difficult to obtain a clear picture of the metallicity gradient when the sampling of stars within particular spatial and magnitude limits is incomplete. In contrast, at a distance of ~ 1 Mpc, a single pointing and 12 orbits with HST yields reliable metallicities of RGB stars within 2 R_e of Tucana with a high level of completeness, as illustrated in Figs 4.3 and 4.7.

Comparison to Cosmological Simulations

As a means of illustrating the connection of our results to theory, we compare our measured gradient[3] for Tucana to a subset of isolated, simulated dwarf galaxies from the publicly available core suite of FIRE-2 simulations [321]. The simulated galaxies

[3]FIRE-2 dwarf galaxies are known to struggle with producing mean metallicities that are lower than many observed dwarf galaxies. This tension also exists between Tucana and the comparison simulations. Since we are only interested in metrics of relative metallicity across the galaxy, we do not include mean metallicity comparisons in our discussion. Efforts to resolve agreement in mean metallicities are well underway e.g., [103].

have evolved in isolation, and are dispersion-supported systems, which make them good matches to Tucana for this comparison.

Figure 4.12 compares metallicity gradients from FIRE-2 to our Tucana measurement. In all three panels we provide the circularly averaged 2D gradient and dispersion measured over 100 random projections for each simulated galaxy. The error bars on the simulations represent the maximum and minimum values. The simulated dwarf galaxies do not display a strong correlation with gradient as a function of stellar mass, and the addition of our Tucana measurement, a single galaxy, does not provide new insight into this trend. The absence of a trend between stellar mass and metallicity has been seen in early empirical results [295] as well as in other simulations (e.g., [243], [271]).

The center panel compares the Tucana gradient measurement to simulated gradients as a function of median stellar age, t_{50} [217]. In the FIRE-2 simulations, these two parameters are strongly correlated, where galaxies with older stellar populations have stronger gradients. This relationship was first pointed out by [214] using a similar sample of FIRE-2 simulated dwarf galaxies not included in the public data release. Because star formation tends to flatten pre-existing radial trends, metallicity gradients are best preserved in the oldest galaxies that stopped forming stars early on. We include the trend that they report in this panel as the orange dashed line, and find that the simulations we use are in good agreement with their study. The T20 gradient for Tucana ($-0.13 \pm 0.07\ dex\ R_e^{-1}$) is too shallow to be in agreement with this relationship, whereas our measurement for Tucana's gradient affirms it well.

Our well-sampled MDFs also enable measurements of metallicity dispersion as a function of radial extent. In the right panel we make comparisons between our measurements and those from the FIRE-2 simulations. Our results are comparable to those of the simulations, where the gradients within the inner R_e of a galaxy and the gradient within the adjacent bin are comparable.

In FIRE-2 simulated dwarf galaxies, metallicity gradients are formed primarily through feedback from successive episodes of star formation, which add energy to the orbits of older (i.e., more MP stars) and drive outward radial migration over the course of a galaxy's lifetime [e.g., 16]. Metallicity gradient measurements made from a complete sample of stars further down the LF of isolated LG dwarf galaxies can better determine whether this prediction bears out in the dwarf galaxy population more generally, and not just in the case of Tucana.

Radial metallicity dispersion trends have not been previously well-quantified in a dwarf galaxy due to limited sample sizes observed. Similarly, radial dispersion trends have also not been examined in simulations prior to this work. Given that not all simulations agree that feedback drives gradient formation (e.g., [193], [251], [123], [222]), metallicity dispersions are another metric that may be useful for under-

standing the interplay of different processes that drive or wash out dwarf metallicity gradients. Our results for Tucana reveal the promise of CaHK narrowband imaging for enabling the exploration of radial metallicity dispersion trends in dwarf galaxies across the LG, and we recommend further exploration of this metric as part of developing the picture of observational imprints from different processes that drive spatial trends within a dwarf galaxy.

Metallicity Gradients as Probes of Cored DM Profiles

The "too big to fail" (TBTF) problem [36] describes the overdensity of DM halos in simulated dwarf galaxies, compared to the actual observed central DM density of dwarf galaxies based on velocity measurements. Efforts to reconcile theory to observation has invoked the chaotic effects of baryonic processes, particularly whether the energetics of SNe can sufficiently reduce the central DM density of halos to form cores, though the extent to which this is possible remains a point of controversy ([104], [190]).

The most direct probe of central DM density are stellar velocity measurements, and in the case of Tucana, the central density of its DM halo has been a subject of controversy within spectroscopic studies: it is either an exception to the TBTF problem compared to its other LG analogs because it has a dense central DM halo [115], or its properties are consistent with the properties of LG dwarfs [296]. These studies have been limited by sample size because of limited ability for spectroscopy to reach an adequate number of stars to construct a high-confidence, detailed profile.

Given the current limitations of spectroscopic studies in this arena, it is important to make predictions for ancillary observations that could weigh in on this theoretical picture. Thus, an important contribution of [16] is proposing that age and metallicity gradients are also an observational consequence of cored DM halo formation from SNe feedback. Age gradients have historically been difficult to detect in Tucana due to degenerate effects in age and metallicity particularly for old stellar populations ([128]), and evidence of a metallicity gradient was detected using the different concentrations of HB stars of different metallicity and age, but it was not well-quantified ([121], [264]).

As established previously, we robustly detect a metallicity gradient in Tucana. The gradient is consistent with predictions from the FIRE simulations, which produce both gradients and dark matter cores through the same baryonic processes. With the advent of high-confidence dwarf metallicity gradients measured using CaHK imaging, we propose additional theoretical exploration into the utility of metallicity gradients as an indirect probe for the underlying kinematics of dwarf galaxy DM halos. Any such theory will also need to account for the interpretation of metallicity gradients

and different kinematic properties of MP and MR components that are being robustly detected in nearby MW satellites ([235], [302]).

The MDF of Tucana in Context

Tucana's isolated, quenched status makes it an outlier compared to its field, star-forming analogs, as well as its satellite, quenched analogs. Its contested status as a backsplash galaxy ([298], [259]), as opposed to galaxy that has truly evolved in the field away from the influence of more massive hosts, also complicates its interpretation. Here, we compare the broad features of its MDF to those of other LG dwarf galaxies to determine potential insights offered.

First, we compare the MDF of Tucana to the MDFs of MW dSphs that are close to mass analogs of Tucana. We reference the detailed MDFs measured by [166]. Whereas the MDF of Tucana does not deviate strongly from Gaussianity, the MDF of Draco demonstrates a long MP tail. The MDF of Ursa Minor is closer to symmetrical, though it has a slightly stronger MR tail. Although their SFHs are comparable to Tucana's in duration and age, the mean metallicity of these galaxies are lower than Tucana's by ~ 0.4 dex, suggesting that they experienced slower chemical enrichment over the course of their lifetimes compared to their isolated counterpart. This may be related to different mechanisms driving the depletion of gas in these dwarf galaxies: while Draco and UMi could have had their gas stripped by the proto-MW, Tucana may have consumed gas largely through star formation, resulting in a higher overall metallicity for its stellar population.

Second, we compare the MDF of Tucana to the MDFs of other isolated dwarf galaxies on the periphery of the LG. These galaxies are all currently forming stars. [163] presents spectroscopic metallicities of Leo A, Aquarius, and the SagDIR, all of which have stellar masses comparable to Tucana, but are currently star-forming. The resulting MDFs of 113, 23, and 43 stars respectively appear qualitatively similar to that of Tucana's, in that they do not display skewness. Tucana also has a mean metallicity comparable to that of Leo A and Aquarius to within ~ 0.1 dex, and is more MR than SagDIG by 0.3 dex.

The similar metallicity properties between Tucana and some of its star-forming analogs is interesting to consider further. Taken at face value, the implication is that field dwarf galaxies of different morphological properties end up at comparable metallicities, whether they arrived there 10 Gyr ago after 3-4 Gyr of star formation (e.g. Tucana; [217]) in isolation, or whether they have been slowly forming stars throughout cosmic time and recently accelerated the process within the last 3 Gyr (e.g. Leo A; [61]). This comparison implies that there are enrichment processes op-

erating on different timescales that can produce degenerate observational signatures in [Fe/H].

Articulated in a different way, the evolutionary pathways of star-forming isolated galaxies in the near-present is presumably different from the evolutionary pathways of isolated galaxies quenched in the distant past. In this framing, the interpretation of Tucana as a splashback galaxy that was previously bound to M33 (e.g., [298], [259]) can rule out evolutionary narratives contingent upon isolation, but it alone would not be able to provide a full detailed account of Tucana's chemical enrichment in comparison to its LG stellar mass analogs. Addressing these questions would also have implication for our detailed understanding of the physics setting the present-day mass-metallicity relation for dwarf galaxies, which generally holds across a range of morphological types [166].

Interpretation of the Split RGB

In this section, we discuss possible evolutionary histories of Tucana implied by observations of its split RGB. We show in §4.5 that the bifurcation is driven in large part by metallicity differences between the two respective populations. Additionally, stars belonging to the metal-poor, blue branch are more spatially extended than stars in the red branch (Figure 4.10), affirming our measurement of a significant global gradient in Tucana. Given that chemodynamical populations have been found in other dwarf galaxies (e.g. [235], [302]), we compute velocity and velocity dispersions for stars in the respective bifurcations, using data from T20. We find no kinematic difference between these populations, although this calculation is likely limited due to small number of stars with velocities in Tucana.

We note that the MDF of the blue RGB (Figure 4.9) has comparable mean metallicity and dispersion to the MDFs of the MW satellites. That is, removal of the red RGB from Tucana would produce a stellar population whose global MDF properties more closely resemble Ursa Minor or Draco. As the ratio of blue and red RGB stars are roughly order unity in our sample, we proceed assuming that their populations are roughly 10^5 $M_\odot$ each in stellar mass.

We consider how these features could have formed *in-situ* in Tucana. The SFH of Tucana from [264] uses HB stars to resolve effectively two major star-forming episodes that are spaced roughly 1-2 Gyr apart. Following this finding, we consider the possibility that each respective bifurcation corresponds to one SF episode, with the blue, MP RGB corresponding to the earlier episode, and the red, MR RGB corresponding to the more recent episode. The first round of SF produces a more metal-poor MDF resembling those of MW satellites. During the quiescent period, the ISM is enriched further by a number of SNe, including Type Ia, so that the

second episode of SF proceeds from a more MR ISM and results in the MDF traced out by the red RGB. Qualitatively, this picture would also be consistent with the formation of feedback-driven metallicity gradients in dwarf galaxies, where older, MP stars are more spatially extended than younger, MR stars. Chemical evolution modeling that treats each component separately should ascertain the feasibility of this scenario and possibly characterize the physics driving star formation at different epochs of Tucana's lifetime.

We next consider the possibility that these two RGB branches are the result of the merging of two distinct populations. Simulation literature is not conclusive about the ubiquity of low-mass dwarf galaxy mergers, with some studies suggesting that dwarf galaxy formation is characterized by numerous merger events (e.g., [28], [143]) and others strongly discouraging this scenario (e.g., [89]). Given this ambiguity, we consider this possibility for narrative completeness. At a stellar mass of roughly 10^5 $M_\odot$, the blue RGB of Tucana could have the properties of a dwarf galaxy consistent with the mass-metallicity relation. On the other hand, the red RGB would be too metal-rich compared to expectations for a dwarf galaxy (i.e., from the mass-metallicity relation), and its large metallicity dispersion rules out the possibility that it is a metal-rich star cluster. Thus, a theoretical stellar population represented by the red RGB would be an outlier in the current observational and theoretical landscape of galaxy formation. On the other hand, the blue RGB has a steeper metallicity gradient than UMi ([295], using [235] spectroscopic data subtending ~ 2.5 R_e of the dwarf), so the blue RGB is not a perfect analog to known dSphs. The sum of this evidence suggests that it is unlikely Tucana's bifurcated RGB is the product of low-mass galaxy mergers.

More broadly, we situate the split RGB feature within the broader landscape of known dwarf galaxy stellar populations. The split RGB feature is itself rare, and to-date other galaxies that display this feature are the Sextans dwarf spheroidal [25] and the And II dwarf galaxy ([208], [282]). On the other hand, morphologically distinct features that trace out separate stellar populations are common in LG dwarf galaxies, even if they don't manifest in the RGB. For example, the Carina dSph, with multiple discrete bursts of SFH and corresponding MSTO sequences, does not display a split in its RGB [70]. Why some galaxies have split RGBs while others, with extended SFHs, metallicity dispersions, and other distinct morphological features in their CMDs, do not, is still an outstanding question. While we've demonstrated with Tucana that the level of observed separation is driven in large part by metallicity differences of ~ 0.7 dex between the two populations, it's possible that a combination of higher-order effects such as age and α may influence the prevalence of split RGBs more broadly. These effects are not yet well-understood and require additional studies.

4.7 Conclusion

In this paper, we present the MDF of the isolated quenched dwarf galaxy Tucana measured using HST CaHK narrow-band imaging. In a single HST pointing, we are able to measure metallicities for stars brighter than 25 mag in $F475W$ within $\sim 2.5\ R_e$ of Tucana, to a higher level of completeness than has been previously possible via spectroscopic surveys. From this dataset with vastly improved sampling both along the luminosity function of the galaxy as well as its spatial extent, we present the key conclusions for Tucana:

- From a sample of 374 stars, we measure $\langle[\mathrm{Fe/H}]\rangle = -1.55^{+0.04}_{-0.04}$ and $\sigma_{[\mathrm{Fe/H}]} = 0.54^{+0.04}_{-0.04}$. Additionally, we quantify higher-order moments in the MDF such as skew and kurtosis, and find that the MDF of Tucana does not deviate significantly from a Gaussian.

- Across the $\sim 2.5\ R_e$ subtended by our imaging, we measure $\nabla_{[\mathrm{Fe/H}]} = -0.54 \pm 0.07$ dex R_e^{-1}. In circular units, we detect $\nabla_{[\mathrm{Fe/H}]} = -0.57 \pm 0.1$ dex arcmin-1, which corresponds to $\nabla_{[\mathrm{Fe/H}]} = -2.1 \pm 0.3$ dex kpc^{-1} in units of physical distance.

- We characterize the metallicity features of stars along the respective bifurcations of Tucana's RGB. The blue RGB has $\langle[\mathrm{Fe/H}]\rangle = -1.78^{+0.07}_{-0.06}$ and $\sigma_{[\mathrm{Fe/H}]} = 0.44^{+0.07}_{-0.06}$, whereas the red RGB has $\langle[\mathrm{Fe/H}]\rangle = -1.08^{+0.06}_{-0.06}$ and $\sigma_{[\mathrm{Fe/H}]} = 0.42^{+0.06}_{-0.06}$. Stars in the more MP blue RGB are also more spatially diffuse than stars in the red RGB, consistent with our metallicity gradient fit to the global sample. For the blue and red RGB stars respectively, we measure $\nabla_{[\mathrm{Fe/H}]} = -0.62 \pm 0.11$ dex R_e^{-1} and $\nabla_{[\mathrm{Fe/H}]} = -0.42 \pm 0.14$ dex R_e^{-1} respectively.

- We compare our gradient measurement of Tucana to simulated gradients of isolated dwarf galaxies from the FIRE-2 suite, and find that our measurement affirms the gradient strength-median stellar age law as found by [214]. As the same feedback mechanisms driving gradients are also expected to form cored dark matter halo profiles that might alleviate small-scale tensions with ΛCDM ([16], [43]), we recommend additional studies investigating possible relationships between metallicity gradient strength and host halo properties.

- Compared to the MDF of MW dSphs Ursa Minor and Draco, most similar in mass and SFH to Tucana, the MDF of Tucana is more MR on average by

~ 0.4 dex and more consistent with Gaussianity, implying that MW satellite dwarfs may have enriched more slowly than field dwarfs throughout a similar period of SF. On the other hand, removal of the red RGB component in Tucana would result in an MDF more consistent with those of MW satellites.

- We compare the MDF of Tucana to MDF of other star-forming, LG dwarf galaxies of similar mass [163] and find qualitatively similar results, suggesting that the physics driving different evolutionary pathways of field dwarf galaxies across morphological type can produce degenerate [Fe/H] signatures observed in the present-day.

- Chemical evolution modeling of the MDF of Tucana will be essential for obtaining a full detailed picture of the physics driving Tucana's observed properties. Constraints on SNe energetics governing Tucana's chemical evolution may also inform whether such processes can give rise to the observed metallicity gradient. Modeling efforts will also have to account for the split RGB and the attendant metallicity properties of each bifurcation. These efforts will have strong scientific synergy with forthcoming chemical abundance measurements, particularly [α/Fe], from *JWST* GO-3788 (PI: Weisz), as well as future efforts to push stellar spectroscopy to further depths within the Local Group and beyond [255].

More broadly, our work affirms the power of CaHK narrow-band imaging to measure stellar metallicities, and recover spatially resolved stellar MDFs of distant galaxies at a higher efficiency compared to what has been previously done. This technique will continue to be highly complimentary with science capacities from the newly-launched *JWST* for mapping the detailed chemistry of distant dwarf galaxies of high scientific value. Homogeneous metallicity and chemical abundance measurements and attendant chemical evolution studies of LG dwarf galaxies will be essential for fleshing out the full explanatory picture of the observed diversity of dwarf galaxies across mass, morphological type, and environment. Their application to interpreting observations of distant dwarf galaxies will realize the promise and power of near-field cosmological studies for providing detailed insight into the evolution of dwarf galaxies across cosmic time (e.g., [38]).

4.8 Impact of α Assumptions on MDF Measurement

In this section, we present MDF measurements of Tucana from assuming different levels of [α/Fe] across all of its stars. Figure 4.13 presents the results of MDF inference against different [α/Fe] relationships, and Table 4.3 tabulates the corresponding MDF summary statistics. The upper row is our fiducial assumption, while the middle and bottom rows shift the location of the ankle and knee by 0.5 dex backwards and forwards respectively. The change in mean metallicity and metallicity dispersions are attributed to the recovery of MR stars that determine the strength of the MR tails: a MP knee results in the recovery of more MR stars, while a MR knee results in the recovery of fewer MR stars. In any case, the corresponding mean metallicity and metallicity dispersions are still within 2σ agreement with the values of the MDF measured from the fiducial [α/Fe] assumption. The skew and kurtosis are also altered between different assumptions, but remain consistent with one another to 2σ. We find that different assumptions for the [α/Fe] vs. [Fe/H] relationship do not fundamentally change the conclusions presented in this paper.

Table 4.3: Tucana MDF Assuming Different [α/Fe] vs. [Fe/H] Relationships

Feature	**Parameter**	**Value**
Fiducial	$\langle$[Fe/H]$\rangle$	$-1.55^{+0.04}_{-0.04}$
	$\sigma_{\rm [Fe/H]}$	$0.54^{+0.03}_{-0.03}$
	Skew	$-0.16^{+0.11}_{-0.11}$
	Kurtosis	$-0.02^{+0.28}_{-0.21}$
[α/Fe] knee, ankle = -2.5, -1.5	$\langle$[Fe/H]$\rangle$	$-1.46^{+0.04}_{-0.04}$
	$\sigma_{\rm [Fe/H]}$	$0.61^{+0.04}_{-0.04}$
	Skew	$0.0^{+0.1}_{-0.1}$
	Kurtosis	$-0.1^{+0.2}_{-0.2}$
[α/Fe] knee, ankle = -1.5, -0.5	$\langle$[Fe/H]$\rangle$	$-1.59^{+0.03}_{-0.03}$
	$\sigma_{\rm [Fe/H]}$	$0.47^{+0.03}_{-0.03}$
	Skew	$-0.2^{+0.1}_{-0.1}$
	Kurtosis	$0.1^{+0.3}_{-0.3}$

Note. Summary of metallicity properties of Tucana' s MDF, assuming different [α/Fe] to [Fe/H] relations.

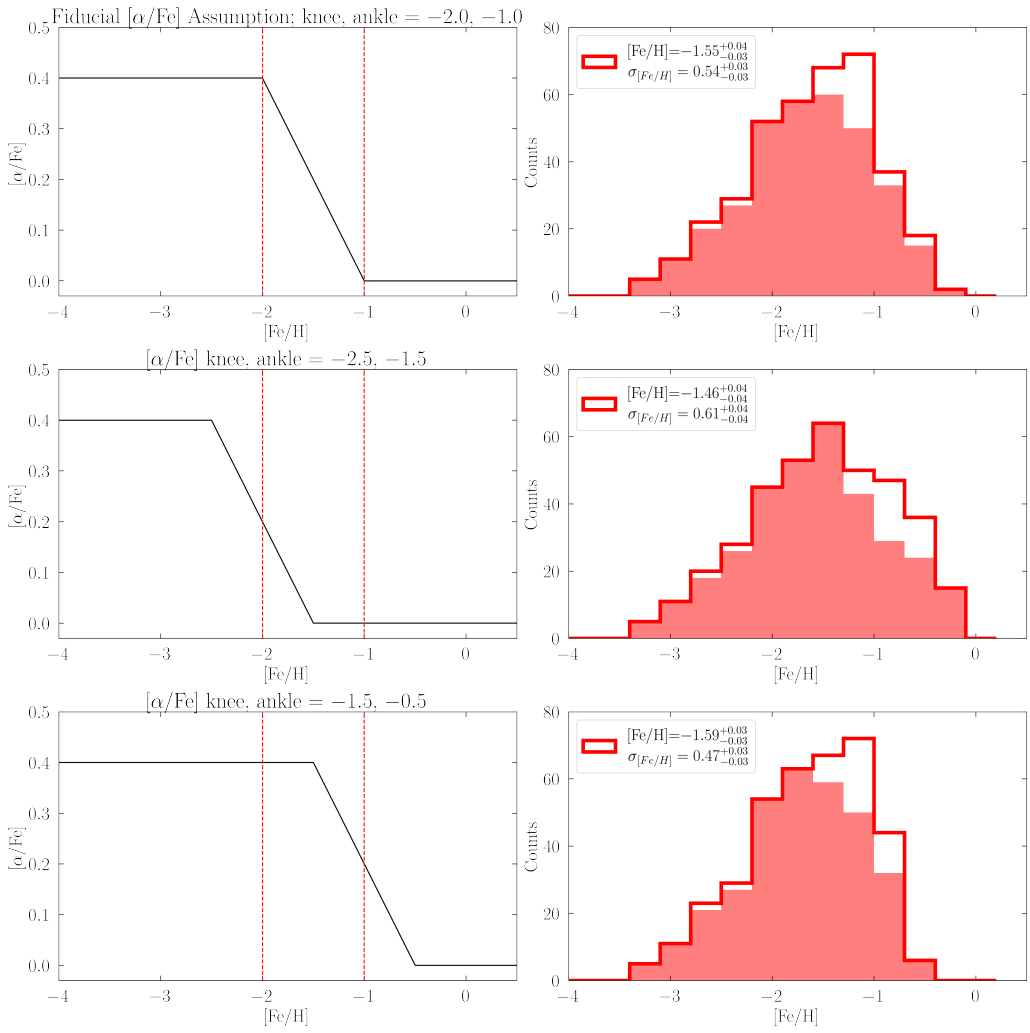


Figure 4.13: Impact of varying the [α/Fe] assumption on the recovered MDF of Tucana. The top row presents our fiducial assumption, while the middle and bottom rows present the recovered mean metallicity and dispersion by assuming a relation that shifts the ankle and knee by 0.5 dex backwards and forwards respectively. Additional summary statistics are presented in Table 4.3. The different α do not change the major conclusions of this work.

4.9 Metallicity Gradient Measurements

Metallicity Gradient Corner Plots

Figure 4.14 presents the corner plot corresponding to the metallicity gradient value reported in the main body of this paper. The figure shows correlations between the intercept, gradient, and a fractional uncertainty underestimation value inferred by the gradient measurement procedure outlined in §4.5.

Metallicity Gradient Using Circular Arcmin

We provide fits to the metallicity gradient in units of on-sky distance, or arcmin, from the center of Tucana, following the method outlined in §4.5. By nature of this metric, this gradient fit necessarily assumes circular distance. Figure 4.15 shows the resulting gradient fit against the data, and Figure 4.16 shows the corresponding corner plots. The fit that we find in this case is comparable to the fit using elliptical half-light radii.

Metallicity Gradient Corner Plots for Split RGB Components

In Figure 4.17 and 4.18, we present the correlation plots corresponding to the metallicity gradient fits to Tucana's split RGB components.

4.10 Table of Metallicity Measurements

In this section, we present the tables of individual stellar metallicity measurements. Table 4.4 presents measurements for all the stars in our sample, Table 4.5 presents the EMP star candidates identified in this work, and Table 4.6 presents the MR stars in Tucana.

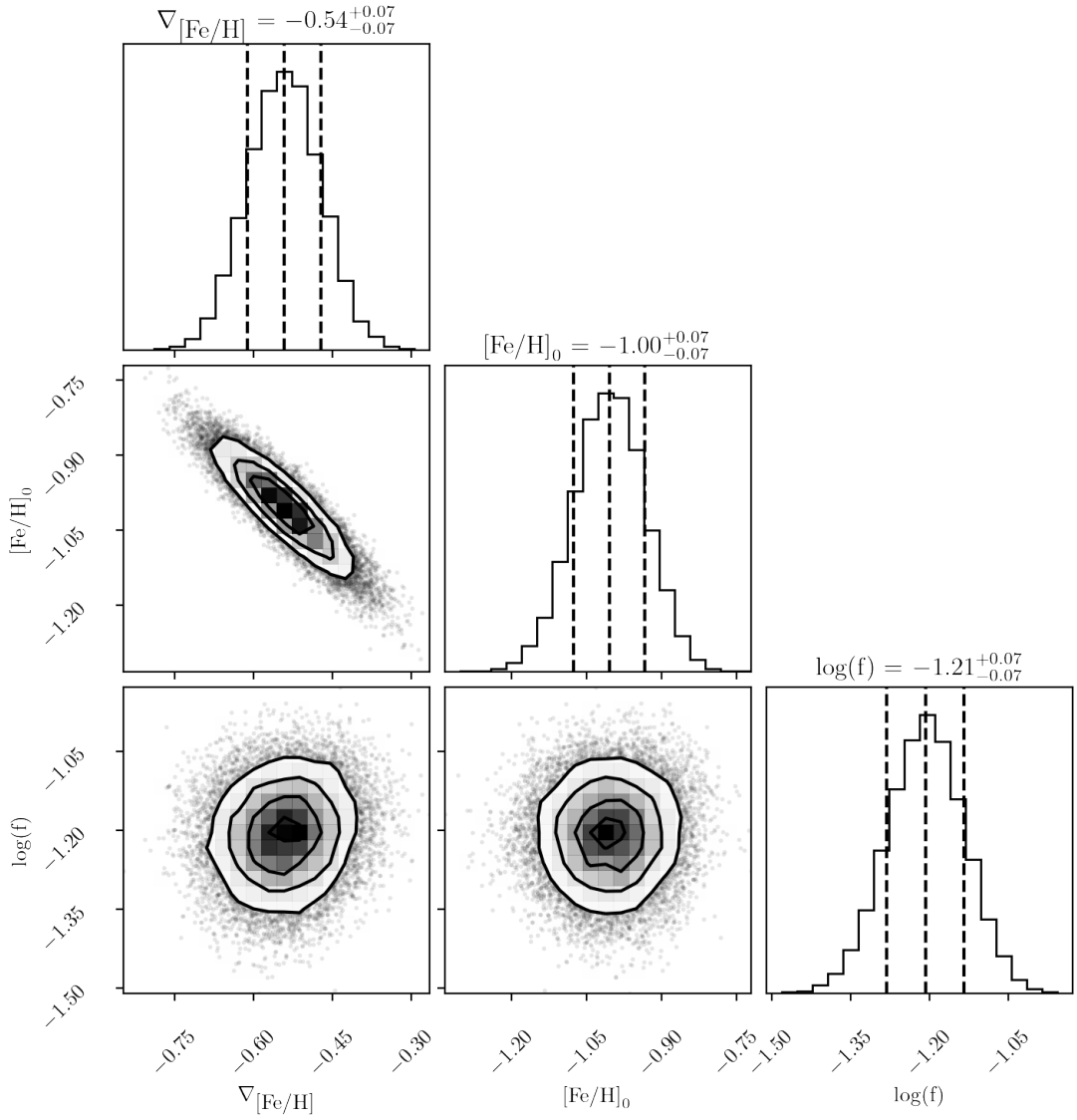


Figure 4.14: Corner plot of metallicity gradient fit using elliptical R_e.

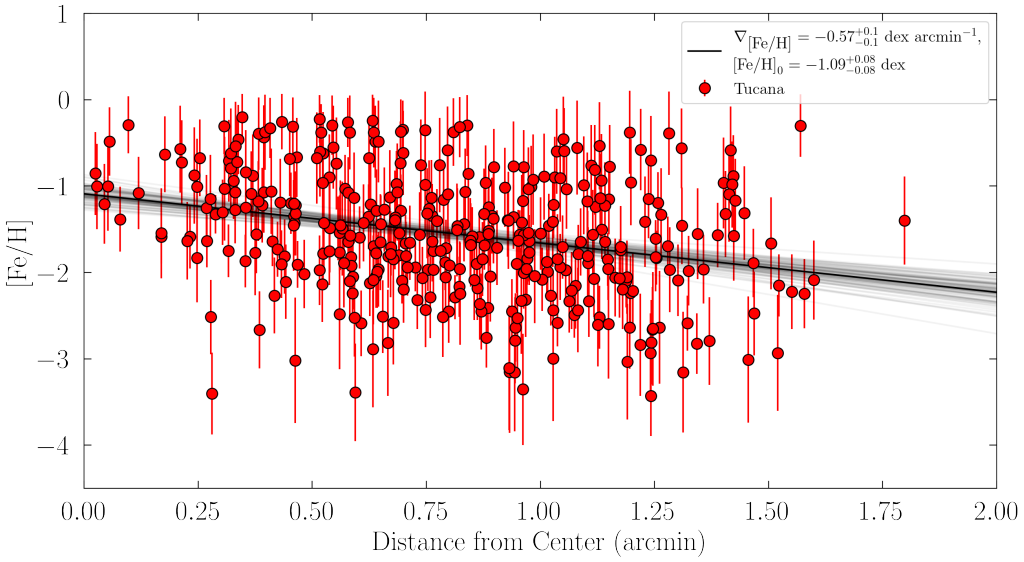


Figure 4.15: Result of fitting line to our Tucana data as a function of circular arcmin from the center. The gradient from this method is comparable to the gradient from fitting as a function of elliptical half-light radius.

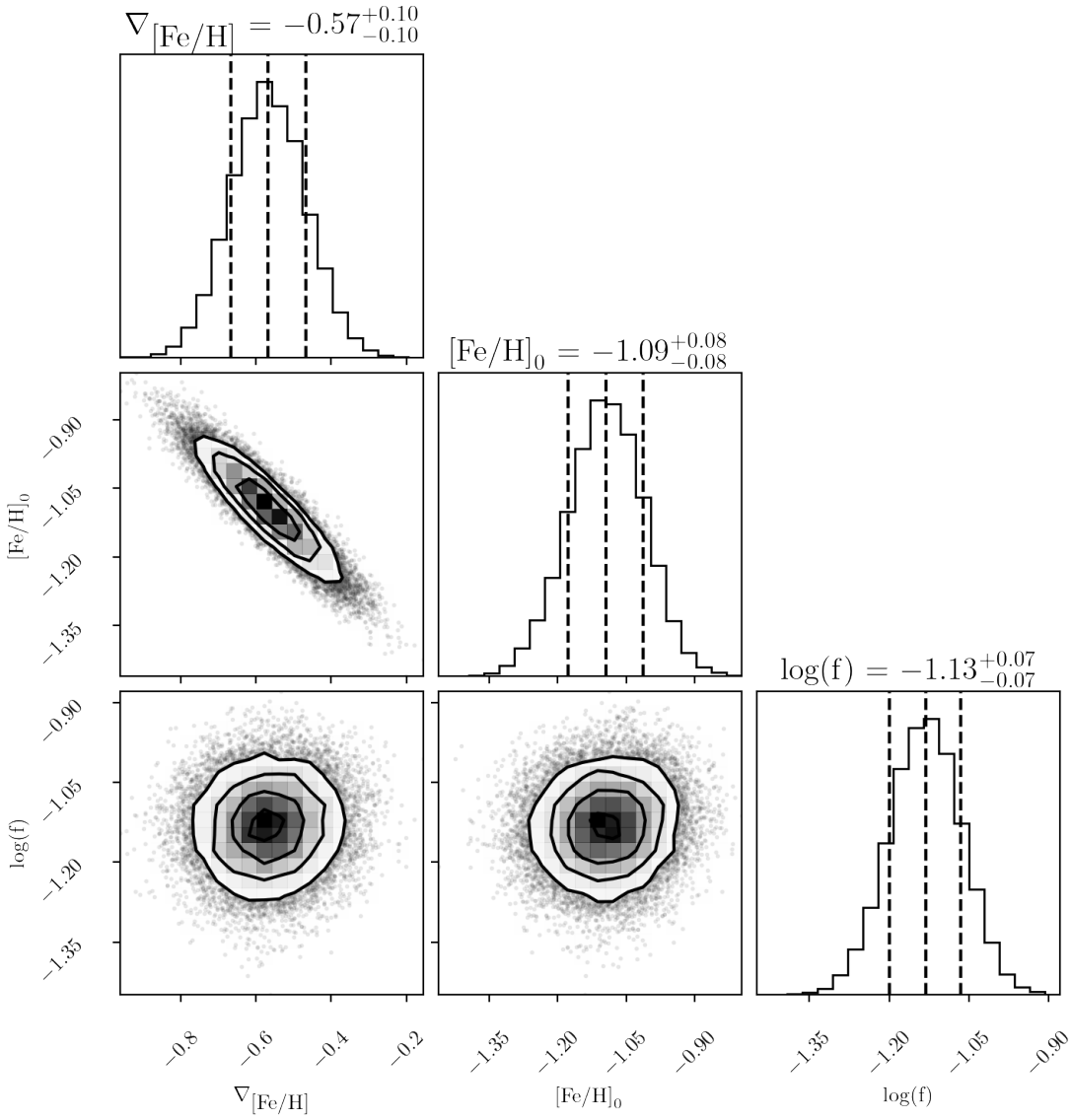


Figure 4.16: Corner plot of metallicity gradient fit using distance from the center of Tucana in circular arcmin.

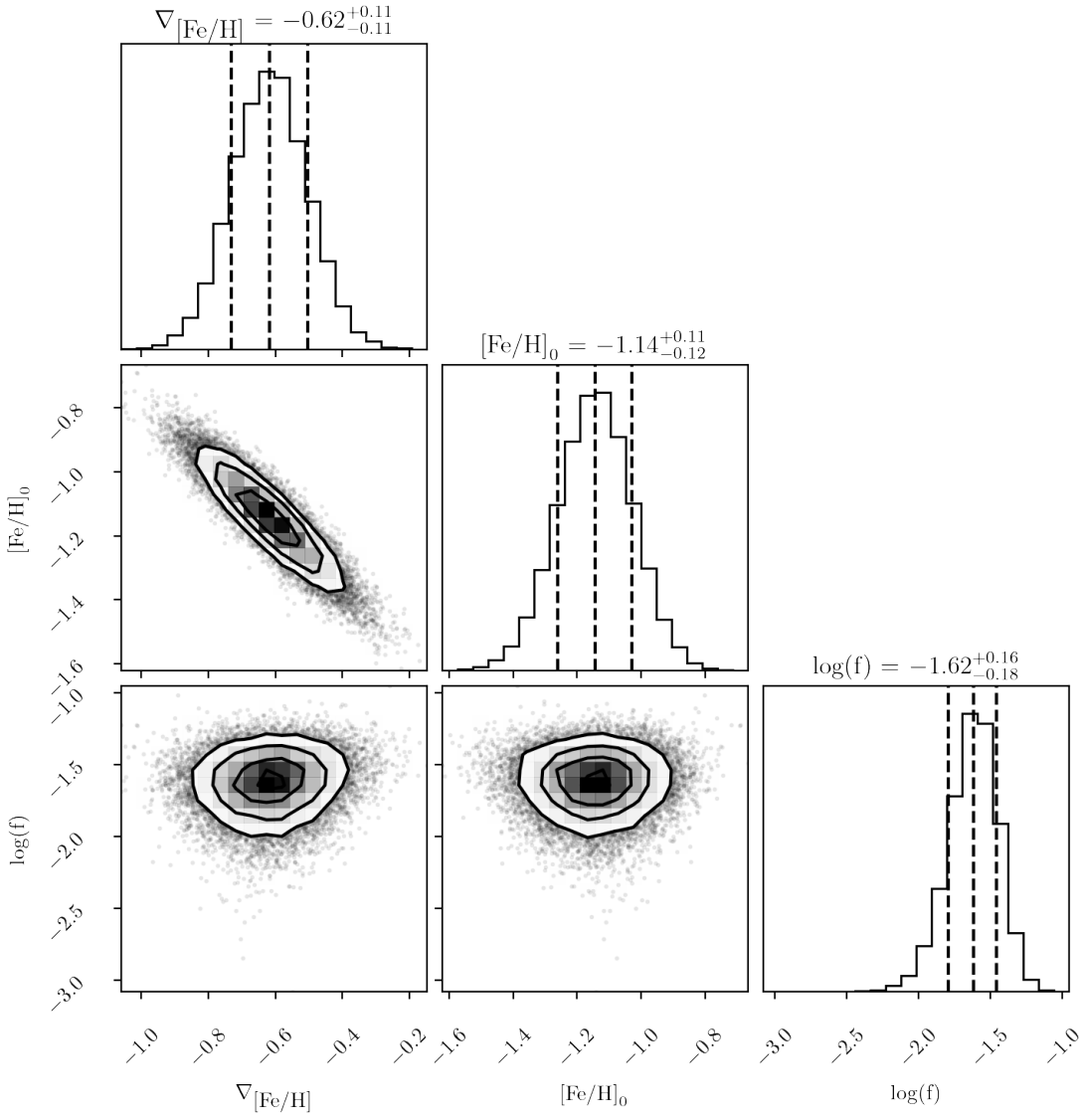


Figure 4.17: Corner plot of metallicity gradient fit to Tucana's blue RGB, using elliptical R_e distance from the center of Tucana.

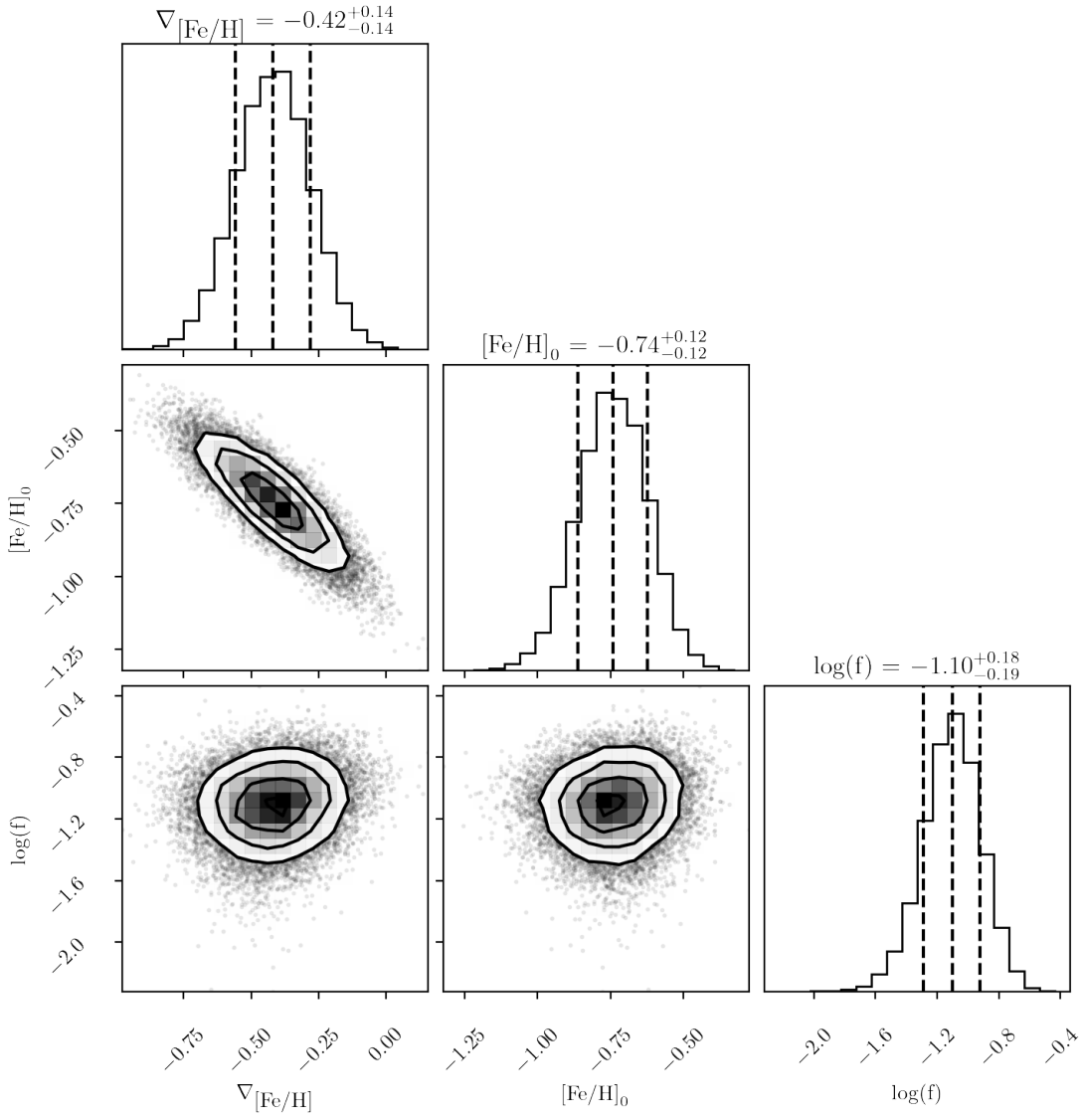


Figure 4.18: Corner plot of metallicity gradient fit to Tucana's red RGB, using elliptical R_e distance from the center of Tucana.

Table 4.4: Metallicity Measurements for All Stars

Star	R.A. (deg)	Decl. (deg)	F814W (mag)	F475W (mag)	F395N (mag)	VI (mag)	CaHK (mag)	[Fe/H] (dex)	Split RGB?
0	340.467365	−64.418107	20.760 ± 0.001	23.132 ± 0.002	25.762 ± 0.110	2.372 ± 0.002	−0.928 ± 0.110	$-1.33^{+0.12}_{-0.09}$ ± 0.2 (syst.)	R
1	340.503553	−64.424886	20.911 ± 0.001	23.068 ± 0.003	25.397 ± 0.129	2.157 ± 0.003	−0.907 ± 0.120	$-1.19^{+0.33}_{-0.26}$ ± 0.2 (syst.)	B
2	340.446929	−64.422353	20.876 ± 0.001	23.150 ± 0.002	26.046 ± 0.131	2.274 ± 0.002	−0.515 ± 0.130	> -0.83	R
3	340.408890	−64.416230	20.848 ± 0.001	23.075 ± 0.002	25.281 ± 0.065	2.227 ± 0.002	−1.134 ± 0.060	$-1.61^{+0.11}_{-0.06}$ ± 0.2 (syst.)	R
4	340.442112	−64.423851	20.899 ± 0.001	23.176 ± 0.002	25.617 ± 0.086	2.277 ± 0.002	−0.974 ± 0.080	$-1.35^{+0.16}_{-0.16}$ ± 0.2 (syst.)	R
7	340.432550	−64.416440	20.962 ± 0.001	23.069 ± 0.002	25.215 ± 0.064	2.107 ± 0.002	−1.015 ± 0.060	$-1.44^{+0.31}_{-0.22}$ ± 0.2 (syst.)	B
8	340.454107	−64.428709	20.977 ± 0.001	23.111 ± 0.002	25.130 ± 0.061	2.134 ± 0.002	−1.182 ± 0.060	$-1.77^{+0.18}_{-0.11}$ ± 0.2 (syst.)	B
9	340.496129	−64.411772	21.011 ± 0.001	23.226 ± 0.003	25.644 ± 0.089	2.215 ± 0.003	−0.904 ± 0.080	$-1.24^{+0.32}_{-0.37}$ ± 0.2 (syst.)	R
10	340.474934	−64.427693	21.041 ± 0.001	23.250 ± 0.003	25.787 ± 0.108	2.209 ± 0.003	−0.777 ± 0.100	$-0.97^{+0.29}_{-0.25}$ ± 0.2 (syst.)	R
13	340.466732	−64.418331	21.071 ± 0.001	23.151 ± 0.002	25.193 ± 0.062	2.080 ± 0.002	−1.078 ± 0.060	$-1.64^{+0.25}_{-0.21}$ ± 0.2 (syst.)	B

Note. Measurements for the full sample of stars analyzed in this work. The "Split RGB?" column indicates whether the star was used for characterizing the bifurcated RGB ("B" for the blue RGB, "R" for the red RGB) or not used at all ("0") because it did not pass the magnitude cut described in Section 4.5. Time series HST data suggests that star 22 is variable, so its metallicity measurement may not be fully reliable. A portion of the table is presented here for form and content.
(This table is available in its entirety in machine-readable form.)

Table 4.5: EMP Star ([Fe/H] < -3.0) Candidates

Star	R.A. (deg)	Decl. (deg)	F814W (mag)	F475W (mag)	F395N (mag)	VI (mag)	CaHK (mag)	[Fe/H] (dex)	Split RGB?
139	340.468741	−64.438595	22.237 ± 0.002	23.933 ± 0.003	25.057 ± 0.060	1.696 ± 0.004	−1.420 ± 0.060	$-3.04^{+0.46}_{-0.43} \pm 0.5$ (syst.)	B
222	340.487658	−64.410618	22.765 ± 0.002	24.289 ± 0.004	25.172 ± 0.059	1.524 ± 0.004	−1.403 ± 0.050	$-3.35^{+0.44}_{-0.37} \pm 0.5$ (syst.)	0
254	340.439639	−64.405761	22.933 ± 0.003	24.487 ± 0.005	25.505 ± 0.080	1.554 ± 0.006	−1.313 ± 0.080	$-3.15^{+0.49}_{-0.51} \pm 0.5$ (syst.)	0
297	340.470610	−64.433967	23.129 ± 0.003	24.655 ± 0.005	25.655 ± 0.081	1.526 ± 0.006	−1.289 ± 0.080	$-3.16^{+0.43}_{-0.49} \pm 0.5$ (syst.)	0
301	340.467641	−64.404654	23.148 ± 0.003	24.641 ± 0.005	25.623 ± 0.084	1.493 ± 0.006	−1.257 ± 0.080	$-3.11^{+0.54}_{-0.50} \pm 0.5$ (syst.)	0
302	340.504043	−64.411705	23.156 ± 0.003	24.659 ± 0.005	25.627 ± 0.091	1.503 ± 0.006	−1.287 ± 0.090	$-3.15^{+0.44}_{-0.53} \pm 0.5$ (syst.)	0
323	340.446389	−64.425761	23.284 ± 0.003	24.799 ± 0.005	25.854 ± 0.107	1.515 ± 0.006	−1.217 ± 0.100	$-3.02^{+0.49}_{-0.56} \pm 0.5$ (syst.)	0
329	340.403822	−64.427680	23.310 ± 0.003	24.813 ± 0.005	25.851 ± 0.107	1.503 ± 0.006	−1.217 ± 0.100	$-3.01^{+0.50}_{-0.57} \pm 0.5$ (syst.)	0

Note. The eight EMP ([Fe/H] < -3.0) star candidates identified in our work.
(This table is available in its entirety in machine-readable form.)

Table 4.6: MR Stars ([Fe/H] > -1.0)

Star	R.A. (deg)	Decl. (deg)	F814W (mag)	F475W (mag)	F395N (mag)	VI (mag)	CaHK (mag)	[Fe/H] (dex)	Split RGB?
2	340.446929	−64.422353	20.876 ± 0.001	23.150 ± 0.002	26.046 ± 0.131	2.274 ± 0.002	−0.515 ± 0.131	> -0.83	R
10	340.474934	−64.427693	21.041 ± 0.001	23.250 ± 0.003	25.787 ± 0.108	2.209 ± 0.003	−0.777 ± 0.108	$-0.97^{+0.36}_{-0.29} \pm 0.2$ (syst.)	R
15	340.432114	−64.414623	21.120 ± 0.001	23.352 ± 0.003	26.205 ± 0.134	2.232 ± 0.003	−0.495 ± 0.134	> -0.90	R
21	340.420288	−64.416096	21.185 ± 0.001	23.394 ± 0.003	26.016 ± 0.123	2.209 ± 0.003	−0.692 ± 0.123	$-0.78^{+0.42}_{-0.34} \pm 0.2$ (syst.)	R
27	340.461866	−64.417534	21.289 ± 0.001	23.399 ± 0.003	25.905 ± 0.121	2.110 ± 0.003	−0.659 ± 0.121	$-0.63^{+0.38}_{-0.40} \pm 0.2$ (syst.)	R
34	340.491319	−64.419207	21.391 ± 0.001	23.387 ± 0.003	25.607 ± 0.083	1.996 ± 0.003	−0.774 ± 0.083	$-0.78^{+0.43}_{-0.36} \pm 0.2$ (syst.)	B
38	340.444575	−64.421917	21.470 ± 0.001	23.544 ± 0.003	26.256 ± 0.148	2.074 ± 0.003	−0.399 ± 0.148	> -0.60	R
39	340.465754	−64.426153	21.427 ± 0.001	23.324 ± 0.004	25.389 ± 0.069	1.897 ± 0.004	−0.781 ± 0.069	$-0.67^{+0.40}_{-0.42} \pm 0.2$ (syst.)	B
49	340.465457	−64.428299	21.588 ± 0.001	23.591 ± 0.003	26.147 ± 0.122	2.003 ± 0.003	−0.448 ± 0.122	> -0.66	R
51	340.446115	−64.413465	21.601 ± 0.001	23.617 ± 0.003	25.978 ± 0.115	2.016 ± 0.003	−0.663 ± 0.115	$-0.68^{+0.38}_{-0.38} \pm 0.2$ (syst.)	R

Note. MR stars ([Fe/H] > -1.0) identified in our work.
(This table is available in its entirety in machine-readable form.)

Chapter 5

Stellar Metallicities and Gradients in the Faint M31 Satellites Andromeda XVI and Andromeda XXVIII

5.1 Overview

We present $\sim$ 300 stellar metallicity measurements in two faint M31 dwarf galaxies, Andromeda XVI ($M_V = -7.5$) and Andromeda XXVIII ($M_V = -8.8$) derived using metallicity-sensitive Calcium H & K narrow-band Hubble Space Telescope imaging. These are the first individual stellar metallicities in And XVI (95 stars). Our And XXVIII sample (191 stars) is a factor of $\sim$ 15 increase over literature metallicities. For And XVI, we measure $\langle$[Fe/H]$\rangle = -2.17^{+0.05}_{-0.05}$, $\sigma_{\rm [Fe/H]} = 0.33^{+0.07}_{-0.07}$, and $\nabla_{\rm [Fe/H]} = -0.23 \pm 0.15$ dex R_e^{-1}. We find that And XVI is more metal-rich than MW UFDs of similar luminosity, which may be a result of its unusually extended star formation history. For And XXVIII, we measure $\langle$[Fe/H]$\rangle = -1.95^{+0.04}_{-0.04}$, $\sigma_{\rm [Fe/H]} = 0.34^{+0.05}_{-0.05}$, and $\nabla_{\rm [Fe/H]} = -0.46 \pm 0.10$ dex R_e^{-1}, placing it on the dwarf galaxy mass-metallicity relation. Neither galaxy has a metallicity distribution function with an abrupt metal-rich truncation, suggesting that star formation fell off gradually. The stellar metallicity gradient measurements are among the first for faint ($L \lesssim 10^6\ L_\odot$) galaxies outside the Milky Way halo. Both galaxies' gradients are consistent with predictions from the FIRE simulations, where an age-gradient strength relationship is the observational consequence of stellar feedback that produces dark matter cores. We include a catalog for community spectroscopic follow-up, including

19 extremely metal poor ([Fe/H] < -3.0) star candidates, which make up 7% of And XVI's MDF and 6% of And XXVIII's.

This chapter has been adapted from Fu, Weisz et al. (2024), which was published in the Astrophysical Journal. This chapter was coauthored by the following individuals, and is included in this dissertation with their permission: Daniel R. Weisz, Else Starkenburg, Nicolas Martin, Michelle L. M. Collins, Alessandro Savino, Michael Boylan-Kolchin, Patrick Côté, Andrew E. Dolphin, Mario L. Mateo, Francisco J. Mercado, Jenna Samuel, Nathan R. Sandford, Evan D. Skillman.

5.2 Introduction

Studies of satellite galaxies around the next-nearest spiral galaxy, M31, have proceeded alongside studies of Milky Way (MW) satellite galaxies over the last two decades. The story of M31 satellite discovery is familiar: just as advances in photometric surveys have unearthed many more MW satellites (e.g., [26], [23], [82], [170], [134]), deep and comprehensive photometric surveys have similarly built an abundant census of faint satellites around M31 (e.g., [206], [211], [197], [73]).

Emerging studies of these satellites indicate that their properties are not entirely similar to those of MW dwarf galaxies ([207], [39], [64], [266], [74]). Most notably in the ultra-faint regime ($< 10^5\ L_\odot$), their SFHs tend to be more extended than MW ultra-faint dwarf galaxies (UFDs), suggesting that the low-mass galaxies are not uniformly affected by reionization (e.g., [318], [218], [266]). The distinct SFHs of M31 satellites suggest that they experienced different chemical enrichment histories than MW UFDs. The evidence of this difference should be reflected in their stellar abundance patterns (e.g., distributions in [Fe/H], [α/Fe]), which encode information the baryonic processes (e.g., the balance of inflows vs outflows) that shaped a galaxy's evolution (e.g., [8], [315], [258]). Unfortunately, the large distance of the M31 satellites means that only the brightest have ample robust stellar abundances measured from spectroscopy ([132], [306], [169]). In fainter M31 satellites, only a handful of individual stars are bright enough for ground-based measurements [164].

Photometric metallicity measurement techniques enable recovery of stellar metallicities for fainter stars lower down a galaxy's luminosity function by imaging in filters specifically designed to trace strong, metallicity-sensitive features in stellar spectra. They are an important complement to ongoing spectroscopic efforts to study the M31 dwarf population in great detail. This is a well-established technique that has been utilized for decades of MW studies, including to the present (e.g., [293], [24], [291], [57], [200]). From space, our team has already applied this imaging technique

using HST/WFC3 imaging in the narrow-band $F395N$ filter, targeting the Ca H&K lines, to great success for Milky Way UFDs ([96, 97]), and to a distant isolated dwarf galaxy on the outskirts of the Local Group (Tucana; [99]). The singular and singularly important contribution HST has made to the field of resolved stellar metallicity measurements is enabling measurements for stars 1-2 magnitudes fainter than currently reachable by any ground-based spectroscopic or imaging facility to-date.

In this paper, we present results from an HST program to apply the narrow-band CaHK photometric imaging technique to two of M31's UFD satellite galaxies: Andromeda XVI (And XVI) and Andromeda XXVIII (And XXVIII).

And XVI is a rare system among the ~ 100 cataloged low-mass galaxies in the Local Group [138]. Its stellar mass ($M_V = -7.5$, $M_\star \sim 10^5 M_\odot$) places it among the brightest "ultra-faint" dwarf galaxies (UFDs) known in the LG [277]. At 280 kpc from M31 [265], And XVI lies beyond the spiral's virial radius. While the vast majority of UFDs are characterized by metal-poor, ancient stellar populations that are associated with formation at times during or prior to reionization, deep HST imaging revealed that And XVI only had a low-level of star formation at the earliest times, and instead experienced, extended star formation that lasted until ~ 6 Gyr ago ($z \lesssim 1$; [318], [218], [282]). And XVI's prolonged SFH provided a new link between the faintest UFDs that appear to be quenched by reionization and more massive "classical" dwarfs whose growth appears unaffected by reionization. Detailed stellar MDFs are a crucial component of characterizing the physics driving these remarkable properties, but prior to this work, there have been no resolved stellar metallicity measurements in And XVI: Keck/DEIMOS spectroscopy was only able to obtain mean metallicity measurements $\langle$[Fe/H]$\rangle = -2.1 \pm 0.2, -1.9 \pm 0.2$, and -2.0 ± 0.1 by stacking low-S/N stellar spectra ([179], [62], [63]).

And XXVIII ($M_\star \sim 10^{5.5}\ M_\odot$) is a faint galaxy located ~ 370 kpc from the center of M31 [283, 265]. More massive than And XVI, its SFH is also more strongly weighted to old ages: the majority of its stars formed 12 Gyr ago, with a small remaining fraction forming as recently as 8 Gyr ago; these SFH properties are comparable to that of the Ursa Minor and Draco dSphs [282]. Using Keck/DEIMOS spectroscopy, [284] measured Calcium triplet metallicities for thirteen stars in And XXVIII, finding $\langle$[Fe/H]$\rangle = -1.84 \pm 0.15$ dex and $\sigma_{\rm [Fe/H]} = 0.65 \pm 0.15$ dex. While these measurements are illustrative for tracing out broad properties of its MDF, they are not well-sampled enough to fully trace out its shape and define the tails.

Studying just these two galaxies can offer insight on star-forming physics in dwarf galaxies of different mass and over different timescales in an environment that is not the MW halo. Robust stellar metallicities are a critical missing piece to this emerging picture. The properties of And XXVIII and And XVI formed the basis for an

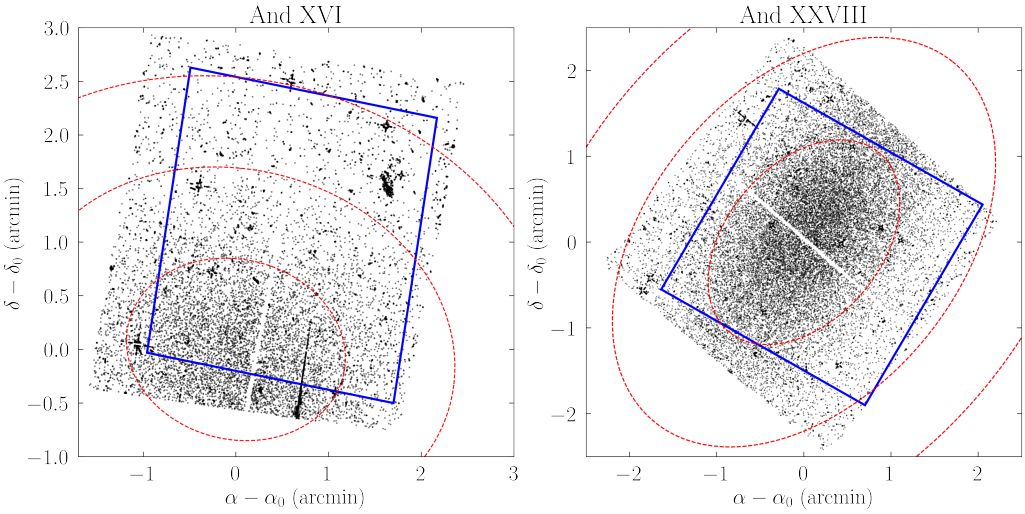


Figure 5.1: Illustrating the coverage of our HST imaging. The black dots are detected sources from the archival ACS archival image for each galaxy from which we measure broadband $F475W$ and $F814W$ photometry. The blue squares are the WFC3/$F395N$ FoV. Each galaxy's elliptical half-light contours are plotted in red, corresponding to 1, 2, and 3 half-light elliptical radii.

approved pilot HST program leveraging Ca H&K imaging on WFC3/UVIS to measure their stellar MDFs. In this paper, we present the first extensive set of resolved stellar metallicities in And XVI and And XXVIII. We present our observations in §5.3, our metallicity inference method in §5.4, and our results in §5.5. We discuss the implications of our results in §5.6, and conclude with forward-facing remarks in §5.7.

5.3 Observations & Data Reduction

We acquired new F395N imaging using HST WFC3/UVIS for And XVI and And XXVIII as part of HST-GO-16686 (PI: Weisz). Our aim was to measure metallicities for ~ 100 red giant stars in each system. Accordingly, the nominal target depth of this program aimed to collect sufficiently high SNR ($\gtrsim 10$) F395N imaging to the approximately the depth of the HB ($M_{\rm F475W} \sim +0.5$). This depth goal is slightly brighter in the more luminous systems, as reaching the HB was not necessary to acquire at least 100 stars.

Table 5.1: Dwarf Galaxy Characteristics

Parameter	And XVI	And XVI Reference	And XXVIII	And XXVIII Reference
R.A. (deg.)	14.8762500	[198]	338.1716667	[283]
decl. (deg.)	32.3761111	"	31.2161667	"
Ellipticity	0.29 ± 0.08	"	0.34 ± 0.13	"
P.A. (deg.)	99 ± 9	"	39 ± 16	"
r_h (arcmin)	1.0 ± 0.1	"	1.11 ± 0.21	"
$E(B-V)$	0.0568	[267]	0.0758	[267]
$(m-M)_0$ (mag)	23.57 ± 0.08	[265]	24.36 ± 0.05	[265]
M_V (mag)	-7.5 ± 0.03	"	$-8.8^{+0.4}_{-1.0}$	"
Luminosity ($\log_{10} L_\odot$)	4.9	"	5.5	"
$M_\star$ ($\log_{10} M_\odot$)	5.2	"	5.8	"
$D_\odot$ (kpc)	517 ± 19	"	745 ± 17	"
D_{M31} (kpc)	280^{+26}_{-27}	"	$368.8^{+7.8}_{-7.3}$	"
r_h in WFC3 FOV	2.7	This work	2.43	This work
F475W exp. time (s)	17194	[282]	26360	[282]
F814W exp. time (s)	13622	"	20880	"
F395N exp. time (s)	30154	This work	24869	This work
F395N obs. dates	Jan. 9–15, 2023	"	Nov. 21–23, 2022	"

Note. Observational characteristics of And XVI and And XXVIII. F395N data are taken for this work from HST GO-16686 (PI: Weisz). Archival broadband data are from the ISLAndS program [282]: GO-13028 (PI: Skillman) for And XVI ([318]; [218]; [282]), and GO-13739 (PI: Skillman) for And XXVIII.

Imaging was acquired between November 21, 2022 and January 15, 2023. We summarize our observations in Table 5.1. We also targeted And XV, but the observations, and the repeat observations, failed due to issues with guide star acquisition.

We centered our UVIS fields on existing HST/ACS broadband F475W and F814W imaging from the ISLAnds program [282]. We used sub-pixel dithers to sample the point spread function, improve cosmic ray rejection, etc. and used the post-flash level (`FLASH`= 20) advised by STScI to mitigate CTE effects. We observed And XI for 11 orbits and And XXVIII for 9 orbits. Visits for both sets of observations consisted of 1-2 orbits. Long integrations were used in order to increase the S/N for bright stars in order to aid with astrometric alignment of the images. More observational details can be found in our public Phase II file. Figure 5.1 shows the WFC3 footprint overlaid on the ACS image of each galaxy, overplotted with elliptical contours at 1, 2, and 3 half-light radii.

We performed point spread function (PSF) photometry simultaneously on all F395N, F475W, and F814W HST images of And XVI and And XXVIII using DOLPHOT ([78], [76]). DOLPHOT is a crowded field stellar photometry package that is widely used to analyze resolved star observations of nearby galaxies and star clusters. We followed the DOLPHOT reduction procedure that our team has applied to HST Ca H&K studies of other nearby galaxies ([96, 97, 99]).

Following [97], we culled the raw DOLPHOT output in order to select high quality stars. We created a noise model for our data using $\sim 500,000$ artificial star tests (ASTs). The ASTs were distributed across the red giant branch (RGB) in F395N, F475W, and F814W, following the method described in [99].

The left column of Figure 5.2 shows the broadband $F475W - F814W$ CMDs of And XVI (top) and And XXVIII (bottom), zoomed-in on their RGBs. We use the kinematic catalogs of each dwarf used in [62, 64, 63], to remove 2 radial velocity interlopers in And XXVIII and 4 interlopers in And XVI for stars as faint as $F475W \sim 24$; these stars are represented in the figure as cyan circles. We color-code the RGB stars used in this analysis by their F395N signal-to-noise. The F395N data reached the anticipated depth (i.e., approximately the HB) in both cases. Following [97], we only measure metallicities for stars with $SNR_{\rm F395N} \geq 10$. After measuring metallicities, we remove additional obvious interlopers by hand; namely, stars whose metallicities are inconsistent with their color on the CMD (e.g., metal-rich stars on the blue end of the RGB). This resulted in the removal of an additional 3 stars in And XXVIII and 4 stars in And XVI. These vetting results are within the range of predicted MW foreground contamination from the TRILEGAL model [304], which we expect to have a minimal contribution to the MDFs due to the small FoV of HST [97].

In total, our sample includes 191 stars in And XXVIII and 95 stars in And XVI.

5.4 Metallicity Property Determination

Individual Stellar Metallicities

We measure stellar metallicities following the procedures laid out in [97], with adaptations adopted in [99] for the case of dwarf galaxies with extended SFHs. Here, we briefly summarize this technique.

We construct a set of basis functions from the MESA Stellar Isochrones and Tracks (MIST) stellar evolution models [58, 79] over a range of metallicities ($-4 \leq$[Fe/H]≤ 0) for a 13 Gyr stellar population. These models are the forthcoming v2 models which are scaled to the [116] solar abundances, and include variations in [α/Fe]. Because the RGB is only weakly sensitive to age, the exact age adopted does not affect Ca H&K metallicity measurements. The basis functions are projected into the standard Ca H&K color-color space, as shown in the middle panels of Figure 5.2. The color-space is pixelated (i.e., similar to a Hess diagram used in fitting CMDs). We adopt bins that are 0.025 in size in both color indices. Each basis function is then convolved with the noise model determined from the ASTs. We compare the location of each observed star in Ca H&K color-color space to each basis function, using a Poisson likelihood function and flat priors in [Fe/H].

We follow [99] to account for the effects of varying α-elements. Specifically, for [Fe/H]< -2.0, we only use basis functions with [α/Fe]$= +0.4$ and for [Fe/H]> -1.0

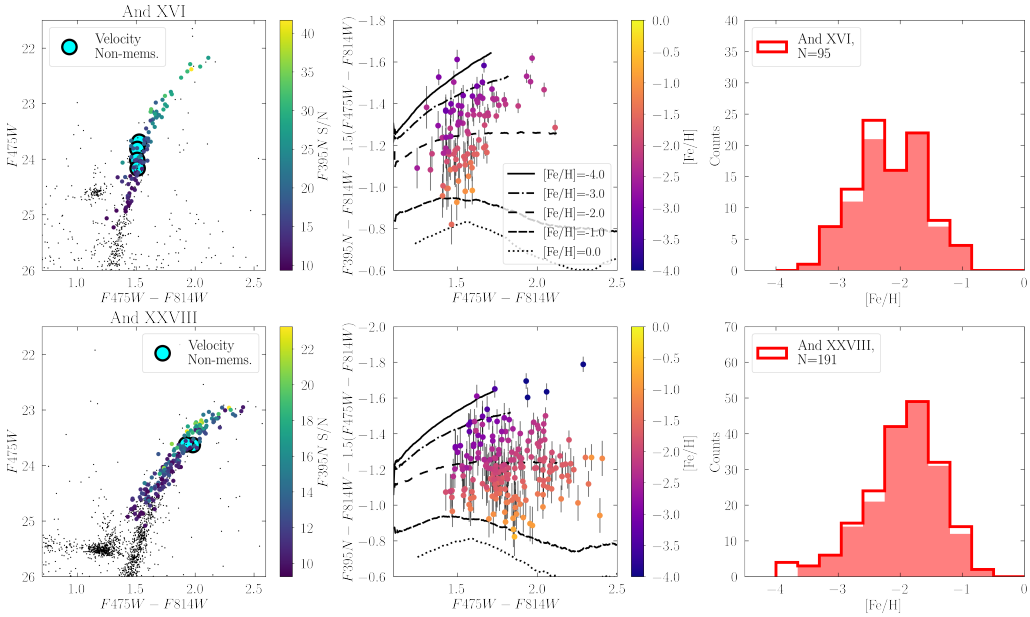


Figure 5.2: Presenting the CMD, CaHK color data, and resulting MDF for And XVI **(top row)** and And XXVIII **(bottom row)**. **Left column:** Broadband CMD of each galaxy, centered on its RGB, with stars analyzed color-coded by their $F935N$ S/N. Stars in cyan circles are velocity interlopers determined using the datasets of [62, 64, 63]. **Center column:** The position of analyzed stars in the *Pristine*-like color-color space, color-coded by their inferred metallicities. Mono-metallic CaHK tracks, convolved by the AST error profile of a star of median luminosity in each galaxy's sample, are overplotted to guide the eye. Since stars of different luminosity have different AST error profiles, the CaHK model tracks used to infer the metallicity of each star may be different from the ones presented here. Some of these metallicities are inferred upper limits due to either falling at the edge of the model grid for bright stars, or being low S/N for fainter stars. **Right column:** The resulting MDF for each galaxy. Solid histograms are well-constrained measurements, and empty histograms are stars for which we can only derive an upper limit.

we only use basis functions with [α/Fe]= +0.0. Finally, for the range $-2.0 \leq$[Fe/H]≤ -1.0, we use basis functions with [α/Fe]= +0.2. This criteria approximates the plateau, knee, and knee-to-ankle transitions known to exist in the [α/Fe] vs [Fe/H] diagrams of Milky Way satellites (e.g., [301]). As demonstrated in [96], the choice of [α/Fe] introduces a shift in metallicity measurements. For example, adopting [α/Fe]= +0.4 instead of [α/Fe]= +0.0 causes the measured metallicity to be $\sim$ 0.2 dex more metal-rich. In the current analysis technique, we do not consider any scatter in [α/Fe] at fixed [Fe/H]. In addition to random uncertainties on each star, we adopt a 0.2 dex systematic uncertainty owing to uncertainties in [α/Fe] and the impact of additional elements (e.g., [97]).

We evaluate the posterior distribution for each star using `emcee` [90]. We use 50 walkers with a burn-in time of 50 steps per star, and then sample of 10^4 steps to fill out the posterior space. We assess convergence using the Gelman-Rubin statistic ([109]).

Following past work, for stars with probability distribution functions (PDFs) that have clear peaks and are within the metallicity grid, we report the median of each PDF as the metallicity of the star, and the 68% confidence interval for the statistical uncertainty. The statistical uncertainty is set by spacing in the MIST CaHK color tracks, and photometric uncertainty. We sum the statistical uncertainties in quadrature with an additional 0.2 dex systematic uncertainty in RGB star metallicities, as determined by [97]. The handful of extremely metal-poor (EMP) stars in our sample (e.g., [Fe/H] ≤ -3.0), that have either well- or poorly-constrained PDFs (i.e. severe truncation at the grid boundary), tend to have larger statistical uncertainties owing to the closer spacing (i.e., decreased sensitivity) of Ca H&K tracks at lower metallicity. However, a star with very high photometric S/N can have a well constrained metallicity below [Fe/H] ≤ -3.0. For these stars, we increase the value of the systematic uncertainty to 0.5 dex to reflect challenges in accurately modeling metal-poor stars.

MDF Summary Statistics

We compute summary statistics (e.g., fit a Gaussian profile) for the MDFs of And XVI and And XXVIII, and spatial subpopulations, following the methods described in [99] and references therein. We compute the mean metallicity ($\langle$[Fe/H]$\rangle$) and metallicity dispersion ($\sigma_{\rm [Fe/H]}$) of the MDF by using a two-parameter Gaussian likelihood function. We assume a uniform prior on mean metallicity bounded by the most MP and MR star in the MDF. We also require the metallicity dispersion to be greater than zero. Similar to previous procedure, we adopt symmetric Gaussian uncertain-

ties on individual measurements. We sample the posterior distribution using `emcee` [90], initializing 50 walkers to run for 10,000 steps. The autocorrelation time is 50 steps, and we assess convergence using the GR statistic.

For higher-order statistics such as skew and kurtosis, we also assume symmetric Gaussian uncertainties on individual metallicitiy measurements, and use them to construct 10,000 realizations of the MDF. We measure the skew and kurtosis from each realization. We report final skew and kurtosis measurements as the median of the overall distribution, with lower and upper uncertainties set by the 16th and 84th percentiles. We present our table of summary statistics in Table 5.2, and our table of individual stellar metallicities in Table 5.4.

Measuring Metallicity Gradients

The spatial extent of our imaging enables us to characterize spatial metallicity trends across each galaxy. Thus we also quantify the strength of the gradient as the slope ($\nabla_{\rm [Fe/H]}$) obtained by fitting a line to individual stellar metallicities as a function of elliptical R_e from the center. Specifically, we follow the procedure outlined in [133] and implemented in [99], which assumes Gaussian uncertainties on our measurements. We also fit the intercept of the line ($\rm [Fe/H]_0$) and marginalize over an additional parameter f that is the fractional underestimation of measurement uncertainties. We assume uniform priors over the slope, intercept, and logarithmic fractional uncertainty. We sample the distribution using `emcee` by running 32 walkers for 10,000 steps. The burn-in time is about 50 steps. We assess convergence using the GR statistic.

5.5 Results

We present the results of our MDF measurements. The center column of Figure 5.2 presents our sample in the color-color space defined by broadband color $F475W - F814W$ and the *Pristine*-like color index ([291]; $F395N - F475W - 1.5(F475W - F814W)$). Table 5.2 summarizes our global metallicity measurements. We present individual metallicities in Table 5.4, and candidate EMP stars in Table 5.6. In the subsequent sub-sections, we discuss results for individual galaxies.

And XVI

The top row of Figure 5.2 shows the broadband CMD of our member stars (left), their position on the CaHK color space with a representative set of AST-convolved

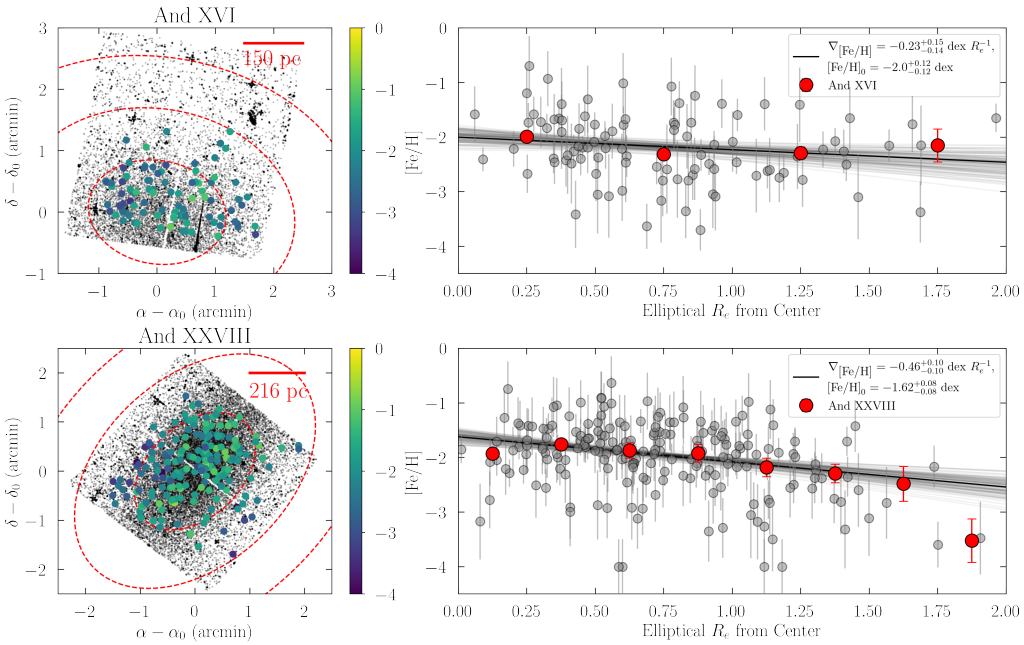


Figure 5.3: **(Left)** Spatial distribution of stars in And XVI **(top)** and And XXVIII **(bottom)**, color-coded by their inferred metallicities. Also presented are each galaxy's half-light contours at 1, 2, and 3 R_e, and a scale bar indicating physical distance. **(Right)** Result of fitting a linear model to our data as a function of elliptical half-light radius. Gray dots are individual data points in each galaxy, while red dots are the mean metallicity in spatial bins of 0.5 R_e for And XVI and 0.25 R_e for And XXVIII. We are able to robustly recover a metallicity gradient for And XXVIII. We also tentatively detect a gradient in And XVI. These are among the few metallicity gradients of M31 satellites more generally, and for And XVI, one of few gradients detected in UFDs to-date.

CaHK mono-metallic tracks (center), and the resulting MDF constructed from measurements of 95 stars (right). The stars in our MDF span a range from -3.5 to -1, with the majority of them between -2.5 and -1.5 (57 stars, 60%). Eleven (12%) stars have metallicities above -1.5. Seven stars (7%) have metallicities below -3; we designate these stars as EMP candidates. We measure an overall mean metallicity of $\langle[\mathrm{Fe/H}]\rangle = -2.17^{+0.05}_{-0.05}$, and quantify higher-order moments in the MDF. We measure a metallicity dispersion of $\sigma_{[\mathrm{Fe/H}]} = 0.33^{+0.07}_{-0.07}$. We also quantify the skew and kurtosis, but do not find deviations from Gaussianity at a $2\,\sigma$ significance. Visually, there appears to be a double peak in its MDF (e.g. Figure 5.2) at ~ -2.5 and ~ -1.7, though the peaks may become washed out by moving a handful of stars within uncertainty into an adjacent bin.

To-date, mean metallicity determinations of And XVI are from co-addition of S/N $\gtrsim 3$ spectra in the Ca II triple line regime ([63], [179], using the [289] calibration), which finds a mean metallicity of $\langle[\mathrm{Fe/H}]\rangle = -2.0 \pm 0.1$. Our mean metallicity is in good agreement with this coarser determination, and places And XVI within 1 σ scatter of the dwarf galaxy mass-metallicity relation [166].

We measure the metallicity gradient in And XVI to 2 R_e. In the top row of Figure 5.3, we show the on-sky spatial distribution of stars, color-coded by our measured metallicity, and their distribution as a function of R_e. We measure a gradient of $\nabla_{[\mathrm{Fe/H}]} = -0.23 \pm 0.15$ dex R_e^{-1}. We consider the implications of this measurement as tentative evidence for a metallicity gradient and discuss its implications further in Section 5.6.

And XXVIII

We present our sample and the resulting inferred MDF in the bottom row of Figure 5.2. The stellar metallicities span a range from as low as -4 to as metal-rich as -0.5. We identify 12 (6%) stars below -3 that we flag as EMP candidates for spectroscopic followup. Eight stars (4%) are more metal-rich than -1.0. The MDF is peaked at ~ -1.8, and majority of the stars (101; 53%) are between -2.0 and -1.0. We measured a mean metallicity of $\langle[\mathrm{Fe/H}]\rangle = -1.95^{+0.04}_{-0.04}$ and dispersion $\sigma_{[\mathrm{Fe/H}]} = 0.34^{+0.05}_{-0.05}$. We also find that the MDF of And XXVIII is skew-negative above 3σ significance- this is reflected in the MDF, which shows a long MP tail.

Our results expand significantly on [284], who measured individual metallicities for 13 And XXVIII stars using Gemini/GMOS spectroscopy. They measure stellar metallicities using the [50] Calcium Triplet (CaT) calibration and from Gaussian equivalent widths of the strongest two CaT lines. Their stars span a range similar to ours: -3.0 and -0.5. Due to their sparse number sampling, the stars are evenly

distributed across this range. From this dataset, they measured $\langle[\mathrm{Fe/H}]\rangle = -1.84 \pm 0.15$, which is in good agreement with our mean metallicity measurement. Their metallicity dispersion measurement of 0.65 ± 0.15 disagrees with our measurement by 2σ. This discrepancy is in part due to the improved sampling of our MDF about the mean. Spatial sampling also matters here, given the strong metallicity gradient in And XXVIII: the broader spatial coverage of the [284] dataset gives MP stars more weight in the MDF, therefore broadening the dispersion.

Of the 7 stars that we have in common with [284], our metallicities appear to be more MR by $\sim$ 1 dex, but this disagreement is also within their uncertainties ($\sim 0.5 - 1.0$ dex). The formal level of agreement between our measurements is 1 σ. As shown in Figure 6 of [99], our CaHK metallicities are generally in agreement with CaT metallicities from the literature which themselves are derived from different implementations of the CaT calibration.

We resolve a strong gradient for And XXVIII of $\nabla_{[\mathrm{Fe/H}]} = -0.46 \pm 0.10$ dex R_e^{-1}. We present the spatial distribution of stars and their metallicity as a function of R_e in Figure 5.3. Here, the spatial concentration of metal-rich stars in comparison to metal-poor stars is apparent even by eye. We attempted to formally measure the scale radii of the metal-poor and metal-rich stars, but did not find a difference– this is likely because our data do not span sufficient area across the galaxy. Our measurement shows that there is a ~ 0.9 dex difference in mean metallicity between the population at the center of the galaxy and the population out at 2 R_e, across ~ 430 pc. We explore the implications of this gradient more in §5.6.

5.6 Discussion

MDFs: Context and Interpretation

Within the M31 satellite system, the most well-sampled stellar spectroscopic measurements have mostly been made in the more massive satellites [306, 131, 169]. Due to the difficulty of measuring metallicities for individual stars at the large distance of M31 satellites, most metallicities to-date are measured by stacking low S/N stellar spectra or using estimates from broadband photometry (e.g., [63], [196]). These studies report mean metallicities from the result of spectral stacking and provide little information on MDFs.

Of the few faint M31 dwarfs with individual star spectroscopic metalliciites [164], in terms of stellar mass, And V ($M_\star = 10^{5.8}$ $M_\odot$, 81 stars out to 2.5 R_e) is closest to And XXVIII and And X ($M_\star = 10^{5.1}$ $M_\odot$, 21 stars out to 1.5 R_e) is closest to And XVI. The mean metallicities of the dwarf galaxies in each respective comparison

Table 5.2: Metallicity Properties of And XVI and And XXVIII

Feature	**Parameter**	**And XVI**	**And XXVIII**
Global MDF	N	95	191
	$\langle$[Fe/H]$\rangle$	$-2.17^{+0.05}_{-0.05}$	$-1.95^{+0.04}_{-0.04}$
	$\sigma_{\rm [Fe/H]}$	$0.33^{+0.07}_{-0.07}$	$0.34^{+0.05}_{-0.05}$
	Skew	$-0.14^{+0.25}_{-0.24}$	$-0.59^{+0.17}_{-0.18}$
	Kurtosis	$0.21^{+0.53}_{-0.38}$	$-0.76^{+0.10}_{-0.39}$
Metallicity gradient	R_e extent	2	2
	$\nabla_{\rm [Fe/H]}$ (dex R_e^{-1})	-0.23 ± 0.15	-0.46 ± 0.10
	$\nabla_{\rm [Fe/H]}$ (dex arcmin^{-1})	-0.27 ± 0.14	-0.30 ± 0.10
	$\nabla_{\rm [Fe/H]}$ (dex kpc^{-1})	-1.8 ± 0.9	-1.39 ± 0.44
Inner Re	N	72	144
	$\langle$[Fe/H]$\rangle$	$-2.15^{+0.07}_{-0.07}$	$-1.86^{+0.04}_{-0.04}$
	$\sigma_{\rm [Fe/H]}$	$0.37^{+0.08}_{-0.08}$	$0.33^{+0.06}_{-0.07}$
	Skew	$-0.17^{+0.27}_{-0.26}$	$-0.52^{+0.23}_{-0.24}$
	Kurtosis	$0.15^{+0.55}_{-0.40}$	$1.02^{+0.73}_{-0.54}$
Outer Re	N	23	47
	$\langle$[Fe/H]$\rangle$	$-2.23^{+0.10}_{-0.10}$	$-2.28^{+0.10}_{-0.11}$
	$\sigma_{\rm [Fe/H]}$	$0.25^{+0.14}_{-0.14}$	$0.52^{+0.11}_{-0.10}$
	Skew	$-0.09^{+0.48}_{-0.49}$	$-0.39^{+0.27}_{-0.26}$
	Kurtosis	$-0.13^{+0.96}_{-0.60}$	$-0.15^{+0.55}_{-0.40}$

Table 5.3: **Note.** Summarizing metallicity properties of And XVI and And XXVIII derived from this work, along with the number of stars used to infer each property.

pair are comparable, and places them within scatter on the universal dwarf galaxy mass-metallicity relation. Like And XXVIII, And V also has an MDF with a long MP tail. The MDF of And X is also symmetric like that of And XVI, but does not include any stars more metal-rich than −1.5. The MDFs of And V and And X both have 3 stars below [Fe/H] < −3.0. The percentage of EMP stars in And V and And XXVIII are similar. And X has a higher fraction of EMP stars than And XVI, although the sample size of And X's MDF is smaller. Owing to their large distances and weak lines, EMP stars in the M31 satellite system have not been extensively identified in detail in the way that they have been in, e.g., MW satellites [288]. The EMP candidates we designate in this study will be valuable spectroscopic follow-up targets in the era of ELT spectroscopy.

And XXVIII

From the compilation of properties of MW satellites by [166], the closest luminosity analogs to And XXVIII ($L \sim 10^{5.5}\ L_\odot$) are Ursa Minor ($\langle$[Fe/H]$\rangle = -2.13$, $\sigma_{\rm [Fe/H]} = 0.43$), Draco ($\langle$[Fe/H]$\rangle = -1.98$, $\sigma_{\rm [Fe/H]} = 0.42$), and Canes Venatici I ($\langle$[Fe/H]$\rangle = -1.91$, $\sigma_{\rm [Fe/H]} = 0.44$). Comparing qualitatively to these MDFs, the MDF of And XXVIII resembles those of Draco and Canes Venatici I in that the MDFs of all three galaxies are characterized by long, MP tails. In contrast, the MDF of Ursa Minor is more symmetric, with a slightly longer MR tail. Quantitatively, the mean metallicity of And XXVIII is comparable to all three galaxies, although its metallicity dispersion is smaller by ~ 0.1 dex. This smaller dispersion is due to the MP side of the MDF: we assume large uncertainties on our EMP star candidates, which downweighs the most MP stars' contributions to the metallicity dispersion. A re-inference of And XXVIII's MDF without assuming our adopted systematic uncertainties, which mostly affect the most metal-poor stars, yields $\langle$[Fe/H]$\rangle = -1.99 \pm 0.05$ and $\sigma_{\rm [Fe/H]} = 0.54 \pm 0.04$. This suggests that differences in σ for the MW satellites and And XXVIII are not significant. The higher order moments in their MDFs are also comparable.

And XVI

At $L \sim 10^{4.9}\ L_\odot$, And XVI is classified as one of the most luminous ultra-faint dwarf galaxies ($L < 10^5\ L_\odot$; [277]) in the LG . Its closest luminosity analog among MW UFDs is Eri II ($L \sim 10^{4.8}\ L_\odot$, $\langle$[Fe/H]$\rangle = -2.63 \pm 0.06$, $\sigma_{\rm [Fe/H]} = 0.26^{+0.08}_{-0.09}$; [68], [180], [96]). Compared to Eri II, the MDF of And XVI is more MR by 0.5 dex. Since MW UFDs fainter than Eri II also have mean metallicities of about [Fe/H] ~ -2.6

[97], And XVI is more MR than MW UFDs by a similar amount. While And XVI also has an MP tail, it also has a higher fraction of stars more MR than [Fe/H] = −2.0, and, subsequently, a higher $\sigma_{\rm [Fe/H]}$. This may be attributable to its extended SFH relative to Eri II, which allows more time for subsequent generations of stars to enrich. The gradual fall-off of And XVI's MDF suggests that it likely did not experience rapid truncation of SF (e.g., via ram pressure stripping or strong feedback) during the final epochs of its star formation.[1]

The HST CMD-based SFH of And XVI shows that it had two major episodes of SFH: one at 13 Gyr ago that formed $\sim 50\%$ of its stellar mass before being quenched at a time corresponding to reionization, and then another SF at 8 Gyr that built up the remainder of the galaxy's stellar population ([318], [218], [282]). Given this SFH, a speculative interpretation of its potentially double-peaked MDF is that the MP peak ([Fe/H] = −2.5) and MR ([Fe/H] = −1.7) peak respectively correspond to its first and second major episodes of star formation. Following this narrative thread, and assuming a present-day $M_\odot/L_\odot = 2$, And XVI at 13 Gyr ago may have had $M_\star \sim 8 \times 10^4\ M_\odot$, with a mean stellar metallicity of −2.5. At this time, its stellar mass and mean metallicity would have been very comparable to the present-day mass of MW UFDs CVn II, Hya II, and Eri II [250, 97, 317].

However, the age-metallicity relation (AMR) of And XVI from the HST CMD modeling measured by [218] is flat and therefore does not suggest metallicity evolution as a function of time. The uncertainties on the metallicities from the AMR encompass the peaks of the MDF, so it's possible that SFH studies may not have the metallicity sensitivity to be able to resolve this enrichment scenario. Moreover, [218] only use Solar-scaled stellar models, which may not be accurate for the lower metallicity stars in And XVI, possibly affecting the metallicity inference. Obtaining more stellar metallicities through deeper HST CaHK imaging of the current And XVI field, or HST CaHK and broadband imaging across a different field in the galaxy may be the best way to determine whether the double peaked feature in the MDF is real.

Metallicity Gradients in M31 Dwarf Galaxies

From 95 stars spread over 2 R_e, we measure a metallicity gradient in And XVI at 1.5-σ significance. The identification of a gradient in And XVI is interesting, as the extent to which lower-mass galaxies like UFDs can host metallicity gradients, and what the origins of their gradients could be, is still unknown. There are many ongoing efforts to detect stars in the outskirts of MW UFDs, which tend to be even lower in

[1] A stark contrast is the MDF of the more massive And XVIII, which sharply truncates at [Fe/H] = −1.0; this cut-off has been attributed to a sudden stop to star formation [169].

stellar mass than And XVI ([314], [185], [297], [233]). Among these studies, two have suggested the existence of metallicity gradients in the studied UFDs. In Eri II, the metallicities of 67 RR Lyrae stars out to 2 R_e trace out a gradient of ~ 0.3 *dex* R_e^{-1} [202].[2] In the lower mass Tucana II ($L_\star \sim 3 \times 10^3$ $L_\odot$), the metallicity difference between the inner regions ([Fe/H] $= -2.6$) and the two MP ([Fe/H] $= -3.0$) stars beyond 2.5 R_e forms the basis for the gradient [54]. The differential variations here are comparable to the gradient strength that we measure in And XVI.

Given the intrinsic difficulty of detecting metallicity gradients in faint galaxies (e.g., few stars available for targeting, coverage and selection effects), we consider the implications of a metallicity gradient in And XVI. One of its most notable differences from other known UFDs is an extended SFH: MW UFDs universally have old stellar populations of $\sim$ 13 Gyr [41, 319, 250], as do the majority of M31 UFDs with published SFHs [266]. Simulations have posited that metallicity gradients can form in dwarf galaxies more massive than And XVI via mechanisms that require an extended SFH: e.g., stellar feedback from young, short-lived stars that preferentially push old, metal-poor stars to a galaxy's outskirts (FIRE simulations; [16, 214]), gas accretion which triggers centrally-concentrated star formation (e.g., [271]). The detection of a gradient in And XVI, which lies at the threshold of the nominal division ($M_\star \sim 10^5$ $M_\odot$) between UFDs and classical dwarf galaxies, may suggest that similar physics can be significant in shaping the evolution of UFDs at the mass of And XVI. As we discuss later in this section, additional theoretical work is necessary to determine the mechanisms for stellar metallicity gradient formation in such low-mass systems.

We resolve a strong, highly-significant (4.6-σ) metallicity gradient in And XXVIII, where the average metallicity at the center of the galaxy is more MR than stars at 2 R_e by 0.9 dex. A more general population gradient in And XXVIII was also observed by [284] in the different spatial concentrations of its red and blue horizontal branch stars. In addition, stars between 1 and 2 R_e in And XXVIII have a larger metallicity dispersion than stars in its center, which is also seen in the spatially extended metal-poor population of Ursa Minor [235]. Among Local Group dwarf galaxies with population gradients, spatially-compact metal-rich populations and comparatively spatially diffuse metal-poor populations can also have different kinematics (e.g., [21], [310], [154], [235]). The presence or absence of this feature may point to different origins for forming the gradient (e.g., kinematic differences suggestive to dwarf-dwarf mergers; [295]). In this context, And XXVIII is also an ideal target for spectroscopic studies to obtain kinematic information, enabling a full

[2]Our own analysis of Eri II's inner R_e using HST CaHK imaging did not uncover a gradient [96]. The area is small and we did not consider α-enhancements in that analysis, which may contribute to our result.

chemodynamic characterization of the system and its formation history.

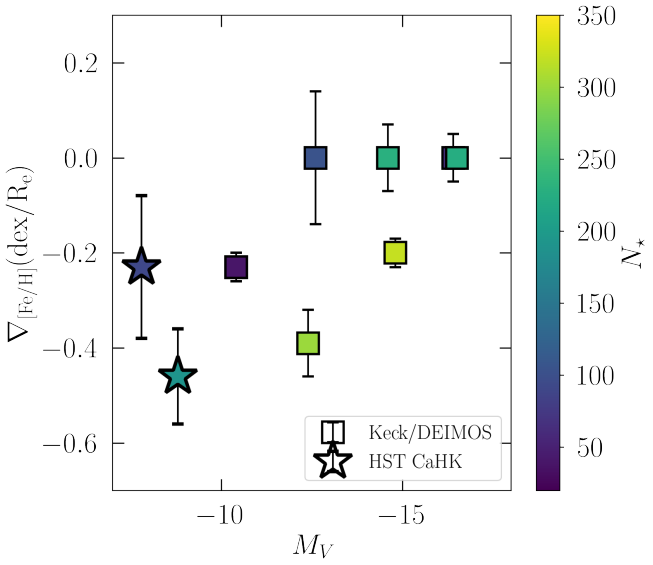


Figure 5.4: Contextualizing our gradient measurements for And XVI and And XXVIII in the current landscape of gradients in M31 dwarfs. Literature gradients for M31 satellites are from the re-analysis of the [131] dataset in [295, NGC205, NGC185, NGC 147, And VII], and [169, And XVIII]. The galaxies are color-coded by the number of stars used to make the gradients measurement. We have measured gradients in these faint galaxies using a comparable number of stars that Keck/DEIMOS spectroscopy was able to reach in dwarf galaxies several orders of magnitude more luminous.

Metallicity gradients are common among "classical" Local Group dwarf galaxies. They have been observed within galaxies spanning a range of kinematic properties, isolated/satellite status, and stellar mass [295]. Within the M31 system, however, metallicity gradients have only been measured in three satellites to-date: And II ($\nabla_{[Fe/H]} = -0.39 \pm 0.07$ dex R_e^{-1}) and NGC 185 ($\nabla_{[Fe/H]} = -0.20 \pm 0.03$ dex R_e^{-1}) from the [306] and [131] dataset that was re-analyzed by [295], and And XVIII ($\nabla_{[Fe/H]} = -0.23 \pm 0.03$ dex R_e; [169]).[3]

[3]Despite measuring the gradient from only 38 stars, the reported uncertainties in And XVIII are smaller than from gradient measurements made with hundreds of stars as in the case of the previous work. [169], as well as [306] and [131], used a least-squares method to infer their gradi-

In Figure 5.4, we emphasize the novelty of our measurements from this paper within the landscape of gradient measurements in M31 dwarfs. In more luminous M31 dwarf galaxies, Keck/DEIMOS spectroscopy has been used to constrain metallicity gradients from measurements of hundreds of stars. In fainter M31 satellites, there simply aren't enough bright stars to construct comparably well-populated MDFs using spectra. The CaHK-based MDFs in this paper, however, can provide large samples of metallicities, enabling the construction of MDFs that are as robust as the more luminous M31 satellites.

Metallicity gradients are one of the few observationally accessible signatures of baryonic processes that shape both luminous and dark matter. For example, stellar feedback has long been invoked as a mechanism for transforming initially cuspy dark matter haloes into cores ([230], [112], [104], [190]). Through this mechanism, cored DM profiles would therefore be consistent with a ΛCDM universe, providing resolution to the long-standing "core-cusp" problem. As one example in the contemporary literature, the FIRE-2 simulations of isolated dwarf galaxies predict a relationship between gradient strength and mean stellar age in dwarf galaxies [214] that would arise as a result of these feedback processes that also produce dark matter cores.

We show this relation in Figure 5.5 and compare it to data. In the left panel, we plot the linear form of the relation fit to [214] simulations, properties of the publicly-available simulated FIRE dwarfs, and the gradient measurements of M31 dwarfs, including those derived in this work. With the exception of And XVIII [154], the mean galaxy ages (t_{50}) are taken from Savino et al. (in prep.) which use deep CMDs from the HST survey of M31 satellites to measure SFHs, and includes re-analyses of CMDs from the literature ([106], [282]).

In the right panel, we compare the same relation against gradient measurements of MW satellites from the [295] analysis, with SFHs from [319]. All dwarfs, simulated and observed, are color-coded by their stellar mass. One notable caveat to data interpretation here is that the area coverage of the SFH measurements and the spectroscopic gradient measurements are often different, with the gradient measurements spanning a larger area over the dwarf due to the nature of spectroscopic targeting.

Our measurements of And XVI and And XXVIII appear to affirm the theoretical relation quite well. This is additionally noteworthy given that the relation was derived from simulations of isolated dwarfs, not satellites. This could be because the bulk of the metallicity information was in place at early times before many of these galaxies were bound satellites. The rest of the M31 satellites, as well as the

ents, which results in smaller gradient uncertainties due to assuming known Gaussian variance on individual stellar metallicities [133]. For a more direct comparison with our inference approach, we instead adopt the [295] re-analysis where available, as we find from [99] that their Gaussian process regression method produces comparable gradient measurements to ours.

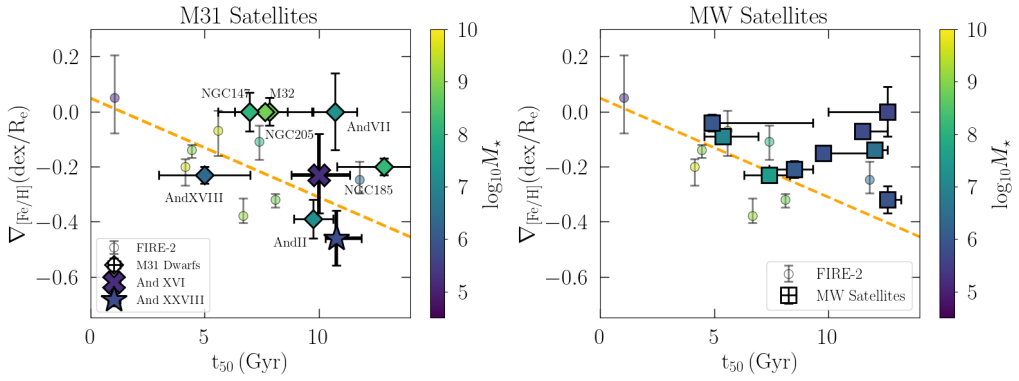


Figure 5.5: Comparing M31 and MW satellite metallicity gradients to predictions from the FIRE-2 simulations. **(Left)** Presenting gradients of M31 satellites relative to the age-metallicity gradient strength relation from FIRE-2 simulations [214]. All galaxies, simulated and observed, are color-coded by their stellar masses. The linear form of the relation is orange, and light circles denote the publicly-available FIRE-2 simulated galaxies. Diamonds are M31 satellites from the literature, and the 'X' and star points are respectively And XVI and And XXVIII. Our dwarf galaxy gradient measurements trace out the age-gradient relation. **(Right)** Presenting gradients of MW satellites as compared to the FIRE-2 simulations. The simulated relations are presented in the same fashion as the previous panel. Gradient measurements are sourced from [295]. The MW satellites show large scatter about the age-gradient relation.

MW satellites, appear to have large scatter about this relation. In particular, there are no galaxies with intermediate t_{50} that have strong gradients. The scatter in gradient strength is largest among galaxies with older stellar populations, ranging from non-detections to gradients as strong as -0.4 dex R_e^{-1}. One simple, qualitative interpretation of this picture is that old galaxies, with metallicity gradients in place in accordance to the age-gradient relation, and had their gradients flattened through close passage(s) with a more massive host that preferentially removes their MP outskirts.[4] The extent to which And XVI and And XXVIII can be described by this scenario is unclear: both currently lie beyond the virial radius of M31, and their orbital histories about M31 are not constrained due to absence of proper motions. Detailed orbital histories of LG dwarf galaxies [238, 234, 20, 30] will be key

[4]Simulations of tidal stripping in dwarf galaxies show that the outskirts of the galaxy are removed first [e.g., 239, 86].

to interpreting the various astrophysical origins of these observed gradients.

The theoretical age-gradient relation is compelling for its potential as an observational diagnostic of dark matter core formation in the dwarf galaxy population. But, its explanatory power needs refinement, given that environmental processes can also set metallicity gradients ([193], [251], [28], [123]). Comparison between observation and theory also have additional caveats, in part due to ongoing challenges in simulating low-mass galaxies to high fidelity. The faintest publicly-available FIRE-2 dwarf galaxy used to infer the age-gradient relation has $M_\star \sim 10^5$ $M_\odot$ and t_{50} of 1 Gyr; these properties are not well-matched to any LG dwarf galaxy regardless of environment, as galaxies in this mass range are dominated largely by old (< 10 Gyr), or in some cases intermediate (~ 6 Gyr) age stellar populations [e.g., 319, 102, 282].

Notably, theoretical work, including the same simulations positing the age-gradient relation, have not identified galaxy stellar mass as a strong driving factor in gradient formation [271, 243, 214]. This runs counter-intuitive to observations, which show that more massive dwarf galaxies tend to have extended SFHs, younger stars, and lower t_{50} values [319]. If stellar age indeed traces gradient strength, then this relation should also have an underlying stellar mass dependence. Given the near-uniformly old stellar ages of faint dwarf galaxies, particularly UFDs, [41, 319, 101, 250, 281], taking the age-gradient relation at face value would imply that nearly all galaxies with $M_\star < 10^5$ $M_\odot$ should have strong metallicity gradients. The current empirical landscape of faint dwarf galaxy studies does not support this prediction, although obtaining high-fidelity gradient measurements for a large sample of UFDs has also been challenging.

Still, in the regime of classical dwarf galaxies, it is notable that the population-level behavior of metallicity gradients can be interpreted as the consequence of stellar feedback-driven breathing modes that form dark matter cores ([292], [16], [214]). A natural question is how low in galaxy stellar or halo mass this framework can still apply, and relatedly, whether metallicity gradients in UFDs imply core formation at all. Indeed, whether UFDs host cores is still an open question: while simulations have suggested that stellar feedback is insufficient to sculpt cores in UFDs (e.g., [222], [14]), observations of the Eri II UFD suggest strong feedback during star formation [101, 258] and a marginally off-center star cluster that is expected to survive to $z = 0$ only if the galaxy has a cored DM profile [6, 280, 317].

The central mass profile of UFDs, and their reconciliability with small-scale predictions under CDM, remains an outstanding question [43]. On the observational side, gradient measurements in UFDs across a range of environments will be important for disentangling secular and external impacts on gradient formation. In particular, isolated low-mass galaxies ($M_\star < 10^6$ $M_\odot$) with a range of SFHs such as Leo P, Tucana B, and Pavo – that are not expected to have interacted with a

massive host throughout their lifetime – are important targets as a comparison foil for studies of MW and M31 satellites [212, 254, 153]. By nature, these high-priority targets also tend to lie at the farthest distances, making spectroscopic studies to obtain adequately sampled stellar metallicity measurements, or stellar velocities for dynamical mass profile studies, especially challenging. As our team's studies thus far have demonstrated, the stellar metallicity gradient measurements enabled by HST CaHK imaging can provide additional constraining power for various gradient formation mechanisms. On the theoretical side, detailed studies of metallicity gradients in high-fidelity simulations of dwarf galaxies, particularly in the UFD class, will be necessary for refining the interpretive lenses to bring to these observations.

5.7 Summary

In this paper, we present the first well-sampled MDFs for And XVI ($L = 10^{4.9}\ L_\odot$) and And XXVIII ($L = 10^{5.5}\ L_\odot$) based on individual stellar metallicities measured using HST Ca H&K narrow-band imaging. With a single HST pointing in each galaxy, we measure stellar metallicities with sample sizes and to precisions that ground-based Keck/DEIMOS spectroscopy has been able to attain only in M31 satellite galaxies that are hundreds or thousands of times brighter. We summarize the key results enabled by this novel dataset:

- From 95 stars in And XVI, we measure $\langle$[Fe/H]$\rangle = -2.17^{+0.05}_{-0.05}$, in good agreement with previous measurements from stacked stellar spectra. We also resolve $\sigma_{\rm [Fe/H]} = 0.33^{+0.07}_{-0.07}$. Though its MDF is well-described by a Gaussian statistically, visually it is also doubly-peaked. We also measure a metallicity gradient ($\nabla_{\rm [Fe/H]} = -0.23 \pm 0.15$ dex R_e^{-1}) at a significance of 1.5 σ.

- Compared to MW UFDs, with mean metallicities about [Fe/H] ~ -2.6 [97], And XVI is more metal-rich by ~ 0.5 dex. This property, alongside the putative double-peaked structure and the metallicity gradient, may result from its extended SFH, which is unusual among the currently-known UFD population.

- From 191 stars in And XXVIII, we measure $\langle$[Fe/H]$\rangle = -1.95^{+0.04}_{-0.04}$, $\sigma_{\rm [Fe/H]} = 0.34^{+0.05}_{-0.05}$, and a strong metallicity gradient within 2 R_e: $\nabla_{\rm [Fe/H]} = -0.46 \pm 0.10$ dex R_e^{-1}.

- And XXVIII is more metal-rich than And XVI despite its shorter star formation history; these results affirm that stellar mass is a fundamental property

setting the overall enrichment level of a galaxy [e.g., 175, 46, 192, 166]. With forthcoming chemical evolution studies, we will present a detailed characterization of the baryon cycle in galaxies of different masses with different SFHs.

- The metallicity gradient measurements for these galaxies follow the age-gradient relation predicted in the FIRE-2 simulations [214], as the observational consequence of gradients formed from the same stellar feedback hypothesized to form dark matter cores at the center of dwarf galaxy halos [292, 16].

As the only other current galactic ecosystem for which we can conduct resolved stellar population studies, M31 and its satellite system offer a necessary comparison point to the MW and its satellites. In particular, their study is critical to ongoing efforts to understand the impact of environment on dwarf galaxy evolution, the extent to which reionization has a universal impact on low-mass halos, and imprints of star formation baryonic feedback processes that can reconfigure luminous and dark matter within a galaxy. As our team has demonstrated in this paper and elsewhere, photometric metallicity techniques are an efficient way to obtain detailed pictures of stellar metallicities in distant galaxies, and will be highly complementary with future resolved stellar spectroscopy campaigns with JWST and ELT in the coming years.

5.8 Table of Metallicity Measurements

In this section, we present Table 5.4, which contains all of the individual stellar metallicity measurements for And XVI and And XXVIII. In Table 5.6, we present all of the EMP star candidates in the two galaxies.

Table 5.4: Individual Stellar Metallicities

Galaxy	Star	R.A.	Decl.	F814W	F475W	F395N	VI	Ca H and K	[Fe/H]		Notes
									Value	Uncert.	
AndXVI	0	14.883476	32.381190	20.064 ± 0.001	22.175 ± 0.002	24.056 ± 0.037	2.111 ± 0.002	−1.286 ± 0.037	$-1.77^{+0.10}_{-0.10}$	±0.2 (syst.)	Constrained
AndXVI	1	14.880947	32.381578	20.291 ± 0.001	22.333 ± 0.002	23.929 ± 0.034	2.042 ± 0.002	−1.467 ± 0.031	$-2.19^{+0.08}_{-0.07}$	±0.2 (syst.)	Constrained
AndXVI	2	14.877938	32.376751	20.332 ± 0.001	22.289 ± 0.002	23.719 ± 0.034	1.957 ± 0.002	−1.506 ± 0.031	$-2.41^{+0.09}_{-0.08}$	±0.2 (syst.)	Constrained
AndXVI	3	14.858829	32.384565	20.414 ± 0.001	22.381 ± 0.002	23.713 ± 0.024	1.967 ± 0.002	−1.618 ± 0.026	< -2.43	–	Ulim
AndXVI	4	14.894606	32.384091	20.487 ± 0.001	22.420 ± 0.002	23.788 ± 0.032	1.933 ± 0.002	−1.532 ± 0.033	$-2.46^{+0.10}_{-0.05}$	±0.2 (syst.)	Constrained
AndXVI	5	14.898027	32.374751	20.652 ± 0.001	22.532 ± 0.002	23.963 ± 0.034	1.880 ± 0.002	−1.389 ± 0.033	$-2.13^{+0.14}_{-0.16}$	±0.2 (syst.)	Constrained
AndXVI	6	14.872155	32.388600	20.995 ± 0.001	22.788 ± 0.003	24.059 ± 0.037	1.793 ± 0.003	−1.418 ± 0.033	$-2.33^{+0.17}_{-0.15}$	±0.2 (syst.)	Constrained
AndXVI	7	14.878955	32.384221	21.030 ± 0.002	22.831 ± 0.003	24.135 ± 0.035	1.801 ± 0.004	−1.397 ± 0.033	$-2.21^{+0.13}_{-0.26}$	±0.2 (syst.)	Constrained
AndXVI	9	14.906816	32.380212	21.117 ± 0.002	22.860 ± 0.003	24.134 ± 0.031	1.743 ± 0.004	−1.340 ± 0.033	$-2.07^{+0.14}_{-0.13}$	±0.2 (syst.)	Constrained
AndXVI	10	14.864351	32.377186	21.269 ± 0.002	23.013 ± 0.003	24.206 ± 0.036	1.744 ± 0.004	−1.423 ± 0.034	$-2.37^{+0.19}_{-0.25}$	±0.2 (syst.)	Constrained

Table 5.5: **Note.** Measurements for all of the stars analyzed in this work.
(This table is available in its entirety in machine-readable form in the online article.)

Table 5.6: Candidate EMP Stars

Galaxy	Star	R.A.	Decl.	F814W	F475W	F395N	VI	Ca H and K	[Fe/H]	
									Value	Uncert.
AndXVI	26	14.867180	32.379153	21.573 ± 0.002	23.239 ± 0.004	24.155 ± 0.034	1.666 ± 0.004	-1.583 ± 0.034	$-3.41^{+0.33}_{-0.39}$	± 0.5 (syst.)
AndXVI	30	14.879237	32.388930	21.763 ± 0.002	23.419 ± 0.003	24.400 ± 0.040	1.656 ± 0.004	-1.503 ± 0.040	$-3.05^{+0.41}_{-0.32}$	± 0.5 (syst.)
AndXVI	37	14.864885	32.388081	22.062 ± 0.003	23.684 ± 0.004	24.633 ± 0.044	1.622 ± 0.005	-1.484 ± 0.044	$-3.09^{+0.33}_{-0.41}$	± 0.5 (syst.)
AndXVI	50	14.864719	32.378416	22.399 ± 0.003	23.935 ± 0.005	24.800 ± 0.051	1.536 ± 0.006	-1.439 ± 0.051	$-3.05^{+0.51}_{-0.51}$	± 0.5 (syst.)
AndXVI	80	14.863572	32.377904	22.892 ± 0.004	24.352 ± 0.006	25.143 ± 0.067	1.460 ± 0.007	-1.399 ± 0.067	$-3.08^{+0.58}_{-0.58}$	± 0.5 (syst.)
AndXVI	89	14.909581	32.370058	23.232 ± 0.005	24.659 ± 0.006	25.435 ± 0.067	1.427 ± 0.008	-1.364 ± 0.067	$-3.10^{+0.59}_{-0.59}$	± 0.5 (syst.)
AndXVI	90	14.864426	32.384401	23.271 ± 0.006	24.698 ± 0.010	25.470 ± 0.076	1.427 ± 0.012	-1.369 ± 0.077	$-3.16^{+0.62}_{-0.54}$	± 0.5 (syst.)
AndXXVIII	4	338.177742	31.228019	20.673 ± 0.001	22.960 ± 0.003	24.602 ± 0.043	2.287 ± 0.003	-1.789 ± 0.043	< -4.00	–
AndXXVIII	21	338.151042	31.219175	21.171 ± 0.001	23.229 ± 0.002	24.681 ± 0.047	2.058 ± 0.002	-1.635 ± 0.047	< -4.00	–
AndXXVIII	50	338.186547	31.203947	21.456 ± 0.002	23.386 ± 0.003	24.586 ± 0.044	1.930 ± 0.004	-1.695 ± 0.044	< -4.00	–
AndXXVIII	51	338.159931	31.215765	21.477 ± 0.001	23.416 ± 0.003	24.721 ± 0.056	1.939 ± 0.003	-1.604 ± 0.056	< -4.00	–
AndXXVIII	119	338.153888	31.224333	22.311 ± 0.002	24.045 ± 0.004	24.995 ± 0.048	1.734 ± 0.004	-1.651 ± 0.048	$-3.50^{+0.38}_{-0.23}$	± 0.5 (syst.)
AndXXVIII	129	338.172690	31.217700	22.487 ± 0.003	24.144 ± 0.005	25.132 ± 0.088	1.657 ± 0.006	-1.497 ± 0.088	$-3.17^{+0.48}_{-0.48}$	± 0.5 (syst.)
AndXXVIII	134	338.155764	31.225169	22.452 ± 0.002	24.150 ± 0.005	25.218 ± 0.056	1.698 ± 0.005	-1.479 ± 0.056	$-3.18^{+0.48}_{-0.48}$	± 0.5 (syst.)
AndXXVIII	145	338.185173	31.188016	22.636 ± 0.003	24.322 ± 0.005	25.314 ± 0.074	1.686 ± 0.006	-1.537 ± 0.074	$-3.47^{+0.52}_{-0.36}$	± 0.5 (syst.)
AndXXVIII	157	338.189276	31.199485	22.746 ± 0.003	24.316 ± 0.005	25.221 ± 0.066	1.570 ± 0.006	-1.450 ± 0.066	$-3.11^{+0.48}_{-0.47}$	± 0.5 (syst.)
AndXXVIII	174	338.142529	31.212665	23.016 ± 0.004	24.598 ± 0.006	25.506 ± 0.073	1.582 ± 0.007	-1.465 ± 0.073	$-3.32^{+0.56}_{-0.46}$	± 0.5 (syst.)
AndXXVIII	192	338.151661	31.218511	23.380 ± 0.004	24.867 ± 0.006	25.770 ± 0.098	1.487 ± 0.007	-1.328 ± 0.098	$-3.05^{+0.62}_{-0.61}$	± 0.5 (syst.)
AndXXVIII	196	338.148343	31.212334	23.508 ± 0.005	25.083 ± 0.008	26.033 ± 0.101	1.575 ± 0.009	-1.412 ± 0.101	$-3.26^{+0.47}_{-0.49}$	± 0.5 (syst.)

Table 5.7: **Note.** All of our identified EMP candidates in And XVI and And XXVIII. (This table is available in machine-readable form in the online article.)

Chapter 6

Conclusion

This dissertation adds a new dimension to *HST*'s legacy in resolved stellar population studies by demonstrating its remarkable potential for extragalactic stellar metallicity measurements through metallicity-sensitive narrow-band imaging. In composite, this dissertation presents 1133 stellar metallicities measured across 16 Local Group dwarf galaxies of high scientific value. Previously in these systems, there were 176. Chapter 2 demonstrates the potential technique in the example of the Eridanus II ultra-faint dwarf galaxy, and Chapter 5 presents 473 measurements in 13 MW UFDs, doubling the number of measured stellar metallicities across the entire $\sim$ 60 known systems [277]. Chapter 4 presents the immense and unprecedented gain in stellar metallicities for the isolated ($D \sim 1$ Mpc) quenched dwarf galaxy, Tucana, which lies at the edge of the Local Group and is an important site for studying secular quenching in low-mass dwarf galaxies. Chapter 5 presents $\sim$ 300 stellar metallicities for two faint ($M_\star < 10^6\ M_\odot$) dwarf galaxies around the M31 system. Notably, it presents 95 metallicities were there were previously none in the And XVI M31 UFD satellite, which, unlike its MW UFD counterparts, formed the vast majority of its stars after reionization in multiple bursts.

The vastly expanded sample of stellar metallicities in these systems pave the way for a myriad of interpretive studies to constrain the baryon cycle of dwarf galaxies. Mean metallicity measurements in dwarf galaxies alone are already a powerful diagnostic for the prescription of feedback and stochasticity in cosmological simulations of low-mass dwarf galaxies (Chapter 3), and achieving agreement between theory and observations is an active area of ongoing work. On the level of interpreting global MDF shape, work by Sandford et al. (2024; [258]) applied the modern chemical evolution models of Weinberg et al. 2017 [315] to the *HST* MDF of Eri II (Chapter 2) to one of the first quantitative measurements of outflow strengths experienced by a $M_\star \sim 10^5 M_\odot$ galaxy over its star-forming lifetime, and this framework should

be applied to all the other MDFs as well. Finally, spatially resolved MDFs within a galaxy – i.e., metallicity gradients – are also important diagnostics of stellar feedback models and their relation to the internal dark matter structure of dwarf galaxies, and there is much theoretical work (Chapter 4, 5) that can still be done to sharpen the interpretation of dwarf galaxy metallicity gradients.

Work in this thesis also opens up a rich landscape of additional observational studies. As long as *HST* is functional, it remains a leading facility to conduct space-based extragalactic photometric metallicity studies, particularly of distant galaxies in the Local Group, and indeed, the Local Volume. The photometric metallicity capabilities of the *James Webb Space Telescope* are still yet untested, but provides a rich avenue for inquiry to extend extragalactic stellar metallicity measurements beyond what is feasible with *HST*. From the ground, the large-FoV Hyper Suprime Cam, installed on the 8.2m Subaru telescope, has added metallicity- and surface gravity-sensitive narrow-band filters to its repertoire within the last decade, and it promises unparalleled capacity for efficient, wide-field photometric metallicity studies within the Local Group.

Narrow-band studies also provide pathfinding capabilities for spectroscopic studies. With contemporary instruments on 10m-class telescopes, spectroscopy can verify galaxy membership via radial velocities, and where possible, provide another metallicity inference through spectral indices. Looking ahead to the future, work from this dissertation alone has produced a sample of $\sim$ 120 Extremely Metal Poor (EMP; [Fe/H] < -3.0) star candidates that will be priority spectroscopic follow-up targets in the era of Extremely Large Telescopes (ELTs).

Bibliography

[1] Oscar Agertz et al. "EDGE: the mass-metallicity relation as a critical test of galaxy formation physics". In: *MNRAS* 491.2 (Jan. 2020), pp. 1656–1672. DOI: 10.1093/mnras/stz3053. arXiv: 1904.02723 [astro-ph.GA].

[2] David S. Aguado et al. "The Pristine survey - VI. The first three years of medium-resolution follow-up spectroscopy of Pristine EMP star candidates". In: *MNRAS* 490.2 (Dec. 2019), pp. 2241–2253. DOI: 10.1093/mnras/stz2643. arXiv: 1909.08138 [astro-ph.GA].

[3] Saundra M. Albers et al. "Star formation at the edge of the Local Group: a rising star formation history in the isolated galaxy WLM". In: *MNRAS* 490.4 (Dec. 2019), pp. 5538–5550. DOI: 10.1093/mnras/stz2903. arXiv: 1909.04040 [astro-ph.GA].

[4] R. K. Alexander et al. "Inhomogeneous Galactic chemical evolution: modelling ultra-faint dwarf galaxies of the Large Magellanic Cloud". In: *MNRAS* 522.4 (July 2023), pp. 5415–5433. DOI: 10.1093/mnras/stad1312. arXiv: 2303.12530 [astro-ph.GA].

[5] Jairo A. Alzate et al. "Star cluster survival in dark matter halos: An old cluster in Eridanus II?" In: *MNRAS* (May 2021). DOI: 10.1093/mnras/stab1322. arXiv: 2105.01797 [astro-ph.GA].

[6] Nicola C. Amorisco. "Deadly Dark Matter Cusps versus Faint and Extended Star Clusters: Eridanus II and Andromeda XXV". In: *ApJ* 844.1, 64 (July 2017), p. 64. DOI: 10.3847/1538-4357/aa745f. arXiv: 1704.06262 [astro-ph.GA].

[7] Deokkeun An et al. "The Stellar Metallicity Distribution Function of the Galactic Halo from SDSS Photometry". In: *ApJ* 763.1, 65 (Jan. 2013), p. 65. DOI: 10.1088/0004-637X/763/1/65. arXiv: 1211.7073 [astro-ph.GA].

[8] Brett H. Andrews et al. "Inflow, Outflow, Yields, and Stellar Population Mixing in Chemical Evolution Models". In: *ApJ* 835.2, 224 (Feb. 2017), p. 224. DOI: 10.3847/1538-4357/835/2/224. arXiv: 1604.08613 [astro-ph.GA].

[9] Barbara J. Anthony-Twarog et al. "CA II H and K Filter Photometry on the UVBY System. I. The Standard System". In: *AJ* 101 (May 1991), p. 1902. DOI: 10.1086/115815.

[10] Elaad Applebaum et al. "A stochastically sampled IMF alters the stellar content of simulated dwarf galaxies". In: *MNRAS* 492.1 (Feb. 2020), pp. 8–21. DOI: 10.1093/mnras/stz3331. arXiv: 1811.00022 [astro-ph.GA].

[11] Elaad Applebaum et al. "Ultrafaint Dwarfs in a Milky Way Context: Introducing the Mint Condition DC Justice League Simulations". In: *ApJ* 906.2, 96 (Jan. 2021), p. 96. DOI: 10.3847/1538-4357/abcafa. arXiv: 2008.11207 [astro-ph.GA].

[12] A. Arentsen et al. "The Pristine Inner Galaxy Survey (PIGS) I: tracing the kinematics of metal-poor stars in the Galactic bulge". In: *MNRAS* 491.1 (Jan. 2020), pp. L11–L16. DOI: 10.1093/mnrasl/slz156. arXiv: 1910.06337 [astro-ph.GA].

[13] Martin Asplund et al. "The Chemical Composition of the Sun". In: *ARAA* 47.1 (Sept. 2009), pp. 481–522. DOI: 10.1146/annurev.astro.46.060407.145222. arXiv: 0909.0948 [astro-ph.SR].

[14] Bianca Azartash-Namin et al. "Bursting with Feedback: The Relationship between Feedback Model and Bursty Star Formation Histories in Dwarf Galaxies". In: *arXiv e-prints*, arXiv:2401.06041 (Jan. 2024), arXiv:2401.06041. DOI: 10.48550/arXiv.2401.06041. arXiv: 2401.06041 [astro-ph.GA].

[15] Kareem El-Badry et al. "Breathing FIRE: How Stellar Feedback Drives Radial Migration, Rapid Size Fluctuations, and Population Gradients in Low-mass Galaxies". In: *ApJ* 820.2, 131 (Apr. 2016), p. 131. DOI: 10.3847/0004-637X/820/2/131. arXiv: 1512.01235 [astro-ph.GA].

[16] Kareem El-Badry et al. "Breathing FIRE: How Stellar Feedback Drives Radial Migration, Rapid Size Fluctuations, and Population Gradients in Low-mass Galaxies". In: *ApJ* 820.2, 131 (Apr. 2016), p. 131. DOI: 10.3847/0004-637X/820/2/131. arXiv: 1512.01235 [astro-ph.GA].

[17] Kareem El-Badry et al. "Where are the most ancient stars in the Milky Way?" In: *MNRAS* 480.1 (Oct. 2018), pp. 652–668. DOI: 10.1093/mnras/sty1864. arXiv: 1804.00659 [astro-ph.GA].

[18] Fabrícia O. Barbosa et al. "The DECam MAGIC Survey: A Wide-field Photometric Metallicity Study of the Sculptor Dwarf Spheroidal Galaxy". In: *arXiv e-prints*, arXiv:2504.03593 (Apr. 2025), arXiv:2504.03593. DOI: 10.48550/arXiv.2504.03593. arXiv: 2504.03593 [astro-ph.GA].

[19] G. Battaglia et al. "Gaia early DR3 systemic motions of Local Group dwarf galaxies and orbital properties with a massive Large Magellanic Cloud". In: *arXiv e-prints*, arXiv:2106.08819 (June 2021), arXiv:2106.08819. arXiv: 2106.08819 [astro-ph.GA].

[20] G. Battaglia et al. "Gaia early DR3 systemic motions of Local Group dwarf galaxies and orbital properties with a massive Large Magellanic Cloud". In: *AAP* 657, A54 (Jan. 2022), A54. DOI: 10.1051/0004-6361/202141528. arXiv: 2106.08819 [astro-ph.GA].

[21] G. Battaglia et al. "The DART imaging and CaT survey of the Fornax dwarf spheroidal galaxy". In: *AAP* 459.2 (Nov. 2006), pp. 423–440. DOI: 10.1051/0004-6361:20065720. arXiv: astro-ph/0608370 [astro-ph].

[22] H. Baumgardt et al. "Stellar mass segregation as separating classifier between globular clusters and ultrafaint dwarf galaxies". In: *MNRAS* 510.3 (Mar. 2022), pp. 3531–3545. DOI: 10.1093/mnras/stab3629. arXiv: 2112.04689 [astro-ph.GA].

[23] K. Bechtol et al. "Eight New Milky Way Companions Discovered in First-year Dark Energy Survey Data". In: *ApJ* 807.1, 50 (July 2015), p. 50. DOI: 10.1088/0004-637X/807/1/50. arXiv: 1503.02584 [astro-ph.GA].

[24] T. C. Beers, G. W. Preston, and S. A. Shectman. "A search for stars of very low metal abundance. I." In: *AJ* 90 (Oct. 1985), pp. 2089–2102. DOI: 10.1086/113917.

[25] M. Bellazzini, F. R. Ferraro, and E. Pancino. "Multiple stellar populations in the Sextans dwarf spheroidal galaxy?" In: *MNRAS* 327.1 (Oct. 2001), pp. L15–L20. DOI: 10.1046/j.1365-8711.2001.04889.x. arXiv: astro-ph/0108504 [astro-ph].

[26] V. Belokurov et al. "Cats and Dogs, Hair and a Hero: A Quintet of New Milky Way Companions". In: *ApJ* 654.2 (Jan. 2007), pp. 897–906. DOI: 10.1086/509718. arXiv: astro-ph/0608448 [astro-ph].

[27] V. Belokurov et al. "Co-formation of the disc and the stellar halo". In: *MNRAS* 478.1 (July 2018), pp. 611–619. DOI: 10.1093/mnras/sty982. arXiv: 1802.03414 [astro-ph.GA].

[28] A. Benítez-Llambay et al. "Mergers and the outside-in formation of dwarf spheroidals". In: *MNRAS* 456.2 (Feb. 2016), pp. 1185–1194. DOI: 10.1093/mnras/stv2722. arXiv: 1511.06188 [astro-ph.GA].

[29] Alejandro Benítez-Llambay et al. "Dwarf Galaxies and the Cosmic Web". In: *ApJL* 763.2, L41 (Feb. 2013), p. L41. DOI: 10.1088/2041-8205/763/2/L41. arXiv: 1211.0536 [astro-ph.CO].

[30] Paul Bennet et al. "Proper Motions and Orbits of Distant Local Group Dwarf Galaxies from a combination of Gaia and Hubble Data". In: *arXiv e-prints*, arXiv:2312.09276 (Dec. 2023), arXiv:2312.09276. DOI: 10.48550/arXiv.2312.09276. arXiv: 2312.09276 [astro-ph.GA].

[31] M. Bettinelli et al. "The star formation history of the Sextans dwarf spheroidal galaxy: a true fossil of the pre-reionization era". In: *MNRAS* 476.1 (May 2018), pp. 71–79. DOI: 10.1093/mnras/sty226. arXiv: 1801.08145 [astro-ph.GA].

[32] B. Binggeli, M. Tarenghi, and A. Sandage. "The abundance and morphological segregation of dwarf galaxies in the field". In: *AAP* 228 (Feb. 1990), pp. 42–60.

[33] Joss Bland-Hawthorn, Ralph Sutherland, and David Webster. "Ultrafaint Dwarf Galaxies—the Lowest-mass Relics from Before Reionization". In: *ApJ* 807.2, 154 (July 2015), p. 154. DOI: 10.1088/0004-637X/807/2/154. arXiv: 1505.06209 [astro-ph.GA].

[34] Antoine Bouchard, Gary S. Da Costa, and Helmut Jerjen. "The Environmental Influence on the Evolution of Local Galaxies". In: *AJ* 137.2 (Feb. 2009), pp. 3038–3052. DOI: 10.1088/0004-6256/137/2/3038. arXiv: 0811.0329 [astro-ph].

[35] Mia S. Bovill and Massimo Ricotti. "Pre-Reionization Fossils, Ultra-Faint Dwarfs, and the Missing Galactic Satellite Problem". In: *ApJ* 693.2 (Mar. 2009), pp. 1859–1870. DOI: 10.1088/0004-637X/693/2/1859. arXiv: 0806.2340 [astro-ph].

[36] Michael Boylan-Kolchin, James S. Bullock, and Manoj Kaplinghat. "Too big to fail? The puzzling darkness of massive Milky Way subhaloes". In: *MNRAS* 415.1 (July 2011), pp. L40–L44. DOI: 10.1111/j.1745-3933.2011.01074.x. arXiv: 1103.0007 [astro-ph.CO].

[37] Michael Boylan-Kolchin and Daniel R. Weisz. "Uncertain times: the redshift-time relation from cosmology and stars". In: *MNRAS* 505.2 (Aug. 2021), pp. 2764–2783. DOI: 10.1093/mnras/stab1521. arXiv: 2103.15825 [astro-ph.CO].

[38] Michael Boylan-Kolchin et al. "The Local Group: the ultimate deep field". In: *MNRAS* 462.1 (Oct. 2016), pp. L51–L55. DOI: 10.1093/mnrasl/slw121. arXiv: 1603.02679 [astro-ph.CO].

[39] Crystal M. Brasseur et al. "What Sets the Sizes of the Faintest Galaxies?" In: *ApJ* 743.2, 179 (Dec. 2011), p. 179. DOI: 10.1088/0004-637X/743/2/179. arXiv: 1106.5500 [astro-ph.CO].

[40] Kaley Brauer et al. "Possibilities and Limitations of Kinematically Identifying Stars from Accreted Ultra-faint Dwarf Galaxies". In: *ApJ* 937.1, 14 (Sept. 2022), p. 14. DOI: 10.3847/1538-4357/ac85b9. arXiv: 2206.07057 [astro-ph.GA].

[41] Thomas M. Brown et al. "The Quenching of the Ultra-faint Dwarf Galaxies in the Reionization Era". In: *ApJ* 796.2, 91 (Dec. 2014), p. 91. DOI: 10.1088/0004-637X/796/2/91. arXiv: 1410.0681 [astro-ph.GA].

[42] Tobias Buck et al. "NIHAO XV: the environmental impact of the host galaxy on galactic satellite and field dwarf galaxies". In: *MNRAS* 483.1 (Feb. 2019), pp. 1314–1341. DOI: 10.1093/mnras/sty2913. arXiv: 1804.04667 [astro-ph.GA].

[43] James S. Bullock and Michael Boylan-Kolchin. "Small-Scale Challenges to the ΛCDM Paradigm". In: *ARAA* 55.1 (Aug. 2017), pp. 343–387. DOI: 10.1146/annurev-astro-091916-055313. arXiv: 1707.04256 [astro-ph.CO].

[44] James S. Bullock and Kathryn V. Johnston. "Tracing Galaxy Formation with Stellar Halos. I. Methods". In: *ApJ* 635.2 (Dec. 2005), pp. 931–949. DOI: 10.1086/497422. arXiv: astro-ph/0506467 [astro-ph].

[45] C. Cáceres and M. Catelan. "The Period-Luminosity Relation of RR Lyrae Stars in the SDSS Photometric System". In: *ApJS* 179.1 (Nov. 2008), pp. 242–248. DOI: 10.1086/591231. arXiv: 0805.3704 [astro-ph].

[46] F. Calura et al. "The evolution of the mass-metallicity relation in galaxies of different morphological types". In: *AAP* 504.2 (Sept. 2009), pp. 373–388. DOI: 10.1051/0004-6361/200911756. arXiv: 0904.2180 [astro-ph.CO].

[47] Sarah A. Cantu et al. "A Deeper Look at DES Dwarf Galaxy Candidates: Grus I and Indus II". In: *ApJ* 916.2, 81 (Aug. 2021), p. 81. DOI: 10.3847/1538-4357/ac0443. arXiv: 2005.06478 [astro-ph.GA].

[48] Leticia Carigi, Xavier Hernandez, and Gerard Gilmore. "Chemical evolution models of local dwarf spheroidal galaxies". In: *MNRAS* 334.1 (July 2002), pp. 117–128. DOI: 10.1046/j.1365-8711.2002.05491.x. arXiv: astro-ph/0201090 [astro-ph].

[49] B. W. Carney. "Subdwarf ultraviolet excesses and metal abundances." In: *ApJ* 233 (Oct. 1979), pp. 211–225. DOI: 10.1086/157383.

[50] R. Carrera et al. "The near-infrared Ca II triplet as a metallicity indicator - II. Extension to extremely metal-poor metallicity regimes". In: *MNRAS* 434.2 (Sept. 2013), pp. 1681–1691. DOI: 10.1093/mnras/stt1126. arXiv: 1306.3883 [astro-ph.GA].

[51] A. J. Cenarro et al. "J-PLUS: The Javalambre Photometric Local Universe Survey". In: *AAP* 622, A176 (Feb. 2019), A176. DOI: 10.1051/0004-6361/201833036. arXiv: 1804.02667 [astro-ph.GA].

[52] W. Cerny et al. "Discovery of an Ultra-faint Stellar System near the Magellanic Clouds with the DECam Local Volume Exploration Survey". In: *ApJ* 910.1, 18 (Mar. 2021), p. 18. DOI: 10.3847/1538-4357/abe1af. arXiv: 2009.08550 [astro-ph.GA].

[53] W. Cerny et al. "Six More Ultra-Faint Milky Way Companions Discovered in the DECam Local Volume Exploration Survey". In: *arXiv e-prints*, arXiv:2209.12422 (Sept. 2022), arXiv:2209.12422. DOI: 10.48550/arXiv.2209.12422. arXiv: 2209.12422 [astro-ph.GA].

[54] Anirudh Chiti et al. "An extended halo around an ancient dwarf galaxy". In: *Nature Astronomy* 5 (Jan. 2021), pp. 392–400. DOI: 10.1038/s41550-020-01285-w. arXiv: 2012.02309 [astro-ph.GA].

[55] Anirudh Chiti et al. "Magellan/IMACS spectroscopy of Grus I: a low metallicity ultra-faint dwarf galaxy". In: *arXiv e-prints*, arXiv:2206.04580 (June 2022), arXiv:2206.04580. arXiv: 2206.04580 [astro-ph.GA].

[56] Anirudh Chiti et al. "Stellar Metallicities from SkyMapper Photometry I: A Study of the Tucana II Ultra-faint Dwarf Galaxy". In: *ApJ* 891.1, 8 (Mar. 2020), p. 8. DOI: 10.3847/1538-4357/ab6d72. arXiv: 2001.07684 [astro-ph.GA].

[57] Anirudh Chiti et al. "Stellar Metallicities from SkyMapper Photometry. II. Precise Photometric Metallicities of ∼280,000 Giant Stars with [Fe/H] < -0.75 in the Milky Way". In: *ApJS* 254.2, 31 (June 2021), p. 31. DOI: 10.3847/1538-4365/abf73d. arXiv: 2103.16660 [astro-ph.GA].

[58] Jieun Choi et al. "Mesa Isochrones and Stellar Tracks (MIST). I. Solar-scaled Models". In: *ApJ* 823.2, 102 (June 2016), p. 102. DOI: 10.3847/0004-637X/823/2/102. arXiv: 1604.08592 [astro-ph.SR].

[59] Gisella Clementini et al. "Variability and Star Formation in Leo T, the Lowest Luminosity Star-forming Galaxy Known Today". In: *ApJ* 756.2, 108 (Sept. 2012), p. 108. DOI: 10.1088/0004-637X/756/2/108. arXiv: 1207.2764 [astro-ph.GA].

[60] Judith G. Cohen and Wenjin Huang. "The Chemical Evolution of the Draco Dwarf Spheroidal Galaxy". In: *ApJ* 701.2 (Aug. 2009), pp. 1053–1075. DOI: 10.1088/0004-637X/701/2/1053. arXiv: 0906.1006 [astro-ph.GA].

[61] Andrew A. Cole et al. "Leo A: A Late-blooming Survivor of the Epoch of Reionization in the Local Group". In: *ApJL* 659.1 (Apr. 2007), pp. L17–L20. DOI: 10.1086/516711. arXiv: astro-ph/0702646 [astro-ph].

[62] Michelle L. M. Collins et al. "A Kinematic Study of the Andromeda Dwarf Spheroidal System". In: *ApJ* 768.2, 172 (May 2013), p. 172. DOI: 10.1088/0004-637X/768/2/172. arXiv: 1302.6590 [astro-ph.CO].

[63] Michelle L. M. Collins et al. "Comparing the Observable Properties of Dwarf Galaxies on and off the Andromeda Plane". In: *ApJL* 799.1, L13 (Jan. 2015), p. L13. DOI: 10.1088/2041-8205/799/1/L13. arXiv: 1411.3324 [astro-ph.GA].

[64] Michelle L. M. Collins et al. "The Masses of Local Group Dwarf Spheroidal Galaxies: The Death of the Universal Mass Profile". In: *ApJ* 783.1, 7 (Mar. 2014), p. 7. DOI: 10.1088/0004-637X/783/1/7. arXiv: 1309.3053 [astro-ph.CO].

[65] Blair C. Conn et al. "On the Nature of Ultra-faint Dwarf Galaxy Candidates. I. DES1, Eridanus III, and Tucana V". In: *ApJ* 852.2, 68 (Jan. 2018), p. 68. DOI: 10.3847/1538-4357/aa9eda. arXiv: 1712.01439 [astro-ph.GA].

[66] Charlie Conroy et al. "Resolving the Metallicity Distribution of the Stellar Halo with the H3 Survey". In: *ApJ* 887.2, 237 (Dec. 2019), p. 237. DOI: 10.3847/1538-4357/ab5710. arXiv: 1909.02007 [astro-ph.GA].

[67] Patrick Côté et al. "Evidence for the Hierarchical Formation of the Galactic Spheroid". In: *ApJ* 533.2 (Apr. 2000), pp. 869–883. DOI: 10.1086/308709. arXiv: astro-ph/9911527 [astro-ph].

[68] D. Crnojević et al. "Deep Imaging of Eridanus II and Its Lone Star Cluster". In: *ApjL* 824.1, L14 (June 2016), p. L14. DOI: 10.3847/2041-8205/824/1/L14. arXiv: 1604.08590 [astro-ph.GA].

[69] Taha Dawoodbhoy et al. "Suppression of star formation in low-mass galaxies caused by the reionization of their local neighbourhood". In: *MNRAS* 480.2 (Oct. 2018), pp. 1740–1753. DOI: 10.1093/mnras/sty1945. arXiv: 1805.05358 [astro-ph.CO].

[70] T. J. L. de Boer et al. "The episodic star formation history of the Carina dwarf spheroidal galaxy". In: *AAP* 572, A10 (Dec. 2014), A10. DOI: 10.1051/0004-6361/201424119. arXiv: 1409.3229 [astro-ph.GA].

[71] T. J. L. de Boer et al. "The star formation and chemical evolution history of the sculptor dwarf spheroidal galaxyâ". In: *AAP* 539, A103 (Mar. 2012), A103. DOI: 10.1051/0004-6361/201118378. arXiv: 1201.2408 [astro-ph.CO].

[72] A. J. Deason, V. Belokurov, and D. R. Weisz. "The progenitors of the Milky Way stellar halo: big bricks favoured over little bricks." In: *MNRAS* 448 (Mar. 2015), pp. L77–L81. DOI: 10.1093/mnrasl/slv001. arXiv: 1501.02806 [astro-ph.GA].

[73] Amandine Doliva-Dolinsky et al. "The PAndAS View of the Andromeda Satellite System. III. Dwarf Galaxy Detection Limits". In: *ApJ* 933.2, 135 (July 2022), p. 135. DOI: 10.3847/1538-4357/ac6fd5. arXiv: 2205.02831 [astro-ph.GA].

[74] Amandine Doliva-Dolinsky et al. "The PAndAS View of the Andromeda Satellite System. IV. Global Properties". In: *ApJ* 952.1, 72 (July 2023), p. 72. DOI: 10.3847/1538-4357/acdcf6. arXiv: 2303.01528 [astro-ph.GA].

[75] A. E. Dolphin. "Numerical methods of star formation history measurement and applications to seven dwarf spheroidals". In: *MNRAS* 332.1 (May 2002), pp. 91–108. DOI: 10.1046/j.1365-8711.2002.05271.x. arXiv: astro-ph/0112331 [astro-ph].

[76] Andrew Dolphin. *DOLPHOT: Stellar photometry*. Aug. 2016. ascl: 1608.013.

[77] Andrew E. Dolphin. "WFPC2 Stellar Photometry with HSTPHOT". In: *PASP* 112.776 (Oct. 2000), pp. 1383–1396. DOI: 10.1086/316630. arXiv: astro-ph/0006217 [astro-ph].

[78] Andrew E. Dolphin. "WFPC2 Stellar Photometry with HSTPHOT". In: *PASP* 112.776 (Oct. 2000), pp. 1383–1396. DOI: 10.1086/316630. arXiv: astro-ph/0006217 [astro-ph].

[79] Aaron Dotter. "MESA Isochrones and Stellar Tracks (MIST) 0: Methods for the Construction of Stellar Isochrones". In: *ApJS* 222.1, 8 (Jan. 2016), p. 8. DOI: 10.3847/0067-0049/222/1/8. arXiv: 1601.05144 [astro-ph.SR].

[80] Aaron Dotter et al. "The Dartmouth Stellar Evolution Database". In: *ApJS* 178.1 (Sept. 2008), pp. 89–101. DOI: 10.1086/589654. arXiv: 0804.4473 [astro-ph].

[81] A. Dressler. "Galaxy morphology in rich clusters: implications for the formation and evolution of galaxies." In: *ApJ* 236 (Mar. 1980), pp. 351–365. DOI: 10.1086/157753.

[82] A. Drlica-Wagner et al. "Eight Ultra-faint Galaxy Candidates Discovered in Year Two of the Dark Energy Survey". In: *ApJ* 813.2, 109 (Nov. 2015), p. 109. DOI: 10.1088/0004-637X/813/2/109. arXiv: 1508.03622 [astro-ph.GA].

[83] Gaspard Duchêne and Adam Kraus. "Stellar Multiplicity". In: *ARAA* 51.1 (Aug. 2013), pp. 269–310. DOI: 10.1146/annurev-astro-081710-102602. arXiv: 1303.3028 [astro-ph.SR].

[84] Nathan R. Eggen et al. "Blow-away in the Extreme Low-mass Starburst Galaxy Pox 186". In: *ApJ* 912.1, 12 (May 2021), p. 12. DOI: 10.3847/1538-4357/abe85d.

[85] Andrew Emerick, Greg L. Bryan, and Mordecai-Mark Mac Low. "Simulating Metal Mixing of Both Common and Rare Enrichment Sources in a Low-mass Dwarf Galaxy". In: *ApJ* 890.2, 155 (Feb. 2020), p. 155. DOI: 10.3847/1538-4357/ab6efc. arXiv: 1909.04695 [astro-ph.GA].

[86] Raphaël Errani et al. "Structure and kinematics of tidally limited satellite galaxies in LCDM". In: *MNRAS* 511.4 (Apr. 2022), pp. 6001–6018. DOI: 10.1093/mnras/stac476. arXiv: 2111.05866 [astro-ph.GA].

[87] Sean P. Fillingham et al. "Characterizing the Infall Times and Quenching Timescales of Milky Way Satellites with *Gaia* Proper Motions". In: *arXiv e-prints*, arXiv:1906.04180 (June 2019), arXiv:1906.04180. arXiv: 1906.04180 [astro-ph.GA].

[88] Alex Fitts et al. "fire in the field: simulating the threshold of galaxy formation". In: *MNRAS* 471.3 (Nov. 2017), pp. 3547–3562. DOI: 10.1093/mnras/stx1757. arXiv: 1611.02281 [astro-ph.GA].

[89] Alex Fitts et al. "No assembly required: mergers are mostly irrelevant for the growth of low-mass dwarf galaxies". In: *MNRAS* 479.1 (Sept. 2018), pp. 319–331. DOI: 10.1093/mnras/sty1488. arXiv: 1801.06187 [astro-ph.GA].

[90] Daniel Foreman-Mackey et al. "emcee: The MCMC Hammer". In: *PASP* 125.925 (Mar. 2013), p. 306. DOI: 10.1086/670067. arXiv: 1202.3665 [astro-ph.IM].

[91] F. Fraternali et al. "Life at the periphery of the Local Group: the kinematics of the Tucana dwarf galaxy". In: *AAP* 499.1 (May 2009), pp. 121–128. DOI: 10.1051/0004-6361/200810830. arXiv: 0903.4635 [astro-ph.CO].

[92] Anna Frebel and John E. Norris. "Near-Field Cosmology with Extremely Metal-Poor Stars". In: *ARAA* 53 (Aug. 2015), pp. 631–688. DOI: 10.1146/annurev-astro-082214-122423. arXiv: 1501.06921 [astro-ph.SR].

[93] Anna Frebel, Joshua D. Simon, and Evan N. Kirby. "Segue 1: An Unevolved Fossil Galaxy from the Early Universe". In: *ApJ* 786.1, 74 (May 2014), p. 74. DOI: 10.1088/0004-637X/786/1/74. arXiv: 1403.6116 [astro-ph.GA].

[94] T. K. Fritz et al. "Gaia DR 2 and VLT/FLAMES search for new satellites of the LMC". In: *AAP* 623, A129 (Mar. 2019), A129. DOI: 10.1051/0004-6361/201833458. arXiv: 1805.07350 [astro-ph.GA].

[95] T. K. Fritz et al. "Gaia DR2 proper motions of dwarf galaxies within 420 kpc. Orbits, Milky Way mass, tidal influences, planar alignments, and group infall". In: *AAP* 619, A103 (Nov. 2018), A103. DOI: 10.1051/0004-6361/201833343. arXiv: 1805.00908 [astro-ph.GA].

[96] Sal Wanying Fu et al. "Metallicity Distribution Function of the Eridanus II Ultra-faint Dwarf Galaxy from Hubble Space Telescope Narrowband Imaging". In: *ApJ* 925.1, 6 (Jan. 2022), p. 6. DOI: 10.3847/1538-4357/ac3665. arXiv: 2111.00045 [astro-ph.GA].

[97] Sal Wanying Fu et al. "Metallicity Distribution Functions of 13 Ultra-Faint Dwarf Galaxy Candidates from Hubble Space Telescope Narrowband Imaging". In: *arXiv e-prints*, arXiv:2306.06260 (June 2023), arXiv:2306.06260. DOI: 10.48550/arXiv.2306.06260. arXiv: 2306.06260 [astro-ph.GA].

[98] Sal Wanying Fu et al. "Stellar Metallicities and Gradients in the Faint M31 Satellites Andromeda XVI and Andromeda XXVIII". In: *ApJ* 975.1 (Oct. 2024), p. 2. DOI: 10.3847/1538-4357/ad76a2. URL: https://dx.doi.org/10.3847/1538-4357/ad76a2.

[99] Sal Wanying Fu et al. "Stellar Metallicities and Gradients in the Isolated, Quenched Low-mass Galaxy Tucana". In: *ApJ* 965.1, 36 (Apr. 2024), p. 36. DOI: 10.3847/1538-4357/ad25ed. arXiv: 2312.05981 [astro-ph.GA].

[100] Sal Wanying Fu et al. "The Origin of the 300 km s^{-1} Stream near Segue 1". In: *ApJ* 866.1, 42 (Oct. 2018), p. 42. DOI: 10.3847/1538-4357/aad9f9. arXiv: 1804.08622 [astro-ph.GA].

[101] C. Gallart et al. "The Star Formation History of Eridanus II: On the Role of Supernova Feedback in the Quenching of Ultrafaint Dwarf Galaxies". In: *ApJ* 909.2, 192 (Mar. 2021), p. 192. DOI: 10.3847/1538-4357/abddbe. arXiv: 2101.04464 [astro-ph.GA].

[102] Carme Gallart et al. "The ACS LCID Project: On the Origin of Dwarf Galaxy Types—A Manifestation of the Halo Assembly Bias?" In: *ApjL* 811.2, L18 (Oct. 2015), p. L18. DOI: 10.1088/2041-8205/811/2/L18. arXiv: 1507.08350 [astro-ph.GA].

[103] Pratik J. Gandhi et al. "Exploring metallicity-dependent rates of Type Ia supernovae and their impact on galaxy formation". In: *MNRAS* 516.2 (Oct. 2022), pp. 1941–1958. DOI: 10.1093/mnras/stac2228. arXiv: 2202.10477 [astro-ph.GA].

[104] Shea Garrison-Kimmel et al. "Can feedback solve the too-big-to-fail problem?" In: *MNRAS* 433.4 (Aug. 2013), pp. 3539–3546. DOI: 10.1093/mnras/stt984. arXiv: 1301.3137 [astro-ph.CO].

[105] M. Geha et al. "A Stellar Mass Threshold for Quenching of Field Galaxies". In: *ApJ* 757.1, 85 (Sept. 2012), p. 85. DOI: 10.1088/0004-637X/757/1/85. arXiv: 1206.3573 [astro-ph.CO].

[106] M. Geha et al. "HST/ACS Direct Ages of the Dwarf Elliptical Galaxies NGC 147 and NGC 185". In: *ApJ* 811.2, 114 (Oct. 2015), p. 114. DOI: 10.1088/0004-637X/811/2/114. arXiv: 1503.06526 [astro-ph.GA].

[107] Marla Geha et al. "The Least-Luminous Galaxy: Spectroscopy of the Milky Way Satellite Segue 1". In: *ApJ* 692.2 (Feb. 2009), pp. 1464–1475. DOI: 10.1088/0004-637X/692/2/1464. arXiv: 0809.2781 [astro-ph].

[108] Doug Geisler, Juan J. Claria, and Dante Minniti. "An Improved Metal Abundance Calibration for the Washington System". In: *AJ* 102 (Nov. 1991), p. 1836. DOI: 10.1086/116008.

[109] Andrew Gelman and Donald B. Rubin. "Inference from Iterative Simulation Using Multiple Sequences". In: *Statistical Science* 7 (Jan. 1992), pp. 457–472. DOI: 10.1214/ss/1177011136.

[110] Gerard Gilmore and Rosemary F. G. Wyse. "Chemical Evolution with Bursts of Star Formation: Element Ratios in Dwarf Galaxies". In: *ApJL* 367 (Feb. 1991), p. L55. DOI: 10.1086/185930.

[111] R. Giovanelli, M. P. Haynes, and G. L. Chincarini. "Morphological Segregation in the Pisces-Perseus Supercluster". In: *ApJ* 300 (Jan. 1986), p. 77. DOI: 10.1086/163784.

[112] F. Governato et al. "Bulgeless dwarf galaxies and dark matter cores from supernova-driven outflows". In: *Nat.* 463.7278 (Jan. 2010), pp. 203–206. DOI: 10.1038/nature08640. arXiv: 0911.2237 [astro-ph.CO].

[113] Andrew S. Graus et al. "How low does it go? Too few Galactic satellites with standard reionization quenching". In: *MNRAS* 488.4 (Oct. 2019), pp. 4585–4595. DOI: 10.1093/mnras/stz1992. arXiv: 1808.03654 [astro-ph.GA].

[114] Claudia Greco et al. "On the Newly Discovered Canes Venatici II dSph Galaxy". In: *ApJL* 675.2 (Mar. 2008), p. L73. DOI: 10.1086/533585. arXiv: 0712.2241 [astro-ph].

[115] Alexandra L. Gregory et al. "Kinematics of the Tucana Dwarf Galaxy: an unusually dense dwarf in the Local Group". In: *MNRAS* 485.2 (May 2019), pp. 2010–2025. DOI: 10.1093/mnras/stz518. arXiv: 1902.07228 [astro-ph.GA].

[116] N. Grevesse and A. J. Sauval. "Standard Solar Composition". In: *SSR* 85 (May 1998), pp. 161–174. DOI: 10.1023/A:1005161325181.

[117] V. Grieco et al. "Chemical evolution of the Galactic bulge: different stellar populations and possible gradients". In: *AAP* 548, A60 (Dec. 2012), A60. DOI: 10.1051/0004-6361/201219761. arXiv: 1209.4462 [astro-ph.GA].

[118] C. J. Grillmair. "A Matched-Filter Map of the 300 km/s Stream". In: *Setting the scene for Gaia and LAMOST*. Ed. by Sofia Feltzing et al. Vol. 298. Jan. 2014, pp. 405–405. DOI: 10.1017/S1743921313006728.

[119] Sang-Il Han et al. "Narrowband Ca Photometry for Dwarf Spheroidal Galaxies. I. Chemostructural Study on Draco, Sextans, and Canes Venatici I". In: *ApJS* 247.1, 7 (Mar. 2020), p. 7. DOI: 10.3847/1538-4365/ab6441. arXiv: 2001.11138 [astro-ph.GA].

[120] Daniel Harbeck et al. "Population Gradients in Local Group Dwarf Spheroidal Galaxies". In: *AJ* 122.6 (Dec. 2001), pp. 3092–3105. DOI: 10.1086/324232. arXiv: astro-ph/0109121 [astro-ph].

[121] Daniel Harbeck et al. "Population Gradients in Local Group Dwarf Spheroidal Galaxies". In: *AJ* 122.6 (Dec. 2001), pp. 3092–3105. DOI: 10.1086/324232. arXiv: astro-ph/0109121 [astro-ph].

[122] F. D. A. Hartwick. "The Chemical Evolution of the Galactic Halo". In: *ApJ* 209 (Oct. 1976), pp. 418–423. DOI: 10.1086/154735.

[123] Loic Hausammann, Yves Revaz, and Pascale Jablonka. "Satellite dwarf galaxies: stripped but not quenched". In: *AAP* 624, A11 (Apr. 2019), A11. DOI: 10.1051/0004-6361/201834871. arXiv: 1902.02340 [astro-ph.GA].

[124] Enrico V. Held, Ivo Saviane, and Yazan Momany. "Stellar populations in the PHOENIX dwarf galaxy". In: *AAP* 345 (May 1999), pp. 747–759. arXiv: astro-ph/9903017 [astro-ph].

[125] Amina Helmi et al. "A New View of the Dwarf Spheroidal Satellites of the Milky Way from VLT FLAMES: Where Are the Very Metal-poor Stars?" In: *ApjL* 651.2 (Nov. 2006), pp. L121–L124. DOI: 10.1086/509784. arXiv: astro-ph/0611420 [astro-ph].

[126] Amina Helmi et al. "Selection of Metal-poor Giant Stars Using the Sloan Digital Sky Survey Photometric System". In: *ApJ* 586.1 (Mar. 2003), pp. 195–200. DOI: 10.1086/367536. arXiv: astro-ph/0211562 [astro-ph].

[127] Amina Helmi et al. "The merger that led to the formation of the Milky Way's inner stellar halo and thick disk". In: *Nat* 563.7729 (Oct. 2018), pp. 85–88. DOI: 10.1038/s41586-018-0625-x. arXiv: 1806.06038 [astro-ph.GA].

[128] Sebastian L. Hidalgo et al. "The ACS LCID Project. IX. Imprints of the Early Universe in the Radial Variation of the Star Formation History of Dwarf Galaxies". In: *ApJ* 778.2, 103 (Dec. 2013), p. 103. DOI: 10.1088/0004-637X/778/2/103. arXiv: 1309.6130 [astro-ph.CO].

[129] Sebastian L. Hidalgo et al. "The Updated BaSTI Stellar Evolution Models and Isochrones. I. Solar-scaled Calculations". In: *ApJ* 856.2, 125 (Apr. 2018), p. 125. DOI: 10.3847/1538-4357/aab158. arXiv: 1802.07319 [astro-ph.GA].

[130] V. Hill et al. "VLT/FLAMES high-resolution chemical abundances in Sculptor: a textbook dwarf spheroidal galaxy". In: *AAP* 626, A15 (June 2019), A15. DOI: 10.1051/0004-6361/201833950. arXiv: 1812.01486 [astro-ph.GA].

[131] Nhung Ho et al. "Metallicity Evolution of the Six Most Luminous M31 Dwarf Satellites". In: *ApJ* 798.2, 77 (Jan. 2015), p. 77. DOI: 10.1088/0004-637X/798/2/77. arXiv: 1405.4424 [astro-ph.GA].

[132] Nhung Ho et al. "Stellar Kinematics of the Andromeda II Dwarf Spheroidal Galaxy". In: *ApJ* 758.2, 124 (Oct. 2012), p. 124. DOI: 10.1088/0004-637X/758/2/124. arXiv: 1209.2116 [astro-ph.CO].

[133] David W. Hogg, Jo Bovy, and Dustin Lang. "Data analysis recipes: Fitting a model to data". In: *arXiv e-prints*, arXiv:1008.4686 (Aug. 2010), arXiv:1008.4686. DOI: 10.48550/arXiv.1008.4686. arXiv: 1008.4686 [astro-ph.IM].

[134] Daisuke Homma et al. "Boötes. IV. A new Milky Way satellite discovered in the Subaru Hyper Suprime-Cam Survey and implications for the missing satellite problem". In: *PASJ* 71.5, 94 (Oct. 2019), p. 94. DOI: 10.1093/pasj/psz076. arXiv: 1906.07332 [astro-ph.GA].

[135] Daisuke Homma et al. "Searches for new Milky Way satellites from the first two years of data of the Subaru/Hyper Suprime-Cam survey: Discovery of Cetus III". In: *PASJ* 70, S18 (Jan. 2018), S18. DOI: 10.1093/pasj/psx050. arXiv: 1704.05977 [astro-ph.GA].

[136] Y. Huang et al. "Milky Way Tomography with the SkyMapper Southern Survey. I. Atmospheric Parameters and Distances of One Million Red Giants". In: *ApJS* 243.1, 7 (July 2019), p. 7. DOI: 10.3847/1538-4365/ab1f72. arXiv: 1901.08033 [astro-ph.GA].

[137] T. -O. Husser et al. "A new extensive library of PHOENIX stellar atmospheres and synthetic spectra". In: *AAP* 553, A6 (May 2013), A6. DOI: 10.1051/0004-6361/201219058. arXiv: 1303.5632 [astro-ph.SR].

[138] R. Ibata et al. "The Haunted Halos of Andromeda and Triangulum: A Panorama of Galaxy Formation in Action". In: *ApJ* 671.2 (Dec. 2007), pp. 1591–1623. DOI: 10.1086/522574. arXiv: 0704.1318 [astro-ph].

[139] Rodrigo Ibata et al. "Charting the Galactic Acceleration Field. I. A Search for Stellar Streams with Gaia DR2 and EDR3 with Follow-up from ESPaDOnS and UVES". In: *ApJ* 914.2, 123 (June 2021), p. 123. DOI: 10.3847/1538-4357/abfcc2. arXiv: 2012.05245 [astro-ph.GA].

[140] M. J. Irwin et al. "Discovery of an Unusual Dwarf Galaxy in the Outskirts of the Milky Way". In: *ApjL* 656.1 (Feb. 2007), pp. L13–L16. DOI: 10.1086/512183. arXiv: astro-ph/0701154 [astro-ph].

[141] Željko Ivezić et al. "The Milky Way Tomography with SDSS. II. Stellar Metallicity". In: *ApJ* 684.1 (Sept. 2008), pp. 287–325. DOI: 10.1086/589678. arXiv: 0804.3850 [astro-ph].

[142] Sydney Jenkins et al. "VLT Spectroscopy of Ultra-Faint Dwarf Galaxies. 1. Bo{ö}tes I, Leo IV, Leo V". In: *arXiv e-prints*, arXiv:2101.00013 (Dec. 2020), arXiv:2101.00013. arXiv: 2101.00013 [astro-ph.GA].

[143] Myoungwon Jeon, Gurtina Besla, and Volker Bromm. "Connecting the First Galaxies with Ultrafaint Dwarfs in the Local Group: Chemical Signatures of Population III Stars". In: *ApJ* 848.2, 85 (Oct. 2017), p. 85. DOI: 10.3847/1538-4357/aa8c80. arXiv: 1702.07355 [astro-ph.GA].

[144] Myoungwon Jeon and Volker Bromm. "Signature of the first galaxies in JWST deep field observations". In: *MNRAS* 485.4 (June 2019), pp. 5939–5950. DOI: 10.1093/mnras/stz863. arXiv: 1812.06116 [astro-ph.GA].

[145] Myoungwon Jeon et al. "The role of faint population III supernovae in forming CEMP stars in ultra-faint dwarf galaxies". In: *MNRAS* 502.1 (Mar. 2021), pp. 1–14. DOI: 10.1093/mnras/staa4017. arXiv: 2012.10012 [astro-ph.GA].

[146] Helmut Jerjen et al. "On the Nature of Ultra-faint Dwarf Galaxy Candidates. III. Horologium I, Pictor I, Grus I, and Phoenix II". In: *arXiv e-prints*, arXiv:1809.02259 (Sept. 2018), arXiv:1809.02259. arXiv: 1809.02259 [astro-ph.GA].

[147] A. P. Ji et al. "Detailed Abundances in the Ultra-faint Magellanic Satellites Carina II and III". In: *ApJ* 889.1, 27 (Jan. 2020), p. 27. DOI: 10.3847/1538-4357/ab6213. arXiv: 1912.04963 [astro-ph.GA].

[148] Alexander P. Ji, Anna Frebel, and Volker Bromm. "Preserving chemical signatures of primordial star formation in the first low-mass stars". In: *MNRAS* 454.1 (Nov. 2015), pp. 659–674. DOI: 10.1093/mnras/stv2052. arXiv: 1508.06137 [astro-ph.GA].

[149] Alexander P. Ji et al. "Chemical Abundances in the Ultra-faint Dwarf Galaxies Grus I and Triangulum II: Neutron-capture Elements as a Defining Feature of the Faintest Dwarfs". In: *ApJ* 870.2, 83 (Jan. 2019), p. 83. DOI: 10.3847/1538-4357/aaf3bb. arXiv: 1809.02182 [astro-ph.GA].

[150] Alexander P. Ji et al. "Kinematics of Antlia 2 and Crater 2 from The Southern Stellar Stream Spectroscopic Survey (S5)". In: *arXiv e-prints*, arXiv:2106.12656 (June 2021), arXiv:2106.12656. arXiv: 2106.12656 [astro-ph.GA].

[151] Alexander P. Ji et al. "Metal Mixing in the R-Process Enhanced Ultra-Faint Dwarf Galaxy Reticulum II". In: *arXiv e-prints*, arXiv:2207.03499 (July 2022), arXiv:2207.03499. arXiv: 2207.03499 [astro-ph.GA].

[152] Alexander P. Ji et al. "R-process enrichment from a single event in an ancient dwarf galaxy". In: *Nat* 531.7596 (Mar. 2016), pp. 610–613. DOI: 10.1038/nature17425. arXiv: 1512.01558 [astro-ph.GA].

[153] Michael G. Jones et al. "Pavo: Discovery of a Star-forming Dwarf Galaxy Just Outside the Local Group". In: *ApJL* 957.1, L5 (Nov. 2023), p. L5. DOI: 10.3847/2041-8213/ad0130. arXiv: 2310.01478 [astro-ph.GA].

[154] Nikolay Kacharov et al. "Prolate rotation and metallicity gradient in the transforming dwarf galaxy Phoenix". In: *MNRAS* 466.2 (Apr. 2017), pp. 2006–2023. DOI: 10.1093/mnras/stw3188. arXiv: 1612.01560 [astro-ph.GA].

[155] S. Karaali, S. Bilir, and S. Tunçel. "New Colour Transformations for the Sloan Photometry, and Revised Metallicity Calibration and Equations for Photometric Parallax Estimation". In: *PASA* 22.1 (Jan. 2005), pp. 24–28. DOI: 10.1071/AS04034. arXiv: astro-ph/0407253 [astro-ph].

[156] I. Karovicova et al. "Fundamental stellar parameters of benchmark stars from CHARA interferometry. I. Metal-poor stars". In: *AAP* 640, A25 (Aug. 2020), A25. DOI: 10.1051/0004-6361/202037590. arXiv: 2006.05411 [astro-ph.SR].

[157] S. C. Keller et al. "The SkyMapper Telescope and The Southern Sky Survey". In: *PASA* 24.1 (May 2007), pp. 1–12. DOI: 10.1071/AS07001. arXiv: astro-ph/0702511 [astro-ph].

[158] L. O. Kerber et al. "A deep view of a fossil relic in the Galactic bulge: the Globular Cluster HP 1". In: *MNRAS* 484.4 (Apr. 2019), pp. 5530–5550. DOI: 10.1093/mnras/stz003. arXiv: 1901.03721 [astro-ph.SR].

[159] Collin L. Kielty et al. "The Pristine survey - XII. Gemini-GRACES chemodynamical study of newly discovered extremely metal-poor stars in the Galaxy". In: *MNRAS* 506.1 (Sept. 2021), pp. 1438–1461. DOI: 10.1093/mnras/stab1783. arXiv: 2012.03960 [astro-ph.GA].

[160] Stacy Y. Kim and Annika H. G. Peter. "The Milky Way satellite velocity function is a sharp probe of small-scale structure problems". In: *arXiv e-prints*, arXiv:2106.09050 (June 2021), arXiv:2106.09050. arXiv: 2106.09050 [astro-ph.GA].

[161] Evan N. Kirby, Joshua D. Simon, and Judith G. Cohen. "Spectroscopic Confirmation of the Dwarf Galaxies Hydra II and Pisces II and the Globular Cluster Laevens 1". In: *ApJ* 810.1, 56 (Sept. 2015), p. 56. DOI: 10.1088/0004-637X/810/1/56. arXiv: 1506.01021 [astro-ph.GA].

[162] Evan N. Kirby et al. "Chemistry and Kinematics of the Late-forming Dwarf Irregular Galaxies Leo A, Aquarius, and Sagittarius DIG". In: *ApJ* 834.1, 9 (Jan. 2017), p. 9. DOI: 10.3847/1538-4357/834/1/9. arXiv: 1610.08505 [astro-ph.GA].

[163] Evan N. Kirby et al. "Chemistry and Kinematics of the Late-forming Dwarf Irregular Galaxies Leo A, Aquarius, and Sagittarius DIG". In: *ApJ* 834.1, 9 (Jan. 2017), p. 9. DOI: 10.3847/1538-4357/834/1/9. arXiv: 1610.08505 [astro-ph.GA].

[164] Evan N. Kirby et al. "Elemental Abundances in M31: The Kinematics and Chemical Evolution of Dwarf Spheroidal Satellite Galaxies". In: *AJ* 159.2, 46 (Feb. 2020), p. 46. DOI: 10.3847/1538-3881/ab5f0f. arXiv: 1912.02186 [astro-ph.GA].

[165] Evan N. Kirby et al. "Multi-element Abundance Measurements from Medium-resolution Spectra. III. Metallicity Distributions of Milky Way Dwarf Satellite Galaxies". In: *ApJ* 727.2, 78 (Feb. 2011), p. 78. DOI: 10.1088/0004-637X/727/2/78. arXiv: 1011.4937 [astro-ph.GA].

[166] Evan N. Kirby et al. "The Universal Stellar Mass-Stellar Metallicity Relation for Dwarf Galaxies". In: *ApJ* 779.2, 102 (Dec. 2013), p. 102. DOI: 10.1088/0004-637X/779/2/102. arXiv: 1310.0814 [astro-ph.GA].

[167] Sergey E. Koposov et al. "Beasts of the Southern Wild: Discovery of Nine Ultra Faint Satellites in the Vicinity of the Magellanic Clouds." In: *ApJ* 805.2, 130 (June 2015), p. 130. DOI: 10.1088/0004-637X/805/2/130. arXiv: 1503.02079 [astro-ph.GA].

[168] Sergey E. Koposov et al. "Kinematics and Chemistry of Recently Discovered Reticulum 2 and Horologium 1 Dwarf Galaxies". In: *ApJ* 811.1, 62 (Sept. 2015), p. 62. DOI: 10.1088/0004-637X/811/1/62. arXiv: 1504.07916 [astro-ph.GA].

[169] Kateryna Kvasova, Evan N. Kirby, and Rachael L. Beaton. "Kinematics and metallicity of the dwarf spheroidal galaxy Andromeda XVIII". In: *arXiv e-prints*, arXiv:2404.11804 (Apr. 2024), arXiv:2404.11804. DOI: 10.48550/arXiv.2404.11804. arXiv: 2404.11804 [astro-ph.GA].

[170] Benjamin P. M. Laevens et al. "Sagittarius II, Draco II and Laevens 3: Three New Milky Way Satellites Discovered in the Pan-STARRS 1 3π Survey". In: *ApJ* 813.1, 44 (Nov. 2015), p. 44. DOI: 10.1088/0004-637X/813/1/44. arXiv: 1507.07564 [astro-ph.GA].

[171] David K. Lai et al. "The [Fe/H], [C/Fe], and [α/Fe] Distributions of the Boötes I Dwarf Spheroidal Galaxy". In: *ApJ* 738.1, 51 (Sept. 2011), p. 51. DOI: 10.1088/0004-637X/738/1/51. arXiv: 1106.2168 [astro-ph.GA].

[172] G. A. Lanfranchi, F. Matteucci, and G. Cescutti. "A comparison of the s- and r-process element evolution in local dwarf spheroidal galaxies and in the Milky Way". In: *AAP* 481.3 (Apr. 2008), pp. 635–644. DOI: 10.1051/0004-6361:20078696. arXiv: 0802.3368 [astro-ph].

[173] Russell J. Lavery and Kenneth J. Mighell. "A New Member of the Local Group: The Tucana Dwarf Galaxy". In: *AJ* 103 (Jan. 1992), p. 81. DOI: 10.1086/116042.

[174] Ryan Leaman. "Insights into Pre-enrichment of Star Clusters and Self-enrichment of Dwarf Galaxies from Their Intrinsic Metallicity Dispersions". In: *AJ* 144.6, 183 (Dec. 2012), p. 183. DOI: 10.1088/0004-6256/144/6/183. arXiv: 1209.4648 [astro-ph.GA].

[175] Henry Lee et al. "On Extending the Mass-Metallicity Relation of Galaxies by 2.5 Decades in Stellar Mass". In: *ApJ* 647.2 (Aug. 2006), pp. 970–983. DOI: 10.1086/505573. arXiv: astro-ph/0605036 [astro-ph].

[176] B. Lemasle et al. "VLT/FLAMES spectroscopy of red giant branch stars in the Carina dwarf spheroidal galaxy". In: *AAP* 538, A100 (Feb. 2012), A100. DOI: 10.1051/0004-6361/201118132. arXiv: 1112.0431 [astro-ph.GA].

[177] B. Lemasle et al. "VLT/FLAMES spectroscopy of red giant branch stars in the Fornax dwarf spheroidal galaxy". In: *AAP* 572, A88 (Dec. 2014), A88. DOI: 10.1051/0004-6361/201423919. arXiv: 1409.7703 [astro-ph.GA].

[178] Dawn D. Lenz et al. "Photometric Separation of Stellar Properties Using SDSS Filters". In: *ApJS* 119.2 (Dec. 1998), pp. 121–140. DOI: 10.1086/313155.

[179] B. Letarte et al. "A Keck/DEIMOS spectroscopic survey of the faint M31 satellites AndXV and AndXVI". In: *MNRAS* 400.3 (Dec. 2009), pp. 1472–1478. DOI: 10.1111/j.1365-2966.2009.15546.x. arXiv: 0901.0820 [astro-ph.SR].

[180] T. S. Li et al. "Farthest Neighbor: The Distant Milky Way Satellite Eridanus II". In: *ApJ* 838.1, 8 (Mar. 2017), p. 8. DOI: 10.3847/1538-4357/aa6113. arXiv: 1611.05052 [astro-ph.GA].

[181] T. S. Li et al. "Ships Passing in the Night: Spectroscopic Analysis of Two Ultra-faint Satellites in the Constellation Carina". In: *ApJ* 857.2, 145 (Apr. 2018), p. 145. DOI: 10.3847/1538-4357/aab666. arXiv: 1802.06810 [astro-ph.GA].

[182] T. S. Li et al. "The First Tidally Disrupted Ultra-faint Dwarf Galaxy?: A Spectroscopic Analysis of the Tucana III Stream". In: *ApJ* 866.1, 22 (Oct. 2018), p. 22. DOI: 10.3847/1538-4357/aadf91. arXiv: 1804.07761 [astro-ph.GA].

[183] Ting S. Li et al. "S ^{5}: The Orbital and Chemical Properties of One Dozen Stellar Streams". In: *ApJ* 928.1, 30 (Mar. 2022), p. 30. DOI: 10.3847/1538-4357/ac46d3. arXiv: 2110.06950 [astro-ph.GA].

[184] Nicolas Longeard et al. "Pristine dwarf galaxy survey - I. A detailed photometric and spectroscopic study of the very metal-poor Draco II satellite". In: *MNRAS* 480.2 (Oct. 2018), pp. 2609–2627. DOI: 10.1093/mnras/sty1986. arXiv: 1807.10655 [astro-ph.GA].

[185] Nicolas Longeard et al. "The Pristine dwarf galaxy survey-V. The edges of the dwarf galaxy Hercules". In: *MNRAS* 525.2 (Oct. 2023), pp. 3086–3103. DOI: 10.1093/mnras/stad2227. arXiv: 2304.13046 [astro-ph.GA].

[186] Nicolas Longeard et al. "The Pristine Dwarf-Galaxy survey - II. In-depth observational study of the faint Milky Way satellite Sagittarius II". In: *MNRAS* 491.1 (Jan. 2020), pp. 356–377. DOI: 10.1093/mnras/stz2854. arXiv: 1902.02780 [astro-ph.GA].

[187] Nicolas Longeard et al. "The pristine dwarf-galaxy survey - III. Revealing the nature of the Milky Way globular cluster Sagittarius II". In: *MNRAS* 503.2 (May 2021), pp. 2754–2762. DOI: 10.1093/mnras/stab604. arXiv: 2005.05976 [astro-ph.GA].

[188] Nicolas Longeard et al. "The Pristine Dwarf-Galaxy survey – IV. Probing the outskirts of the dwarf galaxy Boötes I". In: *arXiv e-prints*, arXiv:2107.10849 (July 2021), arXiv:2107.10849. arXiv: 2107.10849 [astro-ph.GA].

[189] D. Lynden-Bell. "The chemical evolution of galaxies". In: *Vistas in Astronomy* 19.3 (Jan. 1975), pp. 299–316. DOI: 10.1016/0083-6656(75)90005-7.

[190] Piero Madau, Sijing Shen, and Fabio Governato. "Dark Matter Heating and Early Core Formation in Dwarf Galaxies". In: *ApJL* 789.1, L17 (July 2014), p. L17. DOI: 10.1088/2041-8205/789/1/L17. arXiv: 1405.2577 [astro-ph.GA].

[191] Ellen M. Manning and Andrew A. Cole. "From K giants to G dwarfs: stellar lifetime effects on metallicity distributions derived from red giants". In: *MNRAS* 471.4 (Nov. 2017), pp. 4194–4205. DOI: 10.1093/mnras/stx1854. arXiv: 1708.01826 [astro-ph.GA].

[192] F. Mannucci et al. "A fundamental relation between mass, star formation rate and metallicity in local and high-redshift galaxies". In: *MNRAS* 408.4 (Nov. 2010), pp. 2115–2127. DOI: 10.1111/j.1365-2966.2010.17291.x. arXiv: 1005.0006 [astro-ph.CO].

[193] A. Marcolini et al. "The chemical evolution of dwarf spheroidal galaxies: dissecting the inner regions and their stellar populations". In: *MNRAS* 386.4 (June 2008), pp. 2173–2180. DOI: 10.1111/j.1365-2966.2008.13175.x. arXiv: 0803.0385 [astro-ph].

[194] M. Marconi et al. "On a New Theoretical Framework for RR Lyrae Stars. I. The Metallicity Dependence". In: *ApJ* 808.1, 50 (July 2015), p. 50. DOI: 10.1088/0004-637X/808/1/50. arXiv: 1505.02531 [astro-ph.SR].

[195] Nicolas F. Martin et al. "Hydra II: A Faint and Compact Milky Way Dwarf Galaxy Found in the Survey of the Magellanic Stellar History". In: *ApJL* 804.1, L5 (May 2015), p. L5. DOI: 10.1088/2041-8205/804/1/L5. arXiv: 1503.06216 [astro-ph.GA].

[196] Nicolas F. Martin et al. "Spectroscopy of the Three Distant Andromedan Satellites Cassiopeia III, Lacerta I, and Perseus I". In: *ApJL* 793.1, L14 (Sept. 2014), p. L14. DOI: 10.1088/2041-8205/793/1/L14. arXiv: 1408.5130 [astro-ph.GA].

[197] Nicolas F. Martin et al. "The PAndAS View of the Andromeda Satellite System. I. A Bayesian Search for Dwarf Galaxies Using Spatial and Color-Magnitude Information". In: *ApJ* 776.2, 80 (Oct. 2013), p. 80. DOI: 10.1088/0004-637X/776/2/80. arXiv: 1307.7626 [astro-ph.GA].

[198] Nicolas F. Martin et al. "The PAndAS View of the Andromeda Satellite System. II. Detailed Properties of 23 M31 Dwarf Spheroidal Galaxies". In: *ApJ* 833.2, 167 (Dec. 2016), p. 167. DOI: 10.3847/1538-4357/833/2/167. arXiv: 1610.01158 [astro-ph.GA].

[199] Nicolas F. Martin et al. "The Pristine survey - XVI. The metallicity of 26 stellar streams around the Milky Way detected with the STREAMFINDER in Gaia EDR3". In: *MNRAS* 516.4 (Nov. 2022), pp. 5331–5354. DOI: 10.1093/mnras/stac2426. arXiv: 2201.01310 [astro-ph.GA].

[200] Nicolas F. Martin et al. "The Pristine survey – XXIII. Data Release 1 and an all-sky metallicity catalogue based on Gaia DR3 BP/RP spectro-photometry". In: *arXiv e-prints*, arXiv:2308.01344 (Aug. 2023), arXiv:2308.01344. DOI: 10.48550/arXiv.2308.01344. arXiv: 2308.01344 [astro-ph.GA].

[201] Nicolas F. Martin et al. "Triangulum II: A Very Metal-poor and Dynamically Hot Stellar System". In: *ApJ* 818.1, 40 (Feb. 2016), p. 40. DOI: 10.3847/0004-637X/818/1/40. arXiv: 1510.04433 [astro-ph.GA].

[202] C. E. Martínez-Vázquez et al. "Variable stars in Local Group Galaxies - V. The fast and early evolution of the low-mass Eridanus II dSph galaxy". In: *MNRAS* (Sept. 2021). DOI: 10.1093/mnras/stab2493. arXiv: 2109.01177 [astro-ph.GA].

[203] Mario L. Mateo. "Dwarf Galaxies of the Local Group". In: *ARAA* 36 (Jan. 1998), pp. 435–506. DOI: 10.1146/annurev.astro.36.1.435. arXiv: astro-ph/9810070 [astro-ph].

[204] F. Matteucci et al. "The origin of stellar populations in the Galactic bulge from chemical abundances". In: *MNRAS* 487.4 (Aug. 2019), pp. 5363–5371. DOI: 10.1093/mnras/stz1647. arXiv: 1903.12440 [astro-ph.GA].

[205] R. D. McClure and S. van den Bergh. "Five-color intermediate-band photometry of stars, clusters, and galaxies." In: *AJ* 73 (June 1968), pp. 313–337. DOI: 10.1086/110634.

[206] A. W. McConnachie and M. J. Irwin. "Structural properties of the M31 dwarf spheroidal galaxies". In: *MNRAS* 365.4 (Feb. 2006), pp. 1263–1276. DOI: 10.1111/j.1365-2966.2005.09806.x. arXiv: astro-ph/0511004 [astro-ph].

[207] A. W. McConnachie and M. J. Irwin. "The satellite distribution of M31". In: *MNRAS* 365.3 (Jan. 2006), pp. 902–914. DOI: 10.1111/j.1365-2966.2005.09771.x. arXiv: astro-ph/0510654 [astro-ph].

[208] Alan W. McConnachie, Nobuo Arimoto, and Mike Irwin. "Deconstructing dwarf galaxies: a Suprime-Cam survey of Andromeda II". In: *MNRAS* 379.1 (July 2007), pp. 379–392. DOI: 10.1111/j.1365-2966.2007.11969.x. arXiv: 0705.1520 [astro-ph].

[209] Alan W. McConnachie and Kim A. Venn. "Revised and New Proper Motions for Confirmed and Candidate Milky Way Dwarf Galaxies". In: *AJ* 160.3, 124 (Sept. 2020), p. 124. DOI: 10.3847/1538-3881/aba4ab. arXiv: 2007.05011 [astro-ph.GA].

[210] Alan W. McConnachie and Kim A. Venn. "Updated Proper Motions for Local Group Dwarf Galaxies Using Gaia Early Data Release 3". In: *Research Notes of the American Astronomical Society* 4.12, 229 (Dec. 2020), p. 229. DOI: 10.3847/2515-5172/abd18b. arXiv: 2012.03904 [astro-ph.GA].

[211] Alan W. McConnachie et al. "A Trio of New Local Group Galaxies with Extreme Properties". In: *ApJ* 688.2 (Dec. 2008), pp. 1009–1020. DOI: 10.1086/591313. arXiv: 0806.3988 [astro-ph].

[212] Kristen B. W. McQuinn et al. "Leo P: An Unquenched Very Low-mass Galaxy". In: *ApJ* 812.2, 158 (Oct. 2015), p. 158. DOI: 10.1088/0004-637X/812/2/158. arXiv: 1506.05495 [astro-ph.GA].

[213] Andrew McWilliam et al. "A Spectroscopic Analysis of 33 of the Most Metal-Poor Stars.I." In: *AJ* 109 (June 1995), p. 2736. DOI: 10.1086/117485.

[214] Francisco J. Mercado et al. "A relationship between stellar metallicity gradients and galaxy age in dwarf galaxies". In: *MNRAS* 501.4 (Mar. 2021), pp. 5121–5134. DOI: 10.1093/mnras/staa3958. arXiv: 2009.01241 [astro-ph.GA].

[215] Szabolcs Mészáros et al. "Exploring Anticorrelations and Light Element Variations in Northern Globular Clusters Observed by the APOGEE Survey". In: *AJ* 149.5, 153 (May 2015), p. 153. DOI: 10.1088/0004-6256/149/5/153. arXiv: 1501.05127 [astro-ph.SR].

[216] M. Monelli et al. "The ACS LCID Project. III. The Star Formation History of the Cetus dSph Galaxy: A Post-reionization Fossil". In: *ApJ* 720.2 (Sept. 2010), pp. 1225–1245. DOI: 10.1088/0004-637X/720/2/1225. arXiv: 1002.4300 [astro-ph.CO].

[217] M. Monelli et al. "The ACS LCID Project. VI. The Star Formation History of The Tucana dSph and The Relative Ages of the Isolated dSph Galaxies". In: *ApJ* 722.2 (Oct. 2010), pp. 1864–1878. DOI: 10.1088/0004-637X/722/2/1864. arXiv: 1010.2982 [astro-ph.CO].

[218] Matteo Monelli et al. "The ISLANDS Project. I. Andromeda XVI, An Extremely Low Mass Galaxy Not Quenched by Reionization". In: *ApJ* 819.2, 147 (Mar. 2016), p. 147. DOI: 10.3847/0004-637X/819/2/147. arXiv: 1603.00625 [astro-ph.GA].

[219] Stephanie Monty et al. "Chemo-dynamics of outer halo dwarf stars, including Gaia-Sausage and Gaia-Sequoia candidates". In: *MNRAS* 497.1 (Sept. 2020), pp. 1236–1255. DOI: 10.1093/mnras/staa1995. arXiv: 1909.11969 [astro-ph.GA].

[220] Ricardo R. Muñoz et al. "A MegaCam Survey of Outer Halo Satellites. III. Photometric and Structural Parameters". In: *ApJ* 860.1, 66 (June 2018), p. 66. DOI: 10.3847/1538-4357/aac16b. arXiv: 1806.06891 [astro-ph.GA].

[221] Ferah Munshi et al. "Dancing in the Dark: Uncertainty in Ultrafaint Dwarf Galaxy Predictions from Cosmological Simulations". In: *ApJ* 874.1, 40 (Mar. 2019), p. 40. DOI: 10.3847/1538-4357/ab0085. arXiv: 1810.12417 [astro-ph.GA].

[222] Ferah Munshi et al. "Quantifying Scatter in Galaxy Formation at the Lowest Masses". In: *ApJ* 923.1, 35 (Dec. 2021), p. 35. DOI: 10.3847/1538-4357/ac0db6. arXiv: 2101.05822 [astro-ph.GA].

[223] Alexander L. Muratov et al. "Gusty, gaseous flows of FIRE: galactic winds in cosmological simulations with explicit stellar feedback". In: *MNRAS* 454.3 (Dec. 2015), pp. 2691–2713. DOI: 10.1093/mnras/stv2126. arXiv: 1501.03155 [astro-ph.GA].

[224] Burçin Mutlu-Pakdil et al. "A Deeper Look at the New Milky Way Satellites: Sagittarius II, Reticulum II, Phoenix II, and Tucana III". In: *ApJ* 863.1, 25 (Aug. 2018), p. 25. DOI: 10.3847/1538-4357/aacd0e. arXiv: 1804.08627 [astro-ph.GA].

[225] Burçin Mutlu-Pakdil et al. "Resolved Dwarf Galaxy Searches within ∼5 Mpc with the Vera Rubin Observatory and Subaru Hyper Suprime-Cam". In: *arXiv e-prints*, arXiv:2105.01658 (May 2021), arXiv:2105.01658. arXiv: 2105.01658 [astro-ph.GA].

[226] E. O. Nadler et al. "Constraints on Dark Matter Properties from Observations of Milky Way Satellite Galaxies". In: *PRL* 126.9, 091101 (Mar. 2021), p. 091101. DOI: 10.1103/PhysRevLett.126.091101. arXiv: 2008.00022 [astro-ph.CO].

[227] Pranav Nagarajan, Daniel R. Weisz, and Kareem El-Badry. "RR Lyrae-based Distances for 39 Nearby Dwarf Galaxies Calibrated to Gaia eDR3". In: *ApJ* 932.1, 19 (June 2022), p. 19. DOI: 10.3847/1538-4357/ac69e6. arXiv: 2111.06899 [astro-ph.GA].

[228] D. Q. Nagasawa et al. "Chemical Abundance Analysis of Three α-poor, Metal-poor Stars in the Ultrafaint Dwarf Galaxy Horologium I". In: *ApJ* 852.2, 99 (Jan. 2018), p. 99. DOI: 10.3847/1538-4357/aaa01d. arXiv: 1708.02290 [astro-ph.SR].

[229] Rohan P. Naidu et al. "Evidence from the H3 Survey That the Stellar Halo Is Entirely Comprised of Substructure". In: *ApJ* 901.1, 48 (Sept. 2020), p. 48. DOI: 10.3847/1538-4357/abaef4. arXiv: 2006.08625 [astro-ph.GA].

[230] Julio F. Navarro, Vincent R. Eke, and Carlos S. Frenk. "The cores of dwarf galaxy haloes". In: *MNRAS* 283.3 (Dec. 1996), pp. L72–L78. DOI: 10.1093/mnras/283.3.L72. arXiv: astro-ph/9610187 [astro-ph].

[231] Poul Erik Nissen and Bengt Gustafsson. "High-precision stellar abundances of the elements: methods and applications". In: *AAPR* 26.1, 6 (Oct. 2018), p. 6. DOI: 10.1007/s00159-018-0111-3. arXiv: 1810.06535 [astro-ph.SR].

[232] John E. Norris et al. "An Extremely Carbon-rich, Extremely Metal-poor Star in the Segue 1 System". In: *ApJL* 722.1 (Oct. 2010), pp. L104–L109. DOI: 10.1088/2041-8205/722/1/L104. arXiv: 1008.0450 [astro-ph.GA].

[233] Xiaowei Ou et al. "Signatures of Tidal Disruption of the Hercules Ultrafaint Dwarf Galaxy". In: *ApJ* 966.1, 33 (May 2024), p. 33. DOI: 10.3847/1538-4357/ad2f27. arXiv: 2403.00921 [astro-ph.GA].

[234] Andrew B. Pace, Denis Erkal, and Ting S. Li. "Proper Motions, Orbits, and Tidal Influences of Milky Way Dwarf Spheroidal Galaxies". In: *ApJ* 940.2, 136 (Dec. 2022), p. 136. DOI: 10.3847/1538-4357/ac997b. arXiv: 2205.05699 [astro-ph.GA].

[235] Andrew B. Pace et al. "Multiple chemodynamic stellar populations of the Ursa Minor dwarf spheroidal galaxy". In: *MNRAS* 495.3 (July 2020), pp. 3022–3040. DOI: 10.1093/mnras/staa1419. arXiv: 2002.09503 [astro-ph.GA].

[236] B. E. J. Pagel and B. E. Patchett. "Metal abundances in nearby stars and the chemical history of the solar neighbourhood." In: *MNRAS* 172 (July 1975), pp. 13–40. DOI: 10.1093/mnras/172.1.13.

[237] Bernard E. J. Pagel. *Nucleosynthesis and Chemical Evolution of Galaxies*. 1997.

[238] Ekta Patel et al. "The Orbital Histories of Magellanic Satellites Using Gaia DR2 Proper Motions". In: *ApJ* 893.2, 121 (Apr. 2020), p. 121. DOI: 10.3847/1538-4357/ab7b75. arXiv: 2001.01746 [astro-ph.GA].

[239] Jorge Peñarrubia, Julio F. Navarro, and Alan W. McConnachie. "The Tidal Evolution of Local Group Dwarf Spheroidals". In: *ApJ* 673.1 (Jan. 2008), pp. 226–240. DOI: 10.1086/523686. arXiv: 0708.3087 [astro-ph].

[240] Matthew Pereira-Wilson et al. "The cosmic UV background and the beginning and end of star formation in simulated field dwarf galaxies". In: *MNRAS* 519.1 (Feb. 2023), pp. 1425–1436. DOI: 10.1093/mnras/stac3633. arXiv: 2206.05338 [astro-ph.GA].

[241] Adriano Pietrinferni et al. "Updated BaSTI Stellar Evolution Models and Isochrones. II. α-enhanced Calculations". In: *ApJ* 908.1, 102 (Feb. 2021), p. 102. DOI: 10.3847/1538-4357/abd4d5. arXiv: 2012.10085 [astro-ph.SR].

[242] Mateo Prgomet et al. "EDGE: The sensitivity of ultra-faint dwarfs to a metallicity-dependent initial mass function". In: *MNRAS* 513.2 (June 2022), pp. 2326–2334. DOI: 10.1093/mnras/stac1074. arXiv: 2107.00663 [astro-ph.GA].

[243] Yves Revaz and Pascale Jablonka. "Pushing back the limits: detailed properties of dwarf galaxies in a ΛCDM universe". In: *AAP* 616, A96 (Aug. 2018), A96. DOI: 10.1051/0004-6361/201832669. arXiv: 1801.06222 [astro-ph.GA].

[244] M. K. Rodriguez Wimberly et al. "The suppression of star formation on the smallest scales: what role does environment play?" In: *MNRAS* 483.3 (Mar. 2019), pp. 4031–4039. DOI: 10.1093/mnras/sty3357. arXiv: 1806.07891 [astro-ph.GA].

[245] Ian U. Roederer et al. "Detailed Chemical Abundances in the r-process-rich Ultra-faint Dwarf Galaxy Reticulum 2". In: *AJ* 151.3, 82 (Mar. 2016), p. 82. DOI: 10.3847/0004-6256/151/3/82. arXiv: 1601.04070 [astro-ph.SR].

[246] Donatella Romano et al. "Chemical enrichment in very low metallicity environments: Boötes I". In: *MNRAS* 446.4 (Feb. 2015), pp. 4220–4231. DOI: 10.1093/mnras/stu2427. arXiv: 1411.4508 [astro-ph.GA].

[247] Teresa L. Ross et al. "Measuring Metallicities with HST/WFC3 photometry". In: *arXiv e-prints*, arXiv:1310.4553 (Oct. 2013), arXiv:1310.4553. arXiv: 1310.4553 [astro-ph.GA].

[248] Teresa L. Ross et al. "Metallicity Distribution Functions of Four Local Group Dwarf Galaxies". In: *AJ* 149.6, 198 (June 2015), p. 198. DOI: 10.1088/0004-6256/149/6/198. arXiv: 1504.07264 [astro-ph.GA].

[249] Emma V. Ryan-Weber et al. "The Local Group dwarf Leo T: HI on the brink of star formation". In: *MNRAS* 384.2 (Feb. 2008), pp. 535–540. DOI: 10.1111/j.1365-2966.2007.12734.x. arXiv: 0711.2979 [astro-ph].

[250] Elena Sacchi et al. "Star Formation Histories of Ultra-faint Dwarf Galaxies: Environmental Differences between Magellanic and Non-Magellanic Satellites?" In: *ApJL* 920.1, L19 (Oct. 2021), p. L19. DOI: 10.3847/2041-8213/ac2aa3. arXiv: 2108.04271 [astro-ph.GA].

[251] Laura V. Sales, Amina Helmi, and Giuseppina Battaglia. "The Effect of Tidal Stripping on Composite Stellar Populations in Dwarf Spheroidal Galaxies". In: *Advances in Astronomy* 2010, 194345 (Jan. 2010), p. 194345. DOI: 10.1155/2010/194345. arXiv: 0910.0471 [astro-ph.GA].

[252] Mahsa Sanati et al. "How much metal did the first stars provide to the ultra-faint dwarfs?" In: *AAP* 669, A94 (Jan. 2023), A94. DOI: 10.1051/0004-6361/202244309. arXiv: 2206.11351 [astro-ph.GA].

[253] David J. Sand et al. "Tidal Signatures in the Faintest Milky Way Satellites: The Detailed Properties of Leo V, Pisces II, and Canes Venatici II". In: *ApJ* 756.1, 79 (Sept. 2012), p. 79. DOI: 10.1088/0004-637X/756/1/79. arXiv: 1111.6608 [astro-ph.CO].

[254] David J. Sand et al. "Tucana B: A Potentially Isolated and Quenched Ultra-faint Dwarf Galaxy at D $\approx$ 1.4 Mpc". In: *ApJL* 935.1, L17 (Aug. 2022), p. L17. DOI: 10.3847/2041-8213/ac85ee. arXiv: 2205.09129 [astro-ph.GA].

[255] Nathan R. Sandford, Daniel R. Weisz, and Yuan-Sen Ting. "Forecasting Chemical Abundance Precision for Extragalactic Stellar Archaeology". In: *ApJS* 249.2, 24 (Aug. 2020), p. 24. DOI: 10.3847/1538-4365/ab9cb0. arXiv: 2006.08640 [astro-ph.SR].

[256] Nathan R. Sandford, Daniel R. Weisz, and Yuan-Sen Ting. "Validating Stellar Abundance Measurements from Multi-Resolution Spectroscopy". In: *arXiv e-prints*, arXiv:2303.04098 (Mar. 2023), arXiv:2303.04098. DOI: 10.48550/arXiv.2303.04098. arXiv: 2303.04098 [astro-ph.SR].

[257] Nathan R. Sandford et al. "Strong Outflows and Inefficient Star Formation in the Reionization-era Ultra-faint Dwarf Galaxy Eridanus II". In: *arXiv e-prints*, arXiv:2210.17045 (Oct. 2022), arXiv:2210.17045. arXiv: 2210.17045 [astro-ph.GA].

[258] Nathan R. Sandford et al. "Strong outflows and inefficient star formation in the reionization-era ultrafaint dwarf galaxy Eridanus II". In: *MNRAS* 530.2 (May 2024), pp. 2315–2335. DOI: 10.1093/mnras/stae1010. arXiv: 2210.17045 [astro-ph.GA].

[259] Isabel M. E. Santos-Santos, Julio F. Navarro, and Alan McConnachie. "The Tucana dwarf spheroidal: a distant backsplash galaxy of M31?" In: *MNRAS* 520.1 (Mar. 2023), pp. 55–62. DOI: 10.1093/mnras/stad085. arXiv: 2207.02229 [astro-ph.GA].

[260] I. Saviane, E. V. Held, and G. Bertelli. "The stellar populations of the Fornax dwarf spheroidal galaxy". In: *AAP* 355 (Mar. 2000), pp. 56–68. arXiv: astro-ph/9912427 [astro-ph].

[261] I. Saviane, E. V. Held, and G. Piotto. "CCD photometry of the Tucana dwarf galaxy." In: *AAP* 315 (Nov. 1996), pp. 40–51. DOI: 10.48550/arXiv.astro-ph/9601165. arXiv: astro-ph/9601165 [astro-ph].

[262] Ivo Saviane et al. "Population gradients in nearby dwarf galaxies". In: *MEMSAI* 72 (Jan. 2001), pp. 773–778. arXiv: astro-ph/0101250 [astro-ph].

[263] A. Savino et al. "The age of the Milky Way inner stellar spheroid from RR Lyrae population synthesis". In: *AAP* 641, A96 (Sept. 2020), A96. DOI: 10.1051/0004-6361/202038305. arXiv: 2006.12507 [astro-ph.GA].

[264] A. Savino et al. "The HST/ACS star formation history of the Tucana dwarf spheroidal galaxy: clues from the horizontal branch". In: *AAP* 630, A116 (Oct. 2019), A116. DOI: 10.1051/0004-6361/201936077. arXiv: 1909.04052 [astro-ph.GA].

[265] Alessandro Savino et al. "The Hubble Space Telescope Survey of M31 Satellite Galaxies. I. RR Lyrae-based Distances and Refined 3D Geometric Structure". In: *ApJ* 938.2, 101 (Oct. 2022), p. 101. DOI: 10.3847/1538-4357/ac91cb. arXiv: 2206.02801 [astro-ph.GA].

[266] Alessandro Savino et al. "The Hubble Space Telescope Survey of M31 Satellite Galaxies. II. The Star Formation Histories of Ultrafaint Dwarf Galaxies". In: *ApJ* 956.2, 86 (Oct. 2023), p. 86. DOI: 10.3847/1538-4357/acf46f. arXiv: 2305.13360 [astro-ph.GA].

[267] Edward F. Schlafly and Douglas P. Finkbeiner. "Measuring Reddening with Sloan Digital Sky Survey Stellar Spectra and Recalibrating SFD". In: *ApJ* 737.2, 103 (Aug. 2011), p. 103. DOI: 10.1088/0004-637X/737/2/103. arXiv: 1012.4804 [astro-ph.GA].

[268] David J. Schlegel, Douglas P. Finkbeiner, and Marc Davis. "Maps of Dust Infrared Emission for Use in Estimation of Reddening and Cosmic Microwave Background Radiation Foregrounds". In: *ApJ* 500.2 (June 1998), pp. 525–553. DOI: 10.1086/305772. arXiv: astro-ph/9710327 [astro-ph].

[269] Maarten Schmidt. "The Rate of Star Formation. II. The Rate of Formation of Stars of Different Mass." In: *ApJ* 137 (Apr. 1963), p. 758. DOI: 10.1086/147553.

[270] J. Schroyen et al. "Simulations of the formation and evolution of isolated dwarf galaxies - II. Angular momentum as a second parameter". In: *MNRAS* 416.1 (Sept. 2011), pp. 601–617. DOI: 10.1111/j.1365-2966.2011.19083.x. arXiv: 1105.5634 [astro-ph.GA].

[271] J. Schroyen et al. "Stellar orbits and the survival of metallicity gradients in simulated dwarf galaxies". In: *MNRAS* 434.1 (Sept. 2013), pp. 888–905. DOI: 10.1093/mnras/stt1084. arXiv: 1306.4910 [astro-ph.CO].

[272] L. Searle and R. Zinn. "Composition of halo clusters and the formation of the galactic halo." In: *ApJ* 225 (Oct. 1978), pp. 357–379. DOI: 10.1086/156499.

[273] N. Shipp et al. "Stellar Streams Discovered in the Dark Energy Survey". In: *ApJ* 862.2, 114 (Aug. 2018), p. 114. DOI: 10.3847/1538-4357/aacdab. arXiv: 1801.03097 [astro-ph.GA].

[274] J. D. Simon et al. "Birds of a Feather? Magellan/IMACS Spectroscopy of the Ultra-faint Satellites Grus II, Tucana IV, and Tucana V". In: *ApJ* 892.2, 137 (Apr. 2020), p. 137. DOI: 10.3847/1538-4357/ab7ccb. arXiv: 1911.08493 [astro-ph.GA].

[275] J. D. Simon et al. "Stellar Kinematics and Metallicities in the Ultra-faint Dwarf Galaxy Reticulum II". In: *ApJ* 808.1, 95 (July 2015), p. 95. DOI: 10.1088/0004-637X/808/1/95. arXiv: 1504.02889 [astro-ph.GA].

[276] Joshua D. Simon. "Gaia Proper Motions and Orbits of the Ultra-faint Milky Way Satellites". In: *ApJ* 863.1, 89 (Aug. 2018), p. 89. DOI: 10.3847/1538-4357/aacdfb. arXiv: 1804.10230 [astro-ph.GA].

[277] Joshua D. Simon. "The Faintest Dwarf Galaxies". In: *ARAA* 57 (Aug. 2019), pp. 375–415. DOI: 10.1146/annurev-astro-091918-104453. arXiv: 1901.05465 [astro-ph.GA].

[278] Joshua D. Simon and Marla Geha. "The Kinematics of the Ultra-faint Milky Way Satellites: Solving the Missing Satellite Problem". In: *ApJ* 670.1 (Nov. 2007), pp. 313–331. DOI: 10.1086/521816. arXiv: 0706.0516 [astro-ph].

[279] Joshua D. Simon et al. "A Complete Spectroscopic Survey of the Milky Way Satellite Segue 1: The Darkest Galaxy". In: *ApJ* 733.1, 46 (May 2011), p. 46. DOI: 10.1088/0004-637X/733/1/46. arXiv: 1007.4198 [astro-ph.GA].

[280] Joshua D. Simon et al. "Eridanus II: A Fossil from Reionization with an Off-center Star Cluster". In: *ApJ* 908.1, 18 (Feb. 2021), p. 18. DOI: 10.3847/1538-4357/abd31b. arXiv: 2012.00043 [astro-ph.GA].

[281] Joshua D. Simon et al. "Timing the r-process Enrichment of the Ultra-faint Dwarf Galaxy Reticulum II". In: *ApJ* 944.1, 43 (Feb. 2023), p. 43. DOI: 10.3847/1538-4357/aca9d1. arXiv: 2212.00810 [astro-ph.GA].

[282] Evan D. Skillman et al. "The ISLAndS Project. II. The Lifetime Star Formation Histories of Six Andomeda dSphS". In: *ApJ* 837.2, 102 (Mar. 2017), p. 102. DOI: 10.3847/1538-4357/aa60c5. arXiv: 1606.01207 [astro-ph.GA].

[283] Colin T. Slater, Eric F. Bell, and Nicolas F. Martin. "Andromeda XXVIII: A Dwarf Galaxy More Than 350 kpc from Andromeda". In: *ApJL* 742.1, L14 (Nov. 2011), p. L14. DOI: 10.1088/2041-8205/742/1/L14. arXiv: 1110.5903 [astro-ph.GA].

[284] Colin T. Slater et al. "A Deep Study of the Dwarf Satellites Andromeda XXVIII and Andromeda XXIX". In: *ApJ* 806.2, 230 (June 2015), p. 230. DOI: 10.1088/0004-637X/806/2/230. arXiv: 1505.02161 [astro-ph.GA].

[285] Matthew C. Smith, Debora Sijacki, and Sijing Shen. "Cosmological simulations of dwarfs: the need for ISM physics beyond SN feedback alone". In: *MNRAS* 485.3 (May 2019), pp. 3317–3333. DOI: 10.1093/mnras/stz599. arXiv: 1807.04288 [astro-ph.GA].

[286] Simon E. T. Smith et al. "Discovery of a new Local Group Dwarf Galaxy Candidate in UNIONS: Boötes V". In: *arXiv e-prints*, arXiv:2209.08242 (Sept. 2022), arXiv:2209.08242. DOI: 10.48550/arXiv.2209.08242. arXiv: 2209.08242 [astro-ph.GA].

[287] Joshua S. Speagle. "DYNESTY: a dynamic nested sampling package for estimating Bayesian posteriors and evidences". In: *MNRAS* 493.3 (Apr. 2020), pp. 3132–3158. DOI: 10.1093/mnras/staa278. arXiv: 1904.02180 [astro-ph.IM].

[288] E. Starkenburg et al. "The extremely low-metallicity tail of the Sculptor dwarf spheroidal galaxy". In: *AAP* 549, A88 (Jan. 2013), A88. DOI: 10.1051/0004-6361/201220349. arXiv: 1211.4592 [astro-ph.GA].

[289] E. Starkenburg et al. "The NIR Ca ii triplet at low metallicity. Searching for extremely low-metallicity stars in classical dwarf galaxies". In: *AAP* 513, A34 (Apr. 2010), A34. DOI: 10.1051/0004-6361/200913759. arXiv: 1002.2963 [astro-ph.SR].

[290] Else Starkenburg et al. "The oldest and most metal-poor stars in the APOSTLE Local Group simulations". In: *MNRAS* 465.2 (Feb. 2017), pp. 2212–2224. DOI: 10.1093/mnras/stw2873. arXiv: 1609.05214 [astro-ph.GA].

[291] Else Starkenburg et al. "The Pristine survey - I. Mining the Galaxy for the most metal-poor stars". In: *MNRAS* 471.3 (Nov. 2017), pp. 2587–2604. DOI: 10.1093/mnras/stx1068. arXiv: 1705.01113 [astro-ph.GA].

[292] G. S. Stinson et al. "Breathing in Low-Mass Galaxies: A Study of Episodic Star Formation". In: *ApJ* 667.1 (Sept. 2007), pp. 170–175. DOI: 10.1086/520504. arXiv: 0705.4494 [astro-ph].

[293] Bengt Strömgren. "Spectral Classification Through Photoelectric Narrow-Band Photometry". In: *ARAA* 4 (Jan. 1966), p. 433. DOI: 10.1146/annurev.aa.04.090166.002245.

[294] Kung-Yi Su et al. "Discrete effects in stellar feedback: Individual Supernovae, Hypernovae, and IMF Sampling in Dwarf Galaxies". In: *MNRAS* 480.2 (Oct. 2018), pp. 1666–1675. DOI: 10.1093/mnras/sty1928. arXiv: 1712.02795 [astro-ph.GA].

[295] S. Taibi et al. "Stellar metallicity gradients of Local Group dwarf galaxies". In: *AAP* 665, A92 (Sept. 2022), A92. DOI: 10.1051/0004-6361/202243508. arXiv: 2206.08988 [astro-ph.GA].

[296] S. Taibi et al. "The Tucana dwarf spheroidal galaxy: not such a massive failure after all". In: *AAP* 635, A152 (Mar. 2020), A152. DOI: 10.1051/0004-6361/201937240. arXiv: 2001.11410 [astro-ph.GA].

[297] Elisa A. Tau, A. Katherina Vivas, and Clara E. Martínez-Vázquez. "Extended Stellar Populations in Ultrafaint Dwarf Galaxies". In: *AJ* 167.2, 57 (Feb. 2024), p. 57. DOI: 10.3847/1538-3881/ad1509. arXiv: 2312.07279 [astro-ph.GA].

[298] Maureen Teyssier, Kathryn V. Johnston, and Michael Kuhlen. "Identifying Local Group field galaxies that have interacted with the Milky Way". In: *MNRAS* 426.3 (Nov. 2012), pp. 1808–1818. DOI: 10.1111/j.1365-2966.2012.21793.x. arXiv: 1207.2768 [astro-ph.GA].

[299] B. M. Tinsley. "Evolution of the Stars and Gas in Galaxies". In: *FCP* 5 (Jan. 1980), pp. 287–388.

[300] Eline Tolstoy, Vanessa Hill, and Monica Tosi. "Star-Formation Histories, Abundances, and Kinematics of Dwarf Galaxies in the Local Group". In: *ARAA* 47.1 (Sept. 2009), pp. 371–425. DOI: 10.1146/annurev-astro-082708-101650. arXiv: 0904.4505 [astro-ph.CO].

[301] Eline Tolstoy, Vanessa Hill, and Monica Tosi. "Star-Formation Histories, Abundances, and Kinematics of Dwarf Galaxies in the Local Group". In: *ARAA* 47.1 (Sept. 2009), pp. 371–425. DOI: 10.1146/annurev-astro-082708-101650. arXiv: 0904.4505 [astro-ph.CO].

[302] Eline Tolstoy et al. "A 3D view of dwarf galaxies with Gaia and VLT/FLAMES. I. The Sculptor dwarf spheroidal". In: *AAP* 675, A49 (July 2023), A49. DOI: 10.1051/0004-6361/202245717. arXiv: 2304.11980 [astro-ph.GA].

[303] Eline Tolstoy et al. "Two Distinct Ancient Components in the Sculptor Dwarf Spheroidal Galaxy: First Results from the Dwarf Abundances and Radial Velocities Team". In: *ApjL* 617.2 (Dec. 2004), pp. L119–L122. DOI: 10.1086/427388. arXiv: astro-ph/0411029 [astro-ph].

[304] E. Vanhollebeke, M. A. T. Groenewegen, and L. Girardi. "Stellar populations in the Galactic bulge. Modelling the Galactic bulge with TRILEGAL". In: *AAP* 498.1 (Apr. 2009), pp. 95–107. DOI: 10.1051/0004-6361/20078472.

[305] Luis C. Vargas, Marla C. Geha, and Erik J. Tollerud. "The Distribution of Alpha Elements in Andromeda Dwarf Galaxies". In: *ApJ* 790.1, 73 (July 2014), p. 73. DOI: 10.1088/0004-637X/790/1/73. arXiv: 1406.0510 [astro-ph.GA].

[306] Luis C. Vargas, Marla C. Geha, and Erik J. Tollerud. "The Distribution of Alpha Elements in Andromeda Dwarf Galaxies". In: *ApJ* 790.1, 73 (July 2014), p. 73. DOI: 10.1088/0004-637X/790/1/73. arXiv: 1406.0510 [astro-ph.GA].

[307] Luis C. Vargas et al. "The Distribution of Alpha Elements in Ultra-faint Dwarf Galaxies". In: *ApJ* 767.2, 134 (Apr. 2013), p. 134. DOI: 10.1088/0004-637X/767/2/134. arXiv: 1302.6594 [astro-ph.CO].

[308] Kim A. Venn et al. "The Pristine survey - IX. CFHT ESPaDOnS spectroscopic analysis of 115 bright metal-poor candidate stars". In: *MNRAS* 492.3 (Mar. 2020), pp. 3241–3262. DOI: 10.1093/mnras/stz3546. arXiv: 1910.06340 [astro-ph.SR].

[309] A. Katherina Vivas et al. "Variable Stars in the Field of the Hydra II Ultra-faint Dwarf Galaxy". In: *AJ* 151.5, 118 (May 2016), p. 118. DOI: 10.3847/0004-6256/151/5/118. arXiv: 1510.05539 [astro-ph.GA].

[310] Matthew G. Walker et al. "A Universal Mass Profile for Dwarf Spheroidal Galaxies?" In: *ApJ* 704.2 (Oct. 2009), pp. 1274–1287. DOI: 10.1088/0004-637X/704/2/1274. arXiv: 0906.0341 [astro-ph.CO].

[311] Matthew G. Walker et al. "Internal Kinematics of the Fornax Dwarf Spheroidal Galaxy". In: *AJ* 131.4 (Apr. 2006), pp. 2114–2139. DOI: 10.1086/500193. arXiv: astro-ph/0511465 [astro-ph].

[312] Matthew G. Walker et al. "Magellan/M2FS Spectroscopy of the Reticulum 2 Dwarf Spheroidal Galaxy". In: *ApJ* 808.2, 108 (Aug. 2015), p. 108. DOI: 10.1088/0004-637X/808/2/108. arXiv: 1504.03060 [astro-ph.GA].

[313] Matthew G. Walker et al. "Magellan/M2FS Spectroscopy of Tucana 2 and Grus 1". In: *ApJ* 819.1, 53 (Mar. 2016), p. 53. DOI: 10.3847/0004-637X/819/1/53. arXiv: 1511.06296 [astro-ph.GA].

[314] Fletcher Waller et al. "The Cosmic Hunt for members in the outskirts of ultra-faint dwarf galaxies: Ursa Major I, Coma Berenices, and Boötes I". In: *MNRAS* 519.1 (Feb. 2023), pp. 1349–1365. DOI: 10.1093/mnras/stac3563. arXiv: 2208.07948 [astro-ph.GA].

[315] David H. Weinberg, Brett H. Andrews, and Jenna Freudenburg. "Equilibrium and Sudden Events in Chemical Evolution". In: *ApJ* 837.2, 183 (Mar. 2017), p. 183. DOI: 10.3847/1538-4357/837/2/183. arXiv: 1604.07435 [astro-ph.GA].

[316] Daniel R. Weisz and Michael Boylan-Kolchin. "Local Group ultra-faint dwarf galaxies in the reionization era". In: *MNRAS* 469.1 (July 2017), pp. L83–L88. DOI: 10.1093/mnrasl/slx043. arXiv: 1702.06129 [astro-ph.GA].

[317] Daniel R. Weisz, Alessandro Savino, and Andrew E. Dolphin. "On the Reionization-era Globular Cluster in the Low-mass Galaxy Eridanus II". In: *ApJ* 948.1, 50 (May 2023), p. 50. DOI: 10.3847/1538-4357/acc328. arXiv: 2303.11348 [astro-ph.GA].

[318] Daniel R. Weisz et al. "Comparing M31 and Milky Way Satellites: The Extended Star Formation Histories of Andromeda II and Andromeda XVI". In: *ApJ* 789.1, 24 (July 2014), p. 24. DOI: 10.1088/0004-637X/789/1/24. arXiv: 1405.4870 [astro-ph.GA].

[319] Daniel R. Weisz et al. "The Star Formation Histories of Local Group Dwarf Galaxies. I. Hubble Space Telescope/Wide Field Planetary Camera 2 Observations". In: *ApJ* 789.2, 147 (July 2014), p. 147. DOI: 10.1088/0004-637X/789/2/147. arXiv: 1404.7144 [astro-ph.GA].

[320] Daniel R. Weisz et al. "The Star Formation History of Leo T from Hubble Space Telescope Imaging". In: *ApJ* 748.2, 88 (Apr. 2012), p. 88. DOI: 10.1088/0004-637X/748/2/88. arXiv: 1201.4859 [astro-ph.CO].

[321] Andrew Wetzel et al. "Public Data Release of the FIRE-2 Cosmological Zoom-in Simulations of Galaxy Formation". In: *ApJS* 265.2, 44 (Apr. 2023), p. 44. DOI: 10.3847/1538-4365/acb99a. arXiv: 2202.06969 [astro-ph.GA].

[322] Coral Wheeler et al. "Be it therefore resolved: cosmological simulations of dwarf galaxies with 30 solar mass resolution". In: *MNRAS* 490.3 (Dec. 2019), pp. 4447–4463. DOI: 10.1093/mnras/stz2887. arXiv: 1812.02749 [astro-ph.GA].

[323] S. D. M. White and M. J. Rees. "Core condensation in heavy halos: a two-stage theory for galaxy formation and clustering." In: *MNRAS* 183 (May 1978), pp. 341–358. DOI: 10.1093/mnras/183.3.341.

[324] Devin D. Whitten et al. "The Photometric Metallicity and Carbon Distributions of the Milky Way's Halo and Solar Neighborhood from S-PLUS Observations of SDSS Stripe 82". In: *ApJ* 912.2, 147 (May 2021), p. 147. DOI: 10.3847/1538-4357/abee7e. arXiv: 2104.00016 [astro-ph.GA].

[325] B. Willman and J. Strader. ""Galaxy," Defined". In: *AJ* 144.3, 76 (Sept. 2012), p. 76. DOI: 10.1088/0004-6256/144/3/76. arXiv: 1203.2608 [astro-ph.CO].

[326] Beth Willman et al. "A New Milky Way Companion: Unusual Globular Cluster or Extreme Dwarf Satellite?" In: *AJ* 129.6 (June 2005), pp. 2692–2700. DOI: 10.1086/430214. arXiv: astro-ph/0410416 [astro-ph].

[327] Beth Willman et al. "Willman 1 - A Galactic Satellite at 40 kpc With Multiple Stellar Tails". In: *arXiv e-prints*, astro-ph/0603486 (Mar. 2006), astro–ph/0603486. arXiv: astro-ph/0603486 [astro-ph].

[328] Beth Willman et al. "Willman 1—A Probable Dwarf Galaxy with an Irregular Kinematic Distribution". In: *AJ* 142.4, 128 (Oct. 2011), p. 128. DOI: 10.1088/0004-6256/142/4/128. arXiv: 1007.3499 [astro-ph.GA].

[329] K. Youakim et al. "The Pristine survey - III. Spectroscopic confirmation of an efficient search for extremely metal-poor stars". In: *MNRAS* 472.3 (Dec. 2017), pp. 2963–2974. DOI: 10.1093/mnras/stx2005. arXiv: 1708.01264 [astro-ph.GA].

[330] K. Youakim et al. "The Pristine Survey - VIII. The metallicity distribution function of the Milky Way halo down to the extremely metal-poor regime". In: *MNRAS* 492.4 (Mar. 2020), pp. 4986–5002. DOI: 10.1093/mnras/stz3619. arXiv: 2001.04988 [astro-ph.GA].

[331] R. Zinn. "The globular cluster system of the galaxy. I. The metal abundances and reddenings of 79 globular clusters from integrated light measurements." In: *ApJS* 42 (Jan. 1980), pp. 19–40. DOI: 10.1086/190643.

[332] Sebastiaan L. Zoutendijk et al. "The MUSE-Faint survey. I. Spectroscopic evidence for a star cluster in Eridanus 2 and constraints on MACHOs as a constituent of dark matter". In: *AAP* 635, A107 (Mar. 2020), A107. DOI: 10.1051/0004-6361/201936155. arXiv: 2001.08790 [astro-ph.GA].